Spatial and temporal dynamics of retinal ganglion cells with different photoreceptor inputs

Martha Rose Robinson

A thesis presented for the degree of

Doctor of Philosophy

Gene and Cell Therapy Group

UCL

2017

I, Martha Rose Robinson confirm that the work presented in this thesis is my own. Where information has been derived from other sources, I confirm that this has been indicated in the thesis.

Signature _____ Date _____

Abstract

The retina must operate over a wide range of light levels. Two classes of input cells, rods and cones, specialised to different light conditions evolved to achieve this task. This thesis examines how interactions between these two classes shape retinal output as the light level changes, and the extent to which loss of one class can alter processing of the remaining class.

Retinal ganglion cell (RGC) receptive fields were characterised using multielectrode array recordings performed during presentation of spatiotemporal white noise across a 4.5 $\log_{10}$ light level range. Receptive field properties were compared between wild-type mice, mice lacking functional cones (cpfl1 model of achromatopsia), and mice lacking functional rods (rd17 model of congenital stationary night blindness).

The response of RGCs to otherwise identical stimuli changed with ambient light level. In low light conditions, wild-type RGCs had a longer latency to spike and were shifted towards higher temporal and lower spatial frequency tuning. Of those RGCs characterised at multiple light levels, 28% changed the polarity of their receptive fields between ON and OFF. These polarity switches occurred between every possible pair of light levels, and several cells were observed to switch multiple times. RGCs which switched polarity were identified in both rd17 and cpfl1 mice, indicating that at least some circuit mechanisms responsible are driven by a single photoreceptor cell class.

Loss of function in one photoreceptor cell class altered visual processing of inputs from the remaining class. In low light conditions, RGCs in cpfl1 mice showed shorter latency to spike and a marked shift towards higher temporal frequency tuning, a receptive field property that is often understood as indicating tuning to visual motion. This difference in visual processing could result in behavioural differences, for instance these mice may exhibit better contrast sensitivity at temporal frequencies in low light conditions.

Contents

List of Figures

Acknowledgements

This thesis would not have been possible without the support and patience of my principal supervisor, Prof. Robin Ali. In particular, I would like to thank him for creating and maintaining the scientific environment of the lab and for striving to keep me focussed.

I owe a huge debt to Dr Kate Powell and Dr Matteo Rizzi for their extensive support throughout this PhD. Kate, your insight and precision always makes me think more deeply about any question, and your sense of humour has improved many otherwise stressful days. Matteo, your lateral thinking and wide reading always produce useful feedback and interesting discussions, and your kindness and patience have made you a pleasure to work with. I feel very lucky to have been a member of "team neuroscience", and I hope to be able to pay forward the support you have given me to students in the future.

At the start of this project, I was new to visual neuroscience and a novice programmer. I am grateful to Dr Andrea Bennucci for helpful discussions and scientific advice in the early stages, and to all teachers and students involved in OCNC for their insights, advice, and feedback on this work. I am also grateful to the Research Software Development team at UCL, for all the tools, training, mentoring, and support that they offer. Additionally, Prof. Kate Jeffery provided extensive and extremely helpful feedback on

the draft of this thesis, for which I am very thankful.

I am also grateful to all lab members for their friendship and emotional support. In particular, I'd like to thank Dr Mark Basche for his friendship and regular lunch companionship, and Dr Anna Graca for her services as both deskmate and flatmate. I'd also like to thank Heather Kneale for all her administrative support, which made the difference between paying the bills and not more than once.

Finally, I would like to thank my family. To my parents, Karen and David, thank you for always encouraging my interest in science and for supporting me throughout my many, many years of school. To my siblings, Annie and Fred, for their love, humour, and complete unwillingness to learn what it is I actually do. And to Murray - I met you as I was just starting this PhD, and I'm so happy that you decided to stick around. Thank you for all the support you've given me throughout this process, and for building a wonderful home with me.

"Many of you may wonder why anyone would spend the better part of a lifetime doing little more than recording from retinal ganglion cells, as I have done, so, I will give some justification for this a little bit later."

(Chirstina Enroth-Cugell)

Abbreviations

cGMP Cyclic guanyl monophosphate

CSNB Congenital stationary night blindness

Cx36 Connexin 36

ERG Electroretinogram

DoG Difference of Gaussians

DSGC Direction selective ganglion cell

GCL Ganglion cell layer

GPCR G-protein coupled receptor

GTP Guanosine triphosphate

IGL Intergeniculate leaflet

INL Inner nuclear layer

IPL Inner plexiform layer

IS Inner segment

LNP Linear nonlinear Poisson

MEA Multielectrode array

ONL Outer nuclear layer

OPL Outer plexiform layer

OPN Olivary pretectal nucleus

OS Outer segment

OPTICS Ordering points to identify the clustering structure

PCA Principal components analysis

RGB Red green blue colour system

RGC Retinal ganglion cell

RPE Retinal pigment epithelium

SA Starburst amacrine cell

SCN Suprachiasmatic nucleus

STA Spike triggered average

STC Spike triggered covariance

1 Introduction

Visually guided behaviour is possible on a night illuminated only by starlight, and also on a sunny day or in a brightly lit room. To those capable of such visual tasks, this observation may seem pedestrian. In fact, the ability of the eye to respond reliably across an environmental light level range far larger than the dynamic range of any single input cell is a remarkable feat. Humans can detect small numbers of photons (Hecht *et al.*, 1942) and even single photons above chance (Tinsley *et al.*, 2016). Equally, visually guided behaviour is possible in bright sunlight of up to 10 log units higher intensity.

The retinal circuitry combines responses from two classes of input cells - rods and cones - to produce ganglion cell output. When one of these classes is lost or non-functional, the range over which functional vision is possible is reduced.

This thesis examines the role that interactions between these two input classes play in shaping retinal output across the environmental light level range, and the extent to which loss of one class can alter processing of the remaining class.

1.1 Retinal circuitry: Inputs

1.1.1 Photoreceptive cells: Three classes of visual input

In 1866, Max Schultze proposed the duplicity theory of vision: that there are two classes of photosensitive cells in the vertebrate retina, and that they mediate two distinct types of vision. Rods are responsible for scotopic, nocturnal, achromatic vision, and cones for photopic, diurnal, chromatic vision (Schultze (1866), as described in Stabell & Stabell (2013)). There are in fact three classes of photoreceptor cells in the vertebrate retina: rods, cones, and melanopsin-positive ganglion cells (predicted by Keeler *et al.* (1928) and reviewed in Van Gelder (2008)). However, as this additional form of photo-detection appears to primarily mediate circadian rhythms and other 'non-visual' light responses, the duplicity theory of vision remains useful.

Each photoreceptor cell class relies on specific light-sensitive molecules that consist of an opsin protein and a chromophore derived from vitamin A. These molecules are G-protein coupled receptors (GPCRs), and their activation through interaction with photons triggers a phototransduction cascade which modulates the membrane potential of the cell and its resulting output behaviour. Aside from this basic similarity, each photoreceptor cell class is both anatomically and functionally distinct, and the output from each class is processed differently.

It is important to study the differences between each class of visual input, the 'duplicity' in the aspects of vision that they modulate, and the overlap between different photo-detection systems in order to understand the structure and function of the rest of the visual circuitry.

Rods

Rods are named for the rod-like structure of their outer segments. Rods are the most abundant photoreceptor cell in the vertebrate retina, and are absent from the fovea in those animals that have one.

Unlike most neurons, photoreceptor cells maintain a steady synaptic release of transmitter in the absence of input (darkness), and *reduce* this transmitter release to indicate the presence of a signal (light). In darkness, rods are therefore constitutively depolarised and maintain steady synaptic release of glutamate. This depolarisation is due to a steady 'dark current' caused by cations (primarily Na^+) moving into the cell along their concentration gradient, through open cyclic nucleotide gated ion channels. These channels are kept open by the high concentration of cyclic guanyl monophosphate (cGMP) available in these cells in the dark. When a cell is depolarised in this way, voltage-gated calcium channels in the membrane allow Ca^2+ influx, which stimulates the rod photoreceptor cell to release vesicles containing glutamate onto post-synaptic bipolar cells (Yau, 1994).

Rods express rhodopsin as the light-detecting opsin in their outer segments. Rhodopsin has a peak sensitivity of around 500nm (Nickle & Robinson, 2007, Tovee, 1994). In darkness, it is bound to 11-*cis*-retinal, which acts to 'lock' the opsin in an inactive state. In the absence of 11-*cis*-retinal, free opsin would activate the phototransduction cascade constantly, regardless of light input (this phenomenon is observed in the $Rpe65^{-/-}$ mouse (Redmond *et al.*, 1998)).

When a photon is absorbed by 11-*cis*-retinal bound to rhodopsin, the opsin-retinal complex is destabilized and thermally decays to free opsin and all-*trans*-retinal, through a series of intermediates. One of these intermediates, metarhodopsin II (Rh*), binds

to and activates transducin, a GTP binding protein complex (Hargrave & McDowell, 1992). Transducin then activates cGMP-phosphodiesterase, which hydrolyses cGMP, reducing intracellular levels of cGMP as so causing cGMP-gated channels to close. Closure of the cGMP-gated channels reduces the 'dark current' of cations into the cell. As K^+ channels in the membrane remain open, carrying outward potassium current, the depolarised cell begins to hyperpolarise towards potassium's -70mV equilibrium potential. The voltage-grated calcium channels close and glutamate release is reduced (Yau, 1994).

As light exposure causes the conversion of 11-*cis* retinal to all-*trans* retinal, rods must recycle this chromophore in order to maintain light responses. To do this, they rely on a visual cycle that takes place partly in the retinal pigment epithelium (RPE). Thus, in the absence of the RPE (as is common in many *ex-vivo* experiments), rods eventually run out of usable 11-*cis* retinal and become photobleached - no longer responding to light. This can be rectified experimentally by providing the cells with the artificial chromophore 9-*cis*-retinal instead (Kefalov, 2012, Saari, 2000).

Unlike cones, vertebrate rods can detect single photons (Baylor *et al.*, 1979, 1984). This is in part due to low 'dark noise' due to low spontaneous thermal activation of the opsin-retinal complex and other elements in the phototransduction cascade (Rieke & Baylor, 1998). As a psychophysical response, however, this phenomenon is perhaps more reliant on a threshold non-linearity at the rod-rod bipolar synapse that allows selective transmission of single photon responses (Cangiano *et al.*, 2012, Field & Rieke, 2002, Lagnado, 2012, Sampath & Rieke, 2004).

Cones

Cones take their name from their cone-like histological appearance. They are more concentrated in the fovea, in animals in which one is present, and are less numerous across the retina than rods. In mouse retina, cones make up just 2.8% of all photoreceptor cells (Jeon *et al.*, 1998). In humans, they account for approximately 4.9%, with 17,500 cones in the rod-free fovea (Osterberg, 1935).

Cones are responsible for colour vision, and as such express a variety of opsins that respond to different wavelengths of light. Humans and primates are trichromats, with three classes of cones which each express a different opsin. The responses from these can then be combined in a RGB colour system, which makes it possible to distinguish many different hues. Trichromat cones can be divided into 'blue' S cones (short-wavelength, which have a peak spectral absorbance of 420nm), 'green' M cones (medium wavelength, 530nm) and 'red' L cones (long-wavelength, 565nm; Tovee (1994)). Other vertebrates use different numbers of colour-sensors. Many birds, reptiles, and amphibians are tetrachromats, while most rodents and other non-primate mammals are dichromats. As such, mice have only two cone opsins. Cones segregate into S cones (expressing only short wavelength opsin), ML/S cones (expressing both medium-long and short wavelength opsins) and ML cones (expressing only medium-long wavelength opsin). The peak of mouse S opsin is UV-shifted relative to humans, at 360nm, while the ML-opsin response overlaps almost completely with rhodopsin, with a peak at 508nm (Ortin-Martinez *et al.*, 2014, Wang *et al.*, 2011). Cone density in the mouse increases dorso-ventrally, and this increase correlates with an increased S-cone density in the ventral compared to the dorsal retina (Ortin-Martinez *et al.*, 2014).

Much like rods, cones have a 'dark current', release glutamate in darkness, and signal light detection through a reduction in glutamate release (Ayoub & Copenhagen, 1991).

However, cones are around 100 times less photosensitive than rods and have response kinetics that are several times faster (Baylor, 1987). This was initially thought to be due to differences in opsin sensitivity and decay time of photoactivated opsin (Imai *et al.*, 1997). However, when rod or cone specific opsins are transgenically coupled to a rod or cone transduction cascade, the response amplitude and kinetics remain identical to normal expectations for that cell type (Fu *et al.*, 2008, Kefalov *et al.*, 2003). This implies that the phototransduction cascade, rather than the specific opsin, determines the photosensitivity and response time of the cell, and that these cascades differ between rods and cones.

The higher temporal sensitivity of cones when compared to rods is due to faster shut-off of light-induced responses, which sharpens cone kinetics and allows differentiation between flashes of light that arrive closer together in time. Specifically, it is posited that phosphorylation and subsequent binding of arrestin to activated opsin are the relevant steps in determining cone temporal resolution (Kefalov, 2012).

Recycling of chromophore also differs in cones compared to rods. While all-*trans*-retinal from cones is converted back to 11-*cis*-retinal in the RPE through the same mechanism used by rods, a second RPE-independent visual cycle accessible only to cones cn be found within the neural retina. Müller glia cells convert all-*trans*-retinol to 11-*cis*-retinal, which cones are able to oxidise in order to regenerate chromophore. This is then trafficked from the inner to the outer segment through another cone-specific mechanism (Kefalov, 2012). The availability of this additional mechanism helps to explain the much faster dark adaptation and resistance to bleaching displayed by cones relative to rods (Kolesnikov *et al.*, 2011). It also means that, unlike rods, cones are able to respond over long periods of time in retina that has been detached from the RPE, without addition of any chromophore.

Melanopsin-positive ganglion cells

Work on rats indicates that approximately 3% of retinal ganglion cells are intrinsically photosensitive (Berson *et al.*, 2002, Hattar *et al.*, 2002). Unlike rods or cones, these cells use a rhabdomeric-like phototransduction cascade, which results in depolarisation of the cell following photon absorption by melanopsin (Hardie, 2001). The wavelength-sensitivity spectrum of these cells is determined by melanopsin, and peaks at 480nm (Berson *et al.*, 2002).

In addition to their intrinsic photosensitivty, melanopsin-positive ganglion cells also receive excitatory and inhibitory synaptic inputs like any other retinal ganglion cell. This means that the spike trains of these cells contain information about light detected by rods and cones, as well as by melanopsin (Dacey *et al.*, 2005, Wong *et al.*, 2007).

Melanopsin-positive ganglion cells project to many central targets. Projections to the intergeniculate leaflet (IGL), the suprachiasmatic nucleus (SCN), and the olivary pretectal nucleus (OPN) support the argument that they are involved in synchronizing circadian rhythms and in the pupillary light reflex (Hattar *et al.*, 2006). As rod and cone inputs to melanopsin-positive ganglion cells increase their light and temporal sensitivity, these may also be necessary for some features of circadian entrainment and other non-image-forming light responses (Wong *et al.*, 2007). A smaller number of direct and indirect projections are also made to the lateral geniculate nucleus (LGN), indicating that the visual cortex may also receive some information from these ganglion cells (Dacey *et al.*, 2005, Hattar *et al.*, 2006). However, studies in blind patients show that functioning melanopsin-positive ganglion cells that can induce circadian entrainment can be present in individuals that have no apparent conscious perception of light (Czeisler *et al.*, 1995, Klerman *et al.*, 2002). The role of these inputs in the function of the visual cortex, if they have one, is therefore unclear.

Photoreceptor-photoreceptor gap junctions

Rods and cones are electrically coupled through gap junctions at their synaptic terminals in the outer plexiform layer. These junctions have been demonstrated both anatomically (Raviola & Gilula, 1973, Tsukamoto *et al.*, 2001) and electrophysiologically (Asteriti *et al.*, 2014, DeVries & Baylor, 1995).

Rods are coupled to rods, forming population pools of between 1-20 rods in the guinea pig (Li & Verweij, 2012) and 1-10 rods in the macaque (Hornstein *et al.*, 2005). Modelling of this system suggests that while rod-rod coupling would reduce dark-adapted sensitivity by impairing noise filtering at the rod-rod bipolar synapse, it also helps to overcome synaptic saturation. This would improve sensitivity to spatially restricted stimuli or to stimuli which are superimposed over background illumination (Li & Verweij, 2012).

Cones are also electrically coupled to other cones by gap junctions formed primarily by connexin-36 (CX36; Lee *et al.* (2003a)). Results from macaque retina reveal that this occurs between red and green cones, but that blue cones do not share in this coupling. This might lead to a trade-off where red-green colour discrimination is reduced in favour of increased luminance discrimination (Söhl *et al.*, 2005).

Finally, rods and cones are coupled through heterologous gap junctions (Lee *et al.*, 2003a, Tsukamoto *et al.*, 2001). Rod activation can be detected in intracellular recordings from neighbouring cones (Asteriti *et al.*, 2014), implying that rod activation could be transmitted through cone pathways directly via cones. Indeed, recordings from retinal ganglion cells conducted while transmission to rod bipolar cells was pharmacologically blocked initially implied that this may be a main route of information transfer for some ganglion cell subtypes (DeVries & Baylor, 1995). However, these results must

now be interpreted in the light of the discovery of a mixed rod-cone bipolar cell which receives rod input through different receptors than the rod bipolar (Soucy *et al.*, 1998).

Rod-cone gap junctions are modulated by the retinal circadian clock. Activation of dopamine D2-like receptors during the day weakens rod-cone coupling, which is stronger at night. This effectively enables a 'synaptic switch' that can allow cones to receive dim light signals from rods at night, but not during the day (Ribelayga *et al.*, 2008).

1.2 Understanding visual processing: Receptive fields in the retina

The retina is often described to patients as a photographic film or digital camera that captures the visual scene and transmits a faithful point-for-point copy to the brain. In reality, the retina performs a great deal of image processing. Rather than transmitting a one-to-one representation of the light incident on the retina to higher visual areas, it transmits a one-to-many representation. Each rod or cone cell connects to multiple bipolar cells, which themselves (indirectly in the case of rod bipolar cells) connect to multiple ganglion cells (Masland, 2001b, Wässle, 2004). Thus, information about the presence or absence of photons at each photoreceptor cell outer segment can be processed in parallel by multiple retinal microcircuits simultaneously.

Cells in each layer of the neural retina can be described as having 'receptive fields' - characteristics of the visual stimulus that change the output of the cell. Photoreceptors, for example, have receptive fields that reflect their position on the retina - light incident on the cells will cause their glutamate output to be reduced. Photoreceptor receptive fields also encompass the wavelength and intensity spectrum that the cell responds to, as well as the effects on the cell's output from gap junction connections from other

photoreceptor cells, and from lateral horizontal cell input. Receptive fields are able to become more complex with additional layers of processing: bipolar and ganglion cells can have highly specific receptive fields that capture particular temporal and spatial characteristics of the stimulus.

In general, the receptive field of any cell can be thought of broadly as that cell's 'preferred stimulus' - a pattern of inputs that produces a maximal response from the cell (such as an increase in the firing rate). Thus, the full and complete receptive field of any cell can be thought of as the convolution of the primary sensory inputs to that cell (in the retina, the photoreceptor cells), and the properties of the microcircuit that processes those inputs. However, the 'receptive field' measured with any particular stimulus paradigm will by definition be restricted to only those aspects that can be stimulated and differentiated within the chosen paradigm. Stimulus choice and interpretation of data with an understanding of the limits of that choice is therefore an essential step in measuring and characterising retinal computation (Masland & Martin, 2007).

Receptive fields in the retina are commonly described as 'centre-surround' - the receptive field has a concentric ring shape, where light in the central ring induces one response in the cell and light in the surround induces a response of the opposite sign. For instance, a retinal ganglion cell could have an 'ON' centre (light in this region causes an increase in firing) and an 'OFF' surround (light in this region suppresses firing, and a decrease in light intensity in this region may drive firing). This kind of receptive field is dependent on the microcircuit of inputs onto the ganglion cell - information about the light from photoreceptor cells in the surround is communicated to the ganglion cell via inhibitory cells, whereas information about the light from photoreceptor cells in the centre is communicated via excitatory cells (Kuffler, 1952). Centre-surround receptive

fields are useful for improving detection resolution - small point stimuli are able to drive the cells more than broad stimuli that cover large portions of the visual field.

The 'centre-surround' description of a retinal cell's receptive field is not necessarily complete (this is discussed in more detail in section 1.4.2, page 38). However, it forms a useful starting point for building an understanding of information processing through the retina.

1.3 Rod and cone pathways: Information flow through the retina

There are at least 55 morphological neuronal cell types in the mammalian retina, each potentially playing a distinct role in visual processing. These include 9 types of cone bipolar cell, a rod bipolar cell, at least 29 varieties of amacrine cell, two classes of horizontal cell, and up to 22 ganglion cell subtypes (Ghosh *et al.*, 2004, Masland, 2001a, Völgyi *et al.*, 2009). So while the retinal circuitry may seem invitingly simple at first glance (rods and cones synapse with bipolar and horizontal cells in the outer plexiform layer, and bipolar cells synapse with amacrine and ganglion cells in the inner plexiform layer), the potential parallel pathways for information to flow through the retina are varied and complex.

In this section, I will approach this complex system from the perspective of rod and cone inputs, focussing on the transmission of these two different sources of visual information and the general characteristics of the neural pathways. Section 1.4 (page 37) will contain a more detailed look at some of the specific microcircuits that can be formed using these diverse cell types, and how they function to extract useful information from the visual scene.

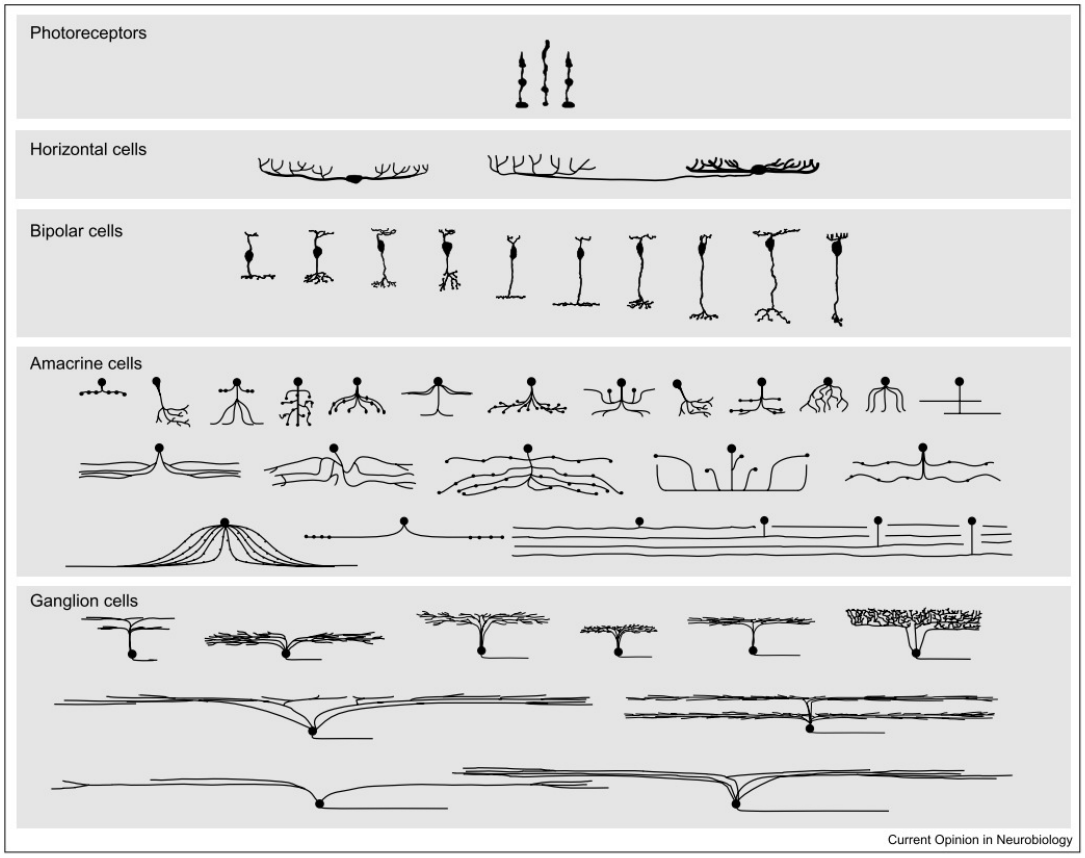

Figure 1.1: **Diversity of neuronal cell types in the retina:** Generic morphological neuronal cell types found in mammalian retinas. Only a subset of wide-field amacrine and ganglion cells are included. Figure from Masland (2001a).

1.3.1 Cone pathways

As cones are evolutionarily older (Lamb, 1995), and as rods are often described as 'parasitic on the cone pathway', I will begin by outlining cone pathways through the retina and then move on to the processing of rod signals.

Cone signals are communicated to retinal ganglion cells through a disynaptic pathway via bipolar cells, with lateral inhibition provided by retinal interneurons. In animals with foveas, cones are responsible for higher-acuity vision than rods. Cone bipolar cells transmit signals from just a few cones and drive ganglion cells with very small receptive fields. In many primate retinas, specialised midget bipolar cells connect to single cones and fully preserve cone acuity (Masland, 2001b). Cones are also responsible for colour

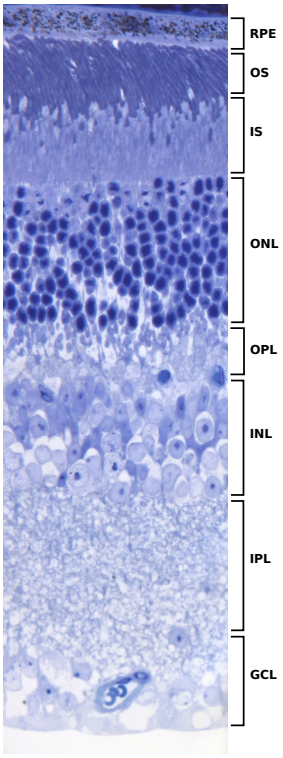

Figure 1.2: **Histology of the retina:** Semithin section of C57BL/6 ('wild-type') mouse retina stained with toluidine blue, kindly provided by Anna Graca and Joana Ribeiro. RPE: retinal pigment epithelium, OS: outer segments of photoreceptor cells, IS: inner segments of photoreceptor cells, ONL: outer nuclear layer, OPL: outer plexiform layer, INL: inner nuclear layer, IPL: inner plexiform layer, GCL: ganglion cell layer.

vision, and colour-selective bipolar, amacrine, and ganglion cells have been identified in many vertebrates (Chen & Li, 2012, Haverkamp *et al.*, 2005, Johnston *et al.*, 2012, Puller & Haverkamp, 2011, Sher & DeVries, 2012).

Cone bipolar cells are divided into two broad categories: ON and OFF. OFF bipolar cells hyperpolarise with light, while ON bipolar cells depolarise with light. This means that an increase in glutamate release at the cone bipolar - ganglion cell synapse can either signal the presence of light detected by cones (via ON bipolar cells) or its absence (via OFF bipolars) (Kolb, 1995, Nelson & Kolb, 1983). As both rods and cones use glutamate as their neurotransmitter (Ayoub & Copenhagen, 1991), the difference in response between ON and OFF bipolar cells is governed by expression of different glutamate receptors at the postsynaptic site (Masland, 2001b).

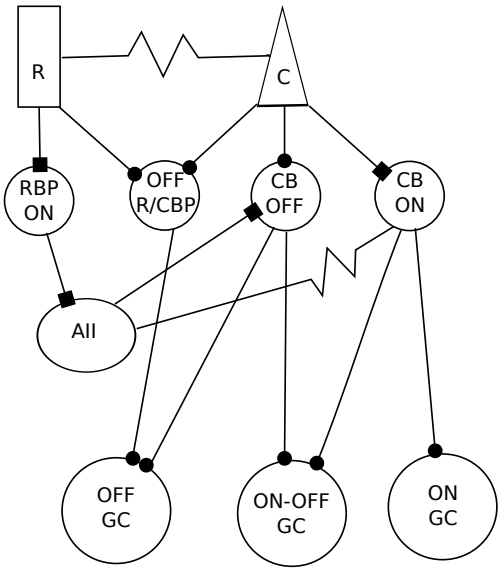

Figure 1.3: **Schematic of rod and cone pathways through the retina:** Schematic diagram adapted from Soucy *et al.* (1998). Sign preserving synapses are indicated by circles, and sign inverting synapses with squares. Electrical coupling via gap junctions is indicated by the 'resistor' symbol. For the sake of clarity, pathways mediating lateral inhibition are not shown. For example lateral inhibition between photoreceptor cells (rods and cones) via horizontal cells, and rods onto rods via A17 and A13 amacrine cells are not included, and neither are amacrine inhibitory inputs onto ganglion cells, which can communicate both rod and cone activation.

OFF bipolar cells express either kainate or AMPA ionotropic receptors selectively. This is one feature that distinguishes distinct OFF bipolar cell populations (Yang *et al.*, 2003). These receptors have different kinetics - AMPA receptors resensitize to glutamate much faster than kainate receptors, and are more selective for transient signal components, rather than sustained characteristics (DeVries, 2000). When activated, both receptors open to act as calcium channels through the cell membrane. In darkness, glutamate release from cones keeps these channels open, and calcium influx acts to depolarise the bipolar cell. When glutamate release from cones drops as they detect light, the channels close and the OFF bipolar cell hyperpolarises.

ON bipolar cells express the metabotropic glutamate receptor mGluR6. Glutamate binding to mGluR6 inhibits the opening of the non-selective cation channel TRPM1-L though an intracellular signalling cascade involving Gαo and G$\beta\gamma$. In darkness, glutamate release from cones inhibits these channels, and the reduction of cation influx

causes the bipolar cell to hyperpolarise. As glutamate release drops during light exposure, so the cation channels are disinhibited and the ON bipolar cell depolarises (Tian & Kammermeier, 2006).

Splitting the visual signal from cones into ON and OFF pathways allows the retina to easily encode successive contrast - temporal changes in light level. Stimuli both brighter and darker than background illumination can be detected and distinguished, providing more information about the visual scene than an absolute brightness measure alone (Kolb, 1995).

ON and OFF bipolar cells are often referred to as ON-centre and OFF-centre, due to the strong centre-surround receptive fields observed in these cells in cold blooded vertebrates. Centre-surround responses are driven by lateral inhibition, which is a common mechanism in the retina that occurs at many levels. The earliest source of lateral inhibition in the cone pathway occurs at the cone triad in the ribbon synapse. Here, horizontal cells provide negative feedback onto cones which form the 'centre' of the bipolar cell responses, modulated by glutamate release from surrounding cones (Baylor *et al.*, 1971). Horizontal cells also provide feedforward lateral inhibition onto bipolar cells themselves (Yang & Wu, 1991).

However, it is important to note that centre-surround responses in bipolar cells are not as strong in mammals as they are in cold blooded vertebrates, and many of the assumptions from research in reptiles and fish cannot easily be applied to mammalian retinal circuitry (Nelson & Kolb, 1983). As strong centre-surround receptive fields are seen in mammalian retinal ganglion cells, it is likely that there are additional lateral-inhibition mechanisms at the level of the bipolar cell-ganglion cell synapse, mediated by amacrine cells (Lebedev & Marshak, 2007).

In the inner plexiform layer (IPL), cone bipolar cells make most of their synapses onto

ganglion cell dendrites, and also some amacrine cells, as well as receiving inhibitory input from amacrine cells (Masland, 2001b). ON and OFF bipolar cells terminate in different sublaminae within the IPL, where specific ganglion and amacrine cell subtypes have their dendrites (Bloomfield & Miller, 1986). The variety in these cell types and circuits form the basis of ganglion cell functional microcircuits.

1.3.2 Rod pathways

There are three pathways available for signals from rods to reach retinal ganglion cells. The first (as outlined in section 1.1.1, page 27), is via cone pathways through gap junctions with cones (Asteriti *et al.*, 2014, Lee *et al.*, 2003a, Tsukamoto *et al.*, 2001). The second is via a dedicated rod bipolar cell. This is an ON cell, which depolarises with light and forms a bulbous arborization in the ON sublamina of the IPL. However, unlike cone bipolars, the rod bipolar cell makes only 0.3% of its synapses with ganglion cells (Strettoi *et al.*, 1990). Instead, rod bipolar dyad synapses form primarily with three different amacrine cell types. Two of these amacrine cells (A17 and A13) form an inhibitory GABAergic reciprocal synapse with the rod bipolar (Bloomfield & Dacheux, 2001). The third amacrine cell type is the AII cell. They receive non-reciprocal synapses from rod bipolar cells, and transfer the rod signals to cone bipolars (Dacheux & Raviola, 1986). The AII amarcine cell forms chemical synapses with OFF cone bipolars and gap junctions with ON cone bipolar axons. Through this route, rod activation can be fed into both ON and OFF computational pathways (Kolb & Famigilietti, 1974).

While rod bipolars do not show classic centre-surround responses, AII amacine cells do, at least in scotopic conditions. GABAergic lateral inhibition from other amacrine cells in the inner retina is likely to be responsible (Bloomfield & Dacheux, 2001).

Finally, there is a third pathway for rod signals through a mixed rod-cone OFF bipolar

cell. Unlike the metabotropic mGluR6 receptors used by the rod bipolar (an ON bipolar), at these synapses glutamate from rods is detected by ionotropic AMPA receptors. These light-hyperpolarising cells have been demonstrated in rodents (Hack *et al.*, 1999, Pang *et al.*, 2012, Soucy *et al.*, 1998, Tsukamoto & Omi, 2013, Tsukamoto *et al.*, 2001) and have now also been identified in primates (Tsukamoto & Omi, 2014).

1.3.3 Horizontal cell mediated photoreceptor-photoreceptor surround inhibition

Cones contact horizontal cell dendrites and rods contact horizontal cell axon terminals. At these sites, horizontal cells form local negative-feedback circuits with photoreceptor cells (Baylor *et al.*, 1971). Horizontal cells create bipolar cell centre-surround receptive fields through feedforward inhibition (Yang & Wu, 1991), but they also provide lateral inhibition onto photoreceptor cells from neighbouring photoreceptor cells. This produces centre-surround receptive fields in the photoreceptor cells themselves. Light at the outer segment (the 'centre') drives hyperpolarisation and reduction in glutamate release. However, light at neighbouring photoreceptor cell segments (the 'surround') drives inhibition via horizontal cells, which acts to depolarise the photoreceptor cell and increase glutamate release. Recent work by Szikra *et al.* (2014) indicates that in mice these inhibitory horizontal cell signals do not only operate locally at the axons and dendrites, mediating lateral inhibition between rods and rods or cones and cones. Instead, the horizontal cell axons also convey information in two directions, allowing cone hyperpolarisation to cause rod depolarisation and rod hyperpolarisation to cause cone depolarisation. The implications of this finding are discussed in more detail in section 1.5.2, page 46.

1.4 Retinal circuitry: Outputs

1.4.1 Retinal ganglion cells: Multiple classes of retinal output

There are between 15 and 22 different vertebrate ganglion cell subtypes, each with their own unique microcircuitry and response properties. Each ganglion cell subtype tiles the retina in a mosaic, so that as well as feeding to multiple ganglion cells, each photoreceptor cell is likely to be an input to multiple different kinds of ganglion cell, each solving an independent visual task (da Silveira & Roska, 2011, Masland, 2001a, Masland & Martin, 2007, Völgyi *et al.*, 2009).

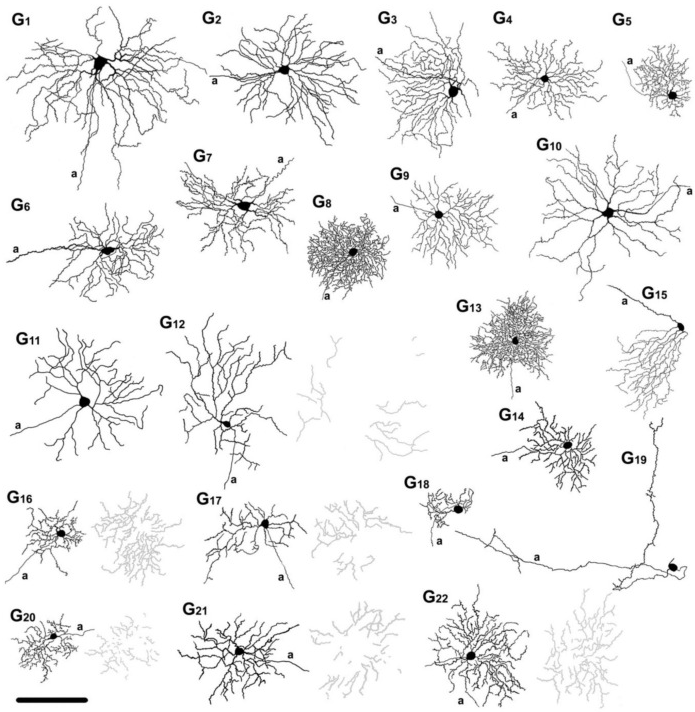

Figure 1.4: **Diversity of ganglion cells in the mouse retina:** There are a large number of morphological subtypes within retinal ganglion cells, which correspond to functional subtypes. Figure from Völgyi *et al.* (2009), scale bar = 100μm.

1.4.2 Defining and characterising receptive fields

As previously outlined, the receptive field of any cell can be considered that cell's 'preferred stimulus' - the pattern of inputs that produces a maximal response from the cell. Applying a signal processing approach to the retina, using spots of illumination of varying diameters, lead to the (now textbook) understanding of retinal ganglion cell receptive fields as having a centre-surround structure. These consist of an excitatory centre and an inhibitory surround. Central responses can be ON (spiking is related to an increase in light intensity) and OFF (spiking is related to a decrease in light intensity), but unlike bipolar cells, ON-OFF centres are also seen, which respond both to increases and decreases in light intensity (Kuffler, 1952).

Building on this textbook view, many non-standard ganglion cells have been discovered in vertebrate retina. These cells have specific response properties - such as direction selectivity or local edge detection - that are not sufficiently explained by a centre-surround description of their receptive field. Additionally, some of these cells are hard to characterise using the now traditional tools of visual neuroscience - spots of light and drifting gratings. Although these cells may be in the minority in primate and human retinas highly specialised for spatial acuity, they still represent a large number of cells, project to the LGN and visual cortex both directly and indirectly, and may be essential to specific visual tasks in other mammals (Gollisch & Meister, 2010, Masland & Martin, 2007).

It should be stressed that emerging evidence on the inability of the centre-surround model to capture all the salient properties of retinal ganglion cell responses should not be taken as a claim that the model is 'wrong'. As da Silveira & Roska (2011) point out, 'sensitivity' does not mean 'exclusivity'. An OFF direction selective cell may also have a centre-surround receptive field organization, and will still respond to a dark flash,

but will also have a suppression of responses to null stimuli not moving in the preferred direction.

1.4.3 Linear and nonlinear integrators

Nonlinearities are a common feature of many neural circuits, and nonlinear operations occur at many levels of the retinal circuitry. Integration of inputs nonlinearly is a key underlying mechanism in 'non-standard' ganglion cell responses (Demb *et al.*, 1999, Schwartz & Rieke, 2011).

Ganglion cells, like most neurons, receive inhibitory and excitatory synaptic inputs, which are integrated by the cell to modulate the firing rate. Linear integration requires that the relationship between inputs and outputs is constant and proportional. That is, the output from activating two inputs can be predicted simply by summing the output measured from activating each input independently. In contrast, when inputs are integrated nonlinearly the response to specific temporal or spatial combinations of inputs can be much larger or smaller than the sum of the independent responses. The mathematical description of the relationship between inputs and outputs is therefore described by a nonlinear function rather than a linear one.

As spike generation itself is an inherently nonlinear process, involving both a threshold and a saturation point, no spiking neural cell is an entirely linear integrator. However, within these constraints there are cells that approach linearity, and those that exhibit extremely nonlinear response properties (Gollisch, 2013).

Work in the cat first demonstrated populations of retinal ganglion cells that integrate inputs roughly linearly ('X' cells) and other that are highly nonlinear ('Y cells'). These cell types can be distinguished by their responses to periodically reversing spatial gratings. X cells only respond to one grating reversal (whichever activates their ON or

OFF centre by increasing or decreasing contrast in their receptive field). By moving the spatial position of the grating it is possible to find a point where neither reversal substantially activates the cell. This is the point at which the grating splits the X cell receptive field in half, and the suppression from the non-preferred contrast change 'cancels out' the activation from the preferred one. Y cells, on the other hand, respond to both grating reversals and respond maximally when positive and negative contrast split the receptive field (Enroth-Cugell & Freeman, 1987, Enroth-Cugell & Robson, 1966, Gollisch, 2013). These features underpin Y cell specificity for selected stimulus features that are more spatiotemporally complex than their centre-surround receptive fields (Gollisch & Meister, 2010).

The distinction between X and Y cells is not a clear boundary separating two distinct cell types. Instead, at least in the mouse retina, linearity to nonlinearity is a continuum (Carcieri *et al.*, 2003), likely representing many cell types which use nonlinear integration for different visual tasks.

Synaptic rectification that would drive nonlinear responses is such a common feature in retinal circuits that it has been suggested that crossover inhibition (i.e. from the ON to the OFF pathway) exists to compensate for rectification and preserve linear responses in those retinal channels that require it (Molnar *et al.*, 2009).

1.4.4 Variety of functions performed by retinal ganglion cells

A wide variety of 'non standard' retinal ganglion cell responses have been identified, particularly from experiments in rabbit, salamander, and cat (for reviews see Masland & Martin (2007) and Gollisch & Meister (2010)). For the sake of simplicity, here I will focus only on the handful that have been well documented in the mouse retina.

Direction Selectivity

ON, ON-OFF, and OFF direction selective ganglion cells (DSGCs) have all been identified in the mouse retina (Kim *et al.*, 2008, Sun *et al.*, 2006, Weng *et al.*, 2005). When a stimulus (for example a bar or a drifting grating) is moved back and forth along a particular axis, these ganglion cells will respond strongly to movement in one direction along this axis and much less or not at all to movement in the opposite (null) direction.

ON-OFF DSGCs can be classified into four subtypes, covering four different preferred directions. They respond to both bright and dark objects crossing their receptive fields over a range of speeds. ON DSGCs, in contrast, can be split into three subtypes covering three preferred directions, and respond only to slow, bright objects (Demb, 2007).

The circuits underpinning direction selectivity depend on an asymmetric distribution of excitation and inhibition. DSGCs receive excitatory inputs from bipolar cells (ON and OFF in the case of ON-OFF DSGCs, and ON-only in the case of ON DSGCs), and inhibitory GABAergic and excitatory cholinergic inputs from starburst amacrine (SA) cells. Movement in the preferred direction results in strong excitation with very little inhibition, and movement in the null direction results in little excitation with strong inhibition.

SA cells are highly specialised computational units in the direction selective circuit. Their dendrites are individually direction selective, and are electrically isolated from each other. This, combined with asymmetric excitation onto these cells from bipolar cells and inhibition from neighbouring SA cells gives them the necessary properties to provide the asymmetric inhibition onto DSGCs (da Silveira & Roska, 2011, Demb, 2007, Yonehara *et al.*, 2011).

OFF DSGCs are unusual for direction selective ganglion cells. They receive little input

from SA cells, and are aligned dorso-ventrally across the retina. This anatomical orientation is potentially responsible for their senstivity to upwards motion (Kim *et al.*, 2008).

Selective feature detector

A ganglion cell highly specialised for detecting specific features in the visual scene has been described in detail by Zhang *et al.* (2012). These 'W3' cells (which correspond to the G5 anatomical subtype described in Völgyi *et al.* (2009)) respond preferentially to changes in illumination within their small central receptive fields, but only when the surrounding scene remains motionless. In most stimulus conditions (such as full-field stimulation with video taken from a head mounted camera while a rat explores a cage) these cells do not spike at all. They appear to be highly specialised for detecting aerial predators, which would be perceived by the mouse retina as small changes in luminance on an otherwise stable background (the sky), and may mediate startle responses. The circuit underpinning these responses therefore involves very high levels of lateral inhibition, sufficient to completely silence the cell when the surround is activated. Additionally, in order to detect changing luminance anywhere in the receptive field, regardless of ON or OFF polarity, the excitatory input onto W3 cells from both ON and OFF bipolar cells must be highly rectified. Rectification that allowed only depolarising, transient changes to be transmitted to the ganglion cell would prevent ON excitation somewhere in the receptive field being 'balanced' by a loss of OFF excitation, and vice versa.

Approach sensitivity

Approach-sensitive ganglion cells in the mouse retina respond preferentially to approaching or looming motion (simulated by an expanding bar) compared with lateral (a drifting bar) or receding motion (a shrinking bar). They have been described in detail by Münch *et al.* (2009) and may mediate flight responses to looming shapes (De Franceschi *et al.*, 2016, Yilmaz & Meister, 2013).

Approach-sensitive ganglion cells have a composite receptive field, composed of many OFF excitation and ON inhibition subunits, which are pooled through rectified synapses resulting in a concave nonlinearity at the ganglion cell. This rectification magnifies strong, local signals while weakening diffuse ones, and so restricts responses to local rather than global image motion.

OFF excitatory subunits consist of OFF cone bipolar cells, which provide glutamate input onto the approach sensitive ganglion cells. The ON inhibitory subunits are more complex: AII amacrine cells provide feedforward inhibition onto the ganglion cells through glycine synapses. The AII cells are driven by rods through the rod bipolar cell in low light conditions, and by ON cone bipolar cells through gap junctions at higher light levels.

The combination of these two subunit pathways enables the cell to differentiate approaching motion from other kinds of motion. A dark object approaching in the visual field would activate OFF bipolar cells and cause OFF excitation, but would not cause a response from ON bipolar cells, resulting in no ON inhibition. Excitation without inhibition would lead the cell to respond strongly. Receding motion of a dark object, on the other hand, would result in responses from ON bipolars but not OFF bipolars. Inhibition without excitation reduces the cell's response. Finally, spiking is suppressed

in the case of lateral motion of a dark object, as its leading edge results in OFF excitation from OFF bipolar cells, which arrives at the same time as fast inhibition from AII cells activated by the trailing edge of the object (Münch *et al.*, 2009).

These ganglion cell subtypes reveal a few of the many possible computations that can be performed by combining retinal cell subtypes into different microcircuits.

1.5 Starlight, twilight, daylight: The multi-purpose retina

The eye encounters light intensities in nature that span a range much greater than the dynamic range available to individual retinal neurons. One adaptation to this has already been outlined in detail: two distinct classes of photoreceptor cells that respond to different but overlapping levels of light intensity. However, the retina has many other mechanisms that enable it to respond dynamically to changing environmental light levels.

1.5.1 Gain control

The retina must adapt to the statistical features of the visual scene and encode useful information at multiple light intensities. Controlling the gain at input cells and key synapses is an essential tool in solving this problem - gain must be high enough at low light intensities to produce a transmittable response, but low enough at high light intensities that synapses aren't saturated and changes in light intensity can still be detected.

Gain control can be split into two types: 'background adaptation' to changes in the mean light intensity, and 'contrast adaptation' to changes in the variability about that mean (Demb, 2008). Photoreceptors themselves, especially cones, have intrinsic mech-

anisms that enable gain control before the first synapse. Additionally, both of these mechanisms can be found within the rod bipolar - amacrine cell synapse synapse. As the rod bipolar cell membrane depolarises (as it does with increasing light levels), or the variance of the membrane increases (as it does with increasing contrast), synaptic gain is reduced through vesicle depletion and calcium channel inactivation. This mechanism is likely to be similar in cone bipolar cells (Jarsky *et al.*, 2011).

1.5.2 Context-dependent circuit re-purposing

As the environment changes from extremely low light levels, through twilight and into bright daylight conditions, the retina does more than simply adjust the gain. Several retinal circuits alter their response properties and functions dramatically. Context-dependent circuit re-purposing is common to many neural tissues, but is still not well understood.

Rod bipolar cell encoding changes with increasing light levels

As discussed above, gain-reduction at the rod bipolar cell synapse is due to increasing depolarisation of the cell membrane (Jarsky *et al.*, 2011). This change in gain at the synapse also fundamentally changes the *kind* of information the bipolar cell communicates about the light incident on rods. As light intensity increases, rod bipolars transition from responding to brief light increments (such as single photon absorption), and instead response preferentially to modulation - periods of darkness enhance responses to light. This has been described as a change from encoding Weber contrast to Michelson contrast at higher light levels (Ke *et al.*, 2014).

Briefly, depolarisation at higher light levels leads to vesicle depletion, which is alleviated by hyperpolarisation when the stimulus intensity decreases as synaptic release is sup-

pressed. This allows some brief recovery from synaptic depression, and therefore more glutamate release onto postsynaptic targets when the stimulus intensity next increases, before depletion occurs again. Therefore, at high background light levels, AII amacrine cells receive stronger input from bipolar cells not when more photons are detected (as in very low light conditions), but instead when the stimulus consists of modulating contrast that drives interspersed periods of rod bipolar depolarisation and hyperpolarisation. This functional change can be measured in AII amacrine cells downstream of these bipolars (Ke *et al.*, 2014). Cone bipolars, ganglion cells and neurons in higher visual areas receive input from these cells regardless of the light level, but these inputs represent different features of the stimulus in an intensity-dependent manner.

Rods are re-purposed at high light levels

As outlined in section 1.3.3 (page 36), recent work by Szikra *et al.* (2014) has demonstrated that horizontal cells can relay cone hyperpolarisation to rods via a sign inverting synapse, causing cone driven rod depolarisation. The authors describe these findings as a 'see-saw circuit' - when rods are saturated, light increments can push the cone end of the circuit down (a hyperpolarisation), and as a result of the sign inverting horizontal cell, the rod end is pulled up (a depolarisation). As rods and horizontal cells are highly coupled with gap junctions, depressing one cone can lift many rods. Effectively, this means that rods can carry surround information about cone activation, even when the rods themselves are saturated. This signal propagates to rod bipolars and also to ganglion cells. Indeed, in mice lacking connexin 36, PV-5 ganglion cells (approach sensitive ganglion cells; Münch & Tikidji-Hamburyan (2014)), which normally receive rod and cone bipolar input via inhibitory AII amacrine cells, reversed the polarity of their response when the background light intensity was increased.

A similar polarity switch has been described by Vlasits *et al.* (2014). Here, an ON cone bipolar carries OFF signals when light levels are increased. The authors hypothesise that this is because at high light levels rods which are depolarised by cones via horizontal cells re-hyperpolarise when cones depolarise in response to a decrease in light intensity. This effectively results in a rod synapse that now signals "cone OFF" rather than "rod ON", and this signal is carried through AII amacrine gap junctions to cone ON bipolar cells.

The 'see-saw circuit' is in direct competition with rod-cone coupling via gap junctions. When a cone is hyperpolarised, it communicates that hyperpolarisation to gap-junction coupled rods, and then also drives depolarisation of rods via horizontal cells. As photoreceptor cell gap junction coupling is highly modulated, which of these two systems forces driving rods 'wins' in any given situation may be dependent on time of day and previous light exposure.

It should be noted that the 'see-saw circuit' can be reversed - at low light levels rod hyperpolarisation causes cone depolarisation through sign inverting horizontal cell synapses (Szikra *et al.*, 2014). Whether this is also communicated to the inner retina has not yet been investigated.

The polarity of bipolar cell responses can change with light level

As outlined above, Vlasits *et al.* (2014) describe a cone ON bipolar cell in the mouse that carries OFF signals at high light levels. Similarly, Odermatt *et al.* (2012) have reported that many ON and OFF bipolar cell synapses in zebrafish change their response polarity as the light level increases, sometimes multiple times. The authors suggest that this may be related to nonlinear encoding of luminance changes that allows these synapses to signal over a larger dynamic range and therefore distinguish more levels of grey than

synapses with a constant polarity. The dynamics of these terminals could be modelled as a combination of an intrinsic component and an antagonistic component driven by recruitment of neighbouring bipolar cells as the light intensity increases, suggesting a role for lateral inhibition in shaping the nonlinearity.

In the Odermatt *et al.* (2012) study, the fish used were 9-12 days post fertilisation, and should have a retina dominated more by cones than adult zebrafish. However, rods in varying stages of development can be found in these retinas between days 4-10 post fertilisation, and so inputs from rods cannot be completely discounted as contributing to this observation (Fadool, 2003).

Rod circuitry is used in daylight

Even in high-light conditions, AII amacrine cells contribute to retinal ganglion cell output. The approach-sensitive circuit described by Münch *et al.* (2009) is one example of this: at high light levels, cone ON bipolar depolarisation is communicated to AII cells via gap junctions, which then provide cone-driven feedforward inhibition onto the approach-sensitive retinal ganglion cell.

Similarly, Manookin *et al.* (2008) have reported that OFF ganglion cells in guinea pig retina receive direct gylcinergic inhibition from AII amacrine cells. During light decrements cone ON bipolar cells hyperpolarise and this is communicated to AII cells via gap junctions, leading to disinhibiton of the OFF ganglion cells.

AII amacrine cells can also set the membrane potential of cone ON bipolar cells in daylight via their gap junction connections. As light levels increase and synaptic release from rod bipolar cells reduces, amacrine cells hyperpolarise (Jarsky *et al.*, 2011, Ke *et al.*, 2014). This hyperpolarisation is passed to ON cone bipolar cell terminals, and changes the synaptic set-point for the cone bipolar - ON ganglion cell synapse. This

results in a positive rectification of the synapse, making transmitter release change non-linearly with contrast, effectively rendering the postsynaptic ganglion cell a non-linear integrator sensitive to fine spatial detail (Grimes *et al.*, 2014).

Ganglion cells have light-level dependent 'switches'

Another example of light intensity dependent circuit re-purposing can be found in ganglion cell responses. Luminance changes have been shown to change both the quantitative and qualitative response properties of retinal ganglion cells (Tikidji-Hamburyan *et al.*, 2015), which could be due in part to light level dependent nonlinearities at the bipolar to ganglion cell synapse (Grimes *et al.*, 2014, Odermatt *et al.*, 2012). Equally, these switches could be driven by changes in bipolar cell polarity driven by changes in the polarity of rod signalling hypothesised by Vlasits *et al.* (2014).

A well described retinal ganglion cell 'switch' occurs in PV-1 and PV-6 cells (Farrow *et al.*, 2013). These cells change their spatial processing at cone threshold, as the weighting of the centre and surround in their receptive fields abruptly and reversibly switches. At low light levels the surround contribution is weak, but as light levels reach cone threshold the surround becomes much stronger. This is driven by an inhibitory amacrine 'switch cell', which receives excitatory drive from cone bipolars via electrical synapses. In low light levels, cone bipolars can drive the PV-1 ganglion cell via high gain chemical synapses, but the drive to the switch cells via the gap junctions is low. However, as cones become activated, they drive cone bipolars enough to lift the switch cells above spiking threshold, resulting in inhibition of the PV-1 cell. This creates a stronger competition in the cell between the excitatory centre and the inhibitory surround, changing the nature of its spatial processing. As this switch is both fast and reversible, the authors propose that it allows each ganglion cell in the PV-1 mosaic to

set its own individual spatial integration properties instantaneously, depending on the local luminance level.

These abrupt switches are not found in all ganglion cells - many recorded in the same study (often with smaller dendritic fields), showed no change in responses to the chosen spot stimulus, or their responses changed continuously with each change in background light level.

1.5.3 Duplicity theory and the multi-purpose retina

Rods and cones are clearly distinct anatomical and functional entities, with different response properties, as originally outlined by Max Schultze. However, rod and cone circuits are coupled by chemical and/or electrical synapses at every level of the retina. 'Rod-specific' pathways are non-existent, and 'cone-specific' ones are rare.

The high level of connectivity between the two pathways appears to be essential for the 'switching' behaviour that causes circuits to perform different computational tasks depending on light level. These switches imply that photoreceptor cell output could be computationally important even when the cells are not light-responsive. For example, as outlined above, the switching off of glutamate release from rods in bright light mediates the hyperpolarisation of amacrine cells that enables rectification at the ON cone - ganglion cell synapse. If rods were instead releasing glutamate as though they were in darkness this rectification would presumably not take place and the postsynaptic ganglion cells might continue to integrate linearly even in photopic conditions.

How complex, highly electrically coupled, task-switching neural tissues function is still very much an open question, and one that studies of retinal circuitry may be able to answer. Additionally, circuit-switching and its modulation has potentially functional implications for a variety of disorders that are thought to affect photoreceptor cells.

Genetic manipulation of rod and cone function is therefore of interest both to basic and translational research. By comparing animal models that lack either rod or cone function with wild-types, we can probe the extent to which this task-switching behaviour really is dependent on interactions between rods and cones.

1.6 Inferring functional connectivity from retinal ganglion cell receptive fields

Understanding the response properties of retinal ganglion cells can provide insights into the input subunits that contribute to their receptive fields. These insights can drive further experiments to fully characterise the specific circuits underlying the receptive fields.

Computational modelling methods can be used to characterise retinal ganglion cell responses, and build functional models that predict the underlying circuitry generating those responses. This section outlines modelling approaches as they pertain to retinal ganglion cells, and methods used to measure and analyse the relationship between visual input space and ganglion cell spike trains.

1.6.1 Why model?

Ultimately, a model of a cell can be anything from a simple description of that cell's response properties to a full biophysical simulation of the dynamics of each ion channel in the membrane and every chemical reaction that occurs within it. There are many reasons to build models of neuronal cells, and the correct model choice is entirely dependent on the specific questions being asked by the modeller.

From the perspective of an experimentalist attempting to gain maximal understanding

of a cell's functionality from experimental data, the aim is to simplify the data in functionally relevant ways. We would like to be able to say something about the functional relationship between the cell's inputs and outputs that, while contained within the raw spike train, is not readily apparent to human observers.

Simple models that reduce the complex dynamics of spike trains to clear mathematical components are useful primarily to drive understanding of cellular and network computations, and therefore help generate further testable hypotheses.

1.6.2 Retinal ganglion cell models: Linear-Nonlinear-Poisson

Perhaps the most commonly used model of retinal ganglion cells is the centre-surround model describing receptive fields. At the other end of the complexity spectrum, it is possible to model the effects of specific retinal ganglion cell ion channels and morphologies on spiking output (Lee *et al.*, 2003b, Sheasby & Fohlmeister, 1999).

One model that has become popular for characterising and analysing retinal ganglion cell spike trains is the Linear-Nonlinear-Poisson model. This breaks the ganglion cell down into a linear stimulus filter (normally temporal or spatiotemporal), representing the receptive field of the cell, and a point nonlinearity that represents the firing rate of the neuron as a function of the linear filter. In the model, the output of this nonlinearity then determines the instantaneous firing rate of a Poisson spike generator (Schwartz *et al.*, 2006). The linear stimulus filter is usually defined as the spike triggered average - the average stimulus that precedes a spike.

These models have proven successful as a very simple format for characterising retinal ganglion cells that integrate their inputs in a relatively linear fashion ('X' or 'X-like' cells), with the nonlinear element of the LNP model representing primarily nonlinearities intrinsic to ganglion cell spike generation. However, the spike triggered average

fails to capture many aspects of retinal ganglion cell responses that rely on nonlinear integration of inputs (Gollisch & Meister, 2008, Schwartz & Rieke, 2011).

1.6.3 Incorporating input nonlinearity into LNP models

The 'sandwich model' of nonlinear 'Y' cells uses multiple subunit pathways (corresponding to bipolar cells and bipolar-amacrine cell sub-circuits), each of which has its own linear receptive field. Each subunit is passed through a rectifier and pooled, and this signal is passed through a second contrast gain control nonlinear function to determine the firing rate of the cell (Enroth-Cugell & Freeman, 1987, Gollisch, 2013).

It is clear how this model can easily be parsed into an LNP framework - most simply by allowing for multiple filters rather than a single filter. Additional filters governing neuronal responses can be uncovered if the covariance of the spike triggered stimulus is examined, instead of just the mean described by the spike triggered average. In a spike triggered covariance (STC) analysis, multiple filters are detected if the stimulus is integrated non-linearly, whereas a stimulus that is integrated primarily linearly will not reveal filters additional to the spike triggered average (Gollisch, 2013, McFarland *et al.*, 2013, Pillow, 2005, Schwartz *et al.*, 2006, Solomon & Tailby, 2010). This can therefore serve as a basis for quantifying nonlinearity in ganglion cell responses. Importantly, the filters uncovered through STC analysis are not literal representations of the neural mechanisms underpinning ganglion cell responses. Each filter could represent multiple subunits which are collectively integrated in a linear fashion (and, indeed, two separate subunits could represent the same inputs being integrated differently).

Each of the detected filters represents the unique subspaces that the filters of the model must span. Any functionally equivalent model must have filters that span these same subspaces, but the filters themselves do not represent a unique solution. Invertible

linear transformations applied to all filters can produce identical functional models (Rust *et al.*, 2005, Schwartz *et al.*, 2006). This can be exploited to find functional bases that are better suited to description in biological terms (Kaardal *et al.*, 2013).

1.6.4 Sampling input space: Selecting appropriate stimuli to generate modelling datasets

The stimulus that an experimenter chooses to use to characterise a cell is an important determinant of the limits on any future analysis (Masland & Martin, 2007). An ideal stimulus would make no assumptions about which features of the visual scene are likely to modulate the firing rate of a ganglion cell, whilst also delivering inputs that sample all the relevant features.

Two different stimulus approaches exist that aim to meet those needs: naturalistic stimuli, such as movies of natural scenes or from head cameras on animals moving about common environments, and noise stimuli. Noise stimuli are easier to standardize, generate, and analyse, and so are particularly popular for characterising receptive fields with as few *a priori* assumptions as possible. Additionally, the use of Gaussian white noise to inform LNP and mutli-filter LNP models is well established (Chichilnisky, 2001, Field *et al.*, 2010, Gollisch, 2013, Schwartz *et al.*, 2006).

It should be noted, however, that neither naturalistic nor noise stimuli are necessarily able to capture all features of a retinal ganglion cell receptive field. Taking the W3 selective-feature detector as an example, no full-field stimulus with intensity changes in many locations simultaneously was able to elicit spiking responses from the cell. Only naturalistic stimuli that actually mimicked the specific features the cell is selective for, or noise stimulation restricted only to the small central receptive field of the cell, were useful in eliciting analysable responses (Zhang *et al.*, 2012).

1.7 Genetic manipulation of rod and cone function

As outlined in this chapter, rod and cone pathways for information transfer through the retina are connected at multiple levels of retinal circuitry, and act together through these connections to re-purpose retinal circuits as environmental light levels change. In order to better understand how these pathways develop and work together, it is desirable to examine how they function when they are disrupted.

Given the interconnected nature of the inputs, and the fact that different pathways in the retina can use the same transmitters and receptors (such as ON rod and ON cone bipolar cells), it is very hard to separate the processing of rod and cone inputs meaningfully using pharmacological tools. While still imperfect, genetic tools offer a cleaner solution and also help to provide insights into human disease.

1.7.1 Silent rods and silent cones: genetic disruption of phototransduction

Many human genetic disorders affect photoreceptor cell function, usually by interfering with the phototransduction cascade, RPE, or photoreceptor cell metabolism. Of these diseases, a large number are degenerative and are classed together broadly in the disease family retinitis pigmentosa (Rattner *et al.*, 1999), whereas others are relatively stationary and the effected cells survive in the retina long-term.

Silent rods: Congenital stationary night blindness

Congenital stationary night blindness (CSNB) is a genetically heterogeneous set of disorders that disrupt rod signalling, and are therefore characterised by nyctalopia (night blindness, or difficulty seeing in scotopic conditions).

There are two broad classes of CSNB that don't involve fundus abnormalities: Schubert Bornschein type, which involves disruption of neurotransmission from the photoreceptor cells onto bipolar cells, and Riggs type, which involves disruption of the rod phototransduction cascade (Zeitz, 2007).

Mutations responsible for Riggs-type CSNB can either cause constitutive hyperpolarisation of rods - leading to reduced glutamate release and subsequent downstream desensitization - or they can prevent rod hyperpolarisation in response to light, leading to constant glutamate release and no light-evoked downstream activity (Zeitz, 2007).

Mutations in the GNAT1 gene that encodes the Gαt subunit of rod transducin have been shown to cause both autosomal recessive (Naeem *et al.*, 2012) and dominant (Dryja *et al.*, 1996) Riggs type CSNB. A GNAT1$^{-/-}$ knockout mouse has been made. These mice (known as rd17) completely lack the rod transducin alpha subunit (Trαt), meaning that activated Rh* cannot be coupled to its effector enzyme, cGMP phosphodiesterase. Without this coupling, activated Rh* cannot lead to a decrease in intracellular cGMP, and so cGMP-gated channels remain open and the dark current is not shut off. rd17 rods should constantly release glutamate as though they were in darkness, regardless of the environmental light level (Calvert *et al.*, 2000).

The retinas of rd17 mice seem anatomically stable for the first 4 postnatal weeks, but by 13 weeks rod outer segment length appears shorter and there are signs in the outer nuclear layer than indicate a loss of approximately 10% of rods. These features then remain stable for up to a year, although year-old mice may have some thinning of the inner nuclear layer as well (Calvert *et al.*, 2000).

Silent cones: Achromatopsia

Achromatopsia describes a range of disorders that lead to lack of colour vision, including some that are cortical in origin. In the context of the retina, achromatopsias are primarily caused by mutations affecting the cone transduction pathway - GNAT2, CNGA3 and CNGB3 are the most commonly implicated genes. Patients present with poor visual acuity, nystagmus, and photophobia (Li *et al.*, 2014, Pang *et al.*, 2010, Sundaram *et al.*, 2014).

The spontaneous mouse mutant cpfl1 (cone photoreceptor function loss 1), first described by Chang *et al.* (2002), is a model of a less common form of autosomal recessive achromoatopsia in humans caused by mutations in the PDE6C gene. PDE6C encodes the catalytic alpha subunit of cone phosphodiesterase. These molecules catalyse the hydroloysis of cGMP during light stimulation, reducing its concentration and eventually leading to the closure of cGMP-gated channels and subsequent membrane hyperpolaization. In the absence of functional cone phosphodiesterase, the cGMP-gated channels will remain open and the cone will not hyperpolarise in response to light (Chang *et al.*, 2009).

This mutation therefore has very similar consequences in terms of the phototransduction cascade, membrane potential, and glutamate release as the rod mutation found in rd17 mice. However, while rd17 is relatively stationary (most of the silent rods remain alive in the retina despite their lack of function), cpfl1 is not. In cpfl1 mice, cone numbers are depleted at 3 weeks old and the number continues to drop rapidly until around 5 months. It has been hypothesised that this cell death might be due to toxic calcium overload (Chang *et al.*, 2009). Thus, responses in young adult cpfl1 mice reflect a circuit where some cones are completely absent, while others are present but not light responsive.

Electrophysiological changes in mouse models

As expected, cone-driven light adapted ERG responses are undetectable in cpfl1 mice (Chang *et al.*, 2009), and rd17 mice show neither a rod b-wave nor a-wave, indicating no light responses at scotopic light levels in either photoreceptor cells or bipolar cells (Calvert *et al.*, 2000).

Additionally, rd17 mice have an altered cone ERG b-wave, which has enhanced amplitude and reduced latency compared to wild-type cone b wave responses. This suggests that tonic rod signals in wild-types may have a suppressive effect on the cone b-wave that is not present in rd17 mice (Cameron & Lucas, 2009).

It should be noted that some subset of rd17 rods have residual light responses. These response share rod opsin spectral efficiency, but are evoked only at intensities within cone sensitivity range. This is thought to be mediated through low level GNAT2 expression in the rods (Allen *et al.*, 2010, Calvert *et al.*, 2000). While these responses cannot mediate scotopic vision, they may act as a source of visual information at higher light intensities.

Possible anatomical changes in mouse models

When an entire class of input cells are congenitally non-functional (as in both rd17 and cpfl1 mice), or are lost (as occurs in particular in cpfl1 mice), neuronal rewiring is often observed.

When one photoreceptor cell class is non-functional, the remaining functioning class can form synapses with the bipolar cells that are missing inputs. For example, in CNGA3$^{-/-}$ mice, ON and OFF cone bipolars form ectopic synapses with rods (but only if the rods are functional themselves; Haverkamp (2006)). Ectopic synapses between

rod bipolars and cones have also been demonstrated in multiple mouse models with silent rods (Haverkamp, 2006, Peng *et al.*, 2000). Therefore, when interpreting retinal ganglion cell output in these or similar conditions, the potential for novel synaptic connections not seen in the wild-type must be kept in mind.

1.8 Conclusions and Hypotheses

At every level of the retina, there are opportunities for light activation at one class of photoreceptor cells to alter the processing of light signals from the other class of photoreceptor cells. Rods and cones can alter each other's membrane potential via gap junctions and through synapses with horizontal cells; rod and cone inputs are combined to produce cone bipolar cell output; and activity communicated from both rods and cones are combined to set the membrane potential of AII amacrine cells.

Given this circuitry, I would expect that even at a light level where one class of photoreceptors is 'silent' (constantly releasing glutamate due to dark current), their constant depolarisation and transmitter release acts to 'set' the circuitry of the retina for processing of the other class of photoreceptor cell inputs. If this is the case, then perturbing this system by removing function in one class of photoreceptor cells should alter processing of the other class even at light levels where the class lacking function is normally considered 'silent' or non-signalling.

This can be re-stated as two core hypotheses: first, that processing of rod inputs is altered when cone function is absent, even at light levels where cones are not normally light responsive. Second, that processing of cone inputs is altered when rod function is absent, even at light levels where rods are not normally light responsive. As a corollary, I would also expect mesopic vision to be computationally distinct when driven by only one class of photoreceptor cells compared to both classes interacting with each other.

These hypotheses are of interest for two key reasons. First, by observing in detail how rods and cones can drive retinal computation relatively 'independently', we can better understand the role played by the interactions between signals from both cell types in normal vision. Secondly, if these hypotheses are true, vision could also be different in patients with similar conditions across the environmental light level range rather than just in certain light conditions. This could have consequences both for how the symptoms of these conditions are interpreted, and for how possible treatments are evaluated.

The impact of rod signals on the processing of cone inputs, and vice versa, is not currently known, and there is potential for paradoxical interactions. For instance, sign-inverting horizontal cell synapses would act in competition with sign-preserving gap junction connections between photoreceptor cells. Rod/cone membrane potential and subsequent changes in transmitter release and downstream processing in the absence of cone/rod function is therefore hard to predict.

At the next level of the circuit, as light levels increase rods act to move the AII amacrine cells and ON cone bipolar cells to a more hyperpolarised membrane potential, on top of which light driven depolarisations communicated from both rods and cones are superimposed (Grimes *et al.*, 2014, Jarsky *et al.*, 2011, Ke *et al.*, 2014). Cone driven depolarisations in the cone ON bipolar cell can also be communicated back into AII amacrine cells (Münch *et al.*, 2009). I would expect these mechanisms to be disrupted in the absence of either functional rods or cones.

A constant rod dark current (as predicted to occur in rd17 mice) should prevent the AII cell hyperpolarisation. However, if cones are able to drive changes in rod glutamate release (either through gap junctions or horizontal cells), the hyperpolarisation may still occur at high light levels. Similarly, a constant cone dark current (as predicted in

surviving cones in cpfl1 mice) would obviously prevent cone driven depolarisations in downstream cone ON bipolar and AII amacrine cells, but this could be compensated for at lower light levels by rod communication with the cone system. Additionally, when cones are lost in cpfl1 mice, the subsequent loss of cone glutamate release could lead cone ON bipolar cells to hyperpolarise, and increase hyperpolarziation in the AII-cone ON bipolar circuit. This again could be mitigated or enhanced by changes in rod glutamate release in the absence of cone inputs to rods (Szikra *et al.*, 2014).

As these many levels of interaction make the specific nature of potential computational differences difficult to predict, I chose to use a relatively unbiased stimulus protocol combined with exploratory data analysis techniques to test these two complimentary hypotheses that 'silent' photoreceptor cells shape processing of inputs from the other photoreceptor cell class. I chose to examine retinal ganglion cell responses, as these are the output cells of the retina, and any differences in processing must be observable in these cells in order to have an impact on further visual processing or visually guided behaviour.

I recorded retinal ganglion cell spike trains in response to visual input across a range of light leveles in cpfl1, rd17, and C57BL/6 mice. These are, respectively, a model of achromatopsia (absence of functional cone input), a model of congenital stationary night blindness (absence of functional rod input), and a 'wild-type' control (with input from both functioning rods and cones).

I chose to use spatiotemporal Gaussian white noise as a visual stimulus, as this samples a large amount of the input space while still being relatively straightforward to generate, analyse, and interpret (Chichilnisky, 2001). This was projected onto the photoreceptor cell layer of each retina at 5 different light levels, spanning a 4.5 $\log_{10}$ range.

This introduction demonstrated that there are multiple classes of retinal ganglion cell,

and that cells of each class may be capable of performing fundamentally different visual computations depending on the ambient light level (and possibly even depending on local light levels within the scene). Many of these processing changes appear to be dependent on interplay between 'rod' and 'cone' circuitry. The changes in balance of excitatory and inhibitory input to RGCs causing a change in balance of ON and OFF responses reported by Tikidji-Hamburyan *et al.* (2015) likely represent a general case of these specific switching circuits.

Tikidji-Hamburyan *et al.* (2015) report that they see a similar prevalence of luminance-dependent response changes in 'rod-only retinas' (cpfl3, cpfl1, and CNGA3$^{-/-}$) as in wild-types. Although this does not rule out more subtle integration changes in specific receptive field types, it hints that luminance dependent changes in processing may in fact be either more reliant on input from the rod system, or be more independent from photoreceptor cell subtype than currently thought.

The data collected for this thesis offers an opportunity to test a third hypothesis: that functional rods are required for luminance-dependent changes in RGC response polarity. If this hypothesis is true, then no light level dependent changes in response polarity should be observed in RGCs in rd17 mice, whereas these changes should be observed in cpfl1 mice in keeping with Tikidji-Hamburyan *et al.* (2015). Alternatively, finding luminance dependent changes in both animal models would instead suggest that they are caused by mechanisms which can be driven by either class of photoreceptor cells.

2 Materials and Methods

2.1 Electrophysiology

2.1.1 Tissue Preparation

Three mouse strains were used in this study, C57BL/6 (n=8), rd17 (n=8), and cpfl1 (n=8). All mice were 6-12 weeks old.

Mice were dark adapted overnight (for a minimum of 12 hours) prior to tissue extraction for *ex vivo* electrophysiology. An overdose of ketamine-dormitor anaesthetic mix was administered via the intra-peritoneal cavity to induce terminal surgical-plane anaesthesia. Animals were then sacrificed by cervical dislocation and enucleated.

Eyes were dissected in carbogen (95% oxygen, 5% carbon dioxide) saturated Ames medium (Sigma), under dim red light. This light was primarily provided by a deep red 660nm mounted LED (Thorlabs), although other light sources in the room included computer screens and a small lamp, all covered with red lighting filter sheets (106 Primary Red, LEE). Illuminance at the position where dissection occurred was measured as 80 lux. The cornea and lens were removed, with care taken to remove as much vitreous from the surface of the retina as possible in order to allow good contact between the retinal ganglion cell layer and the electrodes.

The RPE was separated from the retina and a flat petal 2-5 mm across was cut away from the retinal cup. This was placed ganglion-cell-side down on the surface of the multielectrode array (Multi Channel Systems - 60pMEA100/30iR-Ti).

Throughout recordings, the tissue was perfused with carbogen saturated Ames medium (Sigma) made up to include 9-*cis* retinal (Sigma), at a concentration of 100μM, in 0.2% BSA (Sigma). The medium in the multichannel chamber was continually refreshed using a Gilson Minipuls 3 peristaltic pump.

The media in the multichannel array chamber was maintained at a temperature of 36.5°C using a TC02 temperature control module from MultiChannel Systems. A small amount of suction was applied across the tissue through a perforated base plate (MultiChannel Systems), to pull it into contact with the electrodes. This suction was generated using a second Gilson Minipuls 3 peristaltic pump.

Following tissue extraction and preparation, each recording session began with a 30 minute period of dark adaptation on the experimental rig. To ensure no contamination of recorded responses from other light sources, all recordings were performed in a dim room with all light sources (including computer monitors) covered with red filters (106 Primary Red, LEE). The tissue itself was further protected from external light by a Faraday cage lined with black card and a double-layered curtain of thick black fabric.

2.1.2 Voltage Recording

A perforated 60-electrode recording array, consisting of titanium nitride (TiN) electrodes, each with a diameter of 30 μm and spaced 100 μm apart (Multi Channel Systems - 60pMEA100/30iR-Ti), was used to record ganglion cell extracellular potentials. The electrode array was an 8 by 8 square, with no electrode in each of the four corners. Voltage changes were amplified and digitized at 32000 Hz by an MC_Card system, us-

ing MC_Rack software (MultiChannel Systems). The raw electrode data was collected, including ERG-like local field potentials. This was later filtered offline using a Butterworth second order 300Hz high-pass filter (again using the MC_Rack software), to enable extraction of spikes.

2.1.3 Spike Sorting

Selection of spike sorting algorithm

Extracellular recordings can contain spikes from multiple cells close to the electrode, as well as background noise from cells spiking further away and from other sources of voltage change. This can pose a problem when analysing the raw data from an electrode, as it may represent the activity of multiple cells which have different response properties.

Spikes from different cells can be separated on the basis of the extracellularly recorded spike waveform. The shape of the waveforms depend on the channel distribution along the dendritic arbour of the cell, the size of the cell, the pattern of action potential initiation, and the distance of the cell from the electrode (Gold *et al.*, 2006). This means that different cells recorded on the same channel should have distinct waveform profiles. Spike sorting relies on finding the relevant features of these waveforms, and using them to separate the waveforms (spikes) into clusters that correspond to single cells (Buzsáki, 2004).

There are many clustering algorithms available for spike sorting, many of which take principal components analysis as their basis and make use of human being's superior clustering abilities to manually identify potential clusters in projections of spikes onto their principal components.

However, a more sensitive clustering algorithm that allows for more automation is available. This method makes use of mathematics originally developed to explain the behaviour of ferromagnetic nanoparticles. Briefly, the method simulates interactions between each data point (each spike) and its K nearest neighbours. Spikes have a probability of changing the state of their neighbours which depends on this interaction and on the global 'temperature' value - at high temperatures the probability of inducing state changes is low, and the spikes will switch states randomly and fairly independently (para-magnetic phase). At low temperatures, the probability of state-switching is high even for only weakly-interacting spikes, and so the entire dataset will form a single cluster that changes state en-mass (ferromagnetic phase). However, within a given temperature range, the system reaches a 'superparamagnetic' phase, where only those data points which are grouped will change state together, producing clusters that represent spikes with linked characteristics (Quiroga *et al.*, 2004).

Quiroga *et al.* (2004) have used this algorithm as the basis of an open-source spike sorting software, wave_CLUS, which was used for spike sorting in this study.

Spike sorting protocol

Traces were then exported into the sigTOOL (Lidierth, 2009) '.kcl' format, and related traces from each channel in a single recording period were stitched together using custom software written in MATLAB.

A custom-modified version of the wave_CLUS software (Quiroga *et al.*, 2004) was used to perform spike sorting. Custom-written MATLAB functions, accessible through the modified sigTOOL GUI, separated the spike sorting into an automatic and a supervised phase.

The automatic phase was performed on the Legion computer cluster maintained by

UCL. Filtered traces from all 60 channels representing one recording period were clustered in parallel, reducing the overall clock time needed to return a fully clustered dataset.

First, spikes were detected using a threshold. The threshold was defined as $4\sigma_n$, where x is the high-pass filtered signal and σ_n is an estimate of the standard deviation of the background noise (rather than the standard deviation of the entire signal) (Quiroga *et al.*, 2004).

$$\sigma_n = median\left\{\frac{|x|}{0.6745}\right\} \tag{2.1}$$

When a threshold crossing was detected, a window of 96 data points was extracted around the crossing point (32 time bins preceding the threshold and 64 time bins following the crossing, representing a 3ms time period) and stored as a 'spike'. A detector censor-time (set to 1.5 ms) was used to prevent the same spike from being detected twice. All spikes were then aligned to their maximum data point. This point was determined using interpolated waveforms calculated using cubic splines from 256 samples (Quiroga *et al.*, 2004).

In order to reduce the dimensionality of this dataset of spike waveforms and extract relevant feature information for clustering, the wavelet transform of each spike was calculated using Haar wavelets (Quiroga *et al.*, 2004). This produced 96 wavelet coefficients, constituting a time-frequency representation of the spike. The first 10 coefficients for each spike with the highest deviation from normality (and therefore the best chance of differing between different units) were then chosen as reduced-dimensional representations of spike properties. These coefficients were fed into the superparamagnetic clustering algorithm (Quiroga *et al.*, 2004). Clustering results calculated for each

temperature value were saved for supervised assessment.

The supervised phase was performed on a single desktop PC. In the supervised phase, temperature settings were chosen manually, using three-dimensional projections of the first three wavelet coefficients and overlays of spike waveforms as a guide. Custom modifications to the wave_CLUS interface (written in MATLAB) also provided evaluation plots of residuals, stationarity (how stable the instantaneous firing rate is over the full course of the recording), and spike amplitude relative to the threshold - cluster quality measures recommended by Hill *et al.* (2011). These were used to assess clusters produced at various temperatures, and only those that appeared to be from stationary recordings, with spike waveforms that were not highly variable, and with a spike amplitude large enough that a high percentage of spikes would not be lost below the threshold were classified as putative single units and passed on for further analysis.

All automatic and supervised clustering was performed without knowledge of the relationship between spikes and the stimulus, or any measures of the receptive fields of different clusters.

Spike sorting verification and single unit confirmation

Clustered units may or may not represent the activity of single cells. In order to have confidence in the results of spike sorting, it is useful to have some measures of cluster quality. Hill *et al.* (2011) propose several quality metrics to be used both as feedback during spike sorting and as summary statistics to assess the final clusters. These measures fall broadly into assessing false positive and negative contributions to a cluster that can distort the inferred receptive field of identified cells and suppress the inferred spike rates respectively.

Following clustering, putative single units were automatically assessed using these cri-

teria. Composite false positive and negative summary statistics were measured for both 'single cluster error' (refractory period violations less than 1 ms and the probability of undetected spikes) and 'multiple cluster error' (Hill *et al.*, 2011).

Only clusters that had both false positive and negative summary values < 0.01 (representing a fraction of false positive and negative events of 1% or less) were passed on for further analysis as single units. This means that we can be confident that results based on modulations in the firing rate of 2% or more are due to real changes in firing rate, and not due to false positives or false negatives skewing the data.

Units identified at each light level that were recorded on the same electrode were only determined as being from the same cell if the mean spike waveform at each light level was within 3 standard deviations of the mean spike waveform at all other light levels.

When using a multielectrode array, it is possible to record from the same cell multiple times (for example, once near the soma, and again near the axon on a distant electrode, or from the soma on two neighbouring electrodes). To avoid counting the same cell recorded on two electrodes twice in these analyses, duplicate recordings were identified and eliminated from the data set.

Spiking patterns from all possible pairs of identified units were cross-correlated in MATLAB. A peak at 0 lag in the cross-correlation indicates similarity between the two sequences. Cross-correlations were normalised to have values between 0 and 1, and the difference between the value at 0 lag and the mean value across all lags was taken. For the correlation of a cell with itself, this value should approach 1. Pairs of units which had a normalized peak at 0 lag larger than 90% of the maximum peak were flagged as potentially the same cell. For each flagged pair, one unit was excluded from further analysis. Figure 2.1 shows the correlation scores for all cell-cell pairs, and the threshold. The peak around 1 representing autocorrelations and very similar channels is clearly

separate from the rest of the distribution. The 90% threshold was chosen to separate this peak from the rest of the population of recordings.

Overall, 137 of 1099 recorded units that passed the false positive and negative threshold were excluded as duplicate recordings: 64/405 from C57BL/6, 34/349 from rd17, and 39/345 from cpfl1.

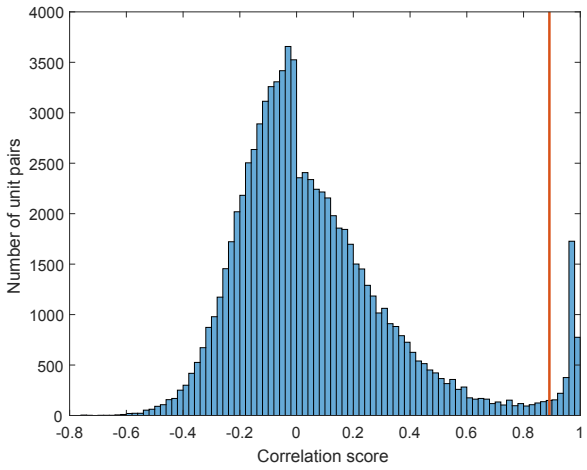

Figure 2.1: **Distribution of cell pair correlations:** Histogram of correlation scores calculated for all cell pairs (including autocorrelations) from all retinal preparations included in this study. The red line indicates the threshold used to flag two units as stemming from the same cell.

2.2 Visual Stimulation

2.2.1 Light Path

Visual stimuli were delivered to the explanted retina using the output of a Digital Light Processing (DLP) projector (Texas Instruments) focused through a 10x objective (Nikon) onto the photoreceptor cell outer segments. Position of the DLP microcrontrolled mirrors that form image pixels were driven by HDMI output produced by custom software written in MATLAB using PsychToolbox. Each image pixel, once magnified, was approximately 50 μm^2 tall and 100 μm^2 across on the retina.

2.2.2 Visual stimuli

Spatiotemporal white noise was delivered to the retina in the form of a 25 by 50 pixel stimulus generated by drawing pixel intensities independently from a Gaussian distribution at each frame refresh (Chichilnisky, 2001, Field *et al.*, 2010, Schwartz *et al.*, 2006). The frame rate was 60Hz, and the stimulus was delivered continuously for 20 minutes, followed by a 5 minute period of unstimulated recording.

Full field flash stimuli were also used to provide feedback during recordings. 50 ms and 16 ms pulses of white light spanning the entire 25 by 50 pixel space were presented over 20 1600 ms sweeps.

2.2.3 Light levels

Stimulus light levels were controlled using neutral density filters (ThorLabs) in the optical path. On this setup, placing a ND 4.4 filter in the light path was empirically identified to create potentially scotopic conditions through the use of a full-field flash stimulus. That is, this filter setting produced reliable light-induced spiking in another loss of cone function model CNGA3-cpfl5, and in C57/Bl6 retinas after dark adaptation and in the presence of 9-*cis*-retinal, but failed to produce visual responses in these retinas following a 30 minute bleaching protocol and 9-*cis* wash-out.

In this study, visual stimuli were repeated across 5 experimental light levels. Each light level was set by placing a different value of neutral density filter in the light path. The settings were: ND 4.5, ND 3, ND 2, ND 1, and ND 0 (no filter).

The peak irradiance of the stimulus was quantified by projecting a full-field white square onto the centre of an ILT17000 radiometer (International Light Technologies), which measured irradiance in Watts/m^2 at each filter setting. The spectral profile was

also measured at each filter setting using a spectrometer (Ocean Optics). Absorption spectra of rods and cones were estimated using the equations provided by Lyubarsky *et al.* (1999).

The measured spectra show that both the green and the blue LED in the DLP are likely to stimulate primarily rods and L/M cones. The red LED, by contrast, is outside the peak absorbance spectra for all mouse photoreceptor cells. Addtionally, the absorbance of the UV shifted mouse S cones is mostly outside of the wavelengths provided by the DLP LEDs, and as such the results of these experiments are unlikely to reflect the optimum light response of these cells.

The measured irradiance was weighted by the normalised spectra for each light level, and converted into photons/m^2/s. This was then weighted by the photoreceptor absorbance spectra and multiplied by the photoreceptor cell collecting area (0.5μm for rods and 0.2μm for cones (Nikonov *et al.*, 2006)) to calculate the number of photoisomerisations per second per cell for each photoreceptor cell subtype, following Farrow *et al.* (2013). Peak rod photoisomerisations per second (R*/s) ranged from 53 at ND 4.5 and 7×10^6 at ND 0 (2 s.f.).

$$Contrast = \frac{MaxPixel - MinPixel}{MaxPixel + MinPixel} \tag{2.2}$$

The Michelson contrast of the white noise stimulus was calculated to be 0.9943 by comparing the irradiance with a full field square set to the minimum pixel value (black) with that at the maximum pixel value (white) using equation 2.2.

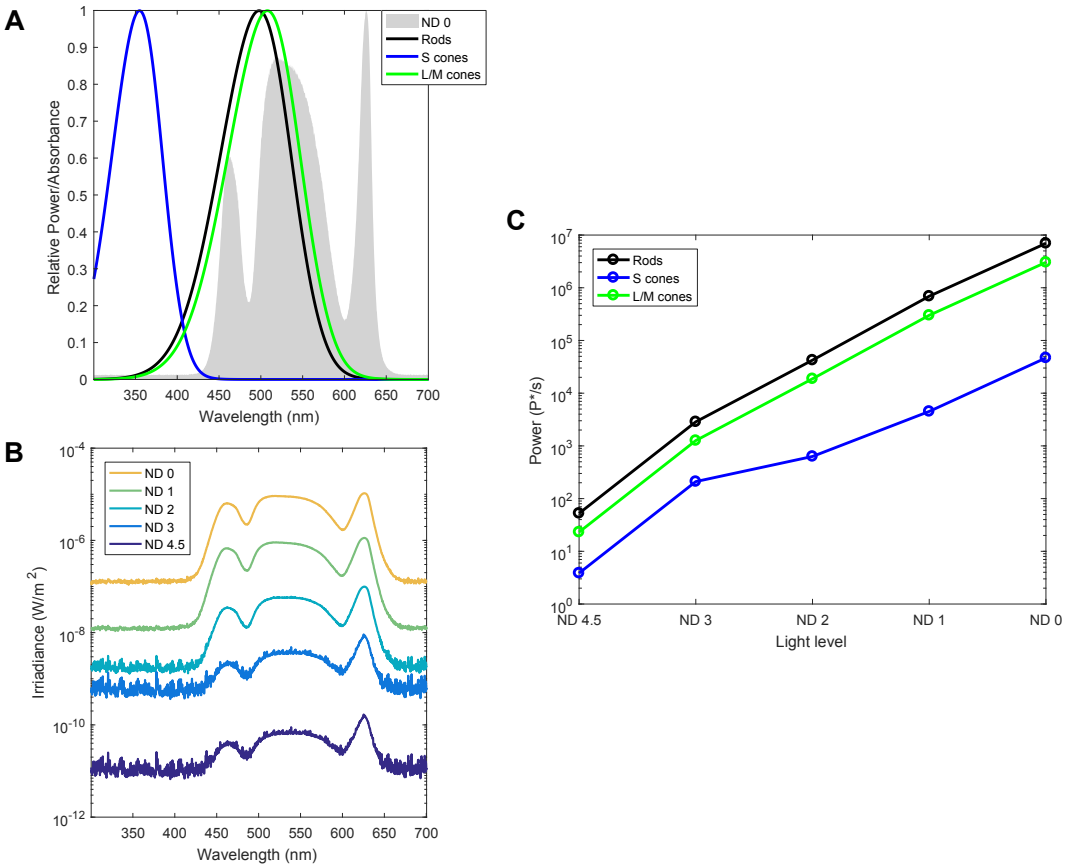

Figure 2.2: **Quantification of experimental light levels:** (**A**) Normalised absorption spectra of mouse rods and cones, based on Lyubarsky *et al.* (1999), compared to the normalised spectra of the stimulus measured at ND 0. The three peaks in the spectra correspond to the three projector LEDs that make up the "white" stimulus. The majority of the observed visual response will be due to the green and the blue LEDs. Additionally, S cones, which are UV shifted in mice, have an absorption spectra which is mostly outside the range covered by the stimulus, and so the majority of the observed visual responses will be driven more by rods and L/M cones. (**B**) Spectral irradiance of the stimulus at each experimental light level. As the lowest light level (ND 4.5) was outside of the range of the spectrometer, the spectral irradiance has been estimated using the relative spectrum of the previous light level (ND 3). (**C**) Power of the stimulus at each experimental light level expressed in terms of photoisomerisations per second per photoreceptor cell, calculated for rods, S cones, and L/M cones.

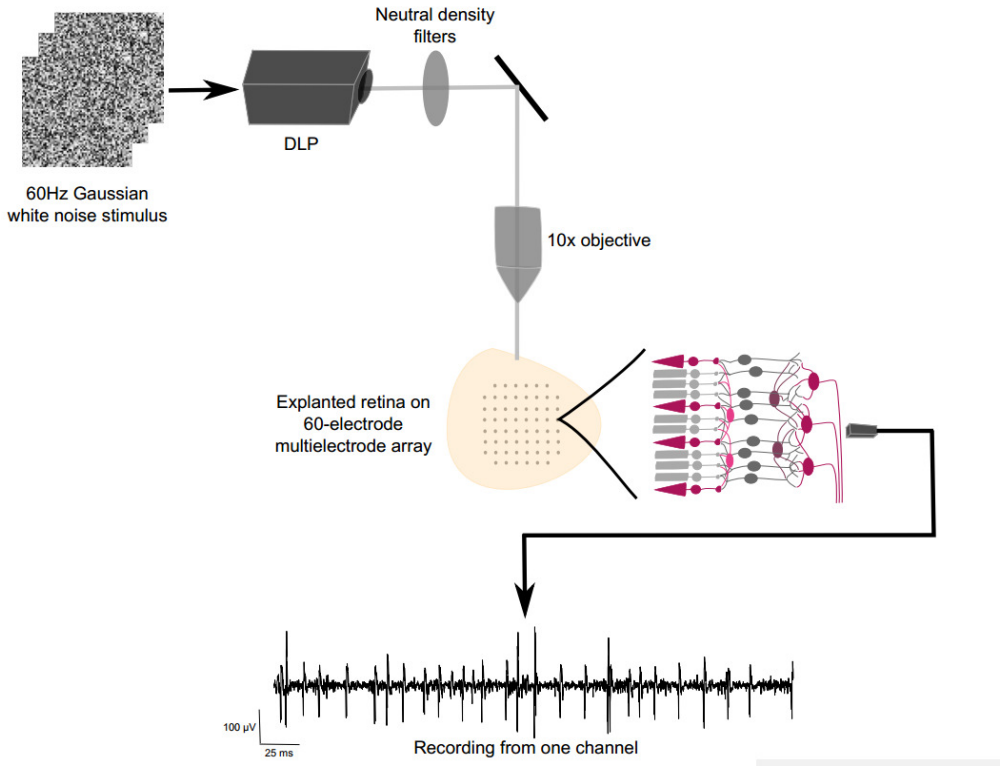

Figure 2.3: **Experimental set-up:** 60 Hz Gaussian white noise visual stimuli are projected onto the photoreceptor cells of explanted retinae, as extracellular potentials are recorded using multiple electrodes in contact with the ganglion cell layer.

2.3 Characterising ganglion cell receptive fields

All analysis was performed on clustered data identified as unique single units, using custom written MATLAB algorithms. Cells were characterised using the first 15 minutes of stimulated data at each light level, leaving 5 minutes available to test model accuracy.

2.3.1 Calculating the STA

The spike triggered average (STA) for each identified single unit was calculated by first taking the 30 stimulus frames (500 ms) preceding the nth spike ($\vec{s}(t_n)$, the nth set in the spike triggered ensemble $\vec{S}$, where t_n is the time of the nth spike), and then calculating the mean of each frame for all detected spikes.

$$\hat{A} = \frac{1}{N}\sum_{n=1}^{N}\vec{s}(t_n) \tag{2.3}$$

This resulted in a three dimensional, spatiotemporal filter representing the mean 30 frames (∼500 ms in total) preceding each spike for a single unit (Schwartz *et al.*, 2006).

Significant STAs were identified by comparison to filters obtained using shifted spike trains. To preserve temporal structure but break the relationship between the stimulus and the spike train, single unit spike trains were shifted randomly relative to the stimulus (with a minimum shift of 100 frames). The magnitude of the observed STA was considered significant if it fell outside of 95% confidence intervals calculated from 100 shifted spike trains (Chichilnisky & Kalmar, 2002).

For analysis, the STAs were then cut down to a 10 by 20 pixel area surrounding the spatial maximum.

Once the full data set of all STAs from all light levels was assembled, the STAs were normalised to have a zero mean and unit standard deviation (zscore normalisation), before being passed on to principal components analysis.

2.3.2 Estimating the Nonlinear Function in the LNP model

In order to determine how the linear filter relates to the firing rate of the neuron within a LNP model, the nonlinear 'generator signal' must be estimated. The firing rate of the neuron can be expressed as a function of responses to the linear filter using Bayes rule:

$$P(spike|\vec{s}) = \frac{P(spike)P(\vec{s}|spike)}{P(\vec{s})} \tag{2.4}$$

$$P(spike|\vec{s}) \propto \frac{P(\vec{s}|spike)}{P(\vec{s})} \tag{2.5}$$

Where $P(spike|\vec{s})$ is the instantaneous firing rate, $P(\vec{s}|spike)$ is the frequency of stimuli that trigger spikes, and $P(\vec{s})$ is the frequency of raw stimuli. For all stimulus sequences that preceded a spike, the linear filter response was calculated by taking the dot product of the filter with the stimulus (the projection of the the stimulus sequence onto the filter). A histogram of these projections represents an estimate of $P(\vec{s}|spike)$. Doing the same for the raw stimulus ensemble provided an estimate of $P(\vec{s})$. $P(spike|\vec{s})$ was then calculated as the ratio of these two histogram values in each bin.

This method can be extended to small numbers of filters, but for highly nonlinear cells additional assumptions must be incorporated. However, for retinal ganglion cells, these methods should be sufficient (Schwartz *et al.*, 2006).

2.4 Exploratory data analysis

Principal components analysis was performed on the full data set of normalised STAs. This was carried out in MATLAB using the inbuilt 'princomp' function which performs eigenvalue decomposition. This returns the principal component coefficients (the loadings), the principal component scores (the representation of the data in the principal component space), and the eigenvalues of the covariance matrix.

The STA data set was also clustered using ensemble clustering. Results from both a density and a distance based metric were combined, following the advice given by Ronan *et al.* (2016). First, OPTICS (Ordering Points To Identify the Clustering Structure) clustering was used as the density metric - this was performed using custom written MATLAB code based on the algorithm and code outlined by Ankerst *et al.* (1999) and

Daszykowski *et al.* (2001, 2002). Briefly, this algorithm selects an object randomly (an object here being one STA) and the 'reachability distance' (the maximum of the distance between the selected object and its ith nearest neighbour (the core distance) and the distance between the selected object and another randomly selected object) is calculated for each pairing of the selected object and all other objects in the data set. The smallest reachability distance found is chosen as the next value in the reachability plot. This is process is repeated for all objects. The resulting reachability plot will have peaks at the boundaries between different clusters - the scanning radius, epsilon, sets the threshold for how large a peak must be in order to be defined as a boundary between clusters (Daszykowski *et al.*, 2002). The minimum number of STAs in a cluster (k) was set to 3.

The OPTICS algorithm was repeated for 1001 values of epsilon equally spaced between 0 and 1. The results from this clustering were combined into a co-occurrence matrix, mapping the mean frequency with which each pair of STAs are assigned to the same cluster.

Next, the data set of all STAs was clustered with a k-means algorithm using the inbuilt MATLAB function 'kmeans'. K-means is a distance based clustering metric. Briefly, all objects (STAs in this case) are sorted into k clusters on the basis of proximity. At the beginning of the algorithm, k cluster centres are chosen at random. The distance between each object and each cluster centre is calculated and each object is assigned to the closest cluster. The average of each cluster is then used to generate k updated centre locations. This is repeated either until cluster assignments stop changing, or until the number of iterations reaches a pre-set maximum.

The k-means algorithm was repeated for values of k between 1 and 15. The results from this clustering were also combined into a co-occurrence matrix.

Finally, the mean of the OPTICS and the k-means co-occurrence matrices was taken as the result of the ensemble clustering. This matrix was then itself clustered using the Ward linkage algorithm (again, a built-in MATLAB function). This is an agglomerative hierarchical clustering method, where a large number of small clusters are merged step by step to uncover structural hierarchy in the data set. In Ward's linkage, each merger should minimize the total variance within the resulting cluster. This is achieved by minimising the increase in the sum-of-squares of distances between every object in the new cluster.

2.5 STA summary statistics

Three dimensional spatiotemporal STAs were separated into spatial and temporal components for the purposes of characterisation. First, the STA was smoothed using a 3x3x3 pixel 'box' (cube) kernel. Then singular value decomposition (performed using the 'svd' MATLAB function) was used to derive a set of orthogonal spatial and temporal kernels from the first left and right singular vectors (Wall *et al.*, 2003). This separation was constrained to only produce spatial filters with positive central values, thus restricting information about the polarity of the STA to the temporal kernel.

If the STA is truly space-time separable, then combining these first components should produce an identical filter (Wolfe & Palmer, 1998). In reality, this is not the case - partly because each recording includes noise, and partly because not all the recorded STAs are meaningfully space-time separable.

All summary statistics were calculated using custom written MATLAB routines unless otherwise stated.

2.5.1 Temporal kernel summary statistics

Several summary statistics were calculated using the temporal kernels obtained through singular value decomposition. These kernels were first normalised so that all the data fell between -1 and +1. They were then resampled using shape preserving piecewise cubic interpolation ('pchip') to estimate kernel values at 0.001 ms increments.

Time to peak was determined as the position of the first peak in the temporal kernel relative to the spike time. The polarity of this peak (whether it is a positive or a negative deflection from the mean) was used as a measure of the polarity of the STA. Time to zero cross was defined as the time between the first peak and the zero crossing that precedes it, relative to the spike time. The biphasic index was defined as the ratio of the absolute values of the minimum and maximum peak of the temporal kernel. This index was constrained to values between 0 (indicating a completely monophasic temporal kernel) and 1 (indicating the presence of at least two peaks of equal magnitude and opposite sign). A diagram of each of these measures is shown in figure 2.4.

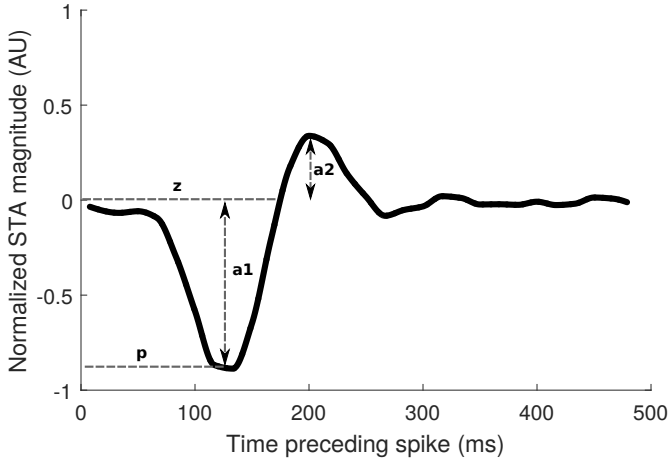

Figure 2.4: **How temporal kinetics are characterised:** Four summary statistics are used to characterise the temporal properties of the collected STAs. The time to peak (**p**) is defined as the position of the first peak of the temporal kernel, relative to the spike at 0 ms. Zero cross time (**z**) is defined as the point where the temporal kernel crosses zero following the first peak. Biphasic index is measured as the ratio between the absolute values of the maximum and the minimum of the temporal kernel (in this example, **a2/a1**). The fourth summary statistic used is the peak of the Fourier transform of the temporal kernel.

For the purposes of measuring temporal frequency tuning, longer STAs were calculated using 100 frames, or 1.67 (2 d.p.) seconds, of the stimulus preceding each spike. This longer temporal window extends the lowest frequency that can be detected to approximately 0.6 Hz (1/T) (Nirenberg *et al.*, 2010). Temporal kernels were extracted as above and normalised so that all the data fell between -1 and +1. The discrete Fourier transform (fft) of these kernels was then calculated in MATLAB, and the magnitude extracted by taking the absolute value of the complex Fourier transform, divided by its length (100 samples).

The location (in Hz) of the peak of the Fourier transform was taken as a measure of the temporal frequency tuning of the STA.

2.5.2 Spatial kernel summary statistics

Spatial kernels obtained through singular value decomposition were used in attempts to quantify the spatial properties of the full spatiotemporal STAs.

First, 10 by 20 pixel kernels were converted to square 20 by 20 kernels using cubic interpolation. Then, difference of Gaussians (DoG) and Gabor filters were fit to them using a nonlinear least squares algorithm (MATLAB code provided by Kay (2013)). The coefficient of determination (R^2, a measure of the goodness-of-fit of the function to the original kernel) was calculated as the percentage of the variance in the kernel that is accounted for by the model function.

The two dimensional discrete Fourier transform of the spatial kernel ('fft2' inbuilt MATLAB function) was calculated and the magnitude (the absolute value of the complex transform) was taken. This was then simplified into one dimensional summaries of spatial frequency and orientation.

The summary of spatial frequency was extracted as the mean of the relative sensitivity

of the two dimensional Fourier transform within a ring encircling 0 cycles per pixel with an expanding radius. The peak spatial frequency was then taken as the location (in cycles per pixel) of the peak of this one dimensional summary. The summary of orientation was extracted as the maximum relative sensitivity within a radial segment extending from the centre (0,0) of the 2D Fourier transform, rotated clockwise from (-0.5,0) cycles per pixel. A symmetry index was then calculated as the ratio between the trough and the peak of this one dimensional summary.

Finally, instability in the spatial kernels was quantified as the absolute difference between the one dimensional summary plots of spatial frequency for a single cell at each light level.

2.6 Statistics

As all the distributions compared in this study were non-parametric and the study had a two-factor design (animal model and light level), I chose to use the permutation methods outlined by Basso *et al.* (2009) and Manly (2007). All statistical analyses were performed using custom written MATLAB functions.

Permutation one and two-factor ANOVAs were performed by taking the F statistics from the relevant ANOVA algorithm (the anova1 or anovan MATLAB functions) for both the original data set and for 100,000 permuted data sets where the data was randomly shifted into different groups (e.g. across light levels and animal models). P values could then be calculated from the distribution of F statistics from the permuted data - the number of times the F statistic from the real data set was larger than that from a permuted data set, divided by the number permutations, gave the p value. If this was smaller than 0.05 for a main effect or an interaction term, post-hoc tests were performed. With 100,000 permutations, p values are accurate to 10^{-5}.

Post-hoc tests were performed similarly, with the F statistic replaced by the absolute difference in means between the two data sets being compared.

Permutation Chi squared tests were performed by taking the Chi-squared value (using the crosstab MATLAB function) as the test statistic. Again, 100,000 permutations were performed. If the results of this test over the entire data set were significant ($p < 0.05$), permutation post-hoc tests were performed using the same test statistic, but calculated only for the two groups of interest to the comparison.

To correct for multiple comparisons in post-hoc tests, Bonferroni correction was used. This adjusts the p value required to flag a difference as statistically significant (the alpha value), based on the number of comparisons performed. In the case of an alpha of 0.05 and 20 comparisons, the new adjusted alpha significance value is 0.05/20 or 0.0025.

Finally, a nonparametric measure of effect size, Cliff's delta, was used in this study (Cliff, 1996). This is a measure of 'dominance', or the degree of overlap between two distributions. An effect size of +/- 1 indicates no overlap, and an effect size of 0 indicates complete overlap between the groups.

3 Exploratory data analysis

3.1 Introduction

White noise stimuli provide a relatively unbiased method of sampling retinal ganglion cell input space, but this stimulus design also introduces some complications. The resulting dataset is rich, but highly variable and difficult to visualise. Each STA consists of a 10 by 20 pixel grid over 30 time points - 6000 pixels overall. When a cell is identified at every experimental light level, there are 30,000 data points for that single cell. In order to summarise and meaningfully compare data of this nature, some form of dimensionality reduction is necessary.

Dimensionality reduction is a feature of any quantitative research. Descriptive statistics such as mean and variance are commonly used to simplify presentation and interpretation of large datasets. The STA itself, as the mean of the ensemble of stimulus frames that preceded each spike, is a form of dimensionality reduction (Pillow & Simoncelli, 2006). In circumstances where the data set is not just large (in this case, a large number of cells), but also multivariate (in this case, thousands of pixel values), feature selection often becomes a necessary step in dimensionality reduction. Feature selection consists of extracting information about relevant features of interest from "raw" data. As a simple example, high dimensional, multivariate imaging data can be converted into

cell count data using feature extraction (either using automatic segmentation tools, or through manual cell counts). At the more extreme end, automated feature extraction performed on patient samples can be used to develop new diagnostic tools (Markiewicz & Osowski, 2006). The kind of features that can be extracted from multivariate data are limited only by the extent to which that feature is encoded in the collected data, and how that feature is defined by the analyser.

In the context of the analysis of white noise STAs from cells in the visual pathway, the options available for feature selection are vast. Most commonly, the measured STA is split into spatial and temporal components. Spatial components tend to be fit with a Gaussian or a difference of Gaussians (mimicking the centre-surround model of retinal receptive fields), enabling a description of receptive field shape and size (Field *et al.*, 2010, Frechette *et al.*, 2005, Sekirnjak *et al.*, 2011, Sher & DeVries, 2012). Temporal profiles (obtained either from separating spatial and temporal aspects of the STA, or by using a full field noise stimulus that only gives temporal information) are frequently summarised using the time to the peak of the response or the time to zero cross. Additionally, information about the temporal frequency tuning of the cell can be extracted by examining the Fourier transform of the temporal STA (Field *et al.*, 2007, Sekirnjak *et al.*, 2011, Sher & DeVries, 2012, Wang *et al.*, 2011).

However, these feature selection methods are not the limit for analysis of STAs. Field *et al.* (2010) used the high resolution of their stimulus to identify the individual photoreceptor cells driving their ganglion cells. Even with a lower stimulus resolution, the spatiotemporal STA provides the opportunity to extract more information about the shape of the receptive field than traditional difference of Gaussian models may reveal.

Given the exploratory aims of this project, the richness of the data, and the number of possible features to measure, I have chosen to use a data-driven approach to guide

feature definition and selection. That is, I will use exploratory data analysis to help define the kind of feature selection methods that would best describe the data.

Data driven feature extraction and dimensionality reduction are widely used in bioinformatics approaches to multivariate data. In particular, studies comparing gene expression data often apply these techniques to identify subtypes of cells, or networks of gene interactions. One of the most commonly used algorithms is principal components analysis (PCA).

PCA, first described by Pearson (1901), can be understood intuitively as a search for a new co-ordinate system or set of axes onto which to plot the data. In the context of a STA with 6000 pixel values, the default co-ordinate system would be the magnitude at each pixel - 6000 axes, each with potentially relevant information about the receptive field, and each potentially correlated with other pixel axes. PCA enables transformation of this data into a new co-ordinate system, where each axis (principal component) is orthogonal to the preceding axis, and accounts for as much of the variance in the data as possible. It is an unsupervised method that enables examination of patterns in complex data (Ben-Hur & Guyon, 2003, Eriksson *et al.*, 2006, Jolliffe, 2002, Ma & Dai, 2011, Ringnér, 2008, Wall *et al.*, 2003).

When used as an exploratory data analysis tool, PCA can be remarkably powerful. Stephens *et al.* (2008) have used the method to generate "eigenworms" - the first few principal components from a PCA based analysis of the movement behaviour of *C. elegans*. This projection enabled characterisation and modelling of whole-organism behaviour using only a few variables, and paved the way for a deeper understanding of how movements are choreographed by *C. elegans*.

PCA has also been used to characterise retinal data, including as a first step towards grouping temporal STAs from primate retinas into functional cell classes (Anderson

et al., 2011, Field *et al.*, 2007).

Alongside PCA, I will employ clustering algorithms to identify classes within the data to help guide the analysis. Clustering of receptive fields into subgroups based on functional responses is now quite widely used in visual neuroscience (Carcieri *et al.*, 2003, Farrow & Masland, 2011, Piscopo *et al.*, 2013, Puchalla *et al.*, 2005). Alongside PCA, this approach will be used here to provide an overview of the data set and the kinds of visual responses it contains, in order to inform further analysis.

3.2 Results

3.2.1 The data set

The final collected data set (C57BL/6 n=8, rd17 n=8, and cpfl1 n=8), consists of 962 unique units (1099 units passed false positive and negative threshold, and 137 duplicate units were removed, as described in section 2.1.3). Once the tissue was on the elecrode array, each recording session lasted approximately 3 and a half hours, including adaptation time.

Overall, 30 mice were used in this study - 12 C57BL/6, 9 rd17, and 9 cpfl1. Recordings from 6 mice (4 C57BL/6, 1 rd17, and 1 cpfl1) were not used, as blockages in the perfusion system did not permit survival of the tissue through all 5 light level repeats. This problem was resolved with the addition of a higher concentration ethanol rinse when cleaning the perfusion system after each experiment.

STAs were calculated for each unit at each light level at which it was identified, and assessed for significance. Out of all the identified units, 602 had a significant STA at one or more light levels. 253 of these units were from C57BL/6 mice, 161 from rd17 mice, and 188 from cpfl-1 mice.

Overall, 1084 significant STAs were identified across all animal models and light levels. These were combined into a 6000 by 1084 data matrix on which exploratory data analysis was performed.

3.2.2 The principal components

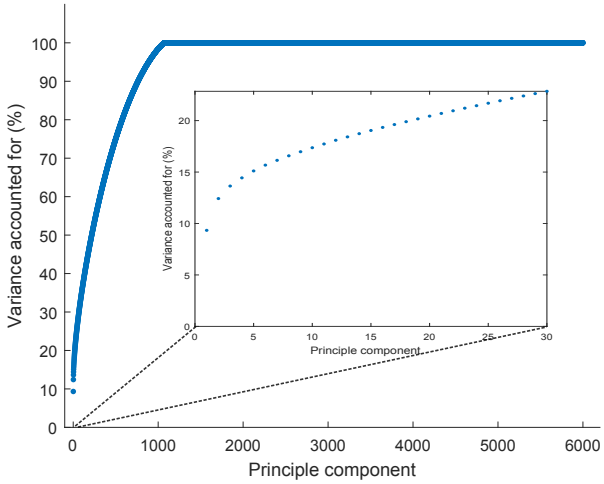

Figure 3.1: **Percentage of variance across all significant STAs explained by each successive principal component:** The first few principal components explain more of the variance in the STAs than successive components, but the majority of the overall variance in the STAs is best explained by a large number of principal components, which individually only account for a small proportion of the variance. 100% of the variance is explained by the first 1084 principal components (one component for each STA filter analysed). Insert shows the variance explained by the first 30 principal components.

Principal components analysis (PCA) of the matrix of all significant STAs was performed in MATLAB using the 'eig' algorithm as described in section 2.4, page 76. Figure 3.1 shows the percentage of the variance in this data set explained by each identified principal component. The results of this analysis demonstrate the complexity of the data - several hundred principal components must be considered to explain 90% of the variance.

Figures 3.2 and 3.3 show the first ten principal components identified using this technique. Each component is a linear combination of variables (in this case, STA pixel

values) that separates the data (Jolliffe, 2002). On examination, the components combine spatial and temporal properties that are commonly observed across the STAs.

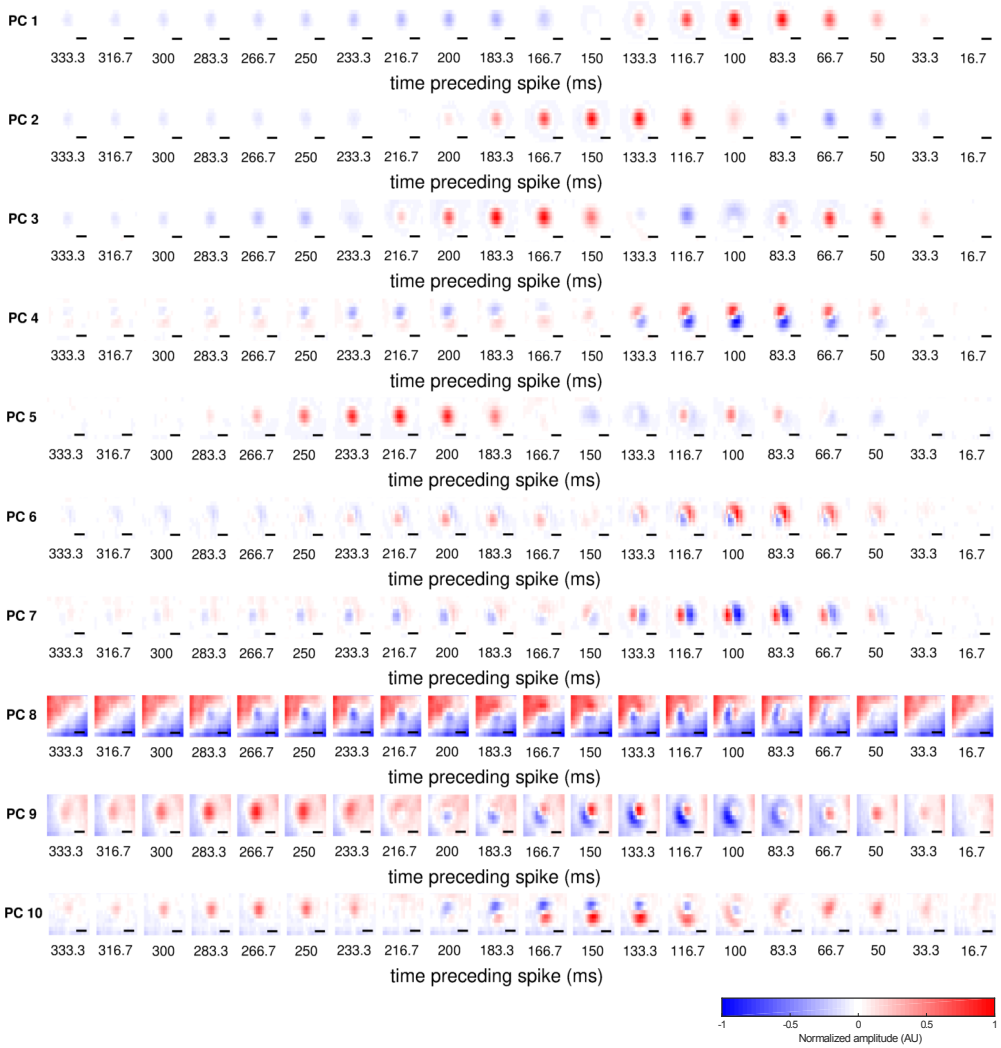

Figure 3.2: **The first ten principal components:** The first ten principal components of the 1084 STAs analysed. For display purposes, only the last 20 frames of each filter are shown, and data have been smoothed using a 3x3x3 pixel box filter. Additionally, the filters have been normalized for display so that the maximum amplitude is constrained to either +1 or -1 (depending on the sign of the filter maxima). Scalebar = 200μm across

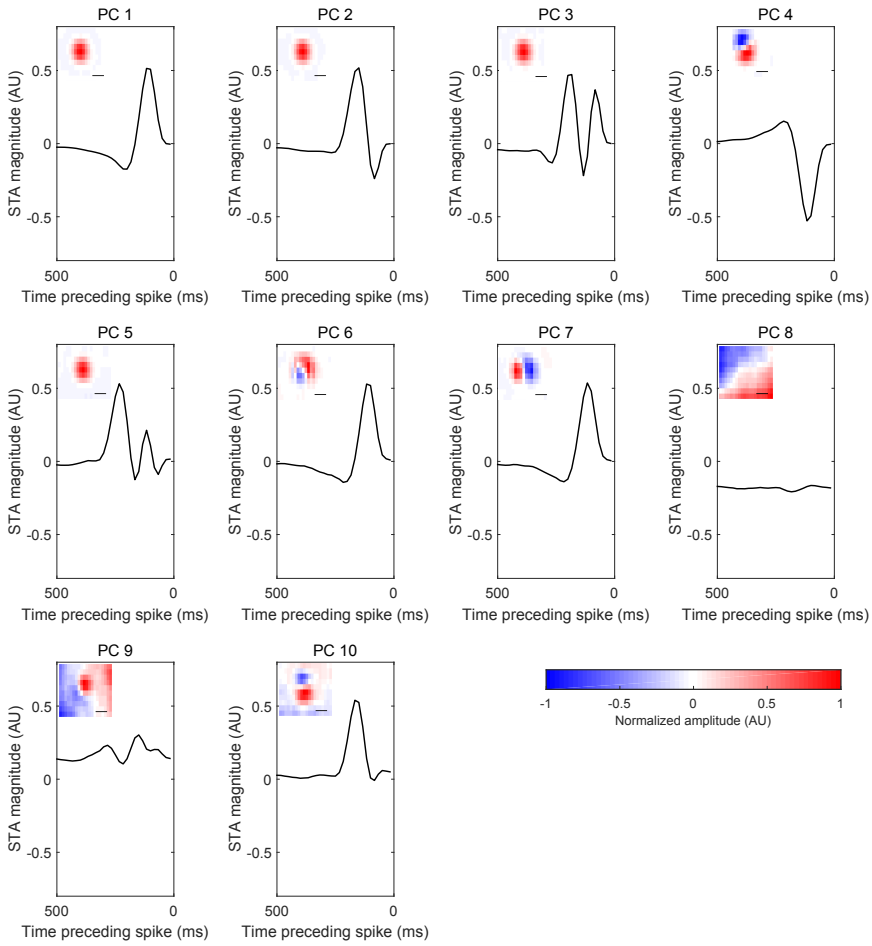

Figure 3.3: **The first ten principal components, decomposed:** The first ten principal components, split into spatial and temporal filters for ease of visualisation. Spatial and temporal filters were obtained from the singular value decomposition of the full smoothed spatiotemporal principal component filter. The amplitude of the spatial filters is constrained to either +1 or -1 (depending on the sign of the filter maxima). Scalebar = 200μm across

It is possible to project each significant STA filter onto each principal component - resulting in a score that reflects the extent to which the STA agrees with the component. The more positive the score, the closer the agreement, and the more negative the score the less agreement there is.

Figure 3.4 shows the projection of all significant STAs onto the first ten principal components. These projections indicate that there are very few distinct clusters in the data, but instead that variation along most principal components is fairly continuous. The exceptions to this are projections onto PC 1, which form two lobes with a third, smaller cluster between them, and projection onto PC3, where a small cluster of STAs

can be identified that project more negatively onto this component than the rest of the data set.

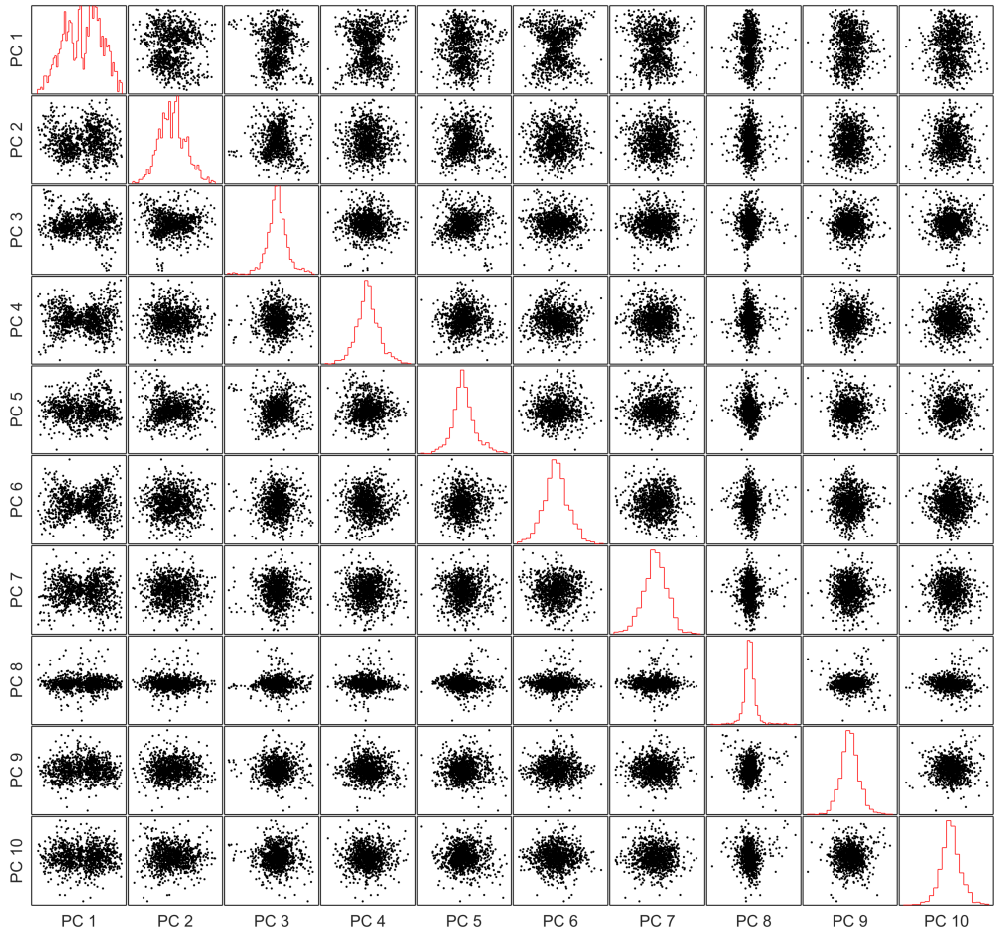

Figure 3.4: **Projection of STAs onto the first ten principal components:** Matrix plot of each STA filter projected onto each possible pairing of the first ten principal components. Histograms of the probability density function of the projection onto each individual principal component are plotted along the diagonal. These plots show the clear bimodal distribution of filters projected onto PC 1. Additionally, a small separable group appears to be present along PC 3, and some separation between filters along PC 2, PC 4, and PC 5.

3.2.3 Ensemble clustering

Due to the shape of the projection onto the first two principal components, I chose to use ensemble clustering employing both a density and a distance based metric, following the advice outlined by Ronan *et al.* (2016). The resulting co-occurance matrix was then clustered using the Ward linkage algorithm, resulting in a hierarchy of relationships

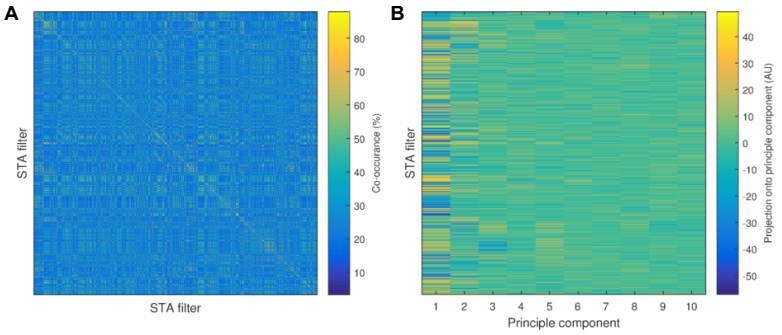

Figure 3.5: **Overview of STA dataset and ensemble clustering prior to applying any groupings: A)** Co-occurrence matrix prior to sorting. Each STA filter has is scored based on the percentage of times it co-clusters with each STA filter. Higher co-occurrence values indicate filters that ought to be assigned to the same cluster. **B)** Projection of each STA filter onto the first 10 principal components, prior to sorting. As shown in Fig 3.1, there is more variance along the first principal component than along subsequent components.

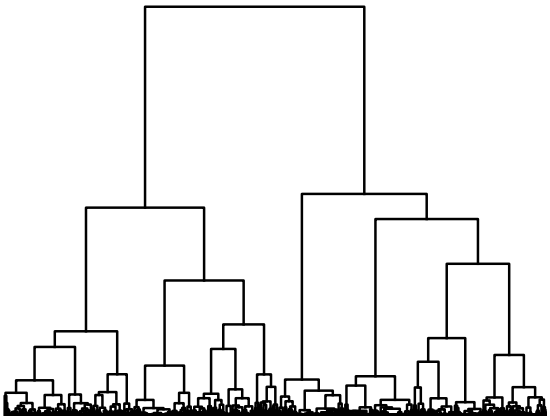

Figure 3.6: **Dendrogram depicting Ward linkage of STA co-occurrence matrix:** The co-occurrence matrix (Fig 3.5 A) obtained through ensemble clustering was itself clustered using the Ward linkage algorithm. A dendrogram of the hierarchical clusters obtained could then be plotted. There is a clear division into three initial groups, with substantial structure within the two larger groups.

depicted in the dendrogram in Figure 3.6. By adjusting the threshold for the number of clusters defined by the Ward linkage results, it was possible to examine the extent to which the clusters identify functional subclasses within the STA dataset.

The co-occurance matrix can be split into three clusters, based primarily on separation along the first principal component, demonstrated in Figure 3.7.C and Figure 3.8. This split divides STAs into positive, negative, and low projection onto PC1. Plotting the mean of each cluster (Figure 3.9) reveals that they identify three functional groups -

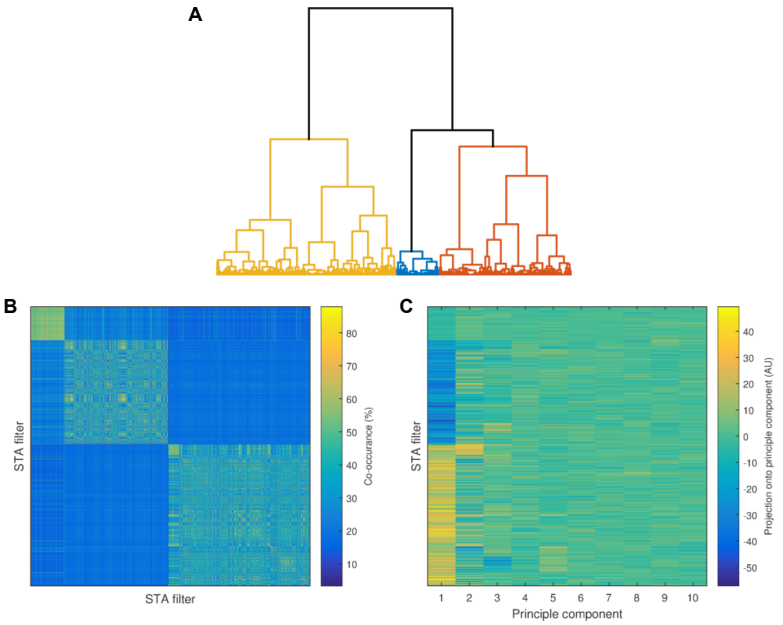

Figure 3.7: **Obtaining three clusters from ensemble clustering:** The co-occurance matrix can be clustered into three groups (**A**), when it is re-ordered according to those groups (**B**), a clear structure emerges indicating that filters assigned to each group are more likely to cluster together than to cluster with filters in the other two groups. When the matrix of projection onto the first ten principal components (**C**) is similarly re-ordered, it is clear that separation into these two groups is based largely on projection onto the first principal component, with filters split into positive, negative, and null scores.

ON STAs, OFF STAs, and responses with noisy timecourses that are harder to identify as ON or OFF. STAs assigned to group 1 (neither ON nor OFF), score close to zero against many of the other first 10 components as well, implying that these STAs may have less structure in general than those assigned to groups 2 or 3.

Separating the co-occurance matrix into five clusters identifies not just the ON and OFF functional classes, which are identifiably separate on projection onto the first component, but also separates STAs which have more biphasic timecourses (mapping to the more continuous distribution of projection onto PC2).

When the co-occurance matrix is split into ten and then twenty clusters (Figures 3.13 - 3.18), more structure is identified along projection onto the first and second principal components. The resulting clusters are more similar to each other, with the primary distinguising feature being temporal shift - how close the peak of the STA is to the

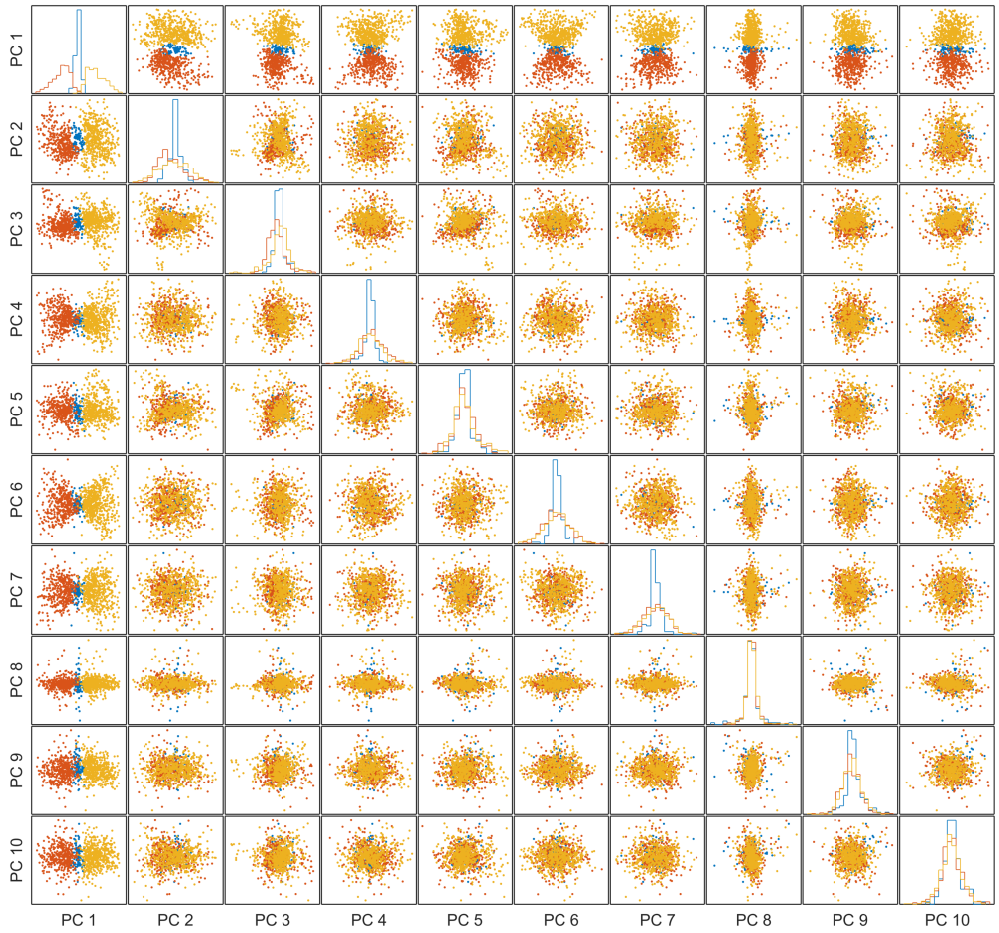

Figure 3.8: **Projection of STA filters onto the first ten principal components, three groups:** Each STA filter, projected onto each pair of principal components. Histograms along the diagonal show probability density functions for projections onto each principal component. It is clear that separation into three clusters depends primarily on projection onto the first principal component. (group 1 = blue, group 2 = red, group 3 = yellow)

spike. Additionally, when the data is forced into a larger number of clusters, structure along the third, fourth, and fifth principal components is also revealed. In particular, group 7 in ten clusters and group 12 in twenty clusters reveal negative projection onto principal component 3, and positive projection onto principal component 5.

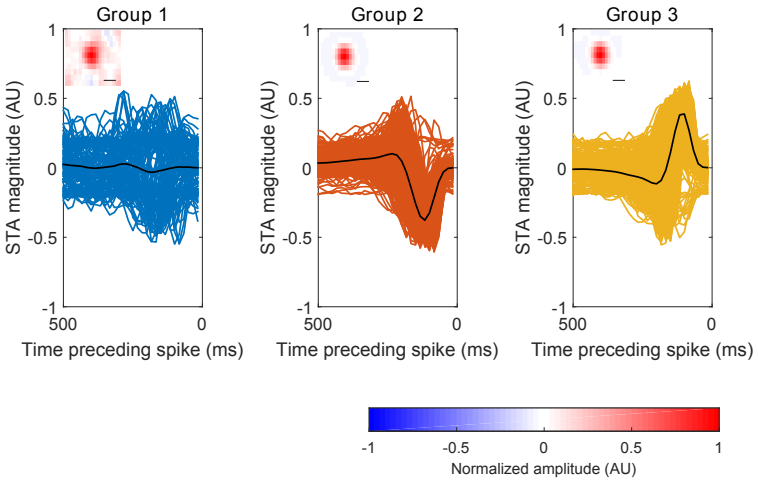

Figure 3.9: **STA filters separated into three groups:** The three groups of STAs correspond to OFF (Group 2) and ON (Group 3) cells, with cells that are not easily categorised as ON or OFF are separate (Group 3). The mean temporal component of each group is plotted in black. Spatial components also represent the mean for each group (scalebar = 200μm across). The amplitude of the spatial filters is constrained to either +1 or -1 (depending on the sign of the filter mean). Smoothed STAs were separated into temporal and spatial components for ease of visualisation using singular value decomposition.

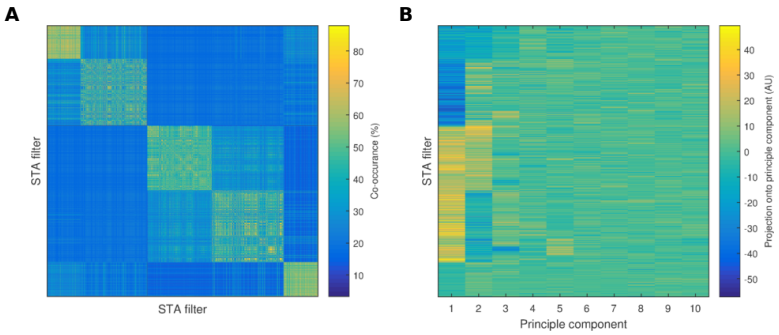

Figure 3.10: **Obtaining five clusters from ensemble clustering:** (**A**) The co-occurrence matrix after separating into five clusters according to the Ward linkage. (**C**) Matrix of projection onto the first ten principal components, re-arranged after separation into five clusters. This demonstrates that projection onto the second principal component, as well as the first, defines these clusters.

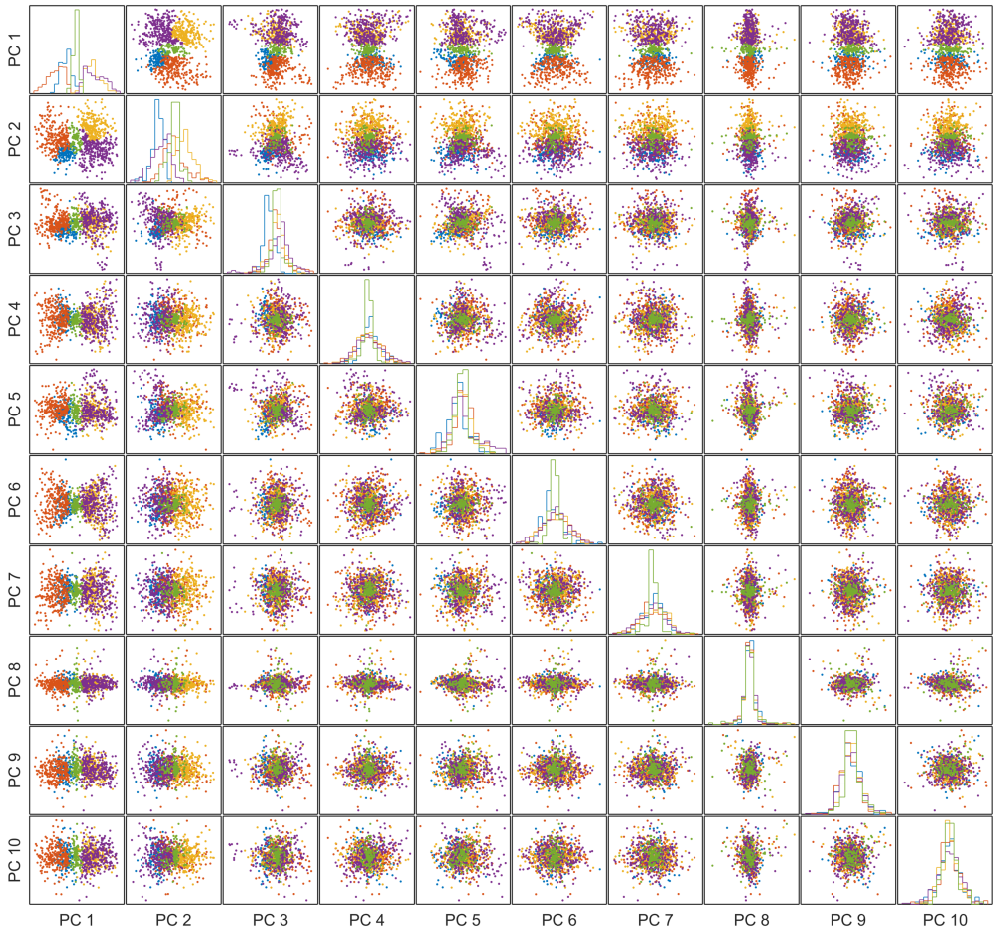

Figure 3.11: **Projection of STA filters onto the first five principal components, five groups:** Each STA filter, projected onto each pair of principal components. Histograms along the diagonal show probability density functions for projections onto each principal component. (group 1 = blue, group 2 = red, group 3 = yellow, group 4 = purple, group 5 = green)

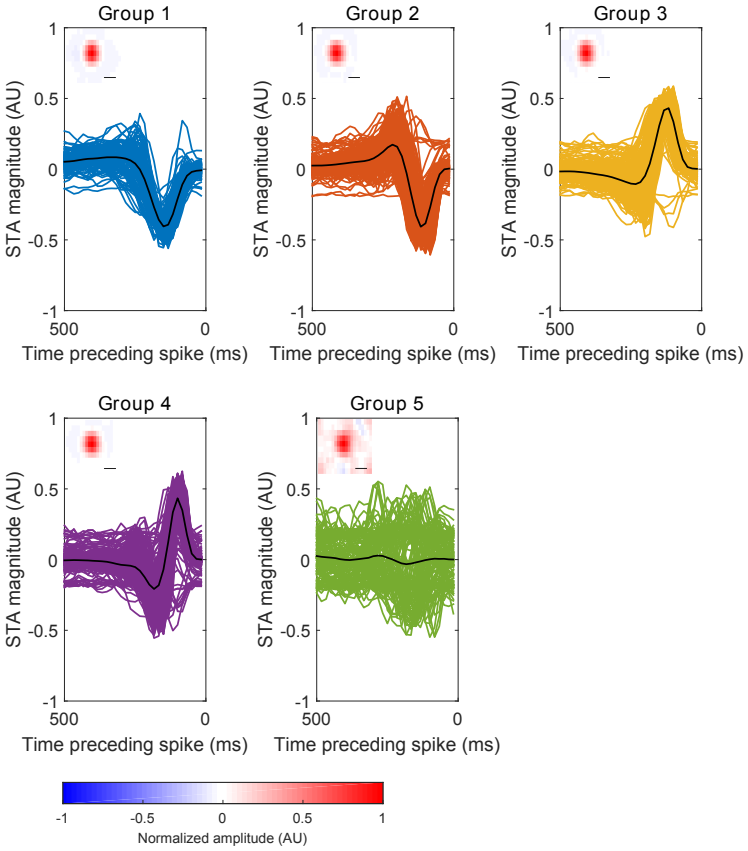

Figure 3.12: **STA filters separated into five groups:** Groups 1 and 2 show OFF filters, and groups 3 and 4 ON filters. Groups 2 and 4 are more biphasic and have a shorter time to peak than groups 1 and 3. Group 5 contains the 'null' responses. The mean temporal component of each group is plotted in black. Spatial components also represent the mean for each group (scalebar = 200μm across). The amplitude of the spatial filters is constrained to either +1 or -1 (depending on the sign of the filter mean). Smoothed STAs were separated into temporal and spatial components for ease of visualisation using singular value decomposition.

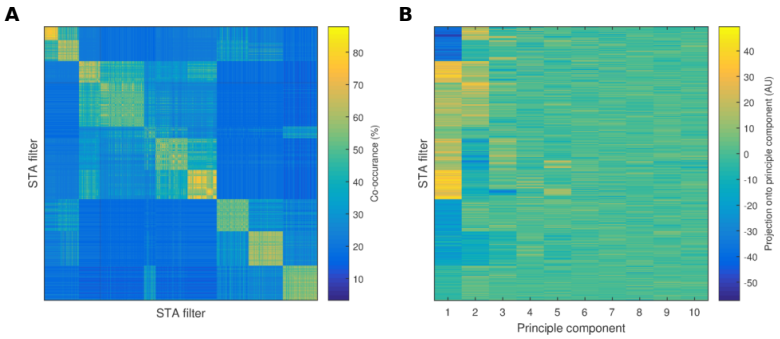

Figure 3.13: **Obtaining ten clusters from ensemble clustering:** (**A**) The co-occurrence matrix after separating into ten clusters according to the Ward linkage. (**C**) Matrix of projection onto the first ten principal components, re-arranged after separation into ten clusters. This arrangement primarily clusters STAs based on closer agreement in projection along the first and second principal component,but there is also some ordering of the matrix along the third component.

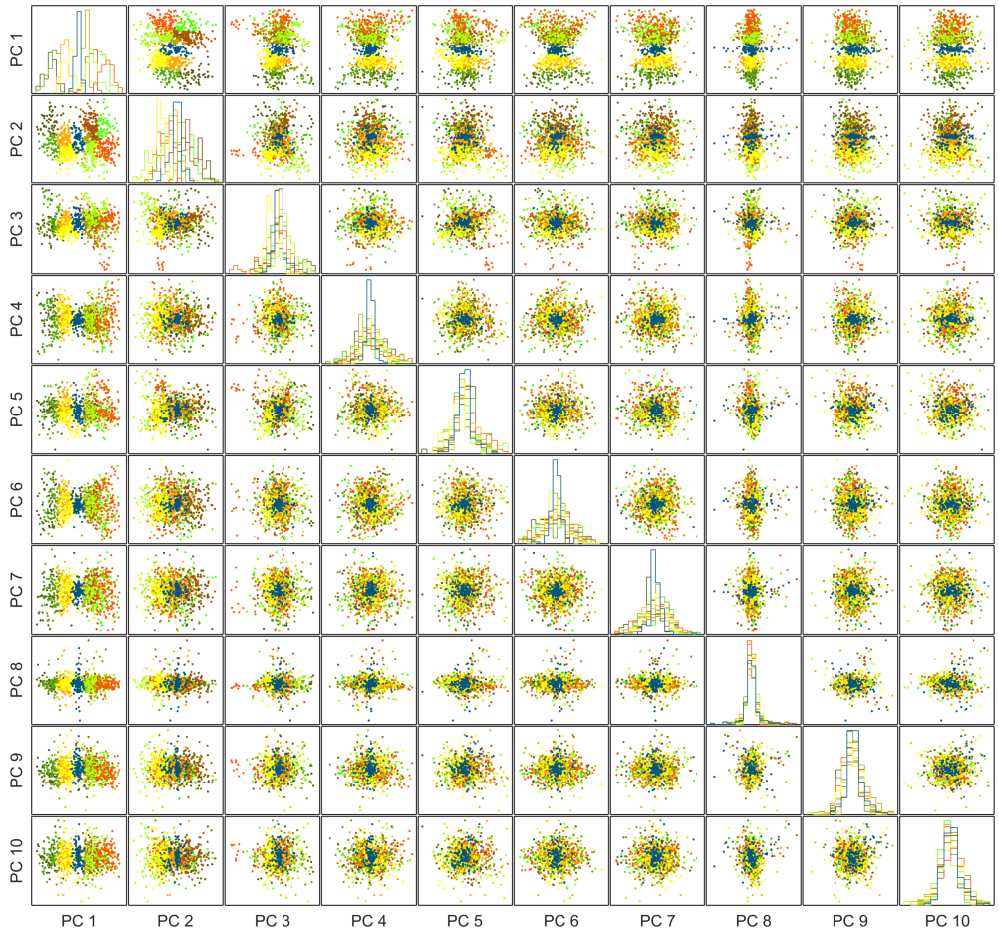

Figure 3.14: **Projection of STA filters onto the first ten principal components, five groups:** Each STA filter, projected onto each pair of principal components. Histograms along the diagonal show probability density functions for projections onto each principal component. (colour coding as in Figure 3.15)

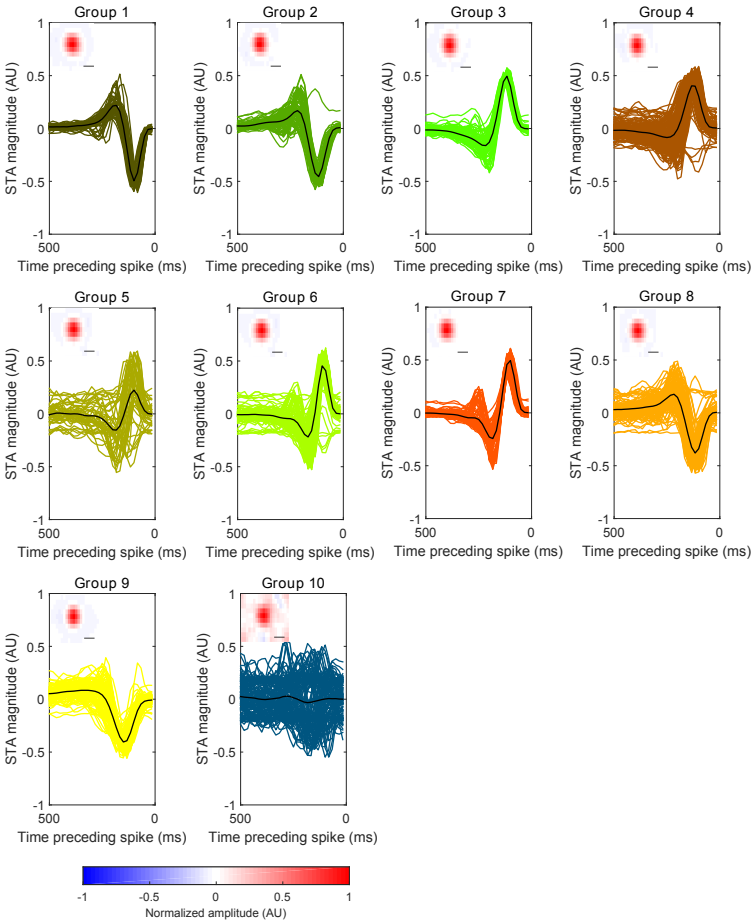

Figure 3.15: **STA filters separated into ten groups:** The mean temporal component of each group is plotted in black. Spatial components also represent the mean for each group (scalebar = 200μm across). The amplitude of the spatial filters is constrained to either +1 or -1 (depending on the sign of the filter mean). Smoothed STAs were separated into temporal and spatial components for ease of visualisation using singular value decomposition.

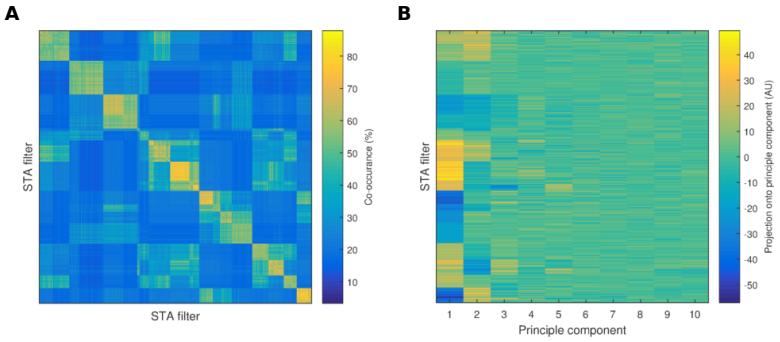

Figure 3.16: **Obtaining twenty clusters from ensemble clustering:** (**A**) The co-occurrence matrix after separating into twenty clusters according to the Ward linkage. (**C**) Matrix of projection onto the first ten principal components, re-arranged after separation into ten clusters. This arrangement clusters STAs based on agreement in projection along the first, second, and third principal components, as well as some organisation along the fourth and fifth principal components.

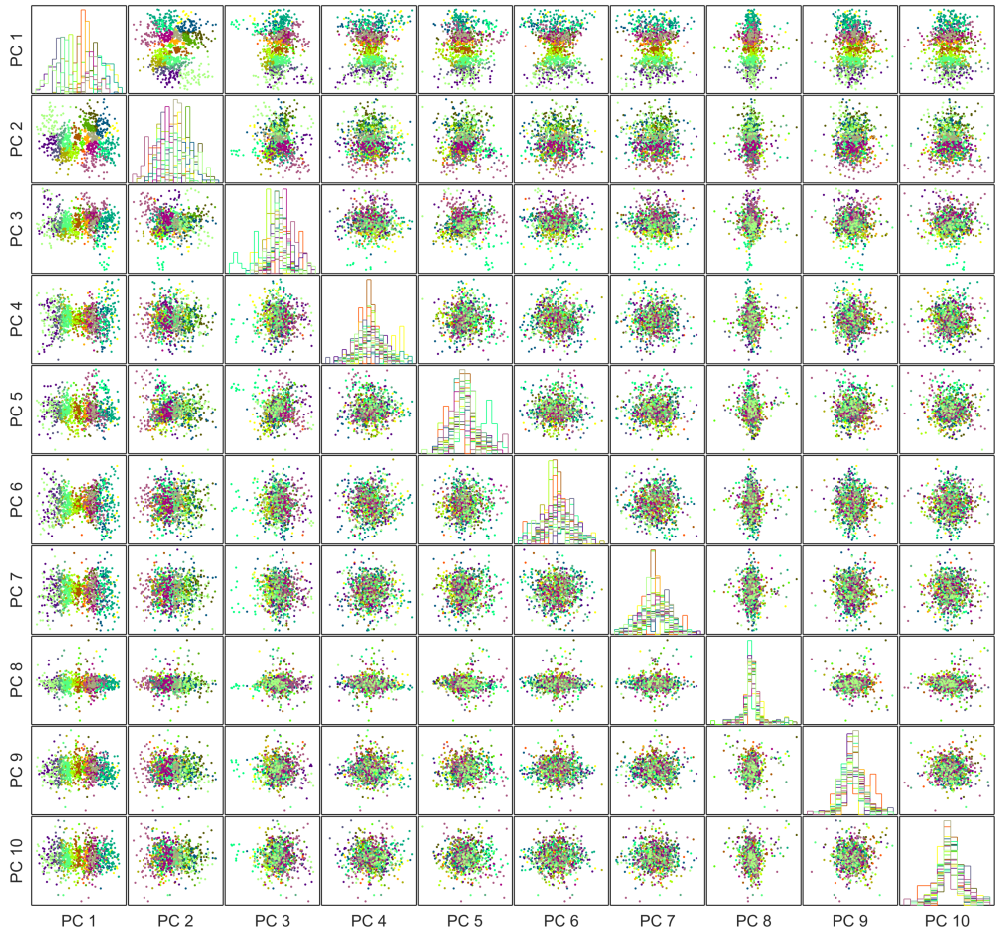

Figure 3.17: **Projection of STA filters onto the first ten principal components, twenty groups:** Each STA filter, projected onto each pair of principal components. Histograms along the diagonal show probability density functions for projections onto each principal component. (colour coding as in Figure 3.18)

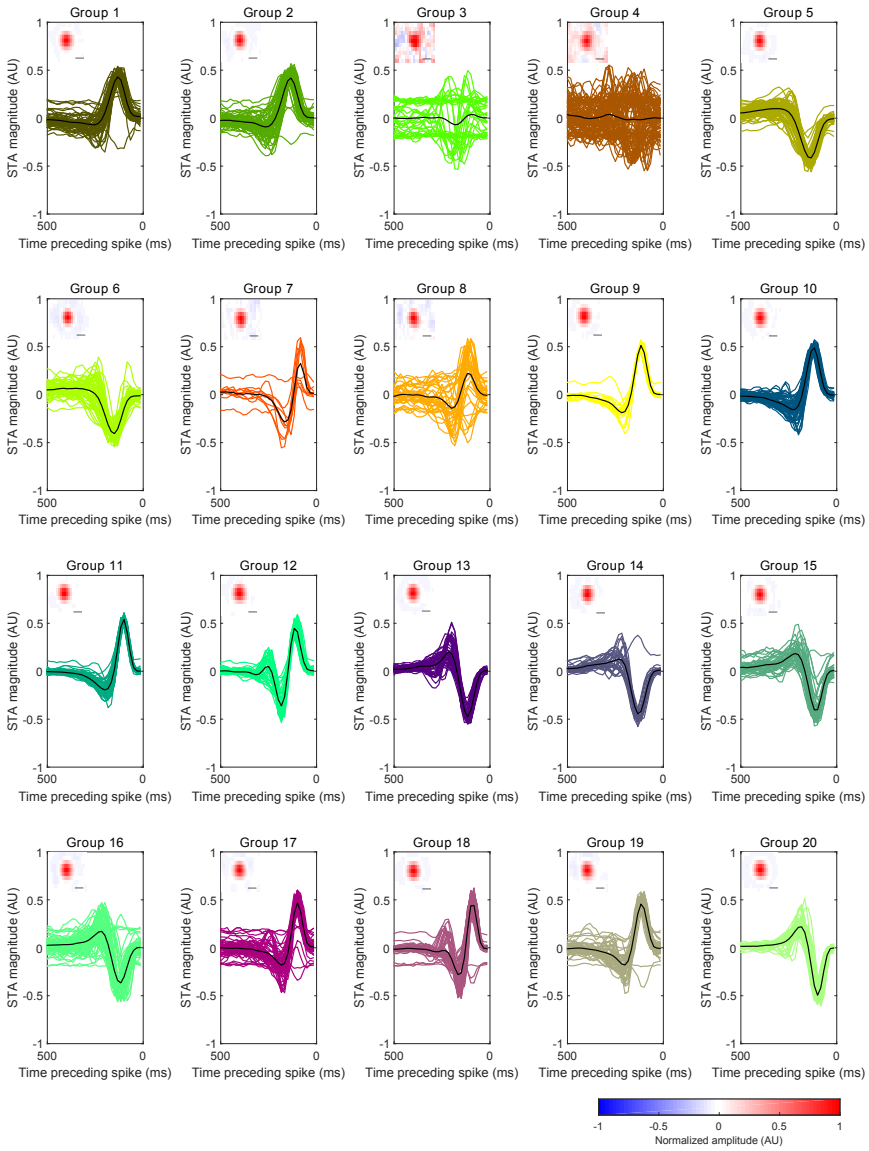

Figure 3.18: **STA filters separated into twenty groups:** The mean temporal component of each group is plotted in black. Spatial components also represent the mean for each group (scalebar = 200μm across). The amplitude of the spatial filters is constrained to either +1 or -1 (depending on the sign of the filter mean). Smoothed STAs were separated into temporal and spatial components for ease of visualisation using singular value decomposition.

3.2.4 Differences in component scores across animal models and light levels

Differences in projection onto the principal components in different experimental conditions can be used as a starting point for thinking about underlying trends in the data.

Figures 3.19 to 3.23 show projection onto the first ten principal components for STAs from C57BL/6 at each experimental light level compared to every other level. These plots show that the spread of scores for projection onto PC 3 and and PC 5 is broader at ND 4.5 than at higher light levels, indicating that the extent to which STAs are triphasic may differ between ND 4.5 and the other experimental conditions. Projection onto PC 1 is also skewed noticeably positive at ND 1, indicating that there may be a higher proportion of ON STAs at ND 1 compared to other light levels.

Projection onto PC 1 and PC 2 is more positively correlated at ND 4.5 than at other light levels, and projection onto PC 1 and PC 3 is more negatively correlated. The results of ensemble clustering, particularly when the limit is set at five clusters as shown in figure 3.11, reveal that positive correlation between PC 1 and PC 2 relates to temporal biphasicity and temporal latency of the STA. Groups 1 and 2 in figure 3.12 are slower and less biphasic OFF and ON filters, and STAs from only these two groups would appear positively correlated between PC 1 and PC 2. Negative correlation between PC 1 and PC 3 is also found for clusters of more triphasic STAs (this can be best seen in figures 3.17 and 3.18), suggesting that broader projection onto PC 3 may be related to the presence of more triphasic STAs at ND 4.5 compared to the other experimental light levels.

Figure 3.24 shows projection onto the first ten principal components for STAs from

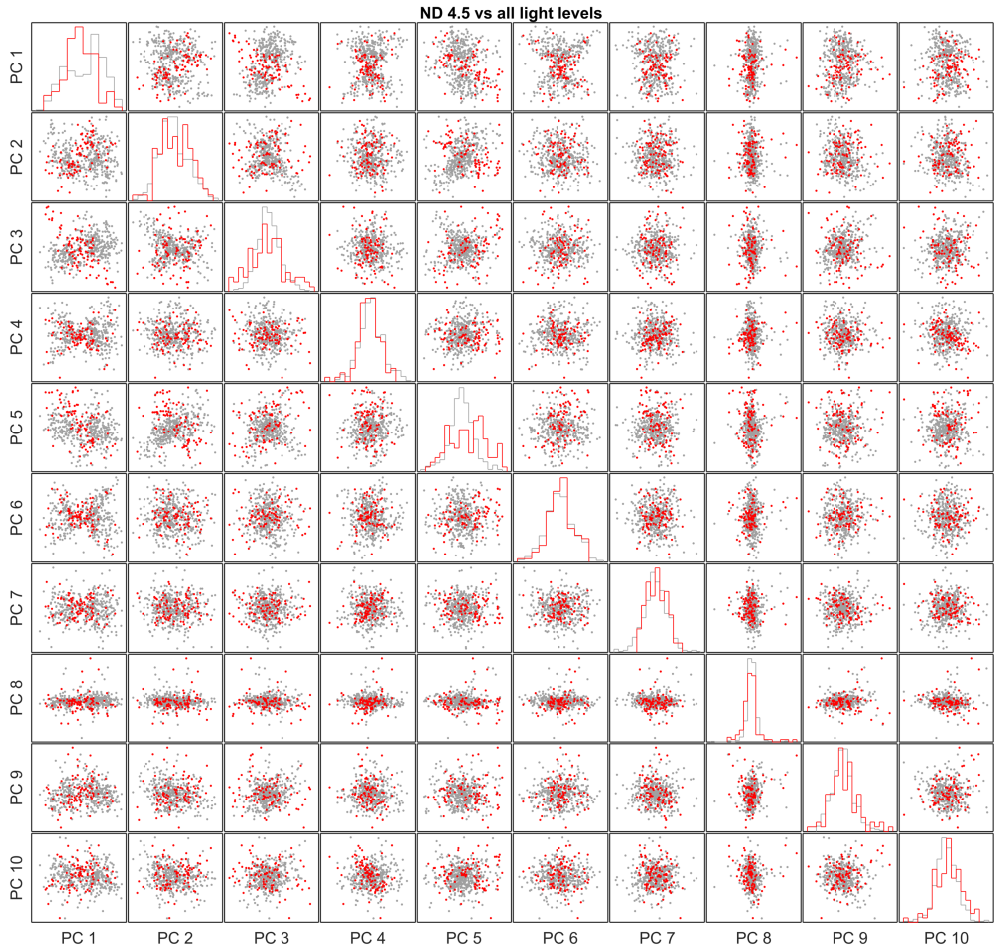

Figure 3.19: **Projection of STAs from C57BL/6 onto the first ten principal components at ND 4.5 compared to all other light levels:** Matrix plot of each STA filter from C57BL/6 mice projected onto each possible pairing of the first ten principal components. STAs recorded at ND 4.5 are show in red, and STAs from all other light levels are shown in grey. Histograms of the probability density function of the projection onto each individual principal component are plotted along the diagonal. This plot shows broader spread of projections onto PC 3 and PC 5 at ND 4.5 compared to other light levels. Positive correlation between projection onto PC 1 and PC 2, and negative correlation between projection onto PC 3 or PC 5 and PC 1.

rd17 mice compared to C57BL/6 mice. This plot shows that rd17 STAs have a much narrower spread of projections onto PC 3, and show very little of the negative correlation shape between projection onto PC 1 and PC 3 that is associated with more triphasic temporal features. This suggests that there may be fewer triphasic STAs in the rd17 population of receptive fields. Additionally, the histogram of projections onto PC 1 indicates a negative skew in STAs from rd17 mice compared to C57BL/6 mice. This suggests that there may be proportionally fewer ON responses recorded in rd17.

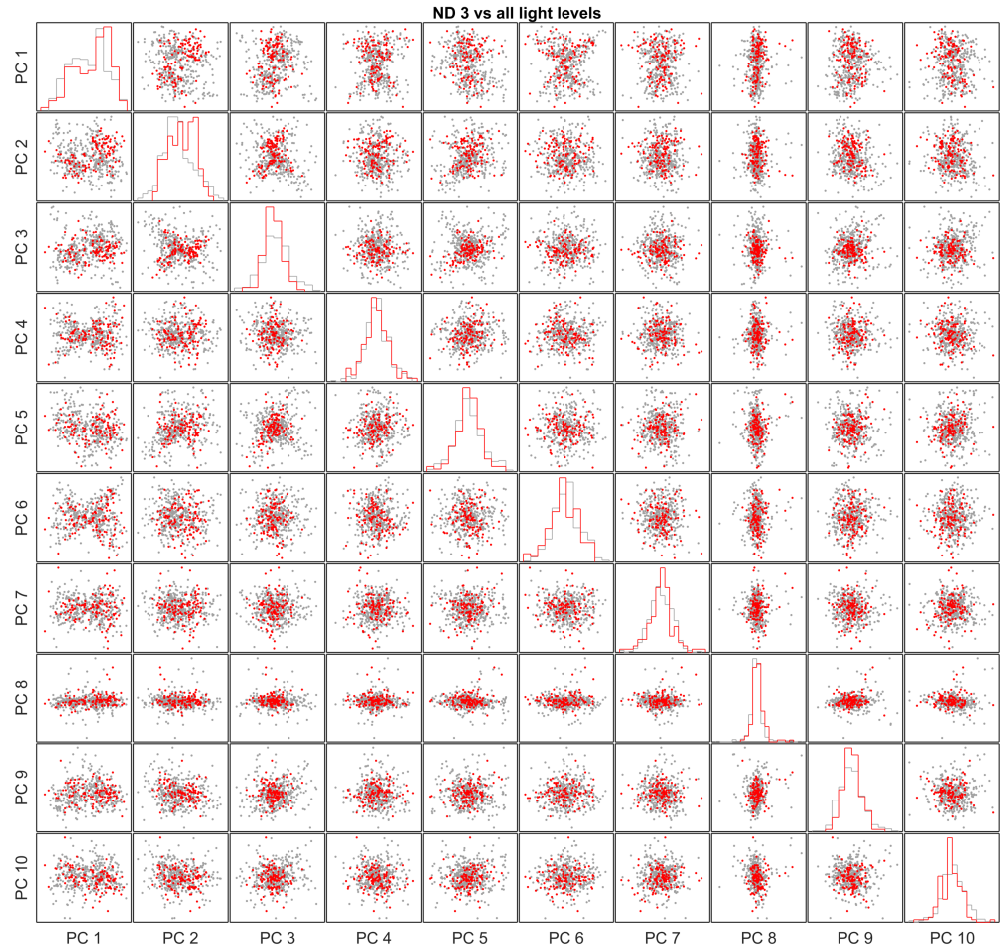

Figure 3.20: **Projection of STAs from C57BL/6 onto the first ten principal components at ND 3 compared to all other light levels:** Matrix plot of each STA filter from C57BL/6 mice projected onto each possible pairing of the first ten principal components. STAs recorded at ND 3 are show in red, and STAs from all other light levels are shown in grey. Histograms of the probability density function of the projection onto each individual principal component are plotted along the diagonal. This plot shows that projection onto PC 3 is narrower at ND 3 than at other light levels, and appears positively correlated with projection onto PC 3.

Figure 3.25 shows projection onto the first ten principal components for STAs from cpfl1 mice compared to C57BL/6 mice. cpfl1 STAs have a much broader spread of projections onto PC 3 compared to C57BL/6. In particular, there is a small distinct cluster of STAs with highly negative projections onto PC 3 that are only present in cpfl1 mice. As outlined above, the results from ensemble clustering (demonstrated in figures 3.17 and 3.18), show that this group, and the broader spread of scores in general, is related to the presence of STAs with very triphasic temporal response profiles.

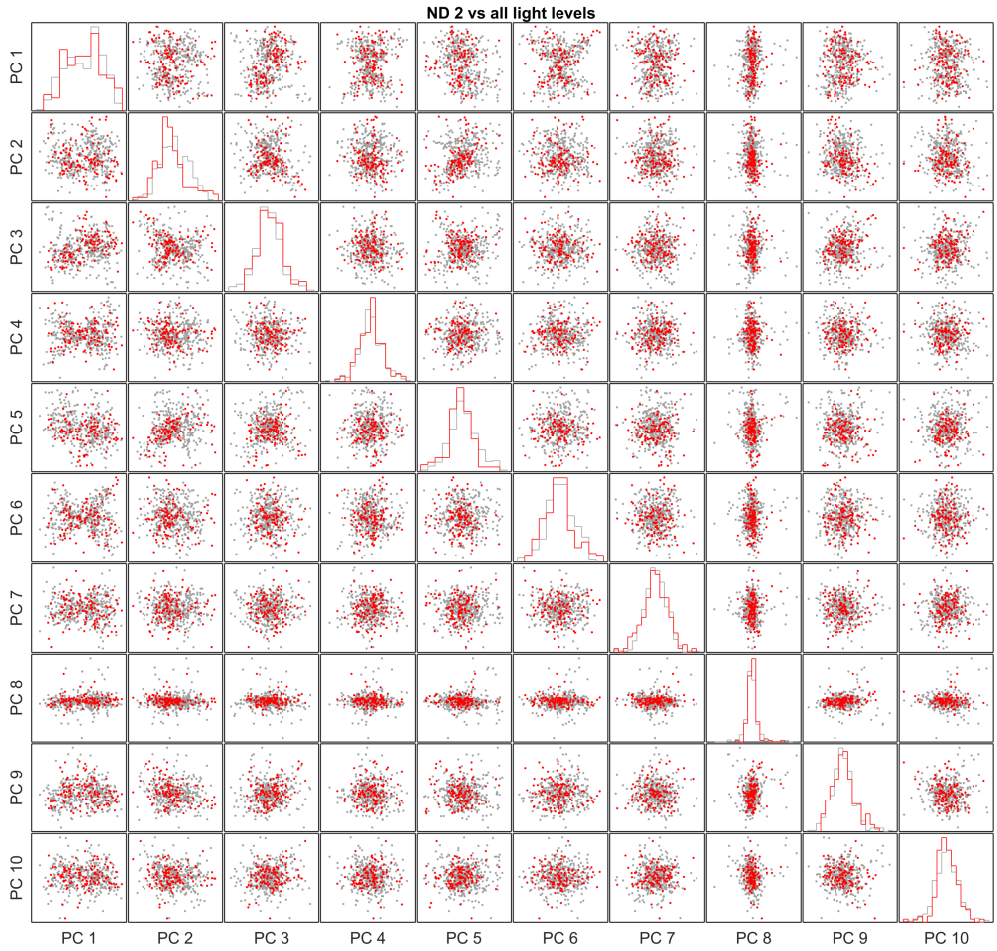

Figure 3.21: **Projection of STAs from C57BL/6 onto the first ten principal components at ND 2 compared to all other light levels:** Matrix plot of each STA filter from C57BL/6 mice projected onto each possible pairing of the first ten principal components. STAs recorded at ND 2 are show in red, and STAs from all other light levels are shown in grey. Histograms of the probability density function of the projection onto each individual principal component are plotted along the diagonal. This plot shows a shift to more negative projections onto PC 2 in STAs at ND 2 compared to other light levels. Additionally, projection onto PC 3 is narrower at ND 2 than at other light levels, and appears positively correlated with projection onto PC 2.

The lack of obvious differences in projection onto more spatially defined principal components (such as PC 4), suggests that although these features describe a lot of the variance in the data set, this may not be correlated with changes in animal model or experimental light level.

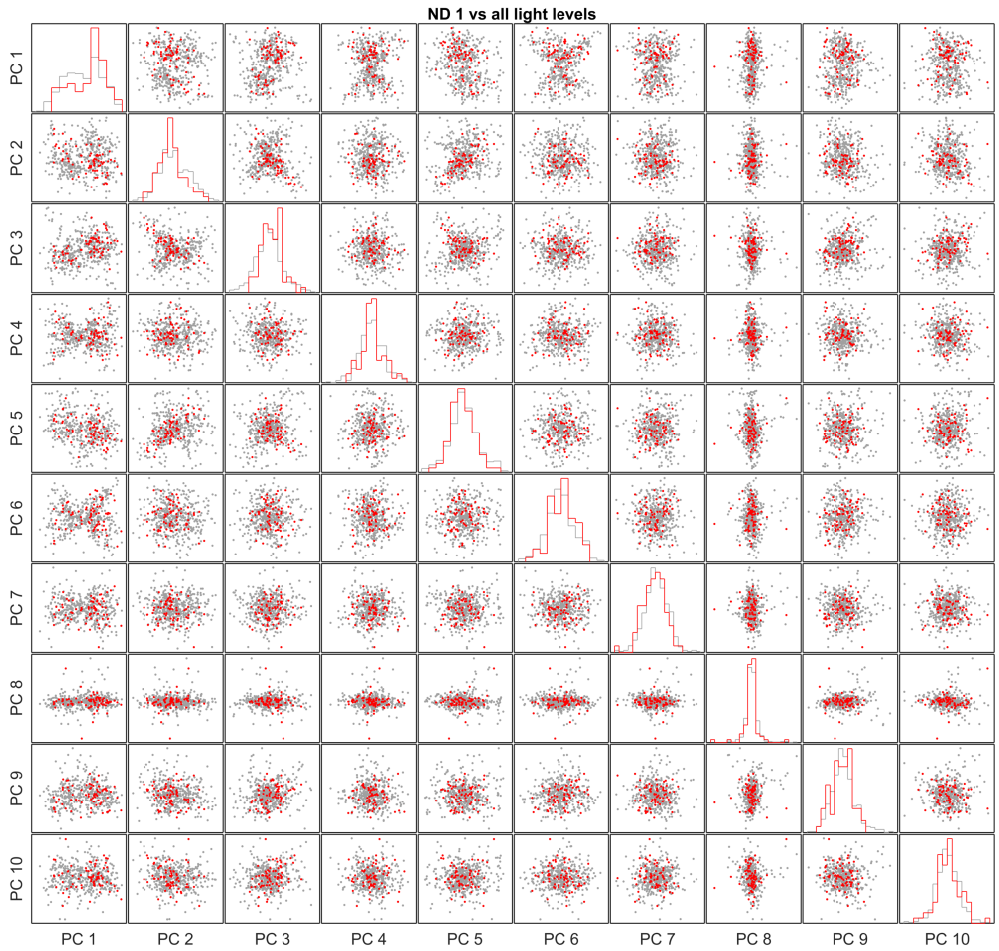

Figure 3.22: **Projection of STAs from C57BL/6 onto the first ten principal components at ND 1 compared to all other light levels:** Matrix plot of each STA filter from C57BL/6 mice projected onto each possible pairing of the first ten principal components. STAs recorded at ND 1 are show in red, and STAs from all other light levels are shown in grey. Histograms of the probability density function of the projection onto each individual principal component are plotted along the diagonal. This plot shows a shift at ND 1 towards more positive projection onto PC 1, and a shift towards more negative projection onto PC 2. Additionally, projection onto PC 3 is narrower at ND 1 than at other light levels, and appears positively correlated with projection onto PC 1.

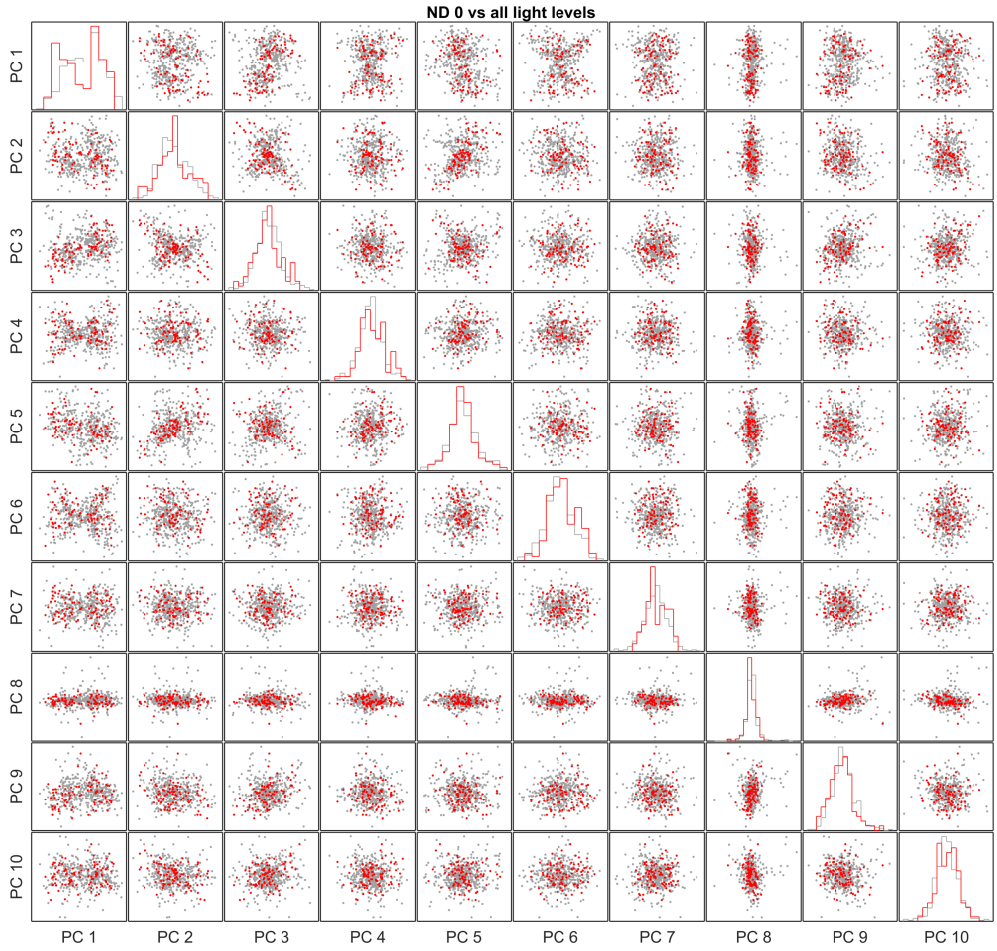

Figure 3.23: **Projection of STAs from C57BL/6 onto the first ten principal components at ND 0 compared to all other light levels:** Matrix plot of each STA filter from C57BL/6 mice projected onto each possible pairing of the first ten principal components. STAs recorded at ND 0 are show in red, and STAs from all other light levels are shown in grey. Histograms of the probability density function of the projection onto each individual principal component are plotted along the diagonal.

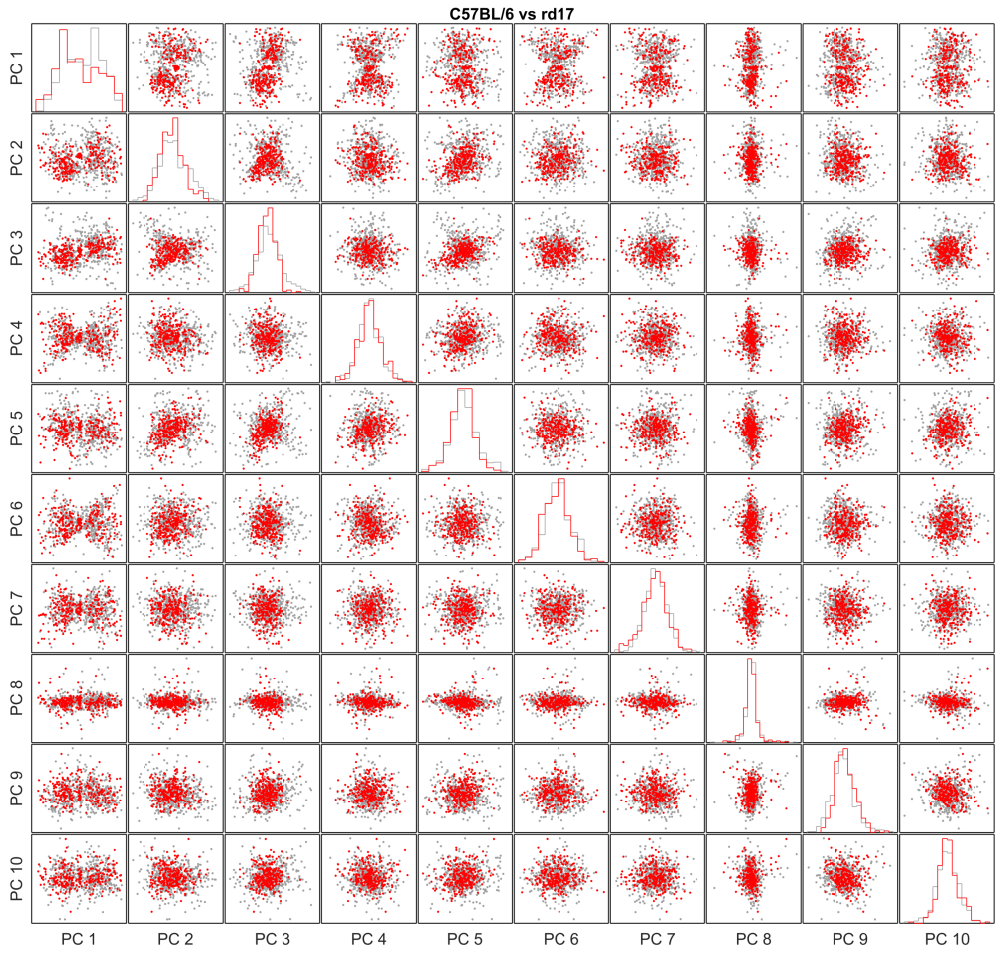

Figure 3.24: **Projection of STAs from C57BL/6 and rd17 onto the first ten principal components:** Matrix plot of each STA filter from C57BL/6 and rd17 mice, from all light levels, projected onto each possible pairing of the first ten principal components. STAs from rd17 are show in red, and STAs from C57BL/6 are shown in grey. Histograms of the probability density function of the projection onto each individual principal component are plotted along the diagonal. This plot shows that rd17 STAs tend to project more negatively onto PC 1 compared to STAs from C57BL/6, and that projections onto PC 3 are narrower in rd17 than C57BL/6.

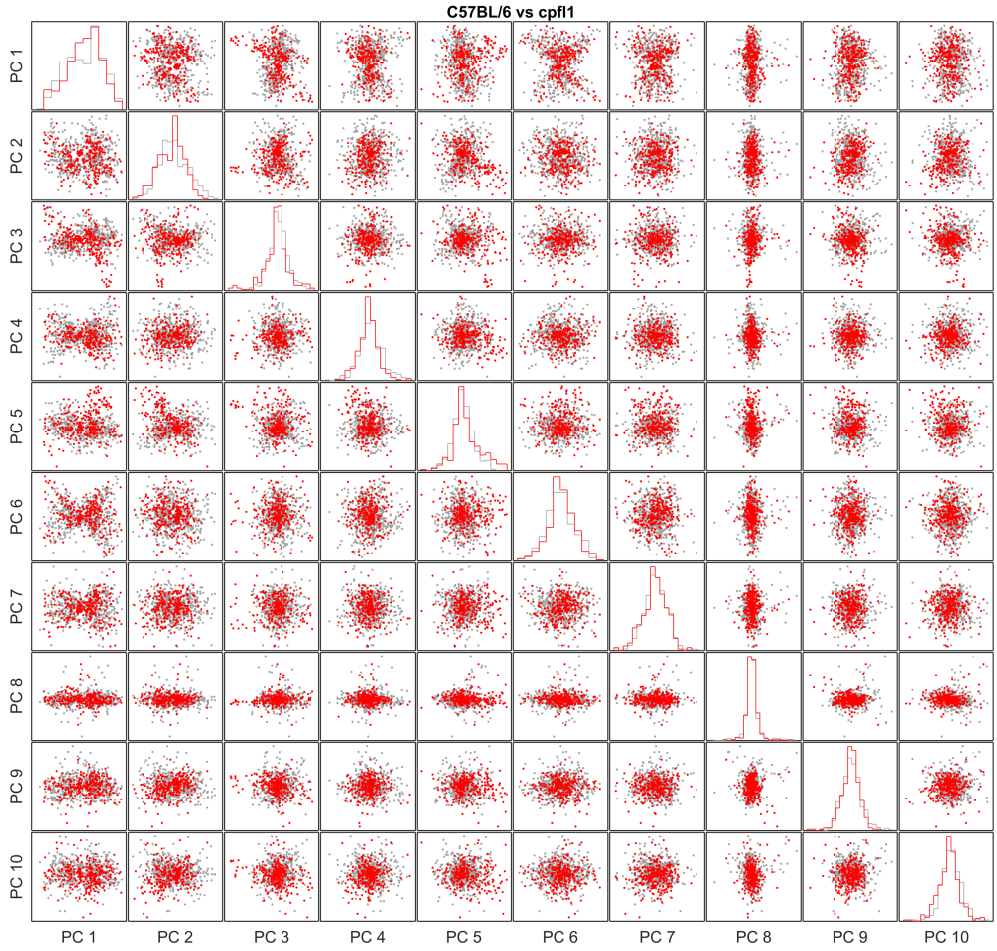

Figure 3.25: **Projection of STAs from C57BL/6 and cpfl1 onto the first ten principal components:** Matrix plot of each STA filter from C57BL/6 and cpfl1 mice, from all light levels, projected onto each possible pairing of the first ten principal components. STAs from cpfl1 are show in red, and STAs from C57BL/6 are shown in grey. Histograms of the probability density function of the projection onto each individual principal component are plotted along the diagonal. This plot shows that STAs from cpfl1 are shifted slightly towards more positive projections onto PC 1 compared to C57BL/6 , and have a broader spread of projections onto PC 3 and PC 5.

3.3 Discussion

Each principal component represents a new axis which captures as much of the variance in the data as possible. As each component is a linear combination of the original variables (Ringnér, 2008), these new axes not directly biological. However, they can be used to infer changes in the underlying biology that can then be interrogated.

PC 1 captures the majority of the variance of the dataset of STAs, and resembles an ON receptive field with a centre-surround spatial structure. When the STAs are projected onto this axis, they can be separated into ON and OFF functional classes. Further clustering along this axis results in groups of filters with similar response properties, which are shifted temporally relative to one another. This indicates that, were we to reduce the dimensionality of the data set down to a single axis that accounted for as much of the variance as possible, the information preserved would consist primarily of response polarity and integration time to spike.

Projection onto PC 2 distinguishes responses according to how biphasic the temporal profile is, and projection onto PC 3 and PC 5 (both similar profiles that are temporally shifted relative to one another) can identify a smaller group of triphasic responses.

Projection onto and clustering using PC 1 and PC 2 indicates that in this dataset we may be able to identify four functional response classes - ON monophasic, OFF monophasic, ON biphasic, and OFF biphasic. These groups broadly map to the STA properties reported by Farrow & Masland (2011) in their work functionally clustering retinal ganglion cells, though their clusters are more fine grained due to their use of a battery of functional measurements alongside the STA (for example, within biphasic OFF responses they are able to tentatively identify OFF transient, OFF sustained, and approach-sensitive responses). These four classes represent broad groups that may

aggregate a variety of cell types and neuronal mechanisms. As the projection on to PC 2 is continuous, it may be that the STAs in the dataset exist along a continuum of more to less biphasic, rather than as two discrete groups.

The triphasic temporal kernels that define the small group of responses that project strongly onto PC 3 and PC 5 indicate that spikes are preceded, on average, by a high degree of contrast modulation in the stimulus. This could represent an additional functional group tuned to modulating, flickering stimuli.

Of the first ten principal components, those remaining all have strong non-Gaussian spatial elements, indicating a diversity of spatial profiles within the STA dataset.

Using the overview of the data set provided by this exploratory data analysis, there appear to be three main groups of features that best separate the receptive fields recorded: the polarity of the STAs (OFF and ON, relating to PC 1), the temporal dynamics of the STAs (relating PC 2, PC 3, as well as clustering along PC 1), and the spatial profile of the STAs (relating to projection onto PC 4, as well as PC 6-10). Examination of these groups of features across light level and animal model will form the basis for the remainder of this thesis.

4 Temporal dynamics of retinal ganglion cells

4.1 Introduction

As outlined in chapter 3, differences in temporal dynamics underlie a lot of the variation within the dataset of all STAs. Filters can be separated according to the shift of the temporal kernel relative to the spike time, how biphasic the response is (projection onto PC 2), and how triphasic the response is (projection onto PC 3 and PC 5).

The temporal dynamics of a cell's receptive field are critical to understanding how it filters sensory information. In particular, how phasic or transient the temporal filter is relates to the kinds of sensory stimuli it is more or less selective for. More bi- (or multi-) phasic temporal kernels indicate a more bandpass stimulus-response filter, meaning that the output cell responds more to modulations in the stimulus within a particular frequency range. In contrast, more monophasic temporal filters suggest low pass temporal filtering.

In the context of the retina, a monophasic temporal filter would indicate a ganglion cell that encodes slow components of the stimulus, and (depending on polarity) responds to increments or decrements from the mean. A more bi- or tri-phasic filter would indicate

a cell that is tuned more for contrast modulations about the mean, such as a flickering stimulus, or contrast modulation induced by visual motion (Kaplan & Benardete, 2001, Suh & Baccus, 2014).

Changes in ambient luminance affect the temporal dynamics of visual responses in photoreceptor cells and bipolar cells. Photoreceptors can be modelled as dynamic adaptors, that at low backgrounds respond proportionally to the stimulus light intensity, and at higher backgrounds respond instead to the time derivative of the light intensity (that is, they become more phasic and encode contrast modulation) (Clark *et al.*, 2013).

This phenomenon has been described by Ke *et al.* (2014) at the rod to rod bipolar cell synapse. At very low light levels, the synapse encodes Weber (step) contrast, but as light intensity increases it begins to encode Michelson contrast (modulation about the mean light intensity) instead. This suggests that the kind of visual information transmitted downstream to retinal ganglion cells changes fundamentally depending on the background light intensity, even within the rod-mediated visual range.

Wang *et al.* (2011) have also demonstrated that ambient luminance can alter the temporal dynamics of retinal ganglion cells. They describe a reduction in temporal latency and a temporal frequency tuning shift to higher frequencies when the ambient light level is increased and cones which express S-opsin are activated with bright UV stimuli.

In order to investigate the variance in temporal response kinetics in the STA data set, I first decomposed the full spatiotemporal STAs into spatial and temporal kernels using singular value decomposition. I then characterised the temporal kernels using four summary statistics.

Time to peak and time to zero cross should capture temporal shift in the filters towards and away from the spike time. The biphasic index quantifies the ratio of the maximum and minimum poles of the response, which is related to how contrast modulated or

bandpass the cell is. Finally, taking the Fourier transform of the temporal kernel reveals the temporal frequency tuning of the STA - the extent to which contrast changes at different frequencies are represented.

4.2 Results

One dimensional temporal kernels were derived from the smoothed three-dimensional spatiotemporal STA using singular value decomposition. Test statistics were calculated, and statistical significance was assessed first using a permutation ANOVA taking into account all five light levels and all three animal models (Basso *et al.*, 2009, Manly, 2007). If this ANOVA revealed a significant main effect or interaction term, relevant permutation post-hoc tests were conducted as described. In the case of a significant interaction term (as reported here), twenty post-hoc tests were performed, comparing the distribution at each light level and model to the relevant C57BL/6 control at each light level. To correct for multiple comparisons, the alpha level used to determine significance was adjusted by Bonferroni correction from 0.05 to 0.0025.

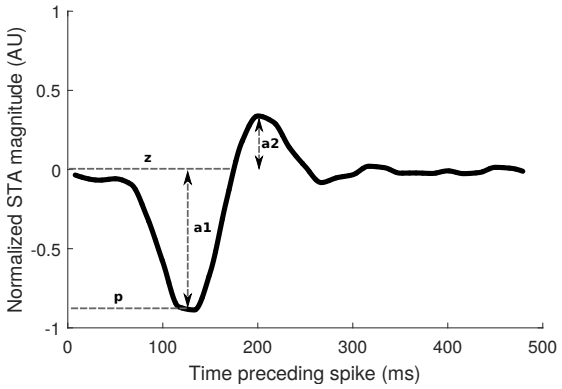

Figure 4.1: **How temporal kinetics are characterised:** Four summary statistics are used to characterise the temporal properties of the collected STAs. The time to peak (**p**) is defined as the position of the first peak of the temporal kernel, relative to the spike at 0 ms. Zero cross time (**z**) is defined as the point where the temporal kernel crosses zero following the first peak. Biphasic index is measured as the ratio between the absolute values of the maximum and the minimum of the temporal kernel (in this example, **a2/a1**). The fourth summary statistic used is the peak of the Fourier transform of the temporal kernel.

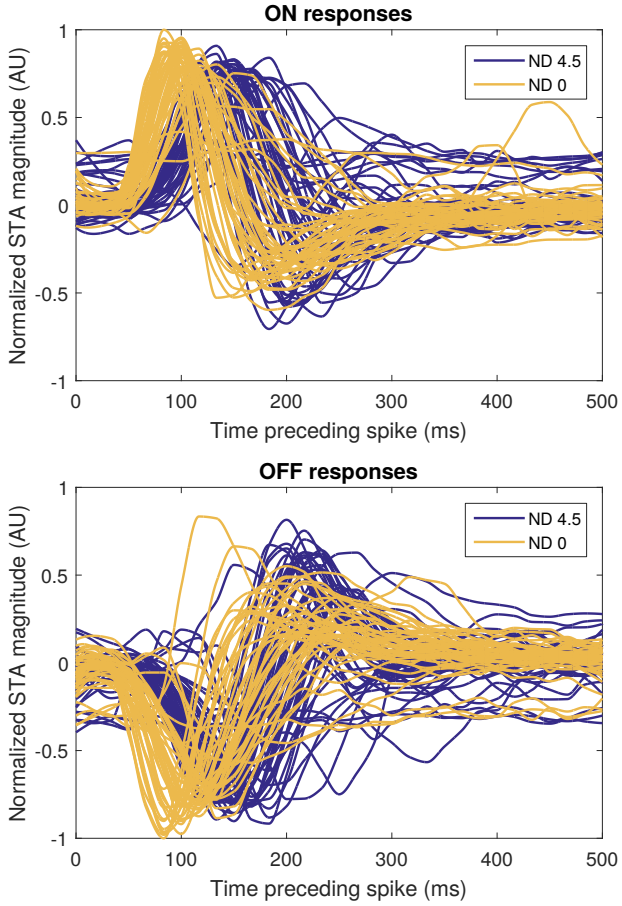

Figure 4.2: **Temporal kernels of ON and OFF responses from C57BL/6 mice at two light levels:** ON and OFF temporal responses (identified by polarity of the first peak) from C57BL/6 mice (n = 8). Responses shown are from the lowest stimulus light level (ND 4.5) and the highest (ND 0). Temporal kernels were obtained from singular value decomposition of the smoothed spatiotemporal STA. The kernels were then interpolated with cubic splines and normalized so that the full dataset falls between 1 and -1.

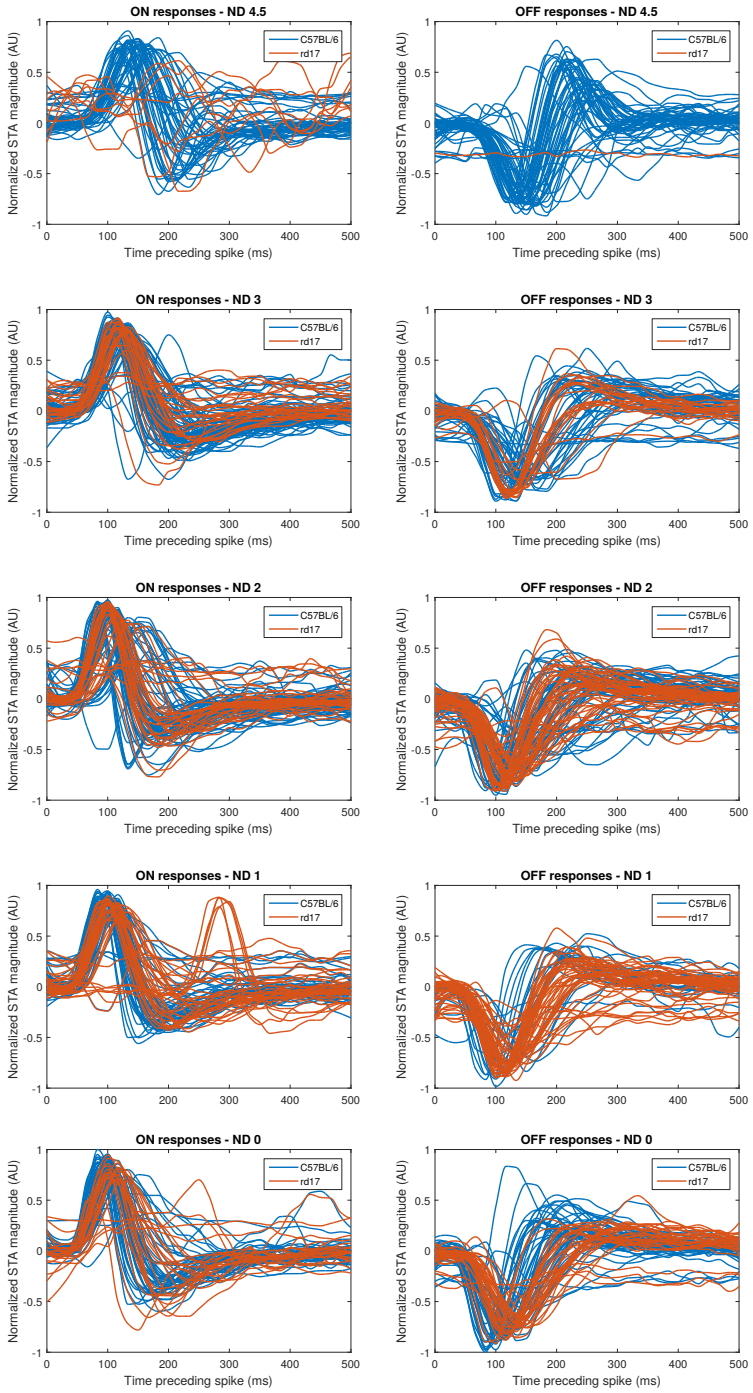

Figure 4.3: **Temporal kernels of ON and OFF responses in rd17 and C57BL/6 across light levels:** All recorded temporal kernels, separated into ON and OFF responses for ease of visualisation, from rd17 (n=8) and C57BL6 (n = 8) at each experimental light level. Temporal kernels were obtained from singular value decomposition of the smoothed spatiotemporal STA. The kernels were then interpolated with cubic splines and normalized so that the full dataset falls between 1 and -1.

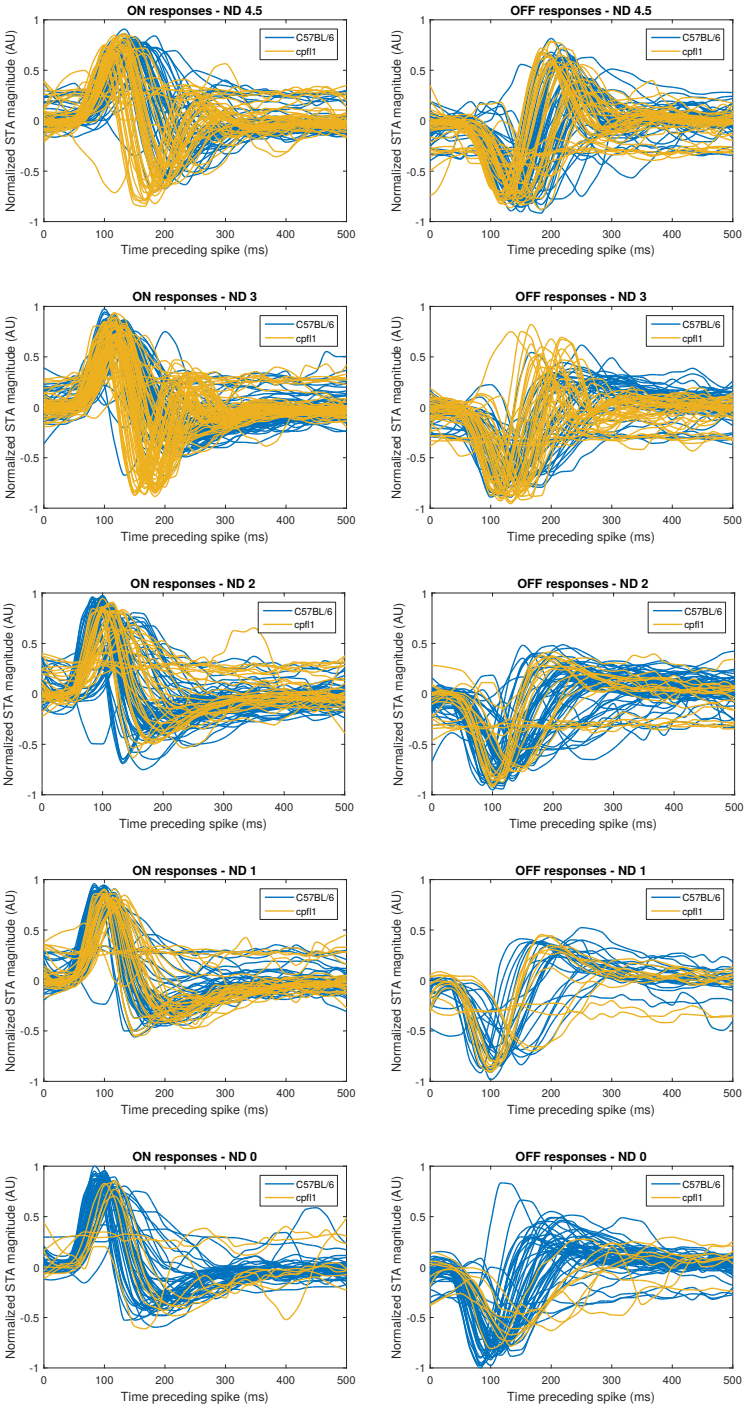

Figure 4.4: **Temporal kernels of ON and OFF responses in cpfl1 and C57BL/6 across light levels:** All recorded temporal kernels, separated into ON and OFF responses for ease of visualisation, from cpfl1 (n=8) and C57BL6 (n = 8) at each experimental light level. Temporal kernels were obtained from singular value decomposition of the smoothed spatiotemporal STA. The kernels were then interpolated with cubic splines and normalized so that the full dataset falls between 1 and -1.

4.2.1 Time to peak

Time to peak was defined as the position of the first peak in the temporal kernel relative to the spike time (Fig 4.1). Permutation ANOVA (Basso *et al.*, 2009, Manly, 2007) performed on all kernels from all conditions revealed a significant interaction between animal model and light level for this measure ($p < 0.0001$). Permutation post-hoc tests were then performed and corrected for multiple comparisons as described. Means and standard deviations are reported to the nearest millisecond.

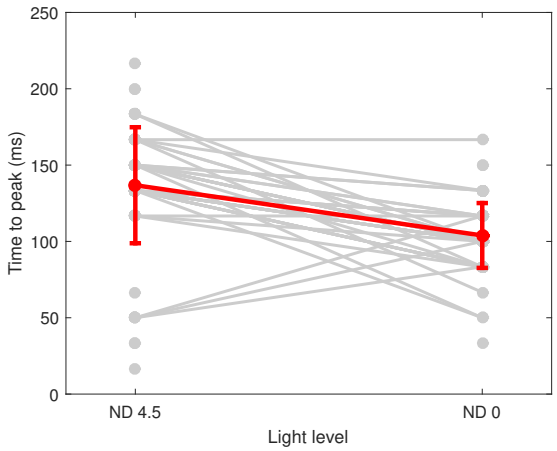

Figure 4.5: **Within unit change in time to peak, C57BL/6:** Plot showing within-unit change in time to peak from the lowest experimental light level (ND 4.5) to the highest (ND 0). Grey dots represent individual identified units. Units that have a significant response at both light levels are connected with a grey line. The red line shows the mean ± standard deviation of all kernels at that light level.

Time to peak decreases with increasing light level in C57BL/6

The time between the spike and the peak of the temporal kernel decreases as the light level increases. This shift is clear when the kernels from the lowest and highest experimental light levels are superimposed (Fig 4.2). The overview in figure 4.6 shows that kernels recorded at both ND 4.5 and ND 3 tend to take longer to peak compared to the higher three light levels. In particular, the mean (± S.D.) time to peak of kernels at ND 4.5 (137 (± 38) ms) is significantly longer than at any other light level measured

($p < 0.0001$), and the mean time to peak at ND 3 (117 ($\pm$ 30) ms) is significantly longer that at ND 1 (100 ($\pm$ 25) ms) and ND 0 (104 ($\pm$ 21) ms) ($p < 0.0001$ and 0.001 respectively). The Cliff's delta effect size for the difference in time to peak between ND 4.5 and ND 0 is 0.673 (3 d.p.).

The decrease in time to peak is not due to different populations of cells responding at low compared to higher light levels, as the same trend can be seen within most of the identified units with significant responses at ND 4.5 and ND 0 (Fig 4.5).

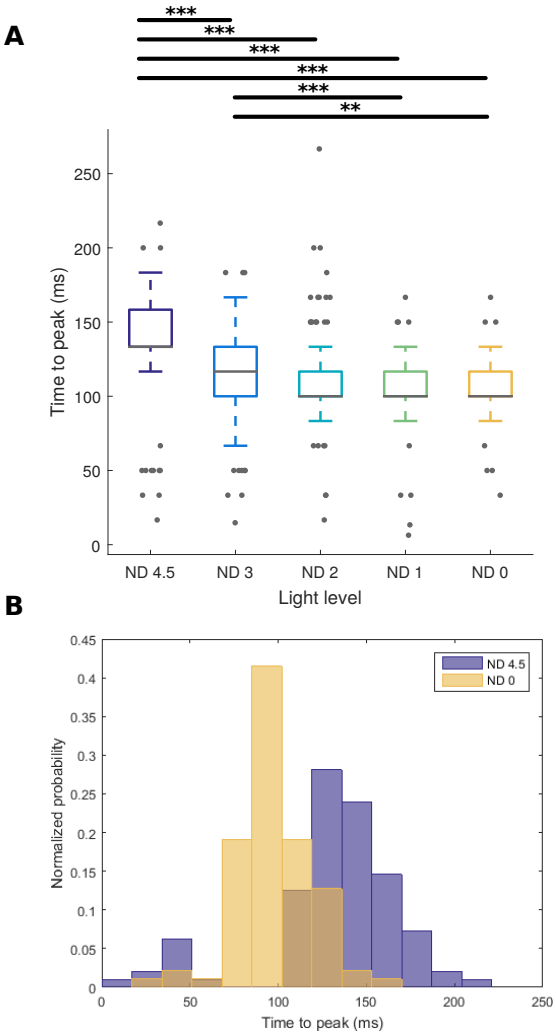

Figure 4.6: **Population time to peak decreases with increasing light level in C57BL/6:** (**A**) Box plot of time to peak values in C57BL/6 mice across all five experimental light levels, showing that the time to peak of recorded STAs tends to be lower as light levels are increased. Boxes show medians and first and third quartiles, whiskers are 1.5 times the interquartile range. Data points beyond this are represented as outliers. Stars represent p-values of difference in means between groups. These were calculated from permutation post-hoc tests following permutation ANOVA on the full dataset which revealed a significant interaction between animal model and light level ($p < 0.0001$). *** = $p < 0.0001$, ** = $p < 0.001$, * = $p < 0.0025$ (Bonferroni correction for alpha = 0.05). n = 8 C57BL/6 mice, with 96 kernels at ND 4.5, 120 at ND 3, 128 at ND 2, 74 at ND 1, and 94 at ND 0. (**B**) Histograms of time to peak values at the lowest (ND 4.5) and the highest (ND 0) experimental light levels, demonstrating shift in time to peak with increasing light level.

Time to peak in rd17 is slower at high light levels compared to C57BL/6 controls

At higher experimental light levels, the time to peak of temporal kernels from rd17 mice tends to be longer than those from C57BL/6 controls. This difference can be seen when the kernels at ND 0 from both groups are superimposed (Fig 4.3), and is summarised using box plots in figure 4.7. The mean (± S.D.) time to peak of C57BL/6 temporal kernels at ND 0 is 104 (± 21) ms, compared to 118 (± 24) ms for rd17 kernels. This difference is significant ($p < 0.001$), and the Cliff's delta effect size is -0.372 (3 d.p.).

Additionally, a significant difference in time to peak is identified at the lowest experimental light level, ND 4.5 ($p < 0.0001$). The 9 kernels identified at ND 4.5 in rd17 mice are very noisy (Fig 4.3), and the "peaks" in these noisy kernels tend to occur closer to the spike time.

Time to peak in cpfl1 is faster at low light levels compared to C57BL/6 controls

At ND 4.5, temporal kernels from cpfl1 tend to have a shorter time to peak compared to kernels from C57BL/6. This shift is clear when the two sets of kernels are superimposed (Fig 4.4), and is summarised in the box plots in figure 4.8. The mean (± S.D.) time to peak of the C57BL/6 temporal kernels at ND 4.5 is 137 (± 38) ms, compared to 116 (± 35) ms for cpfl1 kernels. This difference is significant ($p < 0.001$), and the Cliff's delta effect size is 0.429 (3 d.p.).

From ND 3 to ND 1 the distribution of time to peak values is very similar between cpfl1 and C57BL/6 mice, although at ND 0 the 16 cpfl1 STAs identified as significant show a trend towards a slower time to peak.

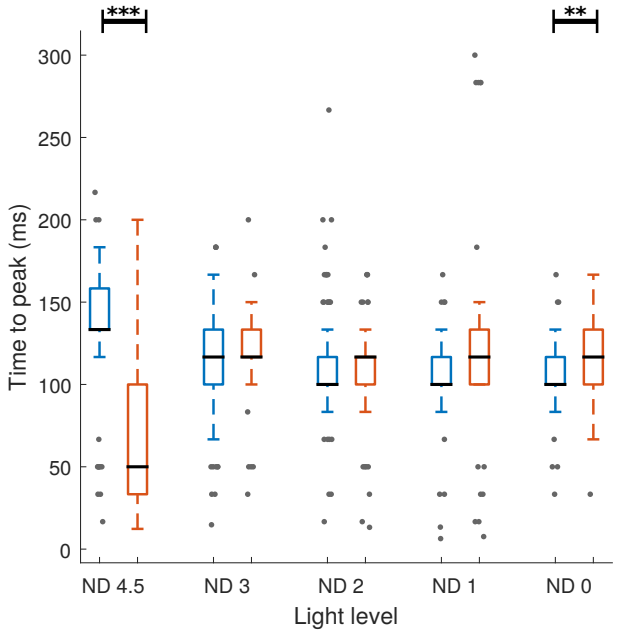

Figure 4.7: **Population time to peak C57BL/6 versus rd17:** Box plot of time to peak values in C57BL/6 and rd17 mice across all five experimental light levels, showing that the time to peak of recorded STAs tends to be slower at higher light levels in rd17 compared to C57BL/6 control. There is also a significant difference in time to peak between C57BL/6 temporal kernels at ND 4.5 and the handful of very noisy kernels identified as significant responses at this light level in rd17. Boxes show medians and first and third quartiles, whiskers are 1.5 times the interquartile range. Data points beyond this are represented as outliers. Stars represent p-values of difference in means between groups. These were calculated from permutation post-hoc tests following permutation ANOVA on the full dataset which revealed a significant interaction between animal model and light level ($p < 0.0001$). *** = $p < 0.0001$, ** = $p < 0.001$, * = $p < 0.0025$ (Bonferroni correction for alpha = 0.05). C57BL/6: n = 8 mice, with 96 kernels at ND 4.5, 120 at ND 3, 128 at ND 2, 74 at ND 1, and 94 at ND 0. rd17 n = 8 mice, with 9 kernels at ND 4.5, 49 at ND 3, 80 at ND 2, 84 at ND 1, and 55 at ND 0.

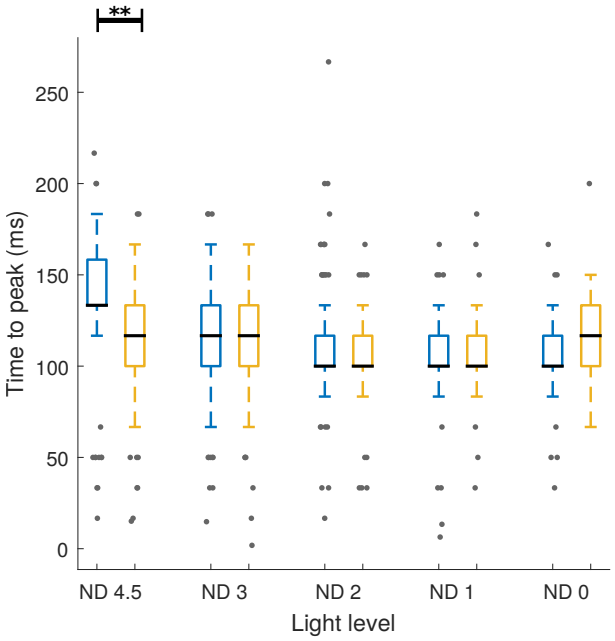

Figure 4.8: **Population time to peak C57BL/6 versus cpfl1:** Box plot of time to peak values in C57BL/6 and cpfl1 mice across all five experimental light levels, showing that at ND 4.5 cpfl1 STAs tend to have a faster time to peak compared to C57BL/6. Boxes show medians and first and third quartiles, whiskers are 1.5 times the interquartile range. Data points beyond this are represented as outliers. Stars represent p-values of difference in means between groups. These were calculated from permutation post-hoc tests following permutation ANOVA on the full dataset which revealed a significant interaction between animal model and light level ($p < 0.0001$). *** = $p < 0.0001$, ** = $p < 0.001$, * = $p < 0.0025$ (Bonferroni correction for alpha = 0.05). C57BL/6: n = 8 mice, with 96 kernels at ND 4.5, 120 at ND 3, 128 at ND 2, 74 at ND 1, and 94 at ND 0. cpfl1 n = 8 mice, with 82 kernels at ND 4.5, 105 at ND 3, 51 at ND 2, 41 at ND 1, and 16 at ND 0.

4.2.2 Time to zero cross

Time to zero cross was defined as the time taken for the temporal kernel to cross zero after the first peak, relative to the spike time (Fig 4.1). A permutation ANOVA (Basso *et al.*, 2009, Manly, 2007) performed on all kernels from all conditions revealed a significant interaction between animal model and light level for this measure ($p < 0.001$). Permutation post-hoc tests were then performed and corrected for multiple comparisons as described. Means and standard deviations are reported to the nearest millisecond.

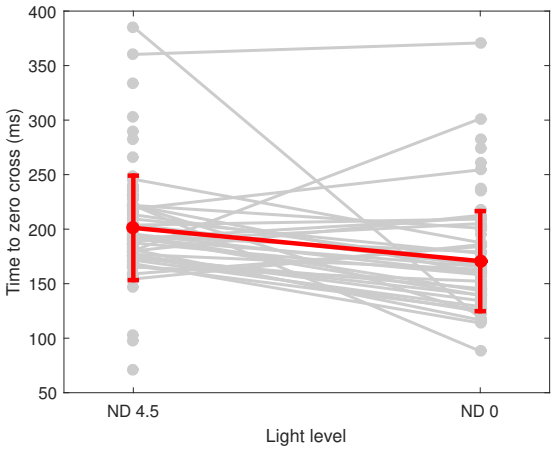

Figure 4.9: **Within unit change in time to zero cross, C57BL/6:** Plot showing within-unit change in time to zero cross from the lowest experimental light level (ND 4.5) to the highest (ND 0). Grey dots represent individual identified units. Units that have a significant response at both light levels are connected with a grey line. The red line shows the mean ± standard deviation of all kernels at that light level.

Time to zero cross decreases with increasing light level in C57BL/6

Temporal kernels identified in C57BL/6 mice have a faster zero cross time at higher light levels compared to lower light levels. This shift can be seen when the kernels from the lowest (ND 4.5) and the highest (ND 0) light levels are superimposed (Fig 4.2), and the trend is demonstrated by the box plots in figure 4.10. The mean (± S.D.) time to zero cross at ND 4.5 (201 (± 48) ms) is significantly longer than that at ND 1 (167 (±

54) ms) and ND 0 (171 (± 46) ms) ($p < 0.0001$ for both), with Cliff's delta effect sizes of 0.490 (3 d.p.) and 0.399 (3 d.p.) respectively. Similarly, the mean (± S.D.) time to zero cross at ND 3 (194 (± 45) ms) is also significantly longer than at ND 1 and ND 0 ($p < 0.001$ for both). The Cliff's delta effect sizes for these differences are 0.431 (3 d.p.) and 0.335 (3 d.p.) respectively.

This decrease in time to zero cross is not due to different populations of cells responding at low compared to higher light levels, as the same trend can be seen within most of the identified units with significant responses at ND 4.5 and ND 0 (Fig 4.9).

The spread of zero cross times is broader at ND 2 than at any other light level, which is not reflected in the distribution of time to peak values at this light level. This suggests a wider range of integration times across temporal kernels at ND 2.

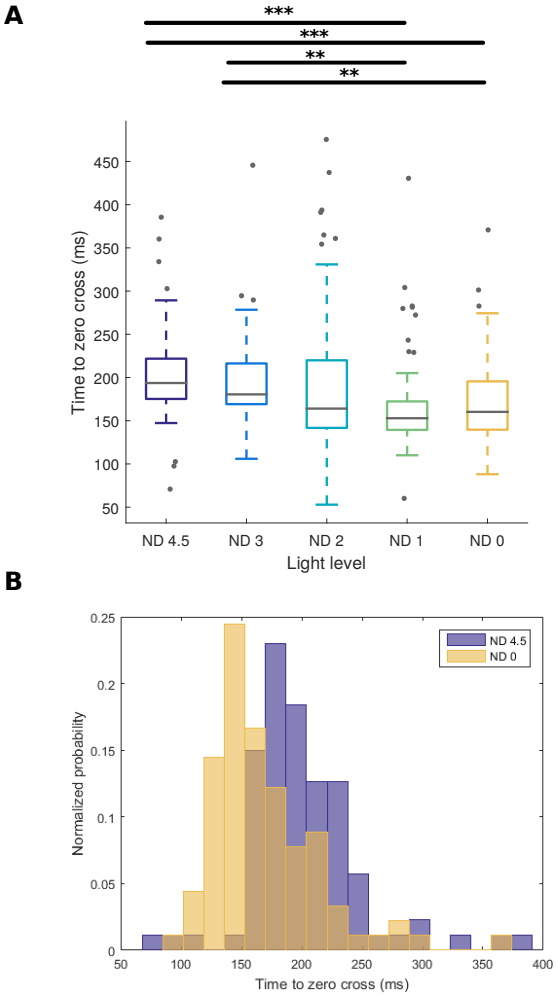

Figure 4.10: **Population time to zero cross decreases with increasing light level in C57BL/6:** (**A**) Box plot of time to zero cross in C57BL/6 mice across all five experimental light levels, showing that the time to zero cross of recorded STAs tends to be lower as light levels are increased. Boxes show medians and first and third quartiles, whiskers are 1.5 times the interquartile range. Data points beyond this are represented as outliers. Stars represent p-values of difference in means between groups. These were calculated from permutation post-hoc tests following permutation ANOVA on the full dataset which revealed a significant interaction between animal model and light level ($p < 0.001$). *** = $p < 0.0001$, ** = $p < 0.001$, * = $p < 0.0025$ (Bonferroni correction for alpha = 0.05). n = 8 C57BL/6 mice, with 96 kernels at ND 4.5, 120 at ND 3, 128 at ND 2, 74 at ND 1, and 94 at ND 0. (**B**) Histograms of time to zero cross at the lowest (ND 4.5) and the highest (ND 0) experimental light levels, demonstrating shift in time to zero cross with increasing light level.

Time to zero cross in rd17 is slower at high light levels compared to C57BL/6 controls

At high experimental light levels (ND 1 and ND 0), time to zero cross tends to be slower for rd17 temporal kernels compared to C57BL/6. This difference is again evident when the two sets of kernels are superimposed (figure 4.3), and is summarised in the box plots in figure 4.11. At ND 1 the mean (± S.D.) time to zero cross is 167 (± 54) ms for C57BL/6 kernels, compared to 203 (± 67) ms for rd17 kernels. The Cliff's delta effect size for this difference is -0.428 (3 d.p.). At ND 0, C57BL/6 kernels have a mean (± S.D.) zero cross time of 171 (± 46) ms, compared to 202 (± 47) ms for rd17 kernels. The Cliff's delta effect size for this difference is -0.366 (3 d.p.). At both ND 1 and ND 0, this difference is significant ($p < 0.001$).

Time to zero cross in cpfl1 is faster at low light levels compared to C57BL/6 controls

At low experimental light levels (ND 4.5 and ND 3), time to zero cross tends to be faster for cpfl1 temporal kernels compared to C57BL/6. This shift is very clear, particularly at ND 4.5, when the two groups of kernels are superimposed (figure 4.4), and can also be seen in the box plots in figure 4.12. At ND 4.5 the mean (± S.D.) time to zero cross for C57BL/6 kernels is 201 (± 48) ms, compared to 172 (± 41) ms for cplf1 kernels. This difference is significant ($p < 0.0001$), and the Cliff's delta effect size is 0.360 (3 d.p.). At ND 3, the mean (± S.D.) time to zero cross for C57BL/6 kernels is 194 (± 45) ms, compared to 169 (± 55) ms for cpfl1 kernels. This difference is also significant ($p < 0.001$), and the Cliff's delta effect size is 0.402 (3 d.p.).

Additionally, the 16 STAs from cpfl1 mice still identified as having significant responses at ND 0 are shifted to have a slower zero cross time compared to C57BL/6 control

kernels. This shift can be seen when the two groups of kernels are superimposed (Fig 4.4), and is significant ($p < 0.0025$ - Bonferroni correction for alpha = 0.05).

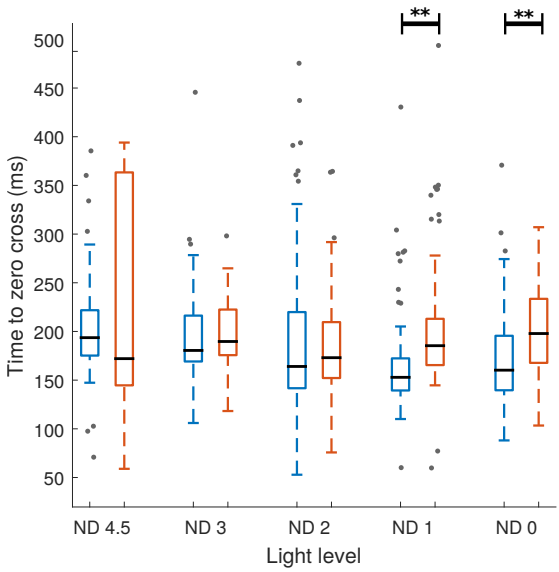

Figure 4.11: **Population time to zero cross C57BL/6 versus rd17:** Box plot of time to zero cross in C57BL/6 and rd17 mice across all five experimental light levels, showing that the time to zero cross of recorded STAs tends to be slower at higher light levels in rd17 compared to C57BL/6 control. Boxes show medians and first and third quartiles, whiskers are 1.5 times the interquartile range. Data points beyond this are represented as outliers. Stars represent p-values of difference in means between groups. These were calculated from permutation post-hoc tests following permutation ANOVA on the full dataset which revealed a significant interaction between animal model and light level ($p < 0.001$). *** = $p < 0.0001$, ** = $p < 0.001$, * = $p < 0.0025$ (Bonferroni correction for alpha = 0.05). C57BL/6: n = 8 mice, with 96 kernels at ND 4.5, 120 at ND 3, 128 at ND 2, 74 at ND 1, and 94 at ND 0. rd17 n = 8 mice, with 9 kernels at ND 4.5, 49 at ND 3, 80 at ND 2, 84 at ND 1, and 55 at ND 0.

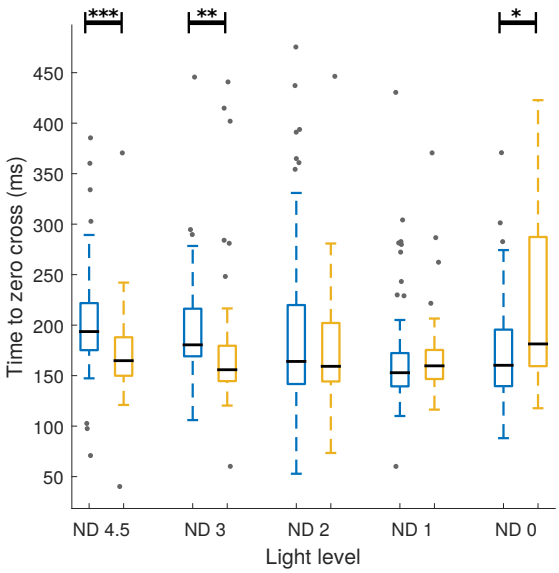

Figure 4.12: **Population time to zero cross C57BL/6 versus cpfl1:** Box plot of time to zero cross in C57BL/6 and cpfl1 mice across all five experimental light levels, showing that at ND 4.5 and ND 3 cpfl1 STAs tend to have a faster time to zero cross compared to C57BL/6. Additionally, the small number of cpfl1 kernels identified as significant at ND 0 tend to have a slower time to zero cross compared to C57BL/6. Boxes show medians and first and third quartiles, whiskers are 1.5 times the interquartile range. Data points beyond this are represented as outliers. Stars represent p-values of difference in means between groups. These were calculated from permutation post-hoc tests following permutation ANOVA on the full dataset which revealed a significant interaction between animal model and light level ($p < 0.001$). *** = $p < 0.0001$, ** = $p < 0.001$, * = $p < 0.0025$ (Bonferroni correction for alpha = 0.05). C57BL/6: n = 8 mice, with 96 kernels at ND 4.5, 120 at ND 3, 128 at ND 2, 74 at ND 1, and 94 at ND 0. cpfl1 n = 8 mice, with 82 kernels at ND 4.5, 105 at ND 3, 51 at ND 2, 41 at ND 1, and 16 at ND 0.

4.2.3 Biphasic index

The biphasic index of the STA was defined as the ratio of the absolute values of the minimum and the maximum peak of the temporal kernel (Fig 4.1). Scores fall between 0 (completely monophasic) and 1 (the kernel has two peaks of equal magnitude). Permutation ANOVA (Basso *et al.*, 2009, Manly, 2007) on all kernels from all conditions revealed a significant interaction between animal model and light level for this measure ($p < 0.0001$). Permutation post-hoc tests were then performed and corrected for multiple comparisons as described. Mean and standard deviations are reported to 2 decimal places.

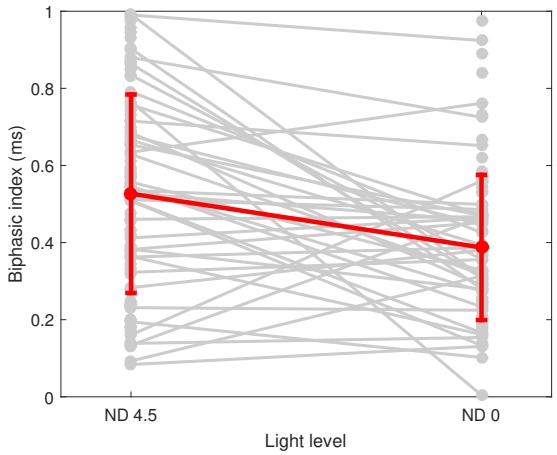

Figure 4.13: **Within unit change in biphasic index, C57BL/6:** Plot showing within-unit change in biphasic index from the lowest experimental light level (ND 4.5) to the highest (ND 0). Grey dots represent individual identified units. Units that have a significant response at both light levels are connected with a grey line. The red line shows the mean ± standard deviation of all kernels at that light level.

Biphasic index is higher in scotopic conditions in C57BL/6

Temporal kernels in C57BL/6 mice have a much broader spread of biphasic index scores at ND 4.5 than at any other light level, with more kernels that have a high biphasic index (closer to 1, indicating that two peaks of similar magnitudes). This difference in biphasicity can be seen when kernels from the highest (ND 0) and the lowest (ND 4.5) light levels are superimposed (Fig 4.2). The box plots in figure 4.14 provide an overview of these differences in biphasic index. The mean (± S.D.) biphasic index at ND 4.5 is 0.53 (± 0.26), compared to 0.37 (± 0.18) at ND 3, 0.38 (± 0.19) at ND 2, 0.39 (± 0.16) at ND 1, and 0.39 (± 0.19) at ND 0. The mean biphasic index is significantly higher at ND 4.5 than at all other light levels ($p < 0.0001$ for comparison with ND 3, ND 2, and ND 0; $p < 0.001$ for comparison with ND 1). The Cliff's delta effect size of the difference between ND 4.5 and ND 0 is 0.314 (3 d.p.).

Examination of changes in biphasic index within identified units (figure 4.13) reveals that many units follow the population trend of decreasing biphasic index from ND 4.5 to ND 0. Many others maintain a relatively stable bipahsic index across both light

levels, and a handful increase biphasic index scores from ND 4.5 to ND 0.

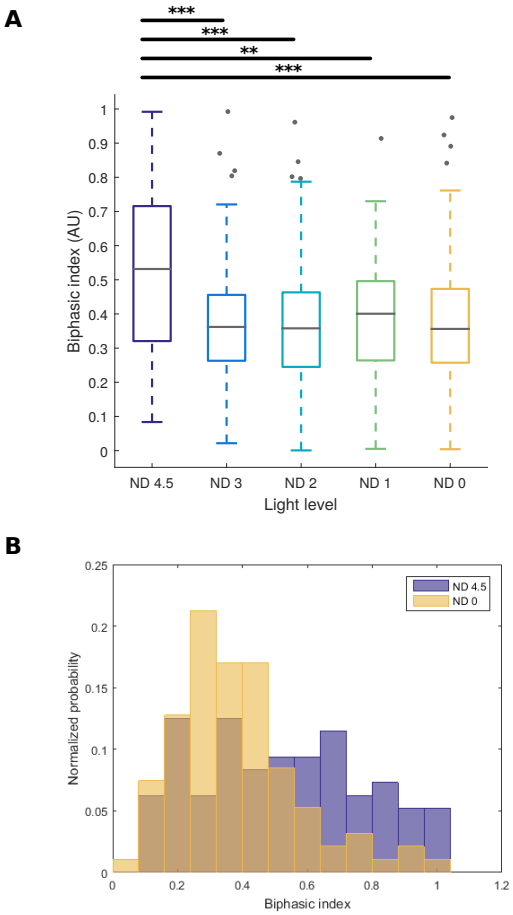

Figure 4.14: **Population biphasic index is higher in scotopic conditions in C57BL/6:** (**A**) Box plot of biphasic index in C57BL/6 mice across all five experimental light levels, showing a broader spread of biphasic index in STAs recorded at ND 4.5 compared to higher light levels, with more cells with biphasic index closer to 1 identified. Boxes show medians and first and third quartiles, whiskers are 1.5 times the interquartile range. Data points beyond this are represented as outliers. Stars represent p-values of difference in means between groups. These were calculated from permutation post-hoc tests following permutation ANOVA on the full dataset which revealed a significant interaction between animal model and light level ($p < 0.0001$). *** = $p < 0.0001$, ** = $p < 0.001$, * = $p < 0.0025$ (Bonferroni correction for alpha = 0.05). n = 8 C57BL/6 mice, with 96 kernels at ND 4.5, 120 at ND 3, 128 at ND 2, 74 at ND 1, and 94 at ND 0. (**B**) Histograms of biphasic index at the lowest (ND 4.5) and the highest (ND 0) experimental light levels, demonstrating shift towards lower biphasic index with increasing light level.

Biphasic index is potentially lower in rd17 at high light levels compared to C57BL/6 controls

Biphasic index scores for temporal kernels from rd17 mice tend to be slightly lower than scores for kernels from C57BL/6 controls, particularly at ND 4.5 to ND 1. This trend can observed in the box plots in figure 4.15. However, these differences are small, are not easily identified when the two sets of kernels are superimposed 4.3, and do not reach significance. As such, the null hypothesis (that units are exchangeable between C57BL/6 and rd17 with respect to biphasic index) cannot be rejected at any light level.

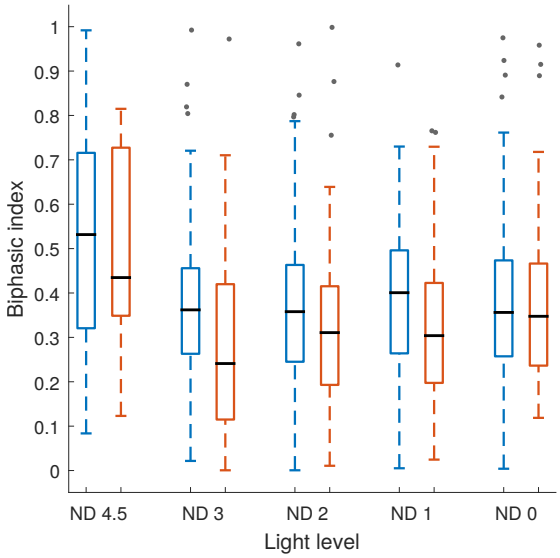

Figure 4.15: **Population biphasic index C57BL/6 versus rd17:** Box plot of biphasic index in C57BL/6 and rd17 mice across all five experimental light levels, showing a slight but not statistically significant trend to slightly lower biphasic index scores in rd17 at the four lower light levels. Boxes show medians and first and third quartiles, whiskers are 1.5 times the interquartile range. Data points beyond this are represented as outliers. Stars represent p-values of difference in means between groups. These were calculated from permutation post-hoc tests following permutation ANOVA on the full dataset which revealed a significant interaction between animal model and light level ($p < 0.0001$). *** = $p < 0.0001$, ** = $p < 0.001$, * = $p < 0.0025$ (Bonferroni correction for alpha = 0.05). C57BL/6: n = 8 mice, with 96 kernels at ND 4.5, 120 at ND 3, 128 at ND 2, 74 at ND 1, and 94 at ND 0. rd17 n = 8 mice, with 9 kernels at ND 4.5, 49 at ND 3, 80 at ND 2, 84 at ND 1, and 55 at ND 0.

Biphasic index is higher in cpfl1 at low light levels compared to C57BL/6 controls

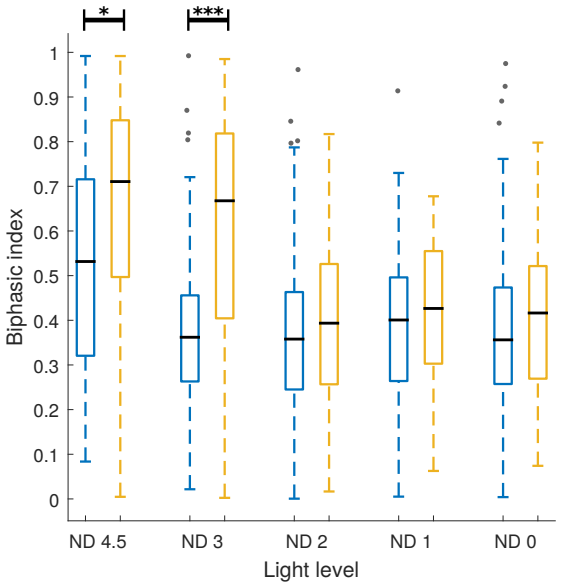

Figure 4.16: **Population biphasic index C57BL/6 versus cpfl1:** Box plot of biphasic index in C57BL/6 and cpfl1 mice across all five experimental light levels, showing that at ND 4.5 and ND 3 cpfl1 STAs skew towards higher biphasic index scores compared to C57BL/6. Boxes show medians and first and third quartiles, whiskers are 1.5 times the interquartile range. Data points beyond this are represented as outliers. Stars represent p-values of difference in means between groups. These were calculated from permutation post-hoc tests following permutation ANOVA on the full dataset which revealed a significant interaction between animal model and light level ($p < 0.0001$). *** = $p < 0.0001$, ** = $p < 0.001$, * = $p < 0.0025$ (Bonferroni correction for alpha = 0.05). C57BL/6: n = 8 mice, with 96 kernels at ND 4.5, 120 at ND 3, 128 at ND 2, 74 at ND 1, and 94 at ND 0. cpfl1 n = 8 mice, with 82 kernels at ND 4.5, 105 at ND 3, 51 at ND 2, 41 at ND 1, and 16 at ND 0.

At ND 4.5 and ND 3, temporal kernels from cpfl1 mice tend to have higher biphasic index scores compared to C57BL/6 controls. Highly bi- or multiphasic temporal kernels at these light levels in cpfl1 can be seen when the two groups are superimposed (Fig 4.4), and the box plots in figure 4.16 provide an overview. The mean (± S.D.) biphasic index of C57BL/6 kernels at ND 4.5 is 0.53 (± 0.26), compared to 0.65 (± 0.24) for cpfl1. This difference is significant ($p < 0.0025$ - Bonferonni correction for alpha = 0.05), and the Cliff's delta effect size is -0.280 (3 d.p.). At ND 3, the mean (± S.D.) biphasic index of C57BL/6 kernels is 0.37 (± 0.18), compared to 0.60 (± 0.27) for cpfl1

kernels. This difference is also significant ($p < 0.0001$), and the Cliff's delta effect size is -0.501 (3 d.p.).

4.2.4 Temporal frequency tuning

Temporal frequency tuning was assessed by examining the Fourier transforms of the temporal kernels. The peak of the Fourier transform for each kernel was then taken as a test statistic. Permutation ANOVA (Basso *et al.*, 2009, Manly, 2007) on all kernels from all conditions revealed a significant interaction between animal model and light level for this measure ($p < 0.0001$). Permutation post-hoc tests were then performed and corrected for multiple comparisons as described. Means and standard deviations are reported to 2 decimal places.

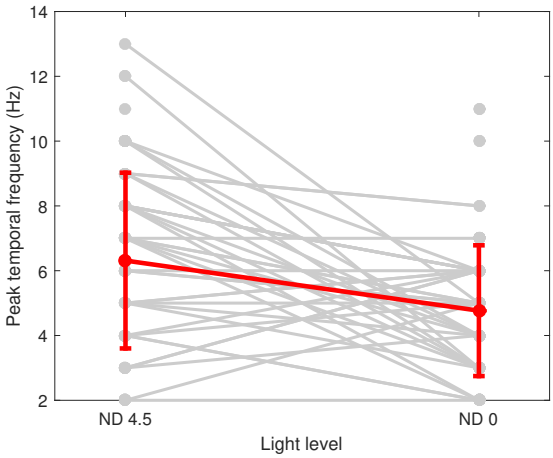

Figure 4.17: **Within unit change in peak temporal frequency, C57BL/6:** Plot showing within-unit change in peak temporal frequency from the lowest experimental light level (ND 4.5) to the highest (ND 0). Grey dots represent individual identified units. Units that have a significant response at both light levels are connected with a grey line. The red line shows the mean ± standard deviation of all kernels at that light level.

Peak temporal frequency is higher in scotopic conditions in C57BL/6

At ND 4.5, temporal frequency tuning tends to be shifted towards higher frequencies in C57BL/6 mice compared to higher light levels. Figure 4.19 suggests that this shift is

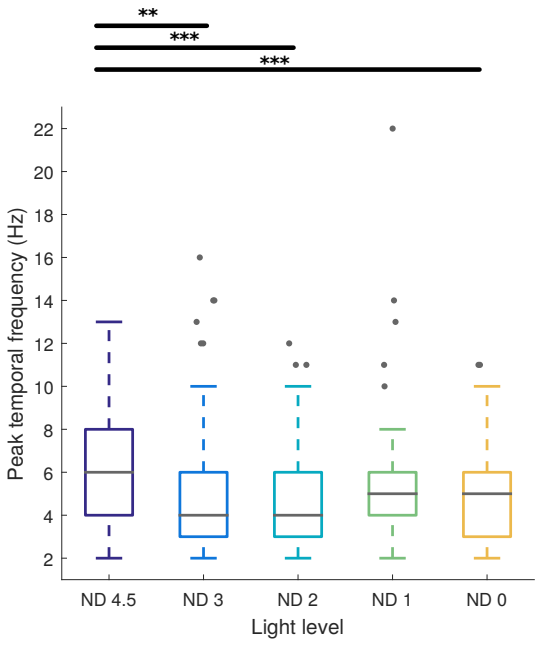

Figure 4.18: **Population peak temporal frequency is higher in scotopic conditions in C57BL/6:** Box plot of peak temporal frequency in C57BL/6 mice across all five experimental light levels, showing that the peak frequency represented in the temporal STA tends to be higher in STAs recorded at ND 4.5. Boxes show medians and first and third quartiles, whiskers are 1.5 times the interquartile range. Data points beyond this are represented as outliers. Stars represent p-values of difference in means between groups. These were calculated from permutation post-hoc tests following permutation ANOVA on the full dataset which revealed a significant interaction between animal model and light level ($p < 0.0001$). *** = $p < 0.0001$, ** = $p < 0.001$, * = $p < 0.0025$ (Bonferroni correction for alpha = 0.05). n = 8 C57BL/6 mice, with 96 kernels at ND 4.5, 120 at ND 3, 128 at ND 2, 74 at ND 1, and 94 at ND 0.

driven by units with tri- or multiphasic responses at ND 4.5 that become less contrast modulated at higher light levels. Figure 4.18 summarises the differences in peak temporal frequency across the experimental light levels. The mean (± S.D.) peak temporal frequency at ND 4.5 is 6.31 (± 2.71) Hz, compared to 4.82 (± 2.76) Hz at ND 3, 4.63 (± 2.12) Hz at ND 2, 5.55 (± 3.02) Hz at ND 1, and 4.77 (± 2.02) Hz at ND 0. These differences in peak temporal frequency are significant between ND 4.5 and ND3 ($p < 0.001$, Cliff's delta = 0.355 (3d.p.)), ND 4.5 and ND 2 ($p < 0.0001$, Cliff's delta = 0.369 (3d.p.)), and ND 4.5 and ND 0 ($p < 0.0001$, Cliff's delta = 0.344 (3d.p.)). The null hypothesis of exchangeability cannot be rejected when it comes to kernels at ND 4.5 and ND 1, partly due to one unit at ND 1 with a very high peak temporal frequency of 22 Hz.

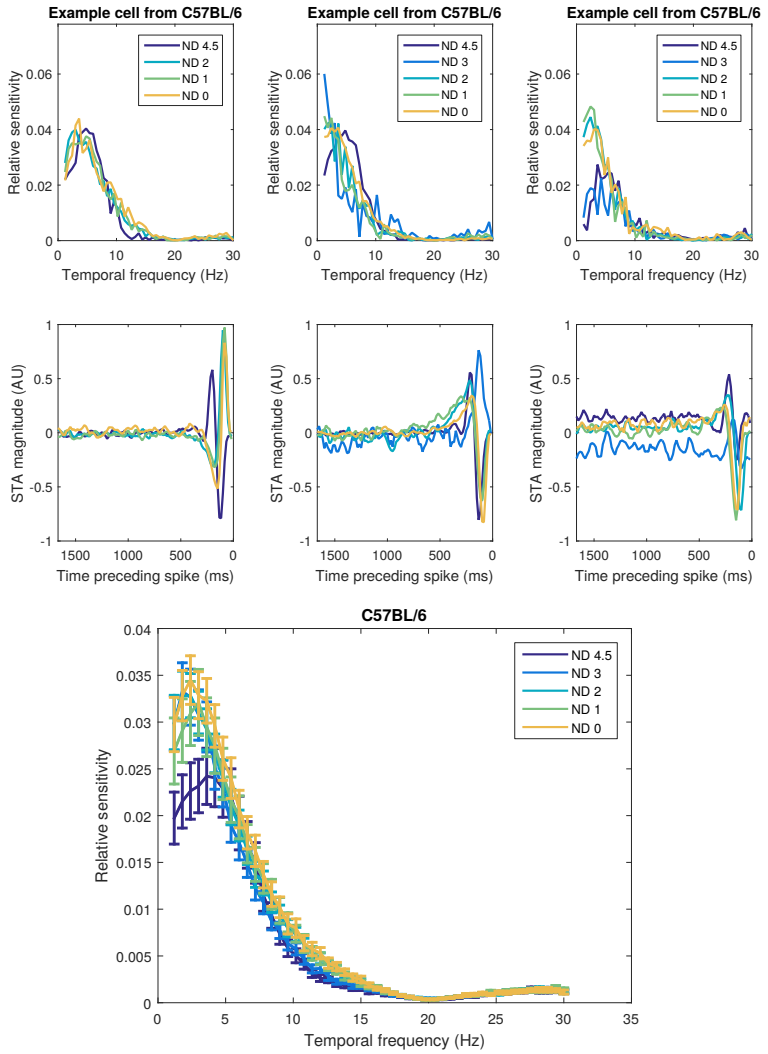

Figure 4.19: **Fourier transforms of C57BL6 temporal kernels across light levels:** Top panel shows Fourier transforms and 100 frame temporal kernels from three example units. Bottom panel shows mean Fourier transform for each light level. Errors bars are 95% confidence intervals. Fourier transforms are shown only for values between 2 Hz and 30 Hz (the Nyquist frequency). n = 8 C57BL/6 mice, with 96 kernels at ND 4.5, 120 at ND 3, 128 at ND 2, 74 at ND 1, and 94 at ND 0.

Temporal kernels from rd17 and C57BL/6 controls may be exchangeable with respect to peak temporal frequency

Temporal frequency tuning of units from rd17 appears to be similar to C57BL/6 controls (figures 4.20 and 4.21), with the possibility of a slight shift towards lower temporal frequencies in rd17 at higher light levels (Fig 4.25). None of the observed differences in mean peak temporal frequency reach significance, meaning that we cannot reject the null hypothesis that units are exchangeable between rd17 and C57BL/6 with respect to peak temporal frequency for any light level.

Peak temporal frequency is higher in cpfl1 at low light levels compared to C57BL/6 controls

At low light levels (particularly ND 4.5 and ND 3), units from cpfl1 are shifted to higher temporal frequencies compared to units from C57BL/6 at the same light levels (figure 4.23 and 4.24). The shift in peak temporal frequency is summarised in figure 4.22. The mean (± S.D.) peak temporal frequency at ND 4.5 in C57BL/6 is 6.31 (± 2.71) Hz, compared to 7.87 (± 3.05) Hz in cpfl1. This difference is significant ($p < 0.001$), with a Cliff's delta effect size of -0.301 (3d.p.). At ND 3, the mean (± S.D.) peak temporal frequency for C57BL/6 kernels is 4.82 (± 2.76) Hz, compared to 8.56 (± 3.81) Hz for cpfl1 kernels. This difference is also significant ($p < 0.0001$), with a Cliff's delta effect size of -0.545 (3d.p.).

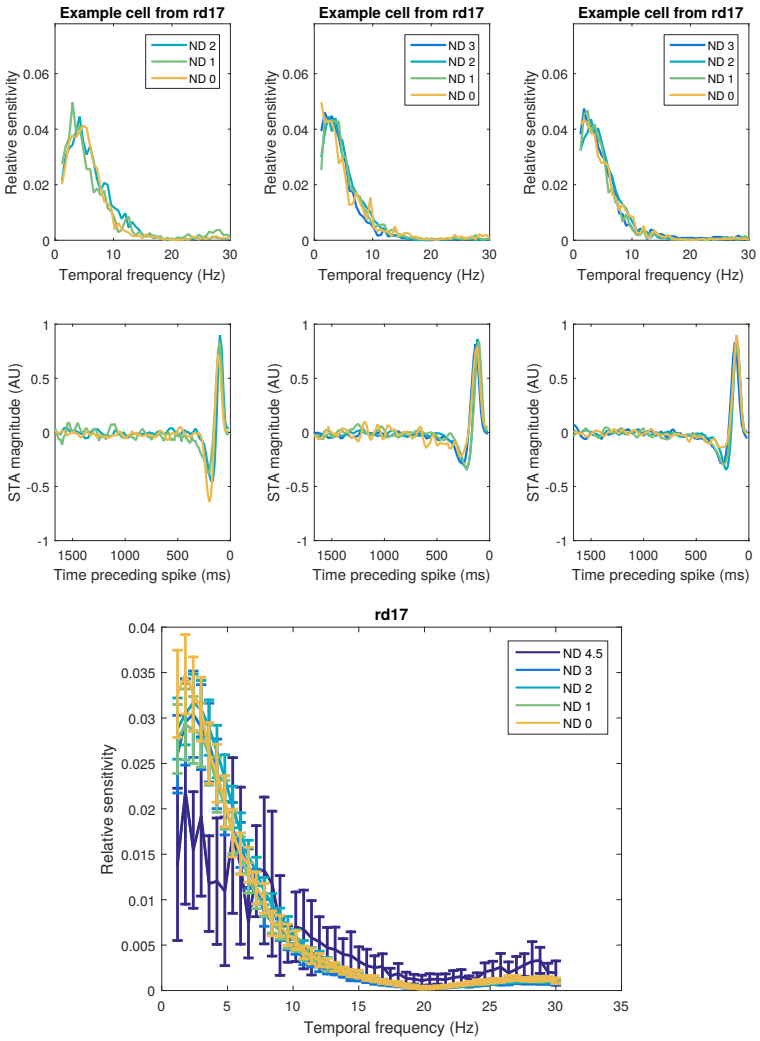

Figure 4.20: **Fourier transforms of rd17 temporal kernels across light levels:** Top panel shows Fourier transforms and 100 frame temporal kernels from three example units. Bottom panel shows mean Fourier transform for each light level. Errors bars are 95% confidence intervals. Fourier transforms are shown only for values between 2 Hz and 30 Hz (the Nyquist frequency). n = 8 rd17 mice, with 9 kernels at ND 4.5, 49 at ND 3, 80 at ND 2, 84 at ND 1, and 55 at ND 0.

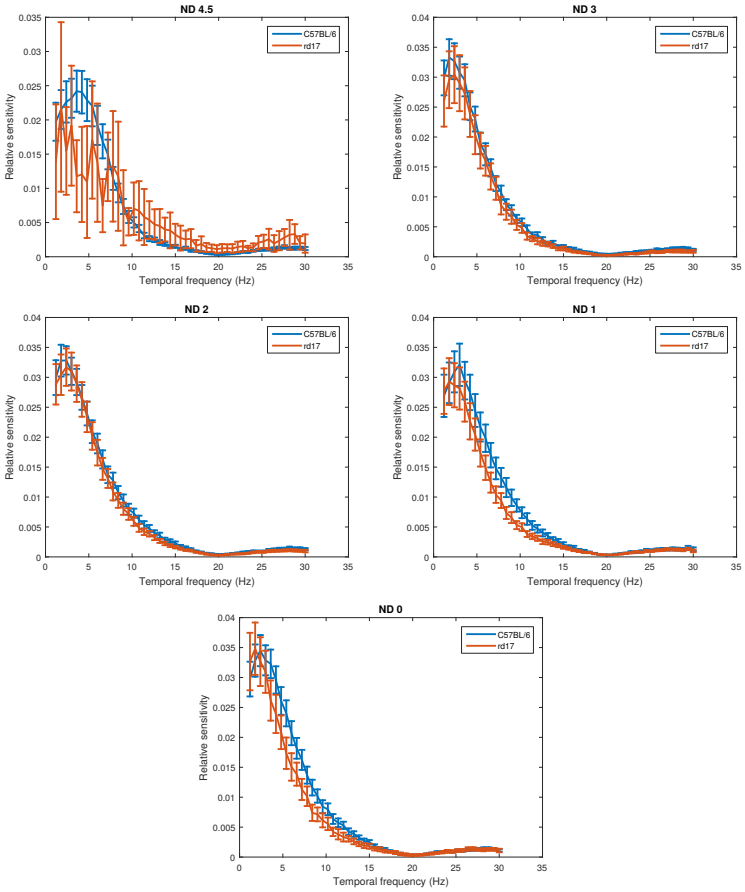

Figure 4.21: **Fourier transforms of rd17 temporal kernels compared to C57BL/6:** Mean Fourier transforms for rd17 and C57BL/6 are shown for each light level. Errors bars are 95% confidence intervals. Fourier transforms are shown only for values between 2 Hz and 30 Hz (the Nyquist frequency). C57BL/6: n = 8 mice, with 96 kernels at ND 4.5, 120 at ND 3, 128 at ND 2, 74 at ND 1, and 94 at ND 0. rd17: n = 8 mice, with 9 kernels at ND 4.5, 49 at ND 3, 80 at ND 2, 84 at ND 1, and 55 at ND 0.

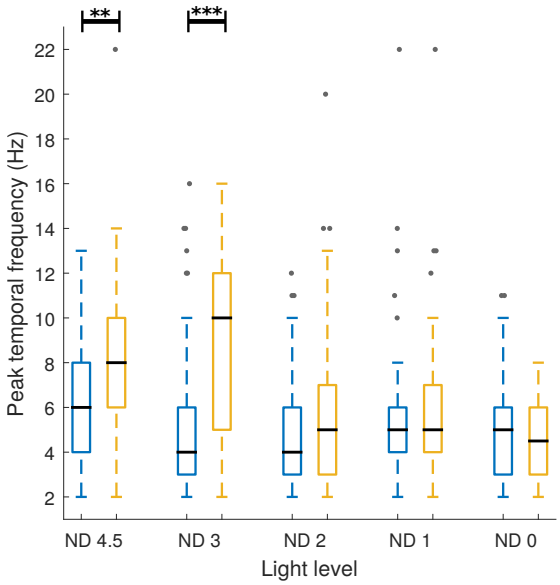

Figure 4.22: **Population peak temporal frequency C57BL/6 versus cpfl1:** Box plot of peak temporal frequency obtained from the Fourier transforms of the temporal kernels in C57BL/6 and cpfl1 mice across all five experimental light levels. This shows a shift towards higher peak temporal frequencies in STAs from cpfl1 compared to C57BL/6 at ND 4.5 and ND 3. Boxes show medians and first and third quartiles, whiskers are 1.5 times the interquartile range. Data points beyond this are represented as outliers. Stars represent p-values of difference in means between groups. These were calculated from permutation post-hoc tests following permutation ANOVA on the full dataset which revealed a significant interaction between animal model and light level ($p < 0.0001$). *** = $p < 0.0001$, ** = $p < 0.001$, * = $p < 0.0025$ (Bonferroni correction for alpha = 0.05). C57BL/6: n = 8 mice, with 96 kernels at ND 4.5, 120 at ND 3, 128 at ND 2, 74 at ND 1, and 94 at ND 0. cpfl1: n = 8 mice, with 82 kernels at ND 4.5, 105 at ND 3, 51 at ND 2, 41 at ND 1, and 16 at ND 0.

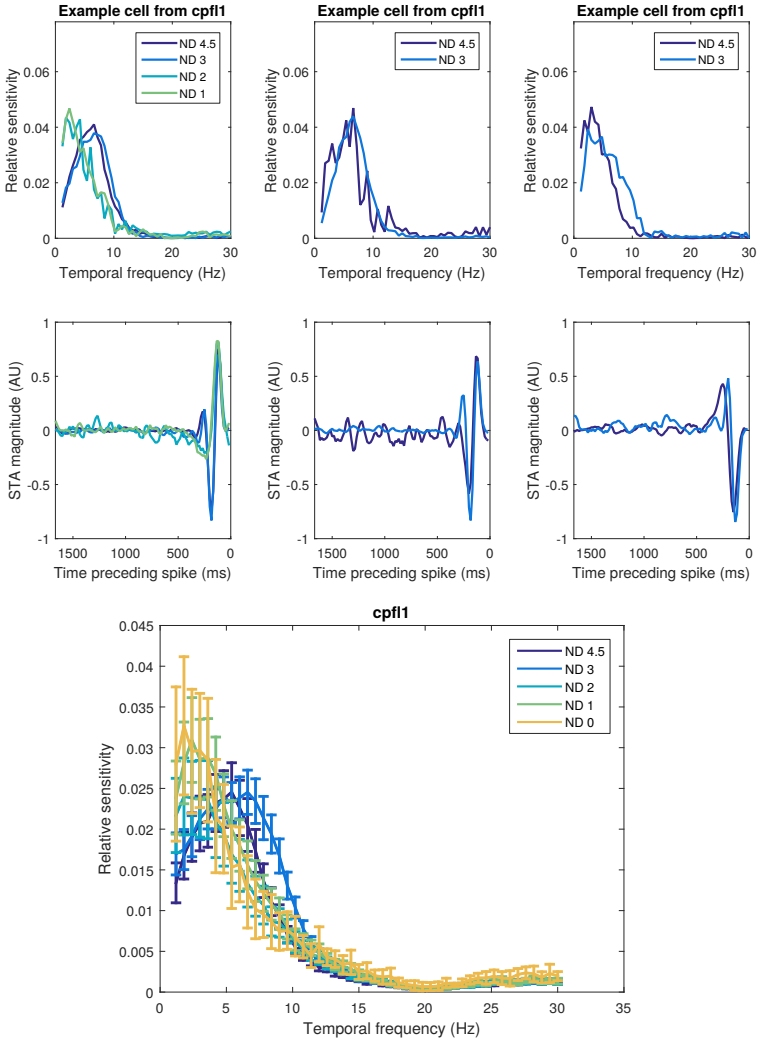

Figure 4.23: **Fourier transforms of cpfl1 temporal kernels across light levels:** Top panel shows Fourier transforms and 100 frame temporal kernels from three example units. Bottom panel shows mean Fourier transform for each light level. Errors bars are 95% confidence intervals. Fourier transforms are shown only for values between 2 Hz and 30 Hz (the Nyquist frequency). n = 8 cpfl1 mice, with 82 kernels at ND 4.5, 105 at ND 3, 51 at ND 2, 41 at ND 1, and 16 at ND 0.

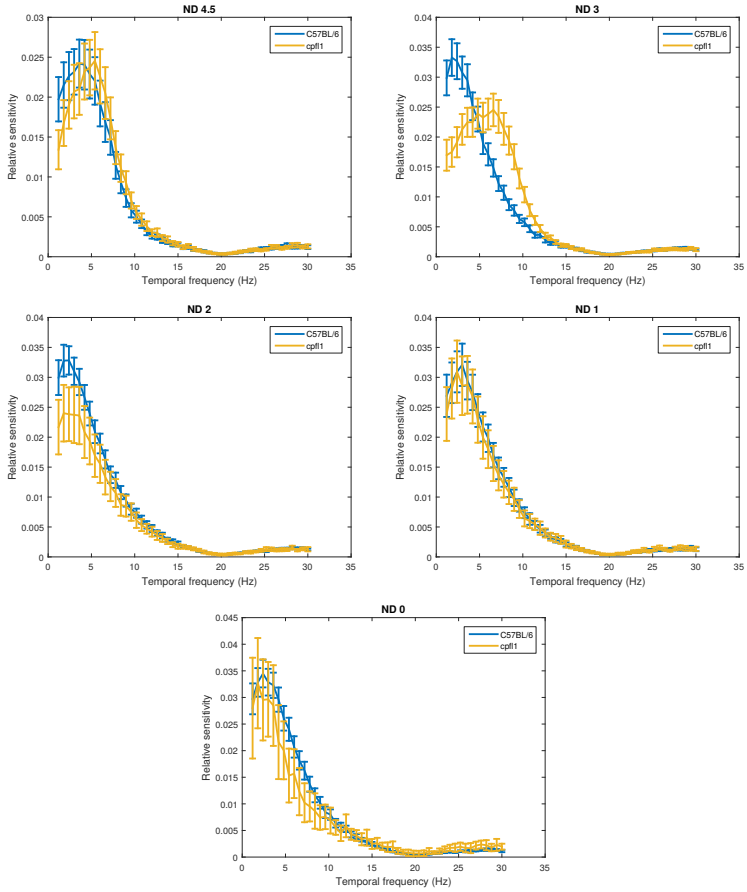

Figure 4.24: **Fourier transforms of cpfl1 temporal kernels compared to C57BL/6:** Mean Fourier transforms for cpfl1 and C57BL/6 are shown for each light level. Errors bars are 95% confidence intervals. Fourier transforms are shown only for values between 2 Hz and 30 Hz (the Nyquist frequency). C57BL/6: n = 8 mice, with 96 kernels at ND 4.5, 120 at ND 3, 128 at ND 2, 74 at ND 1, and 94 at ND 0. cpfl1: n = 8 mice, with 82 kernels at ND 4.5, 105 at ND 3, 51 at ND 2, 41 at ND 1, and 16 at ND 0.

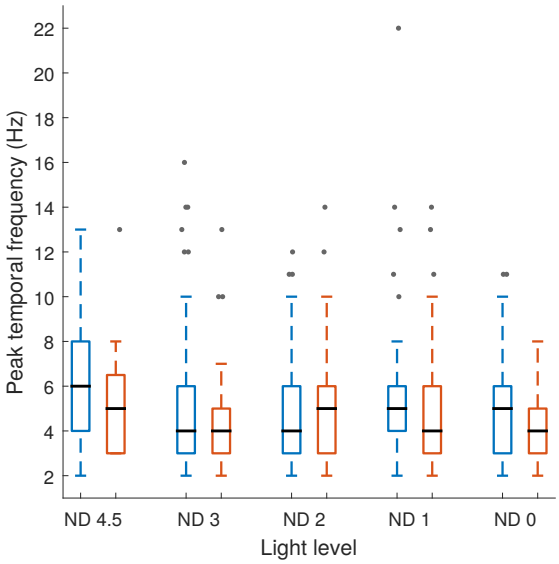

Figure 4.25: **Population peak temporal frequency C57BL/6 versus rd17:** Box plot of peak temporal frequency obtained from the Fourier transforms of the temporal kernels in C57BL/6 and rd17 mice across all five experimental light levels. This shows no significant difference in the peak temporal frequency between rd17 and C57BL/6 mice. Boxes show medians and first and third quartiles, whiskers are 1.5 times the interquartile range. Data points beyond this are represented as outliers. Stars represent p-values of difference in means between groups. These were calculated from permutation post-hoc tests following permutation ANOVA on the full dataset which revealed a significant interaction between animal model and light level ($p < 0.0001$). *** = $p < 0.0001$, ** = $p < 0.001$, * = $p < 0.0025$ (Bonferroni correction for alpha = 0.05). C57BL/6: n = 8 mice, with 96 kernels at ND 4.5, 120 at ND 3, 128 at ND 2, 74 at ND 1, and 94 at ND 0. rd17: n = 8 mice, with 9 kernels at ND 4.5, 49 at ND 3, 80 at ND 2, 84 at ND 1, and 55 at ND 0.

4.3 Discussion

Two broad conclusions can be drawn from these results. The first is that, as expected, the kinetic properties of retinal ganglion cell responses are dependent on the ambient light level in "wild-type" C57BL/6 mice. The second is that in rd17 and cplfl1 mice, which are lacking function in one class of photoreceptor cells, the kinetics of the retinal ganglion cell responses are altered relative to C57BL/6 controls even at light levels where we would expect the remaining functional photoreceptor cells to be dominant. That is, the absence of rod or cone function in the models used here affects retinal processing more profoundly than a simple loss of responses when conditions become scotopic or photopic. There are two possible explanations for the differences observed: the still functioning class of photoreceptor cells is intrinsically different in the models compared to C57BL/6 controls (either due to the named mutation or another overlooked genetic difference), or the absence of the non functional class alters how the retina processes inputs from the remaining functional class.

4.3.1 Temporal kinetics in the presence of functioning rods and cones

C57Bl/6 retinal ganglion cells have faster response kinetics at higher experimental light levels compared to lower light levels. Mean time to peak was reduced by 33 ms and mean time to zero cross was reduced by 30 ms between ND 4.5 and ND 0 (Cliff's delta 0.673 and 0.399 (3 d.p.), respectively). This indicates that stimulus-response and integration time were reduced at higher compared to lower light levels, which is consistent with ganglion cells being driven by shorter latency cones compared to slower rods.

Additionally, C57BL/6 ganglion cells at the lowest experimental light level (ND 4.5) were more likely to have biphasic temporal kernels and more bandpass temporal fre-

quency tuning, with a mean peak temporal frequency 1.54 Hz higher at ND 4.5 compared to ND 0 (Cliff's delta 0.344 (3 d.p.)). Stimuli eliciting spikes at ND 4.5 were more likely to include higher-frequency contrast changes, meaning that ganglion cells at this light level were more contrast modulated than at the higher experimental light levels.

This finding fits with work published by Ke *et al.* (2014), which demonstrated that at high scotopic or low mesopic light levels, the rod bipolar cell synapse begins to encode Michelson contrast (modulation of intensity around the mean luminance), as opposed to Weber contrast (flashes on a background). This is due to use-dependent plasticity at the rod bipolar - amacrine cell synapse. Broadly, when the rod is near saturation it is hyperpolarised for large stretches of time, and so glutamate release is often very low. The downstream rod bipolar cell is therefore constantly depolarised and so is driven to release large volumes of glutamate. This can deplete the transmitter reserves at the rod bipolar - amacrine cell synapse, and so prevent the rod bipolar from communicating information about light increments from the rod. A period of negative contrast (a decrease in light intensity) leading to rod glutamate release and rod bipolar hyperpolarisation enables replenishment of transmitter reserves. In the event that this negative contrast is followed by a positive contrast (increase in light intensity), the rod bipolar will have a sufficient pool of glutamate to communicate this signal on to AII amacrine cells. In this way, the downstream AII cell (and eventually the retinal ganglion cell) will be driven more by contrast modulated stimuli than by unidirectional changes.

Ke *et al.* (2014) observed this phenomenon in experiments performed with stimuli that delivered approximately 200-300 R*/rod/second to the retina. Jarsky *et al.* (2011) report rod bipolar depolarisation at illuminances above 1 R*/rod/second, but particu-

larly between 10 and 100 R*/rod/second. At ND 4.5, the illuminance was calculated to be 53 R*/rod/second, well within this range.

I did not observe the shift towards higher temporal frequency tuning reported by Wang *et al.* (2011) at high light levels in wild type mice. The two experiments differ in a number of ways which may explain this discrepancy. First, Wang *et al.* (2011) use only ventral retina, whereas the retinal segments used for this thesis were from all retinal locations. If the frequency shift is specific to the S-opsin rich ventral retina, this could be masked in my data. Additionally, the light stimuli differ - Wang *et al.* (2011) use a UV LED that provides 12000 P*/cone/second to S-opsin cones, and only 4800 R*/rod/second, resulting in a rod:cone photoisomerisation ratio of 0.4. Conversely, the projector used in this stimulus provided proportionally very little light in the UV region of the spectrum where S cones are most sensitive. At the highest light level (ND 0) S cone P*/cone/second was high (4×10^4), but so was rod R*/rod/second (7×10^6), resulting in a rod:S cone photoisomerisation ratio of 175. As this shift was not observed by Wang *et al.* (2011) in GNAT1$^{-/-}$ (rd17) retina, the balance of rod to cone activation may be relevant to producing the effect.

Finally, the shift demonstrated by Wang *et al.* (2011) is the result of recordings from only 6 retinal ganglion cells. It may be that this study, which compares around 100 kernels at each light level, is a more representative sample of the population of retinal ganglion cells as a whole.

4.3.2 Temporal kinetics in the absence of functional rods

rd17 retinal ganglion cells had slower response kinetics at higher experimental light levels compared to C57BL/6 controls. The mean time to peak was 14 ms slower in rd17 than C57BL/6 (Cliff's delta -0.372 (3d.p.)), and mean time to zero cross was

36 ms slower (Cliff's delta -0.366 (3d.p.)). These differences are small, particularly in the context of a stimulus frame rate interval of 16.67 ms (2d.p.), but they can be observed simply by superimposing the two sets of temporal kernels, and the effect sizes are comparable to the other differences reported here.

Wang *et al.* (2011) have also reported slower response kinetics in rd17 retinal ganglion cells, using zero cross time as a metric. Nikonov *et al.* (2006) found that in loose patch experiments, rd17 cones are slower than C57BL/6 M and S cones, taking the order of tens of milliseconds longer to reach the peak response and also taking longer to return to baseline membrane potential. They attribute this difference as likely due to the use of a rod suppressing background light in C57BL/6 recordings that was not used in rd17 recordings. However, Wang *et al.* (2011) do perform this control in their ganglion cell experiments (applying the bleaching stimulus used to isolate C57BL/6 cone responses to rd17 retinas), and at least at the level of the ganglion cells it actually appears to further increase the temporal latency. This suggests that the difference in background light conditions between rd17 and C57BL/6 in the patch experiments may partially mask the extent to which rd17 cones are slower than C57BL/6 cones, rather than creating the difference by shifting C57BL/6 cones to a faster response profile. In light of the results presented here, and the temporal difference between unbleached C57BL/6 and rd17 ganglion cells reported by Wang *et al.* (2011), it might be sensible to re-assess this potential difference between rd17 and C57BL/6 cones.

The loose patch experiments reported by Nikonov *et al.* (2006) were performed in patches of retinal tissue. As such, if the kinetic difference between rd17 and C57BL/6 cones is real and not an artefact, there are two possible explanations for the observed difference. It could be a result of rd17 cones being intrinsically slower than C57BL/6 cones (perhaps due to some role played by GNAT1 in cones), or it could be due to an

interaction in the retina (between rods and cones, or cones and another cell type) that facilitates the speed of cone responses in C57BL/6 and is altered in rd17 mice.

4.3.3 Temporal kinetics in the absence of functional cones

cpfl1 retinal ganglion cells had faster temporal response kinetics at lower experimental light levels compared to C57BL/6 controls. The mean time to peak was 21 ms faster in cpfl1 than C57BL/6 (Cliff's delta 0.429 (3d.p.)) and mean time to zero cross was 29 ms faster (Cliff's delta 0.360 (3d.p.)) at ND 4.5. This indicates that stimulus-response and integration times are shorter in cpfl1 mice at these light levels.

Temporal kernels in cpfl1 at the first two light levels were very triphasic - the STAs look similar to PC 3 and 5 (shown in Fig 3.2). Biphasic index scores were higher for cpfl1 cells compared to C57BL/6 at ND 4.5 and ND 3, and the temporal frequency tuning was also shifted to higher frequencies, particularly at ND 3. The mean peak temporal frequency of cpfl1 ganglion cells at ND 3 was 1.8 times higher than C57BL/6 cells (a difference of 3.74 Hz, Cliff's delta -0.545 (3d.p.)). These differences all indicate that at lower light levels the ganglion cells in cpfl1 retina are performing more bandpass filtering of the visual scene than in C57BL/6.

One possible mechanism for this difference could be the Michelson contrast encoded at rod bipolar synapses at higher scotopic and mesopic light levels described by Ke *et al.* (2014) and outlined in section 4.3.1, seen in the absence of contaminating cone inputs. If this is the case, then at some point this synapse either becomes less bandpass or rod signals are communicated through a different pathway that is less bandpass, as the temporal kernels become less biphasic and have a lower peak temporal frequency at ND 2, ND 1, and ND 0.

Triphasic temporal STA kernels have also been reported as a consequence of retinal

ganglion cells with ON-OFF centres (cells that spike in response to both light increments and decrements). If the ON and the OFF components of the receptive field centers are temporally mismatched, then this can average to a filter that appears multiphasic from the perspective of the STA (Gollisch & Meister, 2008). These kinds of responses can be distinguished using spike triggered covariance (STC) analysis, where the ON and OFF components of the receptive field can be considered separately.

Are these differences in temporal kinetics a fluke of the cpfl1 model, or a more general feature of retinal processing in the absence of functional cones? There are hints in the published literature that similar differences may occur in at least one other model of cone dysfunction. Wang *et al.* (2011) compare C57BL/6 and cpfl3 (which has a mutation in GNAT2 leading to a loss of cone function). They do not note any difference in zero cross time, but they do see bandpass temporal tuning in the rod-mediated responses, show a cell with a triphasic response at their intermediate light level, and report that cpfl3 ganglion cells became more bandpass when shown stimuli with higher mean luminance. Additionally, Ke *et al.* (2014) report a control experiment recording intracellular currents in 5 cpfl3 ganglion cells compared with 7 C57BL/6 cells. The authors report that cpfl3 show normal responses (compared to the lack of responses seen in rd17), but their plot indicates that the integrated outward currents (OFF responses within the ganglion cell) are stronger in the cpfl3 cells than the C57BL/6 cells (Figure 3, panel E of that paper). These reports are clearly not conclusive, but do suggest that further experiments in cpfl3 may uncover similar results to those reported here for cpfl1.

4.3.4 Future work

In order to be able to generalise from the models presented here to conclusions about the absence of rod and cone function in general, we need to investigate whether similar results can be seen in other models or experimental conditions.

There are several other models of loss of cone function besides cplf1. In particular, as discussed, there is already some evidence from cpfl3 mice (which have a mutation in GNAT2) that the processing differences seen in this study may be replicated in that model. An obvious next step would be to replicate this experiment using additional cone models, including cpfl3 and perhaps cpfl5 (a CNGA3 mutation), to see whether ganglion cell receptive fields in those models are similarly low latency and more bandpass at low light levels compared to wild-type controls.

Finding an alternative model for loss of rod function may be more difficult. Aside from rd17, most mutations that result in loss of rod function are also not stationary, and distinguishing small differences in ganglion cell temporal latency against a background of widespread retinal degeneration is unlikely to be straightforward.

The results from this work suggest that previously reported findings that internal cone responses in rd17 are slower than in C57BL/6 (Nikonov *et al.*, 2006) may not be an artefact. In order to confirm this, loose patch recordings of cones in both rd17 and C57BL/6 would need to be repeated with background light conditions properly controlled. If the cone dynamics are slower in rd17 mice, it would be interesting to compare patching on dissociated cones to recordings done in slice or whole mount retinas, to see if the differences are internal to the cones (suggesting a role for GNAT1 in wild-type cone function), or external (suggesting a role for rod phototransduction in shaping the kinetics of cones).

Finally, the results presented here indicate that in these models the conversion of the visual scene into ganglion cell spiking output is altered, even at light levels where we would expect the functional class of photoreceptor cells to be dominant. It would be interesting to see if this difference in information processing is carried on through the visual pathway (for example, if these differences can still be detected in neurons in the LGN and the visual cortex), and if so how more complex receptive fields are impacted by these changes.

It would also be interesting to explore whether these differences in retinal ganglion cell processing are relevant at the level of behaviour. There is already some indication in previously published work that in the optomotor behavioural paradigm, responses observed in loss of rod and loss of cone function mouse models in the mesopic visual range do not linearly sum to the responses seen in wild-types (Umino *et al.*, 2008). This paradigm is fairly straightforward, and running it at the same light levels used in the work presented here could allow us to relate changes in ganglion cell processing to changes in visual behaviour.

5 Polarity of retinal ganglion cells

5.1 Introduction

As described in section 1.4.2, retinal ganglion cells can be divided broadly into ON, OFF, and ON-OFF responsive cells. ON cells spike in response to light increments, OFF cells spike in response to light decrements, and ON-OFF cells spike in response to both increments and decrements. Principal components analysis and clustering of the full dataset of all STAs recorded in this study reveals two clusters that correspond to STAs in which either light increments or light decrememements dominate the average stimulus preceeding a spike (chapter 3).

Following convention, I have described these STAs as ON and OFF (Chichilnisky & Kalmar, 2002, Pandarinath *et al.*, 2010). However, it is important to remember that this designation is not necessarily analogous to an identification as ON-center or OFF-center, which describes the excitatory input to the central region of the receptive field and is usually determined using a small spot of light (Kuffler, 1952). The STA instead represents the average full field stimulus preceding a spike (section 2.3.1).

As the STA represents the average stimulus before a spike, an ON-OFF cell could generate a variety of STA profiles. If the ON and OFF components of the receptive field are spatially superimposed the cells would either not have a significant STA (as the

ON and OFF components would cancel each other out in the average), or would appear to have either ON or OFF polarity if one component drove the cell more strongly than the other. If the ON and OFF components were spatially distinct, we could expect the STA to have ON and OFF subregions.

The principal components analysis outlined in chapter 3 implies some asymmetry in the number of STAs classified as ON or OFF across experimental light levels and animal models. Projection of C57BL/6 STAs onto PC 1 is skewed positively at ND 1, indicating a higher proportion of ON STAs at this light level. Additionally, there is a negative skew in the projection of rd17 STAs onto PC 1 compared to C57BL/6, which suggests that there may be proportionally fewer ON responses recorded in rd17 mice.

In order to investigate these potential differences in the quantity of ON and OFF STAs, I compared both the absolute numbers of each STA type identfied at each light level in each condition, and also the ratio of ON to OFF STAs recorded in each retinal preparation.

The overall response polarity of retinal ganglion cells is not necessarily constant. In the earliest experimental description of centre-surround receptive fields Kuffler (1952) reported that many cells change their discharge patterns in response to stimulus location, size, intensity, duration, and background light level. Figure 7 in that paper presents an example cell that has an ON response to a spot of light that becomes an ON-OFF response when the background light intensity is increased.

In the salamander, some ganglion cells which usually have OFF responses transiently switch to ON responses following a peripheral image shift (Geffen *et al.*, 2007). These cells receive input from both ON and OFF bipolars (and so are 'classical' ON-OFF cells), but in baseline conditions input from the ON bipolars is inhibited through an amacrine cell pathway. Peripheral image shifts briefly alter this amacrine cell inhibition

and allow the ON input to the ganglion cells to predominate, altering the response properties of the cell.

More recently, Tikidji-Hamburyan *et al.* (2015) have reported related findings in mouse retina and lateral geniculate nucleus. They report that the majority of retinal ganglion cells change their discharge patterns qualitatively depending on the ambient light level - that is, they have an additional ON or OFF response at some light levels, which may also vary in latency. These changes are observed not just in 'classical' ON-OFF cells, but also in 'true' ON and OFF cells which are monostratified in their respective sublaminae of the inner plexiform layer.

When Tikidji-Hamburyan *et al.* (2015) repeated these experiments in several models of loss of cone function (including cpfl1) they found similar proportions of qualitatively switching cells, implying that functional cone inputs are not required to drive these changes. They suggest that changes in inputs to the rod pathway at different ambient light levels may be responsible for some of the observed effects. It should be possible to test this hypothesis using the data collected in this study - if receptive field polarity changes can be detected in C57BL/6 controls, then it should be possible to detect whether they are absent or altered when functional rod input is missing in rd17 mice.

5.2 Results

5.2.1 ON versus OFF responses

The overall ratio of ON to OFF STAs does not change consistently with light level in C57BL/6 mice

Figure 5.1.A shows the overall number of ON and OFF STAs (as defined by the polarity of the first peak of the temporal kernel of the STA) identified at each light level. Overall, the number of ON and OFF STAs are very close to equal at ND 4.5 and ND 0, and more ON than OFF STAs were found at ND 3, ND 2, and ND 1. This matches with the results of the principal components analysis (outlined in section 3.2.4), which indicated that there may be a higher proportion of ON STAs at ND 1 compared to other light levels.

When this difference is examined at the level of each individual retina, as in figure 5.1, it is clear that the proportion of ON versus OFF STAs identified at each light level is highly variable between retinal preparations. While the proportion of significant STAs identified as ON does tend to be higher at ND 1 in particular, a permutation two-factor ANOVA comparing the mean proportion of ON STAs, taking both light level and animal model into account, found no significant main effect or interaction term ($p > 0.05$ for all, see section 2.6, page 81 for methods). This means the null hypothesis - that the proportion of ON STAs is exchangeable between each light level in C57BL/6 mice - cannot be rejected. The high variability of the proportion of ON STAs recorded between retinas lends weight to the hypothesis that the differences seen are due more to sampling than to an underlying biological difference.

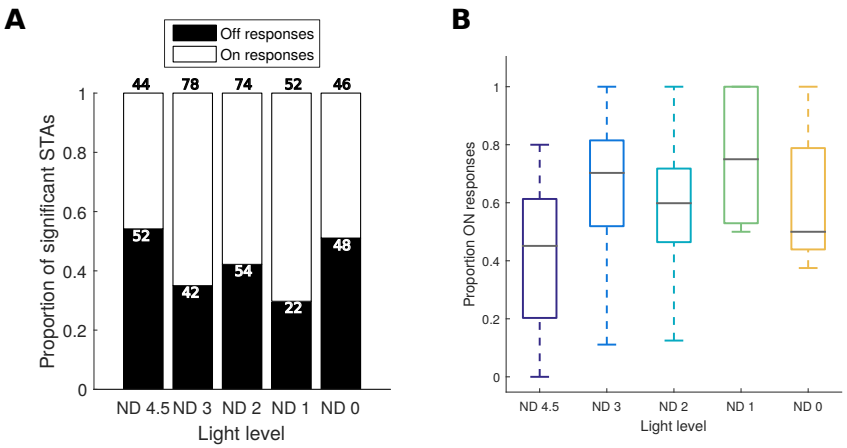

Figure 5.1: **Proportion of ON and OFF receptive fields in C57BL/6 across light levels:** **A**) Proportion of total recorded significant receptive fields identified as OFF or ON in C57BL/6 mice at each light level. The number above each bar indicates the total number of significant receptive fields identified at that light level. **B**) Box plot of proportion of receptive fields that were identified as ON for each individual retina. Receptive fields were classified as ON or OFF based on the polarity of the first peak of the temporal kernel of the STA. Boxes show medians and first and third quartiles, whiskers are 1.5 times the interquartile range. Data points beyond this are represented as outliers. A permutation two-factor ANOVA comparing the mean proportion of ON responses, taking both light level and animal model into account, found no significant main effect or interaction term ($p > 0.05$ for all). $n = 8$ mice.

The overall ratio of ON to OFF STAs is not consistently different between C57BL/6 and rd17 mice

Figure 5.2.A shows that overall, a larger proportion of the STAs recorded from rd17 mice are classified as OFF compared to C57BL/6. This is the case at all light levels other than ND 4.5 (where there are only 9 significant STAs obtained from rd17). These results are consistent with those from the principal components analysis outlined in section 3.2.4.

However, when the proportion of ON STAs per retinal preparation is examined between the two models, it is clear that the variability between preparations is high for both groups. A permutation two-factor ANOVA comparing the mean proportion of ON responses, taking both light level and animal model into account, found no significant main effect or interaction term ($p > 0.05$ for all, see section 2.6, page 81 for methods).

Therefore we cannot reject the null hypothesis that the proportion of ON STAs is exchangeable between C57BL/6 and rd17 mice.

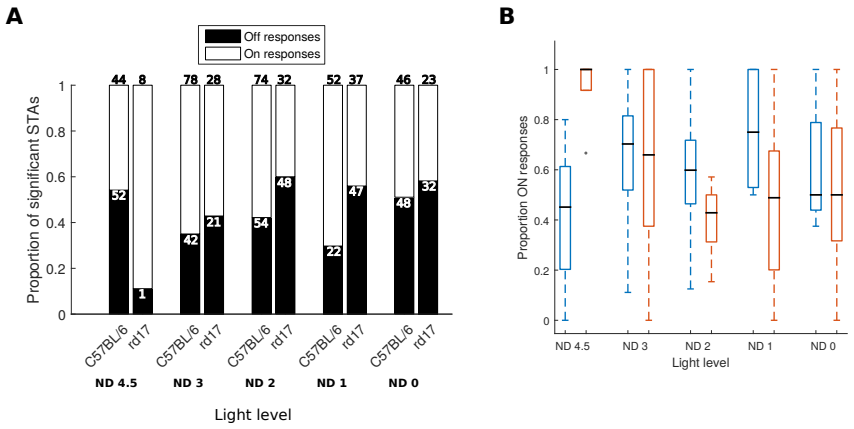

Figure 5.2: **Proportion of ON and OFF receptive fields in rd17 compared to C57BL/6 across light levels:** **A**) Proportion of total recorded significant receptive fields identified as OFF or ON in C57BL/6 and rd17 mice at each light level. The number above each bar indicates the total number of significant receptive fields identified at that light level. **B**) Box plot of proportion of receptive fields that were identified as ON for each individual retina. Blue boxes represent retinas from C57BL/6 mice, and red boxes represent retinas from rd17 mice. Receptive fields were classified as ON or OFF based on the polarity of the first peak of the temporal kernel of the STA. Boxes show medians and first and third quartiles, whiskers are 1.5 times the interquartile range. Data points beyond this are represented as outliers. A permutation two-factor ANOVA comparing the mean proportion of ON responses, taking both light level and animal model into account, found no significant main effect or interaction term ($p > 0.05$ for all). C57BL/6 n = 8, and rd17 n = 8.

The overall ratio of ON to OFF STAs is not consistently different between C57BL/6 and cpfl1 mice

Figure 5.3.A shows that the overall proportions of ON and OFF STAs identified at each light level are very similar in cpfl1 and C57BL/6. Mirroring the data from C57BL/6 mice, there are more ON than OFF STAs recorded in cpfl1 at ND 3, ND 2 and ND 1 than at ND 4.5 or ND 0.

When the proportion of ON STAs per retinal prep is examined between the two models, it is clear that the variability between preparations is high for both groups. A permutation two-factor ANOVA comparing the mean proportion of ON responses, tak-

ing both light level and animal model into account, found no significant main effect or interaction term ($p > 0.05$ for all, see section 2.6, page 81 for methods). Therefore the null hypothesis that the proportion of ON STAs is exchangeable between C57BL/6 and cplf1 mice cannot be rejected.

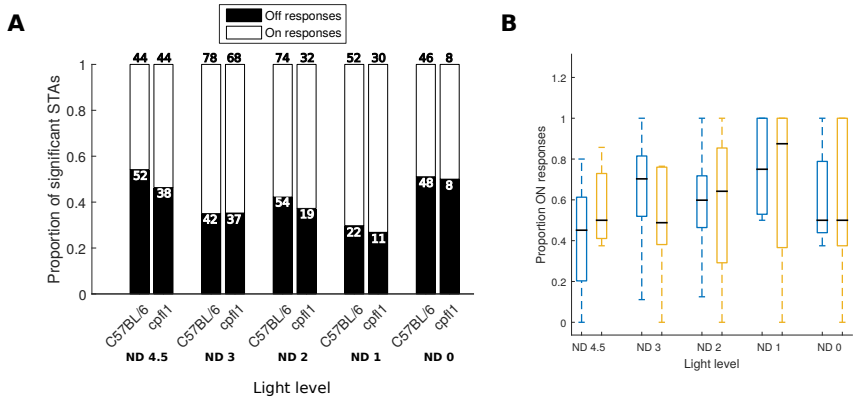

Figure 5.3: **Proportion of ON and OFF receptive fields in cpfl1 compared to C57BL/6 across light levels:** **A**) Proportion of total recorded significant receptive fields identified as OFF or ON in C57BL/6 and cpfl1 mice at each light level. The number above each bar indicates the total number of significant receptive fields identified at that light level. **B**) Box plot of proportion of receptive fields that were identified as ON for each individual retina. Blue boxes represent retinas from C57BL/6 mice, and yellow boxes represent retinas from cpfl1 mice. Receptive fields were classified as ON or OFF based on the polarity of the first peak of the temporal kernel of the STA. Boxes show medians and first and third quartiles, whiskers are 1.5 times the interquartile range. Data points beyond this are represented as outliers. A permutation two-factor ANOVA comparing the mean proportion of ON responses, taking both light level and animal model into account, found no significant main effect or interaction term ($p > 0.05$ for all). C57BL/6 n = 8, and cpfl1 n = 8.

5.2.2 Switching cells

Cells in C57BL/6 mice can switch receptive field polarity between ON and OFF

Of the 142 cells with significant STAs at two or more light levels recorded from C57BL/6 retina, 40 do not have consistent ON or OFF polarity. Examples of these cells are shown in figure 5.4. Some change polarity multiple times during the recording session, while others do so only once. These changes are not restricted to any single pair of

experimental light levels.

For quantification of this phenomenon, cells that switch polarity were defined as cells with STAs in more than one group when the STAs are forced into two clusters (corresponding to ON and OFF) using the ensemble clustering outlined in section 3.2.3.

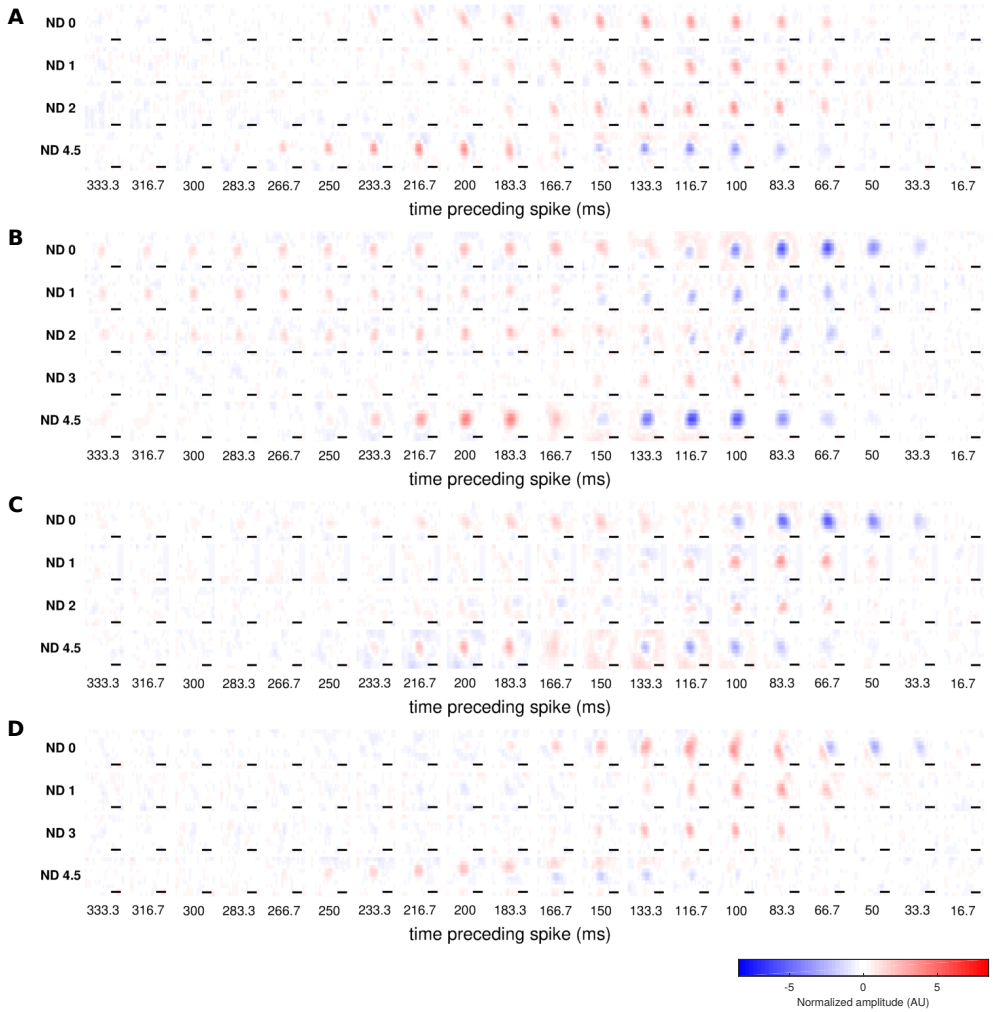

Figure 5.4: **Examples of C57BL/6 cells that switch between ON and OFF responses:** Figures **A**-**D** show four example cells from C57BL/6 mice at each light level where a significant STA was identified. Some cells, such as those shown in **B** and **C** change polarity more than once. For display purposes, only the last 20 frames of each STA are shown, and the filters have been smoothed using a 3x3x3 pixel box filter. All STAs are plotted on a colour map scale where the largest pixel value of all STAs is set as the maximum possible positive (red) or negative (blue) value. Scalebar = 200μm across.

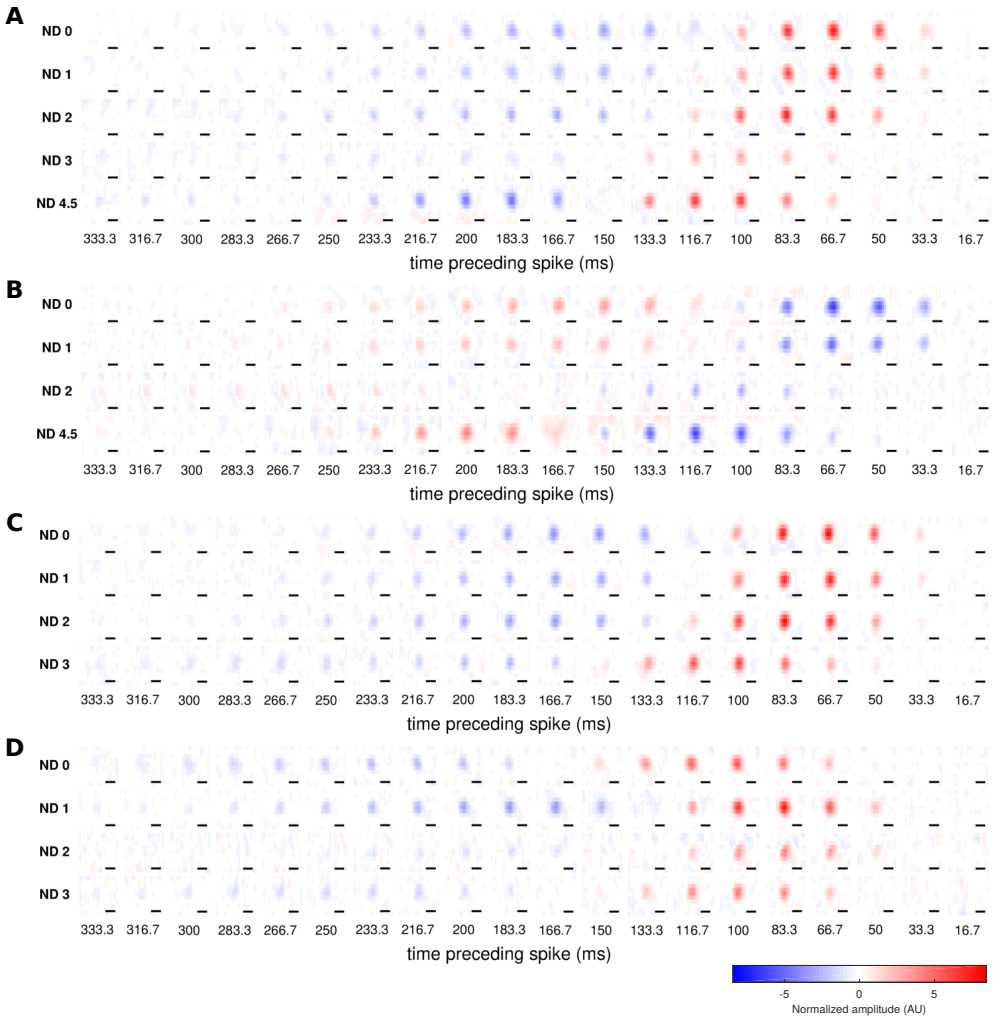

Figure 5.5: **Examples of C57BL/6 cells that maintain consistent ON and OFF responses:** Figures **A-D** show four example cells from C57BL/6 mice at each light level where a significant STA was identified. These cells maintain a consistent response polarity at each experimental light level where a significant STA is identified. For display purposes, only the last 20 frames of each STA are shown, and the filters have been smoothed using a 3x3x3 pixel box filter. All STAs are plotted on a colour map scale where the largest pixel value of all STAs is set as the maximum possible positive (red) or negative (blue) value. Scalebar = 200μm across.

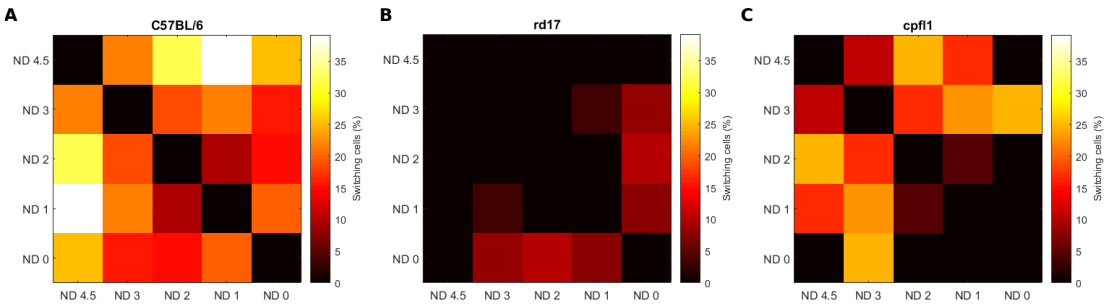

Figure 5.6: **Percentage of cells which switch between OFF and ON between each pair of light levels:** Matrices show the percentage of cells which switch polarity between each pair of light levels. Cells that switch polarity are identified as cells with STAs in more than one group when STAs are forced into two clusters (corresponding to ON and OFF) using the ensemble clustering outlined in section 3.2.3. Analysis is restricted to cells that have a significant STA at at least two light levels. C57BL/6 n = 8, rd17 n = 8, and cpfl1 n = 8.

Fewer cells switch polarity between ON and OFF in rd17 compared to C57BL/6

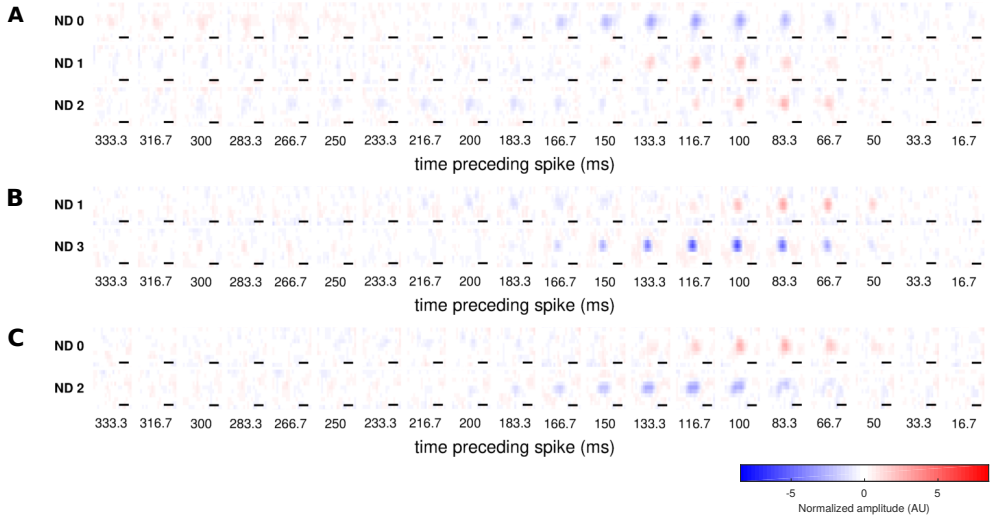

Figure 5.7: **Examples of rd17 cells that switch between ON and OFF responses:** Figures **A-C** show three example cells from rd17 mice at each light level where a significant STA was identified. For display purposes, only the last 20 frames of each STA are shown, and the filters have been smoothed using a 3x3x3 pixel box filter. All STAs are plotted on a colour map scale where the largest pixel value of all STAs is set as the maximum possible positive (red) or negative (blue) value. Scalebar = 200μm across.

Five retinal ganglion cells that exhibit switching between ON and OFF were identified in recordings from rd17 mice. Figure 5.7 shows the three most convincing examples.

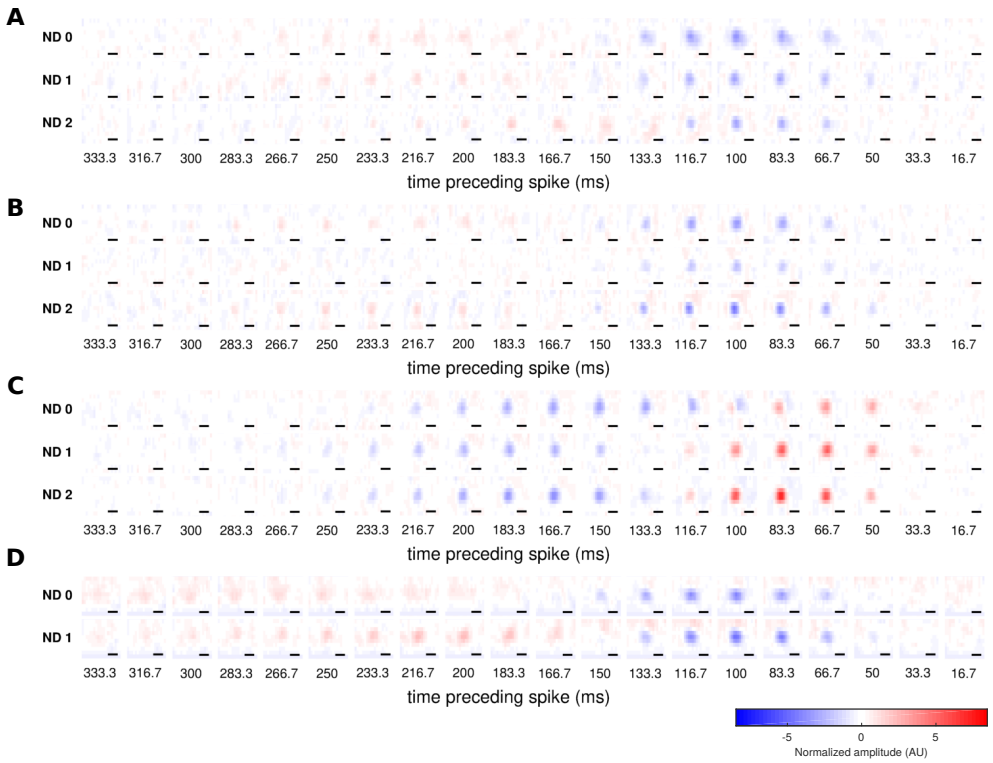

Figure 5.8: **Examples of rd17 cells that maintain consistent ON and OFF responses:** Figures **A**-**D** show four example cells from rd17 mice at each light level where a significant STA was identified. These cells maintain a consistent response polarity at each experimental light level where a significant STA is identified. For display purposes, only the last 20 frames of each STA are shown, and the filters have been smoothed using a 3x3x3 pixel box filter. All STAs are plotted on a colour map scale where the largest pixel value of all STAs is set as the maximum possible positive (red) or negative (blue) value. Scalebar = 200μm across.

All other rd17 cells remained within the same cluster at each light level where they had a significant STA (some examples are shown in figure 5.8).

Figure 5.9 shows the proportion of cells that exhibit switching behaviour in C57BL/6 compared to rd17 (analysis is restricted to cells with a significant STA at a minimum of two light levels). A permutation Chi-squared test performed on counts of switching and non-switching cells from all three animal models indicated that counts were not exchangeable between all three models ($p < 0.001$). Post-hoc permutation Chi-squared tests revealed that counts were not exchangeable between rd17 and C57BL/6 groups ($p < 0.001$, where the Bonferroni corrected threshold equivalent to $\alpha = 0.05$ is 0.025).

In order to check that this difference was not due to the small number of significant

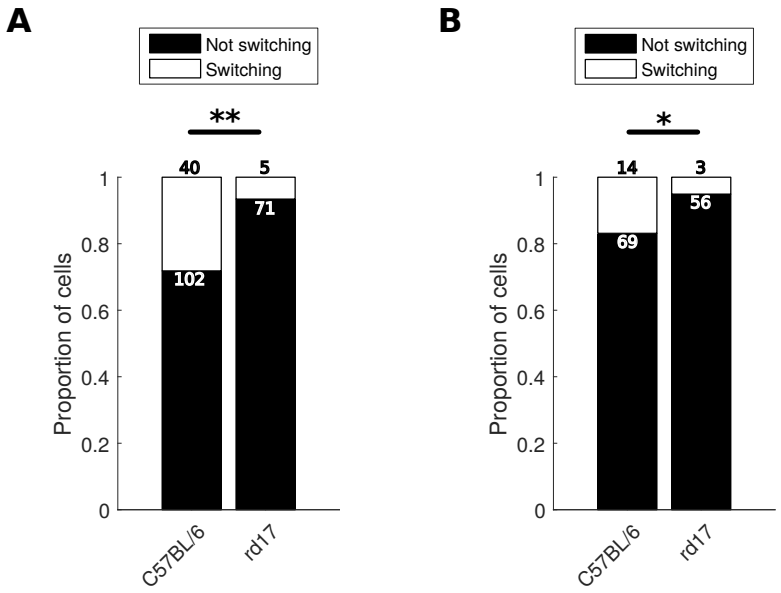

Figure 5.9: **Proportion of cells that switch polarity between ON and OFF in rd17 and C57BL/6:** **A**) The proportion of cells that do or do not switch polarity between any two experimental light levels, showing that fewer cells exhibit this behaviour in rd17 mice compared to C57BL/6. **B**) The proportion of cells that do or do not switch polarity, restricted to the three brightest experimental light levels (ND 2, ND 1, and ND 0). Cells that switch polarity are identified as cells with STAs in more than one group when STAs are forced into two clusters (corresponding to ON and OFF) using the ensemble clustering outlined in section 3.2.3. The total number of cells analysed is printed at the top of each bar. In both plots, analysis is restricted to cells that have a significant STA at at least two light levels. rd17 n = 8, and C57BL/6 n = 8. * = $p < 0.05$, ** = $p < 0.01$

STAs at low light levels in rd17 simply reducing the chances of catching a switching cell, the analysis was repeated using only STAs from the three brightest light levels (ND 2, ND 1, and ND 0). As figure 5.9.B shows, the difference remains. A permutation Chi-squared test was performed on this restricted data set ($p < 0.05$), and a single post-hoc permutation Chi-squared test was then performed to confirm that this was due to non-exchangeabilty between rd17 and C57BL/6 ($p < 0.05$).

These differences were also examined at the level of the individual retinas used in the experiments (figure 5.10). The difference in the proportion of switching cells remains both when all light levels are considered and when analysis is restricted to only the top three light levels. A permutation one-way ANOVA comparing the mean proportion of switching cells across all three animal models and light levels revealed a significant

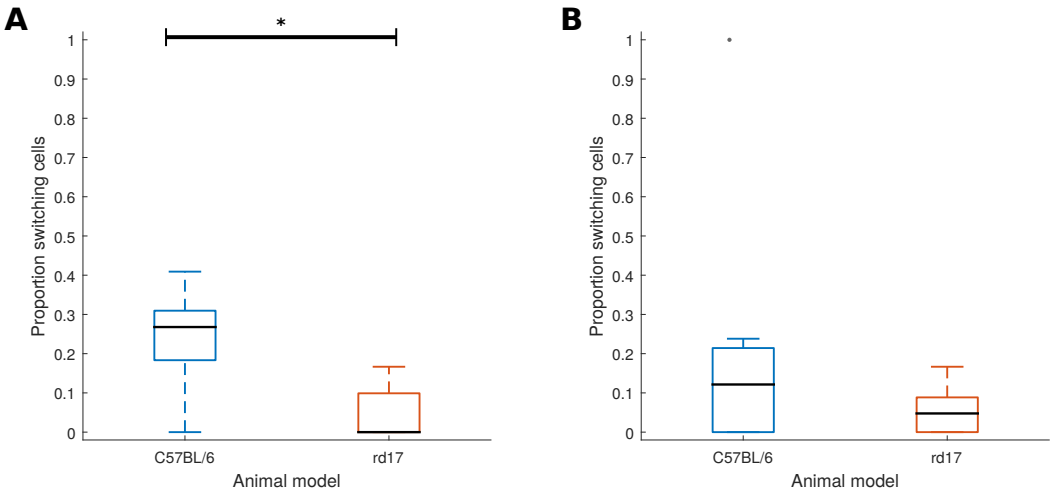

Figure 5.10: **Proportion of cells that switch polarity between ON and OFF in rd17 and C57BL/6, per retina:** Box plots of proportion of cells that were identified as switching for each individual retina. Blue boxes represent retinas from C57BL/6 mice, and red boxes represent retinas from rd17 mice. Boxes show medians and first and third quartiles, whiskers are 1.5 times the interquartile range. Data points beyond this are represented as outliers. **A**) The proportion of cells that do or do not switch polarity between any two experimental light levels, showing that fewer cells exhibit this behaviour in rd17 mice compared to C57BL/6. A permutation one-way ANOVA comparing the mean proportion of switching cells across all three animal models found a significant effect ($p < 0.05$). *** = $p < 0.0001$, ** = $p < 0.001$, * = $p < 0.025$ (Bonferroni correction for alpha = 0.05). **B**) The proportion of cells that do or do not switch polarity, restricted to the three brightest experimental light levels (ND 2, ND 1, and ND 0). A permutation one-way ANOVA comparing the mean proportion of switching cells across all three animal models within this restricted light level range found no significant effect ($p > 0.05$). Cells that switch polarity are identified as cells with STAs in more than one group when STAs are forced into two clusters (corresponding to ON and OFF) using the ensemble clustering outlined in section 3.2.3. In both plots, analysis is restricted to cells that have a significant STA at at least two light levels. rd17 n = 8, and C57BL/6 n = 8.

effect ($p < 0.05$ and $p < 0.025$ (Bonferroni correction for alpha = 0.5) for the post hoc comparison between C57BL/6 and rd17). However, when this was repeated with the analysis restricted to the top three light levels, the null hypothesis of exchangeability between retinas from rd17 and C57BL/6 mice with respect to the proportion of switching cells could not be rejected.

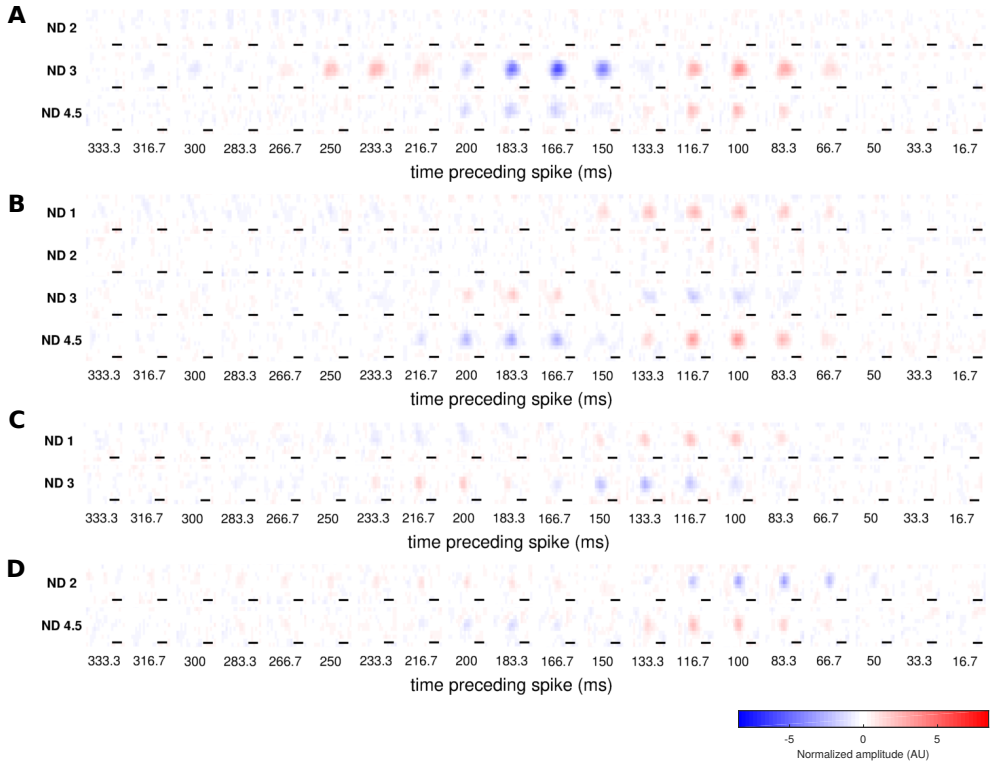

Figure 5.11: **Examples of cpfl1 cells that switch between ON and OFF responses:** Figures **A**-**D** show four example cells from cpfl1 mice at each light level where a significant STA was identified. Some cells identified as switching response polarity (such as **A**) may lose responses rather than change polarity. For display purposes, only the last 20 frames of each STA are shown, and the filters have been smoothed using a 3x3x3 pixel box filter. All STAs are plotted on a colour map scale where the largest pixel value of all STAs is set as the maximum possible positive (red) or negative (blue) value. Scalebar = 200μm across.

Cells that switch polarity between ON and OFF can also be identified in cpfl1

Thirteen cells that switch polarity between ON and OFF were identified in cpfl1 experiments. Examples of these cells are shown in figure 5.11. All other cpfl1 cells remained within the same cluster at each light level where they had a significant STA (examples of these cells are shown in figure 5.12).

Figure 5.13 shows the proportion of cells that exhibit switching behaviour in C57BL/6 compared to cpfl1 mice (analysis is restricted to cells with a significant STA at a minimum of two light levels). A smaller proportion of cells are identified as switching in

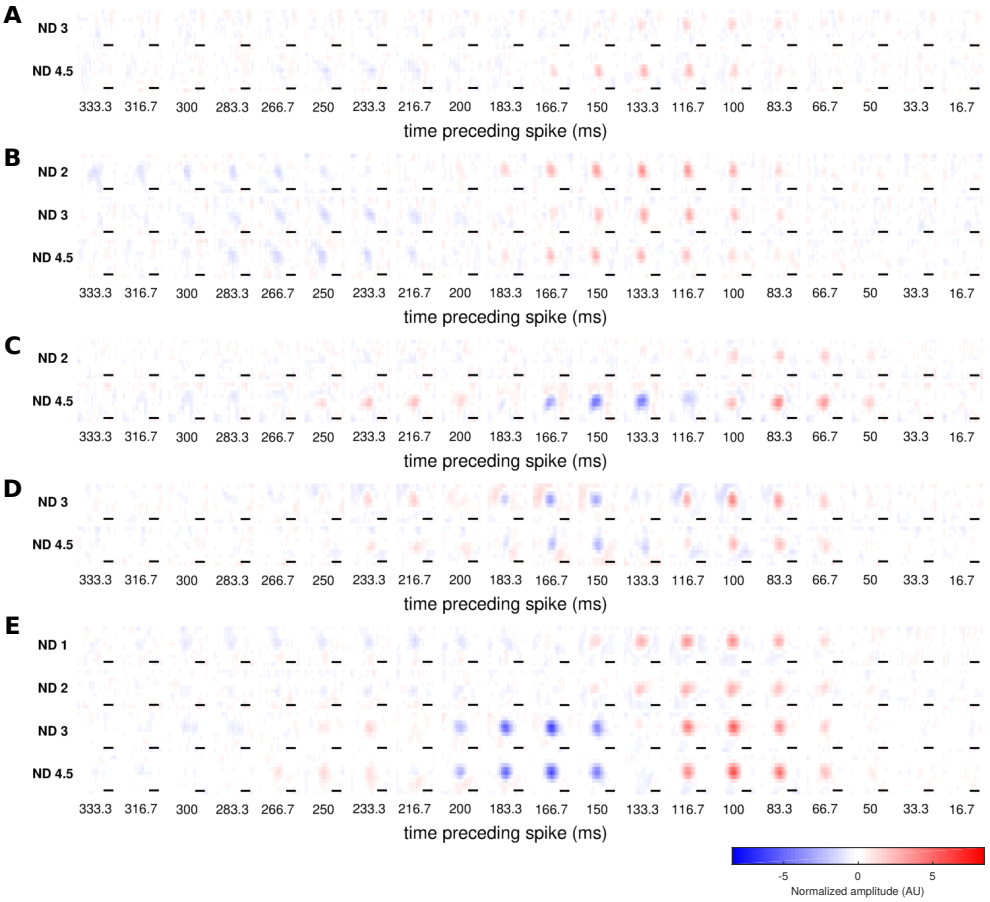

Figure 5.12: **Examples of cpfl1 cells that maintain consistent ON and OFF responses:** Figures **A-E** show five example cells from cpfl1 mice at each light level where a significant STA was identified. These cells maintain a consistent response polarity at each experimental light level where a significant STA is identified. For display purposes, only the last 20 frames of each STA are shown, and the filters have been smoothed using a 3x3x3 pixel box filter. All STAs are plotted on a colour map scale where the largest pixel value of all STAs is set as the maximum possible positive (red) or negative (blue) value. Scalebar = 200μm across.

cpfl1 compared to C57BL/6. A permutation Chi-squared test performed on counts of switching and non-switching cells from all three animal models indicated that counts were not exchangeable between the models ($p < 0.001$). However, post-hoc permutation Chi-squared tests revealed that this was not due to the difference between cpfl1 and C57BL/6 ($p > 0.05$, where the Bonferroni corrected threshold equivalent to $\alpha = 0.05$ is 0.025). This means that the null hypothesis that C57BL/6 and cpfl1 are from the same distribution, and counts are exchangeable between the two groups, cannot be rejected.

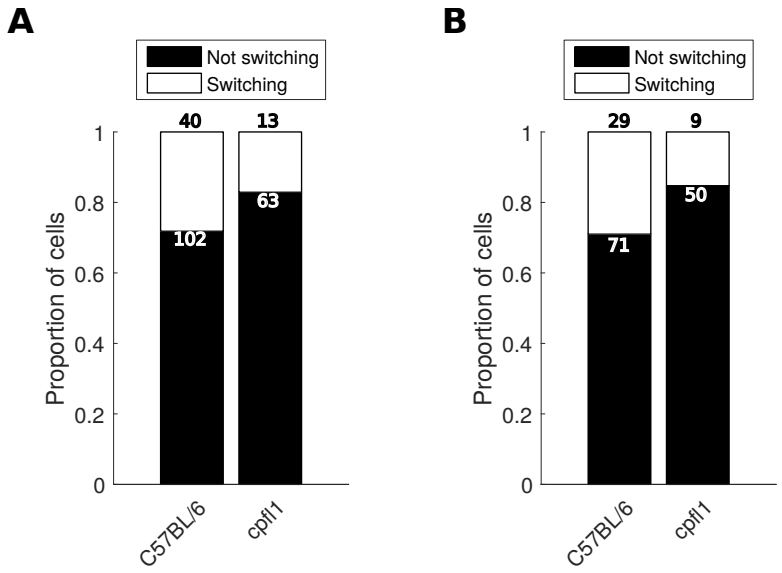

Figure 5.13: **Proportion of cells that switch polarity between ON and OFF in cpfl1 and C57BL/6:** **A**) The proportion of cells that do or do not switch polarity between any two experimental light levels, showing that fewer cells exhibit this behaviour in cpfl1 mice compared to C57BL/6. **B**) The proportion of cells that do or do not switch polarity, restricted to the three dimmest experimental light levels (ND 4.5, ND 3, and ND 2). Cells that switch polarity are identified as cells with STAs in more than one group when STAs are forced into two clusters (corresponding to ON and OFF) using the ensemble clustering outlined in section 3.2.3. The total number of cells analysed is printed at the top of each bar. In both plots, analysis is restricted to cells that have a significant STA at at least two light levels. cpfl1 n = 8, and C57BL/6 n = 8.

For completeness, the proportions of switching and non switching cells are also shown for C57BL/6 and cpfl1 using STAs only from the three dimmest experimental light levels (ND 4.5, ND 3, ND 2). The difference in counts between the two groups persists with this restriction.

These differences were also examined at the level of the individual retinal preparations (figure 5.14). The difference in the proportion of switching cells remains both when all light levels are considered and when analysis is restricted to only the lowest three light levels. A permutation one-way ANOVA comparing the mean proportion of switching cells across all three animal models that included all light levels revealed a significant effect ($p < 0.05$). However, a post hoc permutation test revealed that this was not due to the difference between cpfl1 and C57BL/6 ($p > 0.025$ (Bonferroni correction for

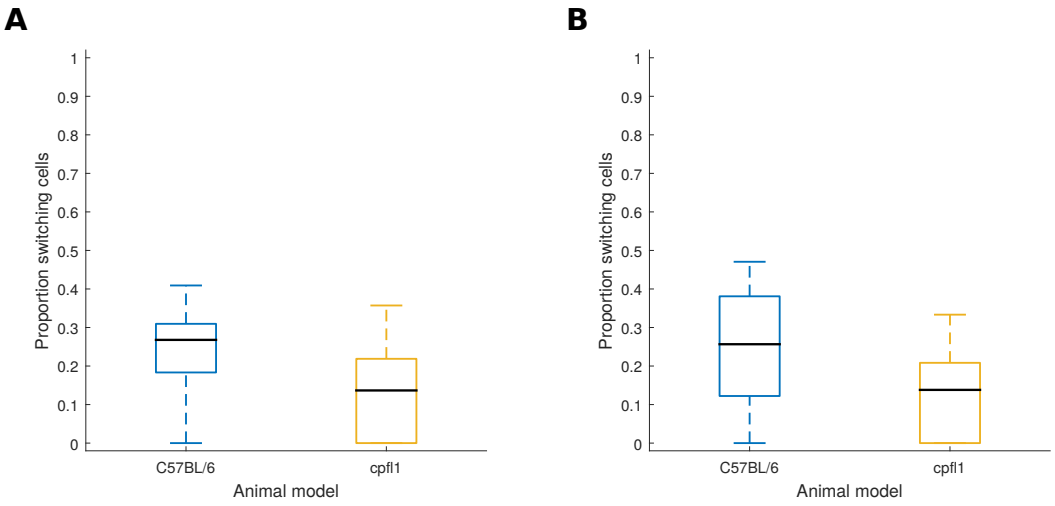

Figure 5.14: **Proportion of cells that switch polarity between ON and OFF in rd17 and C57BL/6, per retina:** Box plots of proportion of cells that were identified as switching for each individual retina. Blue boxes represent retinas from C57BL/6 mice, and red boxes represent retinas from rd17 mice. Boxes show medians and first and third quartiles, whiskers are 1.5 times the interquartile range. Data points beyond this are represented as outliers. **A**) The proportion of cells that do or do not switch polarity between any two experimental light levels, showing that fewer cells exhibit this behaviour in rd17 mice compared to C57BL/6. A permutation one-way ANOVA comparing the mean proportion of switching cells across all three animal models found a significant effect ($p < 0.05$). *** = $p < 0.0001$, ** = $p < 0.001$, * = $p < 0.025$ (Bonferroni correction for alpha = 0.05). **B**) The proportion of cells that do or do not switch polarity, restricted to the three dimmest experimental light levels (ND 4.5, ND 3, and ND 2). A permutation one-way ANOVA comparing the mean proportion of switching cells across all three animal models within this restricted light level range found a significant effect ($p > 0.05$), but a subsequent permutation post-hoc test showed that this was not due to a difference between cpfl1 and C67BL/6 in this instance ($p > 0.025$ (Bonferroni correction for alpha = 0.05)). Cells that switch polarity are identified as cells with STAs in more than one group when STAs are forced into two clusters (corresponding to ON and OFF) using the ensemble clustering outlined in section 3.2.3. In both plots, analysis is restricted to cells that have a significant STA at at least two light levels. rd17 n = 8, and C57BL/6 n = 8.

alpha = 0.5)). Therefore, the null hypothesis is also not able to be rejected on the level of individual retinas. These results were unchanged when analysis was restricted to the lowest three light levels.

5.3 Discussion

5.3.1 Proportion of ON versus OFF responses

As predicted by projection onto the principal components (chapter 3), there were more ON STAs detected at ND 1 than at other light levels (figure 5.1). When examined on a prep-by-prep level, this difference was still observed in the distribution of the proportion of STAs that were classified as ON. However, this property was highly variable across retinal preparations, and the null hypothesis that populations were exchangeable across light levels could not be rejected (section 5.2.1). Thus, the observed difference in the number of ON and OFF STAs at ND 1 compared to other light levels in C57BL/6 mice may simply be due to experimental variation rather than a real biological difference.

Similarly, as predicted by projection onto the principal components, there were proportionally fewer ON STAs identified in rd17 mice compared to C57BL/6 controls. While in C57BL/6 mice, ON STAs outnumbered OFF STAs, in rd17 mice the number of ON and OFF STAs was more equal at every light level that reliably produced significant STAs (figure 5.2). Again, the null hypothesis of exchangeability between groups could not be rejected, and this difference may simply be due to experimental variability.

The number and relative proportions of ON and OFF STAs was more consistent between cpfl1 and C57BL/6 mice (figure 5.3).

5.3.2 Switching cells

Cells that switched STA polarity between ON and OFF were identified in all three animal models. In C57BL/6 mice, both majority-ON and majority-OFF cells were observed to switch polarity, and some cells switched more than once (figure 5.4). Po-

larity switches were observed between every possible pair of light levels. However, STA polarities were most likely to be different between ND 4.5 and ND 1, and switching was in general more likely between ND 4.5 (the lowest experimental light level) and all higher light levels (figure 5.6.A). This suggests that larger differences in ambient light level may more effectively drive these changes.

Functional rods are not required for all polarity switches

A small number of cells which switched STA polarity with experimental light level were detected in retinae from rd17 mice (figure 5.7), indicating that functional rods are not necessary to observe this behaviour. However, the proportion of all cells identified as switching polarity was much smaller. Even when analysis was confined to only the top three light levels (where rd17 cells were to reliably produce significant STAs), the proportion of cells which switched polarity was over three times larger in C57BL/6 mice compared to rd17 (16.87% versus 5.08% (2 d.p.), figure 5.9).

While this difference in overall counts pooled from all retina was statistically significant, the null hypothesis that retina from both groups are exchangeable in terms of proportion of switching cells at the top three light levels could not be rejected (figure 5.10). This may be because the observed differences are simply due to experimental variation, or it may be because the number of switching cells identified in this light level range was small in both groups and therefore the difference was below the threshold for a study of this power to reliably detect.

Functional cones are not required for all polarity switches

Cells which switch STA polarity between ON and OFF were also identified in cpfl1 mice (figure 5.11). The proportion of cells identified as switching was smaller in cpfl1

compared to C57BL/6 controls. When analysis was constrained to only the lowest three light levels (where cpfl1 cells reliably produced significant STAs), the proportion of cells which switched polarity was almost twice as high in C57BL/6 mice compared to cpfl1 (29.00% versus 15.25% (2 d.p.), figure 5.13).

This difference was not statistically significant, either in terms of overall counts or when proportions of switching cells identified in each retinal preparation were compared. Again, this may be because the observed difference was simply the result of experimental variability, or because the difference was too small for the power of this study.

Possible circuit mechanisms underlying STA polarity switching

As discussed in section 5.1, a switch between ON and OFF STA polarity could be produced by a change in the balance of ON and OFF inputs (either from bipolar cells in the case of true ON-OFF cells, or through the inhibitory pathway).

The polarity switch reported by Geffen *et al.* (2007) is mediated through disinhibition of ON bipolar cell inputs by a wide-field amacrine cell. A similar mechanism may underlie the switches observed here. Amacrine cells can interact differently with the ON and the OFF pathway. The AII amacrine cell, for example, forms chemical synapses with OFF cone bipolar cells, and gap junctions with ON cone bipolar cells (Kolb & Famigilietti, 1974). As outlined in section 1.5.2, depolarisation at the amacrine cell drives synaptic release and subsequent hyperpolarisation in the OFF cone bipolar, and depolarisation in the amacrine cell can be communicated directly to the ON cone bipolar. In both cases this will contribute to changing the cone bipolar cell membrane potential and therefore changing the likelihood of synaptic release. However, hyperpolarisation of the AII cell (as occurs at higher light levels when rod bipolar cells saturate) is passed on to ON cone bipolars and not OFF cone bipolars. This change in membrane potential

could make ON cone bipolars less likely to release transmitter in response to input from cones, while disinhibiting OFF cone bipolars though a reduction in AII mediated inhibition. Changes in the background light level could therefore alter the balance of ON and OFF inputs at a downstream ON-OFF retinal ganglion cell.

Tikidji-Hamburyan *et al.* (2015) have reported that cells which receive only ON or OFF bipolar cell inputs ('true' ON or OFF ganglion cells) can also be driven to fire at some light levels by changes of the opposite sign. If the balance in these cells is shifted sufficiently, these 'additional' ON or OFF responses may be strong enough to reverse the polarity of the STA.

One potential mechanism for opposite sign responses in cells that receive only ON or OFF bipolar cell input involves disinhibition from an amacrine cell. Cross-over inhibition between the ON and the OFF pathway at the level of both bipolar and ganglion cells has been demonstrated to shape the temporal and spatial properties of retinal receptive fields (Marco *et al.*, 2013, Rosa *et al.*, 2016). Taking an ON cell as an example, the ganglion cell could receive both excitatory input from ON cone bipolar cells and tonic inhibition from an amacrine cell. The spike rate would then increase following either synaptic release from the ON bipolar, or a reduction in inhibition from the amacrine cell. This circuit is often used to describe a centre-surround receptive field, where the amacrine cell carries the surround inhibition. In the context of an ON-centre, OFF-surround cell, a light increase in the surround would cause amacrine cell inhibitory input to the ganglion cell. However, a light decrease in this region would reduce synaptic drive from the amacrine cell, and could be sufficient to allow the ganglion cell membrane potential to rise above threshold and spike (Huang & Protti, 2016).

A change in response polarity of an ON or OFF ganglion cell could also be driven

by a change in the response polarity of an upstream bipolar cell. These changes have been described by Odermatt *et al.* (2012) in fish and by Vlasits *et al.* (2014) in mouse. Similar mechanisms relating to the balance of inhibition and photoreceptor cell driven excitation at bipolar cell terminals could be responsible for these switches. Alternatively, Vlasits *et al.* (2014) propose a mechanism whereby hyperpolarised rods in bright light conditions, which can no longer directly signal changes in light intensity, are depolarised by a sign-inverting synapse when cones are hyperpolarised by light (most likely via the horizontal cell surround mechanism described in section 1.5.2 (Gao *et al.*, 2013, Szikra *et al.*, 2014)). This depolarisation leads to glutamate release from rods and is likely able to re-set the saturation that occurs in the rod-rod bipolar-AII circuit during light adaptation. Then, when the cones depolarise (in response to a decrease in light intensity), rods re-hyperpolarise. The rod circuit is now able to transduce this rod hyperpolarisation and subsequent reduction in glutamate release, much as it would transduce a rod hyperpolarisation in response to a light flash. Rod bipolar cells depolarise and release transmitter onto AII amacrine cells, which in turn drive depolarisation in an ON cone bipolar via gap junction connections. Thus, the ON cone bipolar now responds to a light decrement as it would to a light increment. Vlasits *et al.* (2014) have demonstrated that this change in cone ON bipolar cell response polarity is able to drive a response polarity reversal in downstream starbusrt amacrine cells, and it is possible that it could do the same in retinal ganglion cells.

These proposed mechanisms seem to require functional cone input combined with changes in rod signalling. The higher frequency of switches between ND 4.5 (below cone threshold) and higher light levels would seem to support this hypothesis. However, consistent with data reported by Tikidji-Hamburyan *et al.* (2015) (supplementary figure 4 in that paper), STA polarity switches can occur in the absence of functional cones in cpfl1 mice.

Polarity switches in cpfl1 mice could be driven by rod synapses with cells other than rod bipolars. Rods form synapses with a mixed rod-cone OFF bipolar cell (Hack *et al.*, 1999, Pang *et al.*, 2012, Soucy *et al.*, 1998, Tsukamoto & Omi, 2013, Tsukamoto *et al.*, 2001), and in cpfl1 mice may also participate in ectopic synapses with cone bipolar cells as has been demonstrated in CNGA3$^{-}/^{-}$ mice (Haverkamp, 2006). If these bipolar cells are more resistant to saturation than the rod bipolar, then this alternate pathway for rod signals could interact with hyperpolarisation from AII cells in a very similar manner to input from functional cones. The observed switching cells may also be driven by rod hyperpolarisation communicated to cone ON and OFF bipolar cells through gap junctions with surviving cones.

Polarity switching can also occur in rd17 mice, although the data presented in this thesis suggest that it may be less common. As rods in rd17 mostly remain depolarised at high light levels, neither AII hyperpolarisation nor cone driven depolarisation followed by high light level induced hyperpolarisation in rods described by Vlasits *et al.* (2014) seem like likely mechanisms to drive the switch. However, it may be possible for rods in rd17 to hyperpolarise in response to light. There are a small number of rods in rd17 that have abnormal residual light responses at high light levels (Allen *et al.*, 2010, Calvert *et al.*, 2000). In addition, hyperpolarisation of cones could be transmitted to retinal ganglion cells through rod-cone gap junctions (Tsukamoto *et al.*, 2001). Changes in the balance between this hyperpolarisation and depolarisation due to cone-driven sign inverting synapses from horizontal cells could then drive the switching behaviour observed in this study.

Alternatively, the residual polarity switching observed in rd17 mice may be completely independent of rods. Instead, these switches could be due to changes in lateral inhibition that occur as more neighbouring bipolar cells are recruited as stimulus intensity

increases, as hypothesised by Odermatt *et al.* (2012).

It is likely that the switching cells reported here represent the extreme end of a spectrum which cannot be properly investigated using the STA. Changes in the balance of ON and OFF inputs could be occurring in other ganglion cells recorded here, but not sufficiently to change the overall polarity of the STA (as in Geffen *et al.* (2007), Tikidji-Hamburyan *et al.* (2015)). Information about these cells is contained in the recorded spike trains, and could be examined by looking at the distribution of ON and OFF elemenents in the spike triggered stimulus. This will be discussed in more detail in section 5.3.3.

Implications for receptive field analysis of retinal ganglion cells

Many studies (Chichilnisky & Kalmar (2002), Pandarinath *et al.* (2010), Tikidji-Hamburyan *et al.* (2015) are just some examples) have relied on the polarity of the linear filter obtained using the STA to separate cells into ON and OFF classes. However, the results from this study, consistent with Geffen *et al.* (2007), suggest that the polarity of this linear filter is mutable for at least some retinal ganglion cells. Additionally, unlike the cells reported in Geffen *et al.* (2007), the changes shown here are not transient and are therefore not averaged out when an STA is taken from a long period of stimulation. These cells, referred to in this study as "switching cells", represent 28% (2 s.f.) of all cells identified at at least two light levels in C57BL/6 mice.

The linear filter polarity obtained at one experimental light level may not be reflective of the behaviour of the cell in general, and it is therefore probably misleading to use an STA obtained at a single light level to categorically classify cells as ON or OFF. This should be considered both when planning new experiments, and when interpreting previously published data.

5.3.3 Future work

As previously outlined, the polarity switching cells described here are likely to respresent the extreme end of a spectrum of cells in which the balance of ON and OFF inputs varies with ambient light level (similar to those described by Tikidji-Hamburyan *et al.* (2015)).

While these cells cannot be identified using the STA alone, they can be investigated without performing any further experiments. Principal components analysis could be applied to the set of all spike triggered stimuli. In a cell that spikes in response to both ON and OFF stimuli, projection onto the principal components should reveal two clusters - one caused by light increments and one by light decrements in the receptive field. The relative size of these clusters can be used to assess the balance between ON and OFF driven spiking in the ganglion cell - how often a spike was triggered by a light increment compared to a light decrement (Geffen *et al.*, 2007).

Using this method to identify cells in which the balance of ON and OFF inputs changes with light level could help to address some of the power issues with the analysis outlined in this chapter. It is difficult to know whether the decrease in polarity switching cells seen in rd17 (and cpfl1) mice compared to C57BL/6 controls is a real biological difference, or simply due to experimental variation. This is partly because the overall fraction of polarity switching cells in all models is low. If, as Tikidji-Hamburyan *et al.* (2015) report, the majority of cells show changes in ON-OFF balance that do not reach the level of altering STA polarity, then we may have a larger pool of cells in which to observe (or not observe) a meaningful difference in response.

6 Spatial properties of retinal ganglion cells

6.1 Introduction

The principal components analysis outlined in chapter 3 revealed that in addition to response polarity and temporal kinetics, much of the variation in the dataset of all STAs was explained by the shape of the receptive field. Several of the identified principal components had a spatial structure very different from the traditional centre-surround model of retinal ganglion cell receptive fields (PC 4, PC 6, PC 7 and PC 10 in particular). Although variation along these components did not appear to be strongly associated with experimental light level or animal model, they are potentially interesting in the context of retinal computation.

The textbook centre-surround description of the spatial profile of a retinal ganglion cell consists of two concentric rings of opposite sign - an excitatory centre and an inhibitory surround. If the cell is ON-centre, light increments within the central region will drive the cell to spike, while light increments within the surround will inhibit spiking. This results in a preferred stimulus of a bright central circle surrounded by a ring of darkness.

The inhibitory surround enables spatial frequency tuning. In the absence of the in-

hibitory component, our example ON cell would fire in response to any light increments that covered the centre. When the inhibitory component is present, light increments that cover both the centre and the surround (including full field changes in luminance) cause excitation and inhibition to balance, and result in only a transient change in firing. Stimuli with higher spatial frequency, such that light increments can occur in the centre of the receptive field but not in the surround, will preferentially activate the cell (Enroth-Cugell & Robson, 1984). It is worth remembering that many of the spatial frequency filtering properties attributed to the combination of central excitation and lateral inhibition that characterise the centre-surround model could also be achieved using spatially adjacent excitatory and inhibitory sub-fields.

As described in section 1.4.2, many retinal ganglion cell subtypes are not well described by the centre-surround model (Gollisch & Meister, 2010). However, studies which use spatiotemporal Gaussian white noise to measure ganglion cell receptive fields often fit difference of Gaussians (DoG) models to each detected STA as a summary of their spatial characteristics, presupposing a centre-surround structure. In applying this spatial model to all ganglion cells, these studies may be flattening out the spatial diversity in their data and missing functionally important information about the role performed by these cells (Schwartz *et al.*, 2012).

The nature of the spatial processing performed by retinal ganglion cells is not necessarily static. The spatial profiles of cat receptive fields change at different ambient light levels. Using sinusoidal spatial gratings to characterise the receptive field, Troy *et al.* (1993) found that the size of the centre is slightly increased and there is less antagonism between the centre and surround in cat nonlinear Y cells in more scotopic conditions. This change is associated with a shift in the spatial-frequency response function from low-pass at low light levels to high-pass at higher light levels. A companion study (Troy

et al., 1999) revealed a similar shift in spatial frequency tuning in cat linear X cells - the receptive fields behaved as low-pass filters at lower light levels, and higher-pass filters at higher light levels. This was interpreted partly as an increase in the radius of the receptive field centre. Additionally, light level dependent changes in the nature of the spatial integration performed by the retina (described in section 1.5.2) may register as changes in the spatial profile of the STA (Farrow *et al.*, 2013, Grimes *et al.*, 2014, Münch *et al.*, 2009).

In order to investigate variations in the shape of receptive fields using the STA data set, I decomposed the full spatiotemporal STAs into spatial and temporal kernels using singular value decomposition (method outlined in section 2.5, page 78). I then attempted to characterise these spatial kernels both by fitting spatial functions and using Fourier transforms.

6.2 Results

Two dimensional spatial kernels were derived from the smoothed three-dimensional spike triggered average using singular value decomposition. Test statistics were calculated, and statistical significance was assessed with a permutation ANOVA taking into account all five light levels and all three animal models (Basso *et al.*, 2009, Manly, 2007). If this ANOVA revealed a significant main effect or interaction term, relevant permutation post-hoc tests were conducted as described in section 2.6. In the case of a significant interaction term, twenty post-hoc tests were performed, comparing kernels at each light level and each model to the relevant control at each light level. To correct for multiple comparisons, the alpha level used to determine significance was adjusted by Bonferroni correction as described.

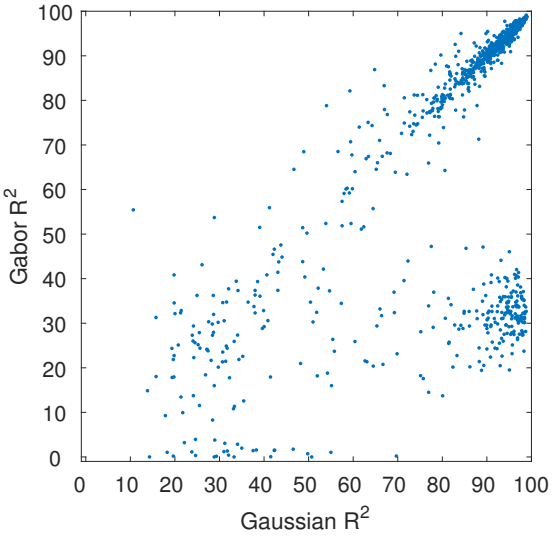

Figure 6.1: **R^2 of both difference of Gaussians and Gabor fits for all spatial STAs:** Spatial STAs were fit with both a difference of Gaussians and a Gabor function, using least-squares minimisation. The R^2 values can be used as a measure of the goodness-of-fit for each model. In this plot, each point represents a single spatial STA from the full data set of 1084 spatial STAs. A small population were poorly fit by both models (lower left quadrant), another population were fit well by difference of Gaussians but poorly by Gabor functions (lower right quadrant), and the majority of the spatial STAs were fit well by both difference of Gaussians and Gabor functions (upper right quadrant).

6.2.1 Characterising the spatial kernels

The majority of spatial kernels are fit well by both difference of Gaussians and Gabor functions

To test the hypothesis that the spatial variation revealed by principal components analysis (described in section 3.3) is due to some ganglion cells with Gabor-like receptive fields, spatial kernels were fit with both Gabor and difference of Gaussians (DoG) functions. Fits were obtained using MATLAB code provided by Kay (2013), using a nonlinear least-squares algorithm. The coefficient of determination (R^2) was calculated as the percentage of the variance in the spatial kernel that is accounted for by the spatial model (Gabor or DoG).

Figure 6.1 shows the R^2 scores for both Gabor and DoG fits for each spatial kernel.

This plot reveals 3 main groups of spatial kernels: those that are not well fit by Gabor or DoG functions, those that are well fit by DoG but not Gabor functions, and those that are fit well by both DoG and Gabor functions. The majority of spatial kernels are in this latter group - 66% (2 s.f.) have both a Gaussian and a Gabor R^2 larger that 70%.

Some examples of both DoG and Gabor fits are shown in figure 6.2. Spatial kernels with a more Gabor-like profile are matched more closely by Gabors than by DoGs, and those with very Gaussian profiles are not fit well by the Gabor model. However, these exampes also demonstrate that the Gabor model can produce a fit very similar to the DoG model, and vice versa. In order to differentiate the features of the spatial kernels, another method must be used.

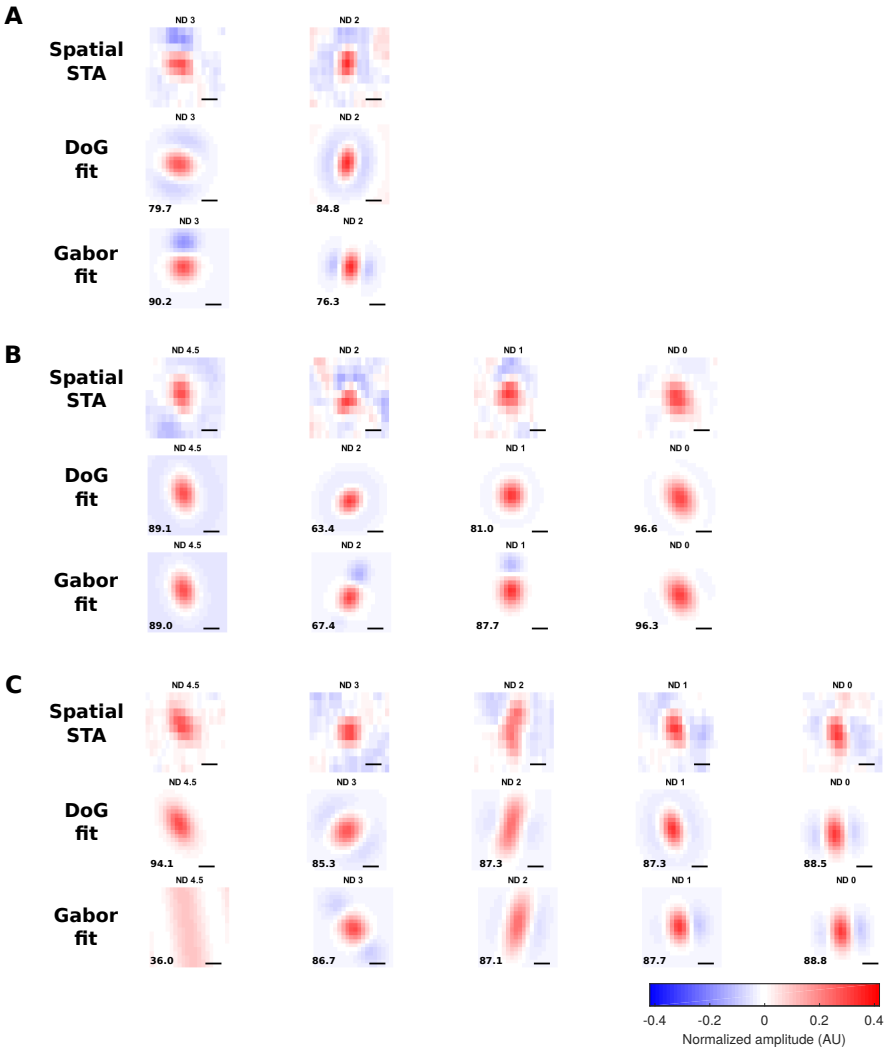

Figure 6.2: **Examples of difference of Gaussians and Gabor fits for spatial STAs:** (**A**-**B**) depict spatial STAs from three example cells at all light levels where a significant STA was identified for that cell, with both difference of Gaussian and Gabor fits. The R^2 measure of error is printed in the bottom left corner of each fit. In particular, (**C**) shows that very similar spatial fits can be obtained using both difference of Gaussians or Gabor functions, including for spatial STAs that have some spatial asymmetry. All three example cells are from recordings from C57BL/6 mice. The colour map scale is set so that the maximum pixel value for all spatial STAs is set as the maximum possible positive (red) or negative (blue) value. Scalebar = 200μm.

The two-dimensional Fourier transform can be used to characterise spatial kernels

The features of any spatial function can be described by the two dimensional Fourier transform of that function. In the context of a spatial receptive field, the two-dimensional Fourier transform can reveal the nature of the spatial filter performed by the retinal circuit.

Figure 6.3 shows the two dimensional Fourier transform of some common spatial functions. For easier visualisation and quantification, the Fourier transform itself can be broken down into two components: the spatial frequency and the orientation. The one dimensional summary of spatial frequency was calculated as the mean of the relative sensitivity of the 2D Fourier transform within a ring around 0 cycles per pixel with an expanding radius. The one dimensional summary of orientation was calculated as the maximum relative sensitivity value within a radial segment extending from the centre (0,0) of the two dimensional Fourier transform to the edge. Radians were measured clockwise from (-0.5,0) cycles per pixel.

The Fourier transform of a Gaussian is a Gaussian (Jones & Palmer, 1987). When split into spatial frequency and orientation components, the spatial frequency plot will have a peak at zero cycles per pixel (the DC frequency), and the orientation plot will be flat. When applied to a DoG function, the Fourier transform reveals a combination of the Gaussian filter with an additional bandpass component surrounding it. For gratings and Gabors the transform is asymmetric, reflecting the spatial orientation of the original function, and the peak of the spatial frequency shifts from zero cycles per pixel, reflecting the bandpass nature of these spatial functions.

Figures 6.4 - 6.7 show some examples of two dimensional Fourier transforms of ganglion

cell spatial kernels obtained from the dataset of STAs. Figure 6.4 is a kernel with an elliptical Gaussian profile, with a roughly Gaussian Fourier transform. The peak of the spatial frequency is at (0,0) cycles per pixel, and the rotational symmetry plot is relatively flat. Figure 6.5 shows another spatial kernel which appears visually very similar to the centre-surround model. The Fourier transform reveals a bandpass filter, with a structure more similar to a sum of several gratings than to a difference of Gaussians (figure 6.3). The bandpass nature of this kernel is clear in the one dimensional summary of spatial frequency tuning, and the plot of rotational symmetry is relatively flat. Figures 6.6 and 6.7 are both spatial kernels with Gabor-like features. The Fourier transforms reveal bandpass filters with an orientation. These features are apparent in the shifted peak in the one dimensional plots of spatial frequency, and the peaks and troughs in the one dimensional plots of rotational symmetry.

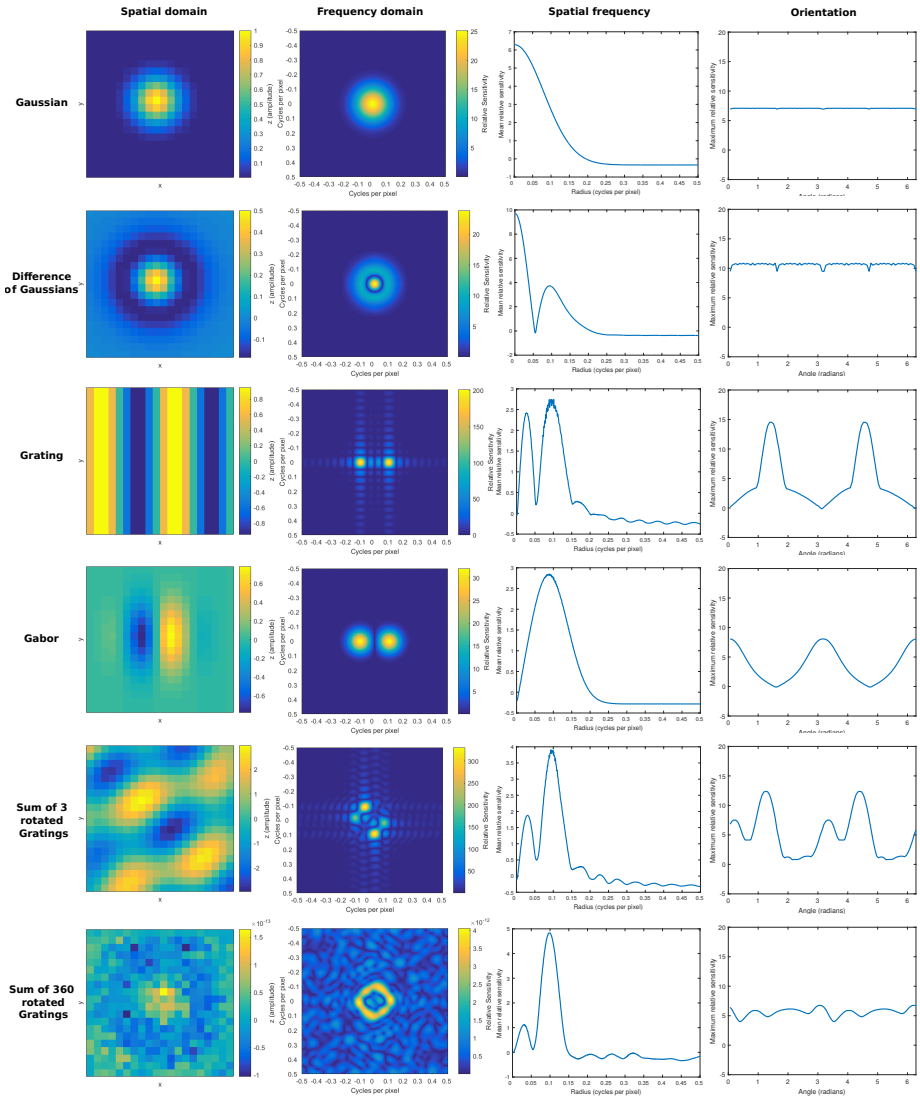

Figure 6.3: **Examples of two-dimensional Fourier transforms of common functions:** The Fourier transform can be used to characterise two dimensional spatial functions. The first column shows some common functions plotted in the spatial domain - the amplitude z is a function of the two Cartesian coordinates x and y. The second column shows the same functions in the frequency domain - relative sensitivity is a function of spatial frequency (the radial axis expanding from 0 cycles per pixel) and orientation (the angular axis encircling 0 cycles per pixel). Spatial frequency and orientation of the function in the frequency domain can be separated. The third column shows plots of spatial frequency for each function, calculated as the mean of the relative sensitivity within a ring around 0 cycles per pixel with an expanding radius. Finally, the fourth column shows plots characterising the orientation of each spatial function. This is calculated as the maximum relative sensitivity value within a radial segment extending from the centre (0,0) of the two dimensional Fourier transform to the edge. Radians are measured clockwise from (-0.5,0) cycles per pixel. Due to the discrete, pixellated nature of the Fourier transforms use, no example has perfect rotational symmetry.

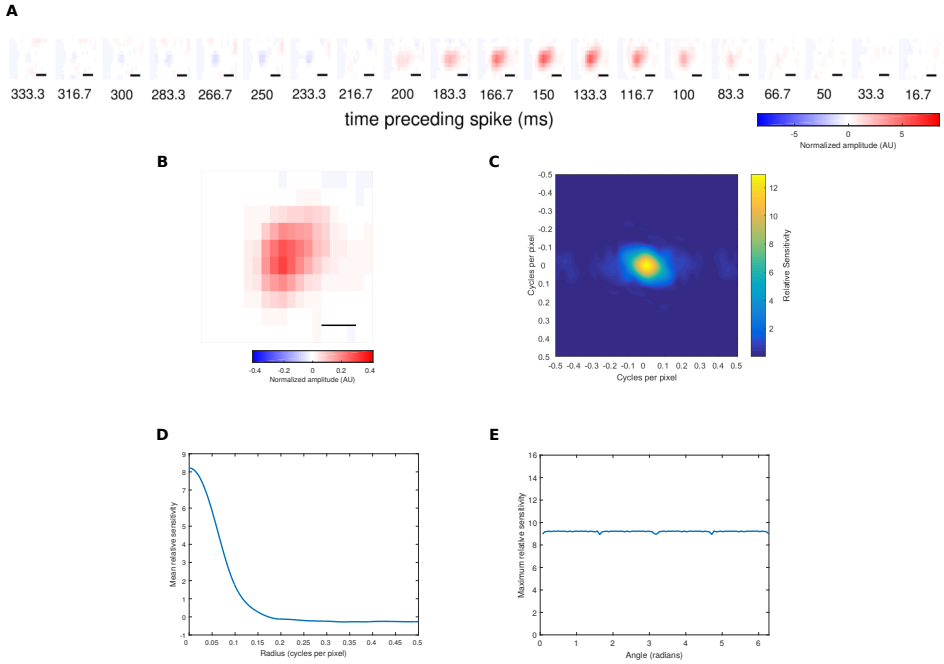

Figure 6.4: **Example of a STA with a Gaussian-like spatial profile:** Characterisation of the spatial features of a STA that has a Gaussian-like profile. (**A**) The last twenty frames of the spatiotemporal STA. This STA has been smoothed used a 3x3x3 pixel box filter. Colour map scale is set such that the largest pixel value of all STAs is set as the maximum possible positive (red) or negative (blue) value. Scalebar = 200μm across. (**B**) The spatial component of the smoothed spatiotemporal STA, obtained through single value decomposition. The colour map scale is set so that the maximum pixel value for all spatial STAs is set as the maximum possible positive (red) or negative (blue) value. Scalebar = 200μm. (**C**) The 2-dimensional Fourier transform of **B**. (**D**) Spatial frequency of the Fourier transform, calculated as the mean of the relative sensitivity within a ring around 0 cycles per pixel with an expanding radius. (**E**) Rotational symmetry of the Fourier transform, calculated as the maximum relative sensitivity value within a radial segment extending from the centre (0,0) of the two dimensional Fourier transform to the edge. Radians are measured clockwise from (-0.5,0) cycles per pixel.

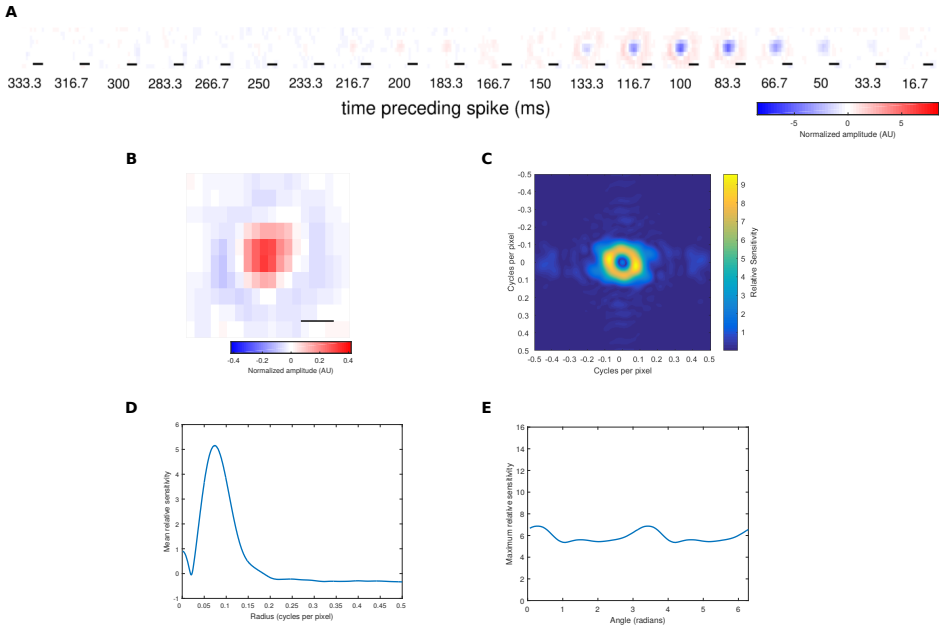

Figure 6.5: **Example of an STA with a centre-surround spatial profile:** Characterisation of the spatial features of a STA that has a centre-surround profile. (**A**) The last twenty frames of the spatiotemporal STA. This STA has been smoothed used a 3x3x3 pixel box filter. Colour map scale is set such that the largest pixel value of all STAs is set as the maximum possible positive (red) or negative (blue) value. Scalebar = 200μm across. (**B**) The spatial component of the smoothed spatiotemporal STA, obtained through single value decomposition. The colour map scale is set so that the maximum pixel value for all spatial STAs is set as the maximum possible positive (red) or negative (blue) value. Scalebar = 200μm. (**C**) The 2-dimensional Fourier transform of **B**. (**D**) Spatial frequency of the Fourier transform, calculated as the mean of the relative sensitivity within a ring around 0 cycles per pixel with an expanding radius. (**E**) Rotational symmetry of the Fourier transform, calculated as the maximum relative sensitivity value within a radial segment extending from the centre (0,0) of the two dimensional Fourier transform to the edge. Radians are measured clockwise from (-0.5,0) cycles per pixel.

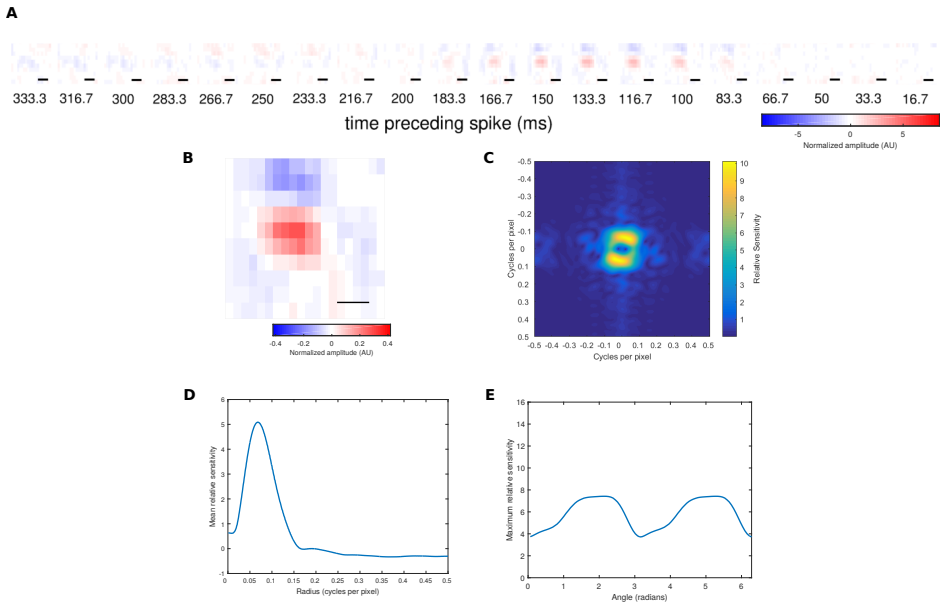

Figure 6.6: **Example of an STA with a Gabor-like spatial profile:** Characterisation of the spatial features of a STA that has a Gabor-like profile. (**A**) The last twenty frames of the spatiotemporal STA. This STA has been smoothed used a 3x3x3 pixel box filter. Colour map scale is set such that the largest pixel value of all STAs is set as the maximum possible positive (red) or negative (blue) value. Scalebar = 200μm across. (**B**) The spatial component of the smoothed spatiotemporal STA, obtained through single value decomposition. The colour map scale is set so that the maximum pixel value for all spatial STAs is set as the maximum possible positive (red) or negative (blue) value. Scalebar = 200μm. (**C**) The 2-dimensional Fourier transform of **B**. (**D**) Spatial frequency of the Fourier transform, calculated as the mean of the relative sensitivity within a ring around 0 cycles per pixel with an expanding radius. (**E**) Rotational symmetry of the Fourier transform, calculated as the maximum relative sensitivity value within a radial segment extending from the centre (0,0) of the two dimensional Fourier transform to the edge. Radians are measured clockwise from (-0.5,0) cycles per pixel.

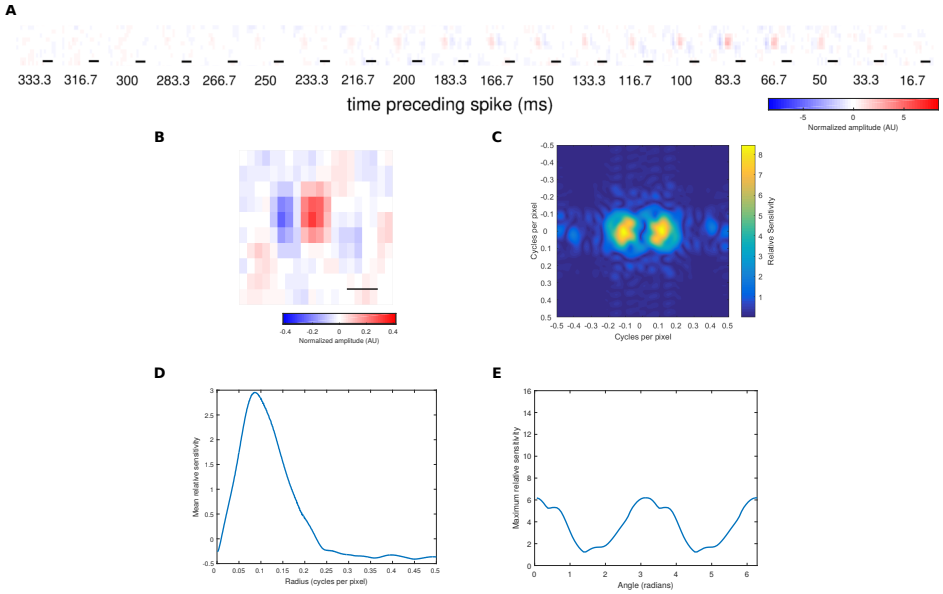

Figure 6.7: **Example of an STA with a Gabor-like spatial profile:** Characterisation of the spatial features of a STA that has a Gabor-like profile. (**A**) The last twenty frames of the spatiotemporal STA. This STA has been smoothed used a 3x3x3 pixel box filter. Colour map scale is set such that the largest pixel value of all STAs is set as the maximum possible positive (red) or negative (blue) value. Scalebar = 200μm across. (**B**) The spatial component of the smoothed spatiotemporal STA, obtained through single value decomposition. The colour map scale is set so that the maximum pixel value for all spatial STAs is set as the maximum possible positive (red) or negative (blue) value. Scalebar = 200μm. (**C**) The 2-dimensional Fourier transform of **B**. (**D**) Spatial frequency of the Fourier transform, calculated as the mean of the relative sensitivity within a ring around 0 cycles per pixel with an expanding radius. (**E**) Rotational symmetry of the Fourier transform, calculated as the maximum relative sensitivity value within a radial segment extending from the centre (0,0) of the two dimensional Fourier transform to the edge. Radians are measured clockwise from (-0.5,0) cycles per pixel.

6.2.2 Peak spatial frequency

The peak spatial frequency of each spatial kernel was defined as the location of the peak of the one dimensional summary of the spatial frequency. A 100,000 repeat permutation ANOVA (Basso *et al.*, 2009, Manly, 2007) comparing means revealed a significant interaction between animal model and light level for this measure ($p < 0.01$). Permutation post-hoc tests were then performed and corrected for multiple comparisons as described. Mean and standard deviation are reported to three decimal places.

Peak spatial frequency is lower at ND 4.5 than at higher light levels in C57BL/6 mice

Figure 6.8 shows the distribution of peak spatial frequency for spatial kernels obtained from C57BL/6 mice across all experimental light levels. The mean peak spatial frequency is lower at ND 4.5 than at all other light levels: the mean ($\pm$ standard deviation) peak spatial frequency in cycles per pixel is 0.034 ($\pm$ 0.028) at ND 4.5, 0.046 ($\pm$ 0.024) at ND 3, 0.048 ($\pm$ 0.025) at ND 2, 0.037 ($\pm$ 0.029) at ND 1, and 0.043 ($\pm$ 0.026) at ND 0.

Permutation post-hoc tests on relevant comparisons revealed that the difference in means is significant between ND 4.5 and ND 3 ($p < 0.0001$, with a Cliff's delta effect size of -0.238 (3 d.p.)) and between ND 4.5 and ND 2 ($p < 0.0001$, with a Cliff's delta of -0.272 (3 d.p.)).

The difference in means between ND 4.5 and ND 1 and 0 do not pass the significance threshold ($p > 0.0025$ - the Bonferroni correction for alpha = 0.05). This means that the null hypothesis that the kernels within the groups are exchangeable on the basis of peak spatial frequency cannot be rejected.

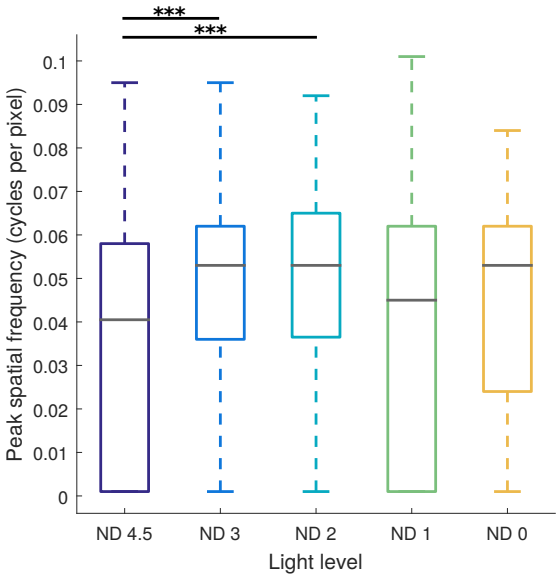

Figure 6.8: **Peak spatial frequency in C57BL/6 mice across light levels:** Box plot of peak spatial frequency in C57BL/6 mice across all five experimental light levels, showing that peak spatial frequency at ND 4.5 is lower than at ND 3 and ND 2. Boxes show medians and first and third quartiles, whiskers are 1.5 times the interquartile range. Data points beyond this are represented as outliers. Stars represent p-values of difference in means between groups. These were calculated from permutation post-hoc tests following permutation ANOVA on the full dataset which revealed a significant interaction between animal model and light level ($p < 0.01$). *** = $p < 0.0001$, ** = $p < 0.001$, * = $p < 0.0025$ (Bonferroni correction for alpha = 0.05). n = 8 C57BL/6 mice, with 96 kernels at ND 4.5, 120 at ND 3, 128 at ND 2, 74 at ND 1, and 94 at ND 0.

Peak spatial frequency is lower at the highest light level in rd17 compared to C57BL/6 mice

Figure 6.9 shows the distribution of peak spatial frequency for spatial kernels from C57BL/6 and rd17 mice across all experimental light levels. At ND 0, the highest light level, the mean (± standard deviation) peak spatial frequency in cycles per pixel is 0.043 (± 0.026) in C57BL/6 mice compared to 0.029 (± 0.025) in rd17 mice. The Cliff's delta effect size for this decrease is 0.345 (3 d.p.), and permutation post-hoc tests show that this difference in means at ND 0 is statistically significant ($p < 0.0025$ - the Bonferroni correction for alpha = 0.05).

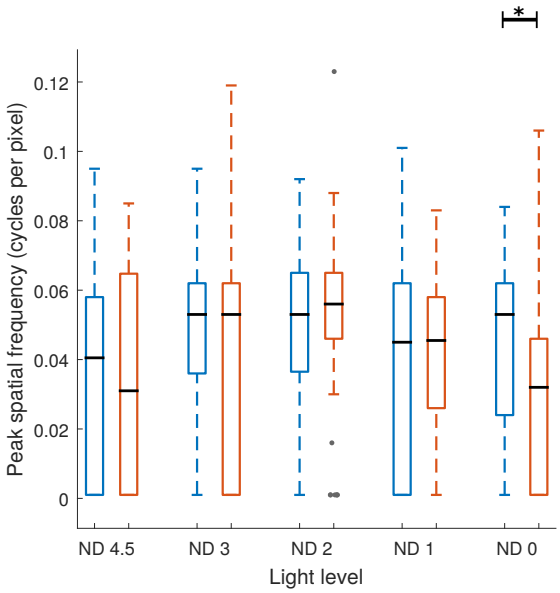

Figure 6.9: **Peak spatial frequency C57BL/6 versus rd17:** Box plot of peak spatial frequency in C57BL/6 and rd17 mice across all five experimental light levels, showing a that peak spatial frequency tends to be lower in rd17 mice at ND 0 compared to C57BL/6 mice. Boxes show medians and first and third quartiles, whiskers are 1.5 times the interquartile range. Data points beyond this are represented as outliers. Stars represent p-values of difference in means between groups. These were calculated from permutation post-hoc tests following a permutation ANOVA on the full dataset which revealed a significant interaction between animal model and light level ($p < 0.01$). *** = $p < 0.0001$, ** = $p < 0.001$, * = $p < 0.0025$ (Bonferroni correction for alpha = 0.05). C57BL/6: n = 8 mice, with 96 kernels at ND 4.5, 120 at ND 3, 128 at ND 2, 74 at ND 1, and 94 at ND 0. rd17 n = 8 mice, with 9 kernels at ND 4.5, 49 at ND 3, 80 at ND 2, 84 at ND 1, and 55 at ND 0.

Spatial kernels from cpfl1 and C57BL/6 mice may be exchangeable with respect to peak spatial frequency

Figure 6.10 shows the distribution of peak spatial frequency for spatial kernels from C57BL/6 and cpfl1 mice across all experimental light levels. Permutation post-hoc tests show that for all comparisons of means between cpfl1 and C57BL/6 mice at each light level $p > 0.0025$ (the Bonferroni correction for alpha = 0.05). The null hypothesis - that spatial kernels from cpfl1 mice are exchangeable with those from C57BL/6 mice within each light level when it comes to peak spatial frequency - cannot be rejected.

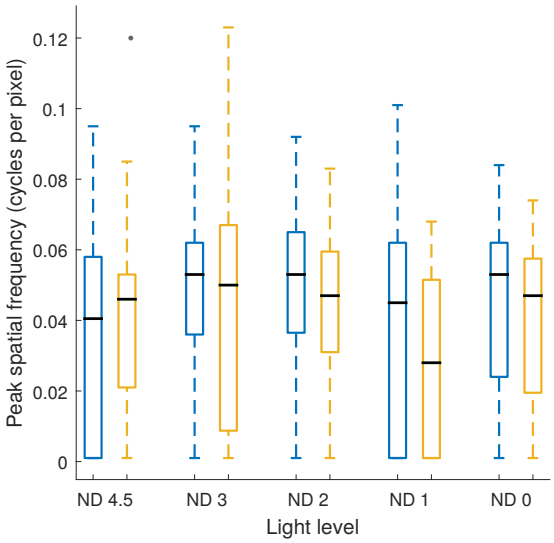

Figure 6.10: **Peak spatial frequency C57BL/6 versus cpfl1:** Box plot of peak spatial frequency in C57BL/6 and cpfl1 mice across all five experimental light levels. Boxes show medians and first and third quartiles, whiskers are 1.5 times the interquartile range. Data points beyond this are represented as outliers. Stars represent p-values of difference in means between groups. These were calculated from permutation post-hoc tests following a permutation ANOVA on the full dataset which revealed a significant interaction between animal model and light level ($p < 0.01$). *** = $p < 0.0001$, ** = $p < 0.001$, * = $p < 0.0025$ (Bonferroni correction for alpha = 0.05). C57BL/6: n = 8 mice, with 96 kernels at ND 4.5, 120 at ND 3, 128 at ND 2, 74 at ND 1, and 94 at ND 0. cpfl1: n = 8 mice, with 82 kernels at ND 4.5, 105 at ND 3, 51 at ND 2, 41 at ND 1, and 16 at ND 0.

6.2.3 Rotational symmetry

The rotational symmetry of each spatial kernel was quantified using a symmetry index - defined as the ratio between the trough and the peak of the one dimensional summary of orientation. A 100,000 repeat permutation ANOVA (Basso *et al.*, 2009, Manly, 2007) revealed a significant interaction between animal model and light level for this measure ($p < 0.0001$). Permutation post-hoc tests were then performed and corrected for multiple comparisons as described. Mean and standard deviations are reported to three decimal places.

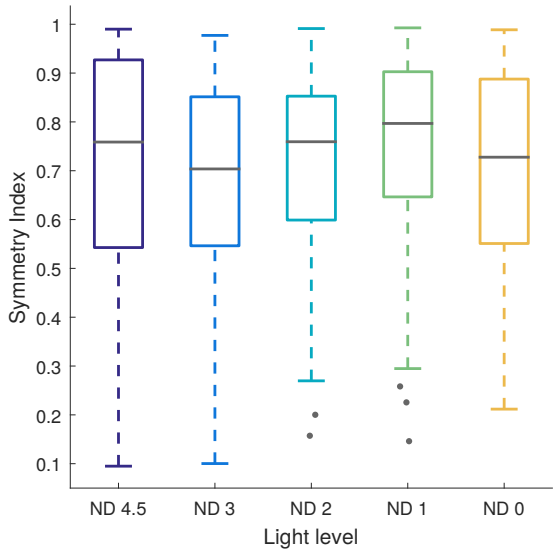

Figure 6.11: **Rotational symmetry in C57BL/6 mice across light levels:** Box plot of rotational symmetry in C57BL/6 mice across all five experimental light levels. Rotational symmetry is quantified as a symmetry index - the ratio between the trough and the peak of the one dimensional orientation plot obtained from the two dimensional Fourier transform. The more symmetric the Fourier transform, the closer to 1 the symmetry index will be. Boxes show medians and first and third quartiles, whiskers are 1.5 times the interquartile range. Data points beyond this are represented as outliers. Stars represent p-values of difference in means between groups. These were calculated from permutation post-hoc tests following permutation ANOVA on the full dataset which revealed a significant interaction between animal model and light level ($p < 0.0001$). However, the null hypothesis of exchangeability between groups could not be rejected for any of the relevant comparisons. *** = $p < 0.0001$, ** = $p < 0.001$, * = $p < 0.0025$ (Bonferroni correction for alpha = 0.05). n = 8 C57BL/6 mice, with 96 kernels at ND 4.5, 120 at ND 3, 128 at ND 2, 74 at ND 1, and 94 at ND 0.

Spatial kernels may be exchangeable with respect to rotational symmetry across light levels and animal models

Figures 6.11 - 6.13 show the distribution of symmetry index across experimental light level and animal model. Although the initial permutation ANOVA revealed a significant interaction between animal model and light level, none of the twenty relevant comparisons reach significance ($p > 0.0025$ (the Bonferroni correction for alpha = 0.05) for all). The interaction term may be due to differences between cpfl1 and rd17 at different light levels, or to differences within one of the models across light level (in rd17 mice, for example, the small number of kernels identified at ND 4.5 are distributed towards

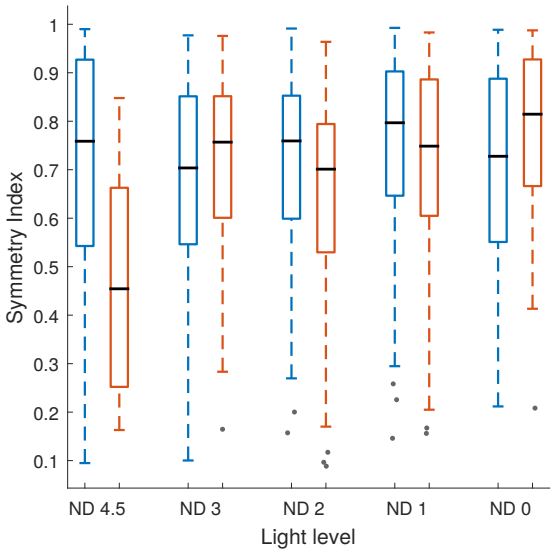

Figure 6.12: **Rotational symmetry C57BL/6 versus rd17:** Box plot of rotational symmetry in C57BL/6 and rd17 mice across all five experimental light levels. Rotational symmetry is quantified as a symmetry index - the ratio between the trough and the peak of the one dimensional orientation plot obtained from the two dimensional Fourier transform. The more symmetric the Fourier transform, the closer to 1 the symmetry index will be. Boxes show medians and first and third quartiles, whiskers are 1.5 times the interquartile range. Data points beyond this are represented as outliers. Stars represent p-values of difference in means between groups. These were calculated from permutation post-hoc tests following a permutation ANOVA on the full dataset which revealed a significant interaction between animal model and light level ($p < 0.0001$). However, the null hypothesis of exchangeability between groups could not be rejected for any of the relevant comparisons. *** = $p < 0.0001$, ** = $p < 0.001$, * = $p < 0.0025$ (Bonferroni correction for alpha = 0.05). C57BL/6: n = 8 mice, with 96 kernels at ND 4.5, 120 at ND 3, 128 at ND 2, 74 at ND 1, and 94 at ND 0. rd17 n = 8 mice, with 9 kernels at ND 4.5, 49 at ND 3, 80 at ND 2, 84 at ND 1, and 55 at ND 0.

the lower end of the symmetry index). Comparisons between cpfl1 and rd17, rather than to C57BL/6, are not necessarily particularly useful, as the levels of degeneration in the two models are so different.

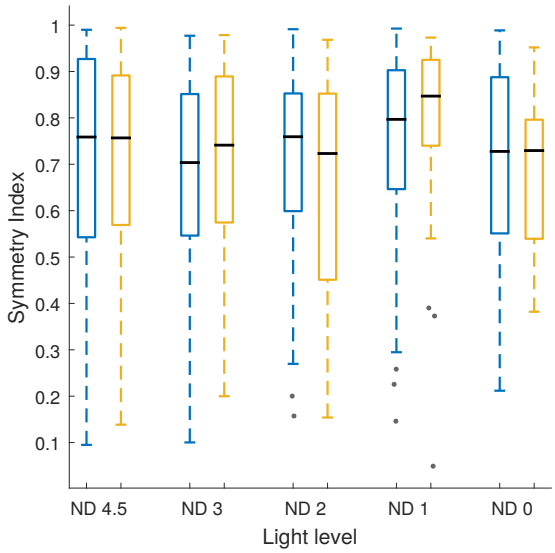

Figure 6.13: **Rotational symmetry C57BL/6 versus cpfl1:** Box plot of rotational symmetry in C57BL/6 and cpfl1 mice across all five experimental light levels. Rotational symmetry is quantified as a symmetry index - the ratio between the trough and the peak of the one dimensional orientation plot obtained from the two dimensional Fourier transform. The more symmetric the Fourier transform, the closer to 1 the symmetry index will be. Boxes show medians and first and third quartiles, whiskers are 1.5 times the interquartile range. Data points beyond this are represented as outliers. Stars represent p-values of difference in means between groups. These were calculated from permutation post-hoc tests following a permutation ANOVA on the full dataset which revealed a significant interaction between animal model and light level ($p < 0.0001$). However, the null hypothesis of exchangeability between groups could not be rejected for any of the relevant comparisons. *** = $p < 0.0001$, ** = $p < 0.001$, * = $p < 0.0025$ (Bonferroni correction for alpha = 0.05). C57BL/6: n = 8 mice, with 96 kernels at ND 4.5, 120 at ND 3, 128 at ND 2, 74 at ND 1, and 94 at ND 0. cpfl1: n = 8 mice, with 82 kernels at ND 4.5, 105 at ND 3, 51 at ND 2, 41 at ND 1, and 16 at ND 0.

6.2.4 Instability of spatial kernels

Spatial kernels are not always stable across light levels

Visual inspection of both spatiotemporal receptive fields and spatial kernels reveals that some cells have very different receptive field shapes (at least in terms of the average stimulus preceding a spike) at different light levels. Examples of this can be seen in figure 6.2. The extent of the difference between spatial kernels at different light levels can be quantified as the absolute difference between the one dimensional summary plots of spatial frequency obtained at the different light levels.

Figure 6.14 shows the mean change in spatial frequency between each pair of experimental light levels in C57BL/6, rd17, and cpfl1 mice (n = 8 mice for each animal model). In C57BL/6 mice, changes are largest between ND 4.5 and the higher light levels. A similar pattern is seen in cpfl1 mice, with the exception of kernels at ND 4.5 compared to the small number of kernels from cells that still have significant responses at ND 0 in this group. In the case of rd17 mice, none of the 9 cells with significant responses at ND 4.5 have significant responses at another light level. The largest changes in rd17 spatial kernels are observed between ND 0, the highest experimental light level, and the lower light levels where significant responses are reliably detected (particularly ND 3).

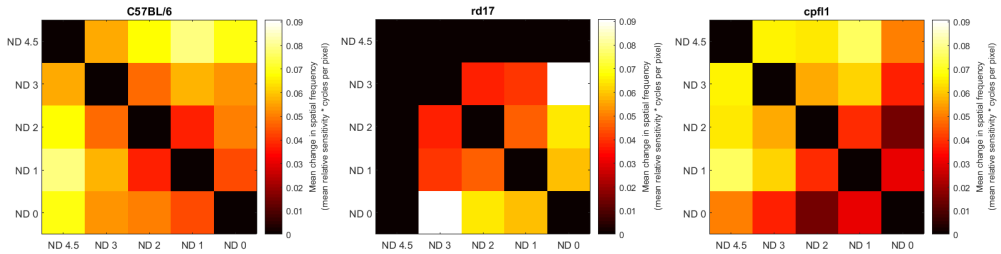

Figure 6.14: **Mean change in spatial frequency between each light level:** Matrices show the mean change in spatial frequency between each pair of light levels. Mean change in spatial frequency was calculated as the mean absolute difference between spatial frequency curves at each pair of light levels.

Cells which switch polarity between ON and OFF also exhibit larger differences in spatial frequency tuning across light levels

The heat map plots of changes in spatial kernels (figure 6.14) appear superficially similar to those depicting polarity switching (outlined in chapter 5, figure 5.6). In order to test the hypothesis that cells which change their STA polarity with light level are also more likely to exhibit changes in the shape of their receptive fields, the mean absolute difference between spatial frequency curves at all light levels was compared between switching and non switching cells for each animal model. Figures 6.15 - 6.17 show the

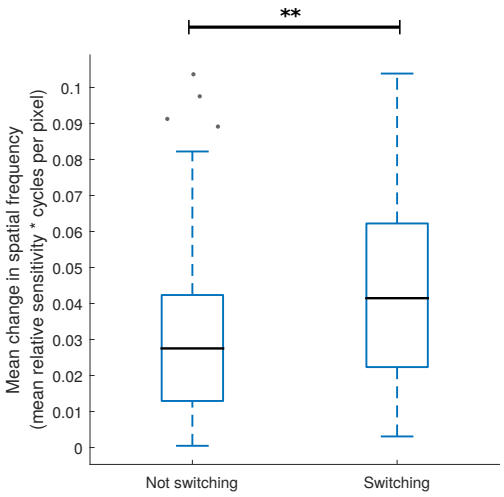

Figure 6.15: **Mean change in spatial frequency in C57BL/6 switching versus non switching cells:** Box plot of mean change in spatial frequency (calculated as the mean absolute difference between spatial freqency curves at all light levels) for cells from C57BL/6 mice which do or do not switch polarity between ON and OFF. The plot shows that switching cells are more likely to have larger differences in spatial frequency tuning across light levels compared to non switching cells. Boxes show medians and first and third quartiles, whiskers are 1.5 times the interquartile range. Data points beyond this are represented as outliers. Stars represent p-values of difference in means between groups. These were calculated from permutation post-hoc tests following a permutation ANOVA on the full dataset which revealed a significant difference between switching and non-switching cells ($p < 0.01$). *** = $p < 0.0001$, ** = $p < 0.001$, * = $p < 0.017$ (Bonferroni correction for alpha = 0.05). n = 142 C57BL/6 cells, 102 non-switching and 40 switching.

distributions of this metric for the two different groups of cells.

The mean ($\pm$ standard deviation) is higher for switching compared to non switching cells in all three animal models. In C57BL/6 mice, non switching cells have a mean spatial frequency change of 0.031 ($\pm$ 0.023), compared to 0.043 ($\pm$ 0.027) for switching cells (Cliff's delta = -0.266). In rd17 mice, non switching cells have a mean spatial frequency change of 0.030 ($\pm$ 0.024), compared to 0.059 ($\pm$ 0.026) for switching cells (Cliff's delta = -0.685). Finally, in cpfl1 mice, non switching cells have a mean spatial frequency change of 0.032 ($\pm$ 0.029), compared to 0.053 ($\pm$ 0.037) for switching cells (Cliff's delta = -0.402). The units of the index of change in spatial frequency are mean relative sensitivity $*$ cycles per pixel. All figures are reported to 3 decimal places.

A permutation ANOVA on the full data set revealed a significant difference in means

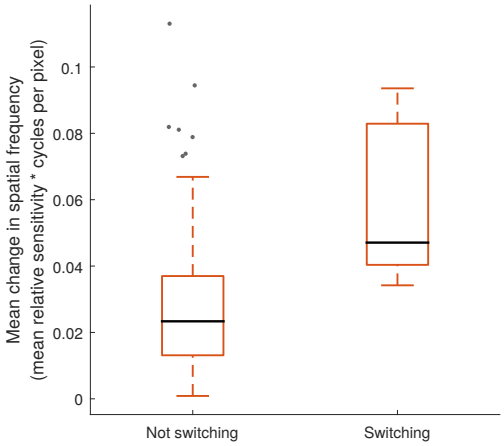

Figure 6.16: **Mean change in spatial frequency in rd17 switching versus non switching cells:** Box plot of mean change in spatial frequency (calculated as the mean absolute difference between spatial freqency curves at all light levels) for cells from rd17 mice which do or do not switch polarity between ON and OFF. The plot shows that switching cells are more likely to have larger differences in spatial frequency tuning across light levels compared to non switching cells. Boxes show medians and first and third quartiles, whiskers are 1.5 times the interquartile range. Data points beyond this are represented as outliers. Stars represent p-values of difference in means between groups. These were calculated from permutation post-hoc tests following a permutation ANOVA on the full dataset which revealed a significant difference between switching and non-switching cells ($p < 0.01$). *** = $p < 0.0001$, ** = $p < 0.001$, * = $p < 0.017$ (Bonferroni correction for alpha = 0.05). n = 76 rd17 cells, 71 non-switching and 5 switching.

between switching and non switching cells ($p < 0.01$). Permutation post hoc tests comparing the two groups of cells within each animal model show that the significance holds in C57BL/6 ($p < 0.001$) and cpfl1 ($p < 0.0001$) mice. In rd17 mice the null hypothesis that switching and non switching cells are exchangeable when it comes to mean change in spatial frequency cannot be rejected. This may be due to the very small sample size of switching cells - as outlined in chapter 5, only 5 cells from rd17 mice were identified as switching polarity.

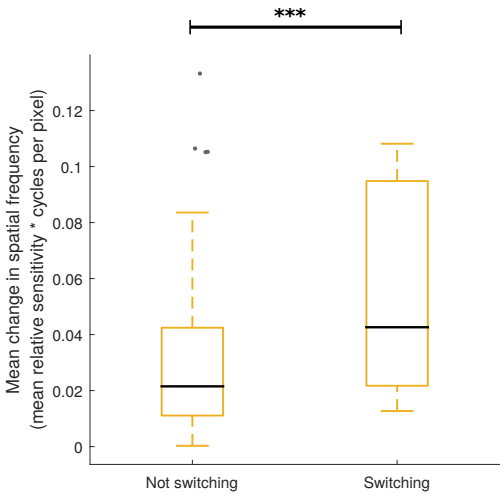

Figure 6.17: **Mean change in spatial frequency in cpfl1 switching versus non switching cells:** Box plot of mean change in spatial frequency (calculated as the mean absolute difference between spatial freqency curves at all light levels) for cells from cpfl1 mice which do or do not switch polarity between ON and OFF. The plot shows that switching cells are more likely to have larger differences in spatial frequency tuning across light levels compared to non switching cells. Boxes show medians and first and third quartiles, whiskers are 1.5 times the interquartile range. Data points beyond this are represented as outliers. Stars represent p-values of difference in means between groups. These were calculated from permutation post-hoc tests following a permutation ANOVA on the full dataset which revealed a significant difference between switching and non-switching cells ($p < 0.01$). *** = $p < 0.0001$, ** = $p < 0.001$, * = $p < 0.017$ (Bonferroni correction for alpha = 0.05). n = 76 cpfl1 cells, 63 non-switching and 13 switching.

6.3 Discussion

6.3.1 Spatial diversity in retinal ganglion cell receptive fields

As demonstrated by principal components analysis (chapter 3), there was variation in the shape of the spatial kernels obtained from the data set of all STAs.

Figures 6.6 and 6.7 are representative of some of the receptive fields identified in this study that do not have a clear centre-surround structure. These STAs have spatially bipolar profiles very similar to PC 4, 6, 7 and PC 10: there are two adjacent lobes of a similar size and with opposite polarity, and neither is easily identified as central to or surrounding the other. Piscopo *et al.* (2013) have described cells with similar STAs in

the mouse lateral geniculate nucleus (LGN). They recorded from 28 cells which exhibited direction or orientation tuning. Of these, two are described as having "adjacent On and Off regions". Cheong *et al.* (2013) describe similar shaped orientation biased receptive fields belonging to K-o cells in the marmoset LGN.

The direction selective retinal ganglion cells identified by Kim *et al.* (2008) may be the source of these distinctive receptive fields, both in this study and in the LGN recordings reported by Piscopo *et al.* (2013). These cells, identified by their expression of junctional adhesion molecule B (JAM-B), have asymmetric dendritic arbors aligned dorso-ventrally and respond when stimuli move in a soma-to-dendrite direction. When the STA of these cells is calculated using a two dimensional white noise stimulus of flickering linear bars, a spatially bipolar profile with two regions of opposite sign can be observed (figure 3b in Kim *et al.* (2008)). These cells project primarily to the superior colliculus, but some were also observed projecting to the dorsal LGN.

It should be noted that JAM-B cells are unusual for direction selective retinal ganglion cells. The majority of the direction or orientation tuned population identified by Piscopo *et al.* (2013) did not have a significant STA at all (presumably due to the non-linearity of the direction selective function), and many that did had an approximately circular spatial kernel. A bipolar spatial profile is therefore not a requirement for either orientation or direction selectivity in retinal ganglion cells or upstream neurons.

However, recently Venkataramani & Taylor (2016) have described a population of orientation selective retinal ganglion cells in the rabbit with similar features to those described here and by Piscopo *et al.* (2013). These are ON rather than OFF cells, but have a receptive field structure consisting of two or more adjacent subunits of opposite sign (figure 2.C and 2.D).

The superficial similarity between these spatially bipolar kernels and simple cells in

the visual cortex is hard to ignore. Simple cells have alternating ON and OFF regions in their receptive fields, and display both orientation and spatial frequency tuning. They are often modelled using Gabor filters - a family of linear filters that maximise resolution in both the frequency and the spatial domain (Jones & Palmer, 1987).

Initially, in an attempt to distinguish spatially bipolar from centre-surround kernels, I fit all kernels with both DoG and Gabor models (figure 6.2). However, the majority were fit well by both spatial models, and this approach seemed limited. Instead, I used the two dimensional Fourier transform to characterise the spatial kernels (figure 6.3). This transformation captures both the spatial frequency and orientation tuning of Gabor functions and simple cells (Jones & Palmer, 1987), and can be used to quantify those features.

6.3.2 Ambient light level can alter receptive field shape

In C57BL/6 mice, the mean peak spatial frequency was approximately 30% lower at the lowest light level compared to higher light levels (figure 6.8). That is, STAs at ND 4.5 tended to be more low-pass for spatial frequency compared to those at ND 3 and ND 2. This shift in spatial frequency tuning with light level is consistent with findings in the cat for both X and Y cells reported by Troy *et al.* (1993, 1999). This shift has been interpreted in the context of the centre-surround model as representing changes in surround antagonism with light level. In more scotopic conditions the surround is weaker relative to the centre, making the spatial profile similar to a simple Gaussian, which behaves as a low-pass spatial filter. At higher light levels, antagonism from the surround is stronger, and so the receptive field has a band-pass component that effectively tunes it to higher spatial frequencies (Huang & Protti, 2016).

The cell depicted in figure 6.2.C follows this pattern - the surround components of the

receptive field were weaker at ND 4.5 and became more apparent at higher light levels. This cell also had an asymmetric receptive field that appeared to have other spatial instabilities across light levels.

However, many of the cells recorded in this study did not display this pattern of behaviour (including the other two example cells in figure 6.2). The range of peak spatial frequencies was similar across light levels, and the difference in means was not statistically significant between ND 4.5 and the two highest light levels. Additionally, the effect sizes of the significant differences were not large (Cliff's delta is -0.238 for ND 4.5 compared to ND 3, and -0.272 for ND 4.5 compared to ND 3 (3 d.p.)). Overall, the observed shift in spatial frequency tuning is unlikely to be a retina-wide phenomenon affecting every ganglion cell.

PV-1 and PV-6 retinal ganglion cells in the mouse have been demonstrated to change the weighting of their centre and surround at cone threshold (Farrow *et al.*, 2013), resulting in a change in spatial processing. As outlined in section 1.5.2 this is driven by an amacrine cell - cone bipolar cell switch similar to the one that underlies changes which enable other cells to become nonlinear integrators sensitive to fine spatial detail at higher light levels (Grimes *et al.*, 2014). The population trend observed in this study and by (Troy *et al.*, 1993, 1999), could be due to processing changes in these spatial switching cells.

The mean rotational symmetry of the two dimensional Fourier transform was similar across all experimental light levels. This suggests that spatially asymmetric receptive fields - such as the spatially bipolar cells described in section 6.3.1 - are not any more or less common at any of the light levels studied. However, there is some indication that cells with spatially biphasic spatial kernels at one light level do not maintain that receptive field shape across all light levels (some examples of this can be seen in figure

6.2).

6.3.3 Differences in spatial frequency tuning are larger in cells which switch polarity

The mean change in spatial frequency across light levels tended to be larger in cells which switched polarity between ON and OFF than in cells which maintained the same STA polarity. This was consistent across all three animal models, and the difference was statistically significant in C57BL/6 and cpfl1 mice (figures 6.15 - 6.10). This suggests that the switching cells described in chapter 5 are also more likely to change their spatial frequency tuning across light levels.

6.3.4 Receptive field shape in the absence of functional rods or cones

Receptive field shape in the absence of functional rods

Peak spatial frequency was 0.014 cycles per pixel lower in rd17 mice than in C57BL/6 mice at ND 0, the highest experimental light level (figure 6.9, Cliff's delta effect size 0.345 (3 d.p.)).

As outlined in section 1.5.2, the circuits which have been proposed to underpin changes in spatial processing with light level (and which could therefore be responsible for differences in spatial frequency tuning), depend on the balance of voltage across a variety of amacrine - cone bipolar gap junctions. Rod activation can set the membrane potential of these amacrine cells. At high light levels, AII amacrine cells hyperpolarise as a result of reduction in synaptic release from rod bipolar cells. This hyperpolarisation can spread to ON cone-bipolar cell axon terminals and alter the way that spatial information is integrated at their synapses (Grimes *et al.*, 2014)).

Rods can also alter information flow in the opposite direction. Cone bipolars can depolarise amacrine cells through their gap junction connections, causing them to inhibit downstream ganglion cells (Münch *et al.*, 2009). Farrow *et al.* (2013) have hypothesised that rod input to "switch" amacrine cells (through rod-cone gap junctions and rod bipolars in mesopic conditions) may be required to allow the cone bipolar depolarisation to push the amacrine cell above spiking threshold.

In the absence of functional rods, these amacrine - cone bipolar switches may behave differently. For instance, homeostatic plasticity in the rod bipolar pathway in the absence of normal signalling, a lack of drive from rods to cones through rod-cone gap junctions, or the temporal changes in cone input described in section 4.3.2 could all change behaviour across these switches. This could alter the spatial processing of ganglion cells driven by this switch, and result in the lower population spatial frequency tuning in rd17 compared to C57BL/6 mice.

While the population wide difference reported here is interesting, it is not in itself conclusive. In order to understand the extent to which spatial processing is different in rd17 mice at high light levels, ganglion cell responses need to be examined at the subtype rather than whole population level. Additionally, to test the hypothesis that any differences are due to changes in the amacrine - cone bipolar balance in these mice, the responses of these cell types would also need to be examined.

The mean rotational symmetry of the two dimensional Fourier transform was similar in rd17 and C57BL/6 mice across all experimental light levels. This suggests that spatially asymmetric receptive fields are found at similar rates in the absence of functional rods.

Receptive field shape in the absence of functional cones

The markers for receptive field shape used in this study (peak spatial frequency and rotational symmetry of the two dimensional Fourier transform) were distributed similarly at each experimental light level in both cpfl1 and C57BL/6 mice (figures 6.10 and 6.13). In terms of these spatial features, the null hypothesis that cpfl1 and C57BL/6 ganglion cells are from exchangeable populations could not be rejected. This suggests that spatial processing - both in terms of the spatial frequency tuning of cells and the presence of spatially asymmetric receptive fields - may be broadly conserved in the absence of functional cones.

6.3.5 Future work

The results presented here, consistent with previously published work, suggest that a sub-population of retinal ganglion cells change their spatial processing with light level. Additionally, this population may be more likely to switch polarity between ON and OFF with ambient light level. In order to better understand these cells, it will be necessary to isolate them rather than analysing the entire population of recorded ganglion cells.

One method for identifying related sub-populations of cells would be to apply the clustering techniques outlined in chapter 3 to the dataset of spatial kernels or simplified Fourier transforms. By combining these spatial profiles for each cell at all light levels into a single vector, receptive fields with similar spatial profiles and similar patterns of change or consistency across light levels could be identified. It may be necessary to generate a larger sample in order to have sufficient data on some less common ganglion cell subtypes.

Once the population of interest is identified, the next step would be to examine whether the difference in spatial frequency tuning at ND 0 observed in rd17 mice compared to C57BL/6 mice is due to a difference in processing in these cells. If this is the case, further experiments would be required to pick apart how an absence of functional rods alters spatial processing.

PV-1 cells can be genetically labelled (Farrow *et al.*, 2013). Crossing these mice with rd17 mice would enable direct recordings from a population of cells that have been posited to require rod input to enable a light-level dependent spatial processing switch. This could be combined with single cell electrophysiology to compare the membrane potential of amacrine and cone bipolar cells across a range of light levels in rd17 and C57BL/6 mice.

Finally, if changes in retinal ganglion cell spatial processing in rd17 mice prove to be robust, it would be interesting to see whether these differences have an impact at the behavioural level. The mouse optomotor response could be used to measure spatial acuity at comparable experimental light levels, to determine whether rd17 mice have a lower spatial acuity at high light levels comparable with the difference in spatial frequency tuning of retinal ganglion cells observed here (Farrow *et al.*, 2013, Umino *et al.*, 2008).

7 Discussion

In this thesis, I have characterised retinal ganglion cell (RGC) receptive fields over a 4.5 $\log_{10}$ light level range, using the spike triggered average (STA) response to Gaussian spatiotemporal white noise. These experiments were performed to compare retina from wild-type mice (C57BL/6), mice lacking functional cones (cpfl1), and mice lacking functional rods (rd17).

The overarching aim of this project was to determine the effect of loss of rod or cone function on retinal ganglion cell output. In particular, I wanted to test the hypothesis that retinal ganglion cell processing in mesopic conditions and at light levels where signalling is thought to be dominated by the still functional class of photoreceptor cell inputs may actually depend on input from the 'silent' cells.

The work outlined here has demonstrated that, at least in the two specific models of loss of rod and cone function used, retinal ganglion cell output is indeed altered in the absence of a functional photoreceptor cell class, even at light levels where stimulus contrast changes are thought to be transduced primarily through the unaffected input cells.

The most striking differences in retinal ganglion cell output between C57BL/6 controls and models without functional rod or cone input were seen at the level of the temporal kinetics of the STA.

In the absence of functional rods, rd17 mice showed slower STA kinetics at higher light levels. This implies that cone driven ganglion cell responses in these animals are slower than in their C57BL/6 counterparts. As discussed in detail in section 4.3.2, this is likely to be due to changes in cone kinetics in rd17 mice reported (and dismissed) by Nikonov *et al.* (2006). Further experiments will be needed to determine whether this is due to an intrinsic cone cell difference in these mice, or because the presence of functional, hyperpolarised rods in bright light conditions is able to shape the kinetics of cone responses in C57BL/6 mice.

In the absence of functional cones, ganglion cells in cpfl1 showed a marked shift in temporal frequency tuning compared to C57BL/6 counterparts, particularly within the mesopic range. As discussed in section 4.3.3, this could be driven by the rod bipolar cell synapse encoding Michelson rather than Weber contrast at high scotopic or low mesopic light levels (Ke *et al.*, 2014). The fact that this shift is not maintained in cpfl1 STAs obtained from higher light levels raises some questions about this mechanism - as light level increases further, the ganglion cells seem to stop encoding Michelson contrast. Perhaps saturation at the rod-AII synapse is somehow circumvented at these light levels, or perhaps the initial temporal frequency shift is driven by a different mechanism that is light level dependent.

These observed differences in the temporal kinetics of retinal ganglion cells in the absence of functional rods and cones could have substantial consequences for visual processing in these mice, and therefore potentially for human patients with analogous mutations.

The slower STA kinetics observed in rd17 ganglion cells implies that changes in the visual scene are converted into retinal ganglion cell output (spikes) with a delay relative to C57BL/6 counterparts at high light levels. If this delay is preserved in the targets

of retinal ganglion cells, a similar delay in visually driven reflex responses and more complex behavioural tasks might be expected.

The shift in temporal frequency tuning in mesopic conditions in cpfl1 mice is intriguing in the context of anecdotal reports that humans with achromatopsia may be better at some low-light visual tasks than their non-achromat counterparts. For example, in his book "The island of the colorblind" Oliver Sacks (1997) reports a claim that has been repeated by many others: that people with achromatopsia on the Micronesian atoll Pingelap are better at catching flying fish while night fishing than their counterparts without achromatopsia. Higher temporal frequency tuning means that retinal ganglion cells will be driven more strongly by visual motion (contrast modulation within the receptive field; (Suh & Baccus, 2014)). One can imagine that someone with a retina driven more strongly by visual motion at low light levels may be better at locating (and then catching) a flying fish at night.

Of course, extreme caution should be exercised in interpreting the findings of this work in this way. As it stands, there is no hard evidence that these reported behavioural differences are real, and certainly none that they are driven by changes in retinal processing rather than plasticity in the visual cortex or more generally due to more diligent practice of the art of fishing by those with achromatopsia. Still, the difference in the temporal frequency tuning of retinal output in cpfl1 mice is substantial, and the potential for changes in the visually guided behaviour of these mice ought to be examined.

Additionally, in the introduction to this thesis I proposed a third hypothesis: that functional rods are required for luminance-dependent changes in RGC response polarity. Instead, changes in STA polarity were observed in all animal models used, including rd17 mice which lack functional rods. Changes in spatial frequency tuning with light level were also observed in all animal models. In cpfl1 and C57BL/6 mice, cells which

switched polarity between ON and OFF tended to have larger differences in spatial frequency tuning. This difference was also observed in rd17 mice, but it was not statistically significant. Changes in STA polarity and spatial frequency tuning can both be driven by a shift in the balance of ON and OFF inputs to the ganglion cell (Geffen *et al.*, 2007, Kuffler, 1952, Tikidji-Hamburyan *et al.*, 2015, Troy *et al.*, 1993, 1999, Vlasits *et al.*, 2014), so observation of both phenomena in the same cell may be the result of a common mechanism.

There are many previously demonstrated circuit mechanisms that could drive ON and OFF inputs to ganglion cells differentially across light levels, which are described in detail in chapters 5 and 6. Most of these mechanisms involve interaction between what are traditionally considered the 'rod' and 'cone' pathways. If they are also responsible for the changes in STA polarity and spatial frequency tuning seen in cpfl1 and rd17 mice, the results presented here suggest that at least some can continue to function in the absence of functional rod input, or in the absence of functional cone input.

Intriguingly, the percentage of cells which switch polarity between any two light levels in cpfl1 mice (17.11% (2 d.p.)) and the percentage which switch in rd17 mice (6.58% (2 d.p.)) sum to close to the percentage of cells identified as switching in C57BL/6 mice (28.17% (2 d.p.)). There is a possibility that these represent two non-overlapping populations of switching cells, with the majority being driven more by cone hyperpolarisation than rod hyperpolarisation. However, the current data are not sufficient to confirm or refute this hypothesis.

An alternative explanation could be that changes in the balance of ON and OFF inputs do not specifically require input from rods or cones. Instead, they could be driven by changes in lateral inhibition as more cells are recruited at higher light levels (Odermatt *et al.*, 2012), independent of photoreceptor cell class.

The degree to which retinal ganglion cell response properties in 'wild-type' animals change with ambient light level, reported both in this study and by others (Kuffler, 1952, Münch *et al.*, 2009, Tikidji-Hamburyan *et al.*, 2015, Troy *et al.*, 1993, 1999), has profound implications for our understanding of retinal function. In fact, some degree of qualitative response switching may be the norm rather than the exception (Tikidji-Hamburyan *et al.*, 2015). A retinal ganglion cell which switches between an OFF-dominated STA and an ON-dominated STA, or changes its spatial or temporal frequency tuning, is communicating radically different information about the visual scene to higher visual neurons. This makes the task of neurons in the LGN and visual cortex, for example, much more difficult. Conversely, the mutability of retinal ganglion cell responses could allow for more of the work of visual computation to be done at the level of the retina. It may help to move away from an understanding of the retina as a collection of (linear or nonlinear) filters and instead consider it as a dynamical system where environmental changes (such as differences in ambient light level) can cause it to shift between different attractor states (Miller, 2016).

Beyond the specific analysis outlined in this thesis, this project has produced a rich data set of 602 white noise stimulated retinal ganglion cells which can be used to probe retinal function across light levels and the role of rods and cones in even more depth.

7.1 Future work

7.1.1 Further analysis of existing data

As outlined at the end of chapter 6, the analysis that forms the bulk of this thesis has been performed on the entire population of recorded retinal ganglion cells with significant STAs. Restricting analysis to specific retinal ganglion cell subtypes could reveal

subpopulations which drive the differences observed at the population level (particularly in terms of polarity switching and changes in receptive field shape). As retinal ganglion cell responses are not necessarily consistent across light levels or animal models, identifying functional sub-populations may prove challenging. Even classifying cells into ON and OFF functional classes becomes complicated by polarity switching cells.

However, it may be possible to apply the clustering techniques employed in exploratory data analysis here to instead identify functional ganglion cell subpopulations, as Farrow & Masland (2011) do. Cells could be clustered using STAs or temporal or spatial kernels from a single, arbitrarily chosen light level. Alternatively, the STAs accross all light levels for each cell could be combined into a single vector and used as a more complete description of each cell for the purposes of functional clustering.

At the end of chapter 5, I noted that the polarity switching cells reported here probably represent the extreme end of a larger population of cells in which the balance of ON and OFF inputs changes with ambient light level (similar to those reported by Tikidji-Hamburyan *et al.* (2015)). These cells could be identified using the existing data, by applying principal components analysis to the spike triggered stimulus ensemble. Two clusters of spike triggered stimuli should exist in these cells - stimulus frames in which a decrease in light intensity preceded a spike, and stimulus frames in which a spike was preceded instead by an increase in light intensity. Comparing the size of these two clusters reveals the relative strength of ON versus OFF drive to the cell (Geffen *et al.*, 2007). The STAs of the ON and OFF clusters of the stimulus ensemble can then be used to construct a two-filter LNP model (Gollisch & Meister, 2008).

This technique can be considered a limited form of the spike triggered covariance (STC) (Schwartz *et al.*, 2006), which itself is an extension of the STA. Instead of recovering one liner filter by taking the mean of the spike triggered ensemble, STC analysis enables

the recovery of multiple linear filters by uncovering directions in the spike triggered ensemble in which the variance differs from that of the raw stimulus. The number and distribution of STC filters can be used to quantify the number of stimulus features the retinal ganglion cell is sensitive to (Fairhall *et al.*, 2006, Solomon & Tailby, 2010).

7.1.2 Further experiments

Characterisation of cone signals

The results from chapter 4 suggest that the retina processes cone inputs more slowly in rd17 mice than in C57BL/6 controls at high light levels. Evidence from Nikonov *et al.* (2006) indicate that this may be due to slower temporal kinetics at the level of the rd17 cones themselves. In order to determine if this is the case, loose patch recordings from cones in rd17 and C57BL/6 mice should be performed in identical experimental conditions.

Ideally, patch experiments should be conducted using both dissociated single cones, and cones *in situ* in patches of retinal tissue. If slower responses are observed even in dissociated cones, then the mechanism must be intrinsic to the cones themselves. This would suggest either that cones also make use of GNAT1 in some way, or that the rd17 mouse has an additional cone phenotype from another source. Alternatively, if responses are only slower when cones are embedded in a retinal circuit, this would suggest that functional rods are somehow involved in setting cone response kinetics.

Confirmation in other models

In order to draw conclusions about the role of rods and cones beyond the specific animal models used here, the experiments must be repeated in other models of loss of rod and

cone function. As discussed in chapter 4, cpfl2 (a mutation in GNAT2) and cpfl5 (a mutation in CNGA3) are good candidates for confirmation of the cpfl1 results.

Finding alternative models for loss of rod function may be more difficult, as most models other than rd17 involve extensive degeneration not only in rods, but also subsequent loss of cones. This would make it hard to draw conclusions about 'cone input only' circuits from these retina.

One possible option for confirming rd17 experimental data would be to use a long-acting depolarising optogenetic tool (Mattis *et al.*, 2012) targeted specifically to rods (under the rhodopsin promoter, for example). Rods in C57BL/6 mice could then be selectively depolarised in high light conditions, momentarily recreating the constant dark current release in rd17 rods (Calvert *et al.*, 2000). If the optically activated channel remains open for a long enough period, white noise stimuli could then be played to the retina, hyperpolarising cones while the rods remain depolarised. Periods of visual stimulation could be interspersed with periods of light designed to activate the optogenetic channels.

This experimental design has the advantage that the presence or absence of functional rod responses can be examined in the same circuit, removing potential complicating factors such as long term homeostatic plasticity or ectopic synapse formation that may occur in a congenital model. However, optically activated tools pose a potentially fatal problem where visual stimulation at precise background light levels is involved. Even if the activation light can be switched off during brief periods of visual stimulation and recording, adaptation to the light needed to activate the optogenetic tool is inevitable.

Rod and cone contributions to visual function can also be separated using silent substitution in the Opn1mwR mouse model, which carry a red-shifted cone opsin enabling spectral isolation of rods from cones (Allen & Lucas, 2016). In this experimental paradigm, rod and cone contrast detection can be fully separated. However, silent sub-

stitution stimuli still appear as a constant light level to the 'silent' class of cells. The background light level would still be detected by rods in this protocol, rather than rods having a constant dark current as in the rd17 mouse.

Improvements to stimulus design

One limitation of the experiments reported here is that the viability of the tissue and the stability of the retinal recording is limited, and the amount of time required to generate an STA is long (20 minutes, plus time to adapt to each new light level). Johnston *et al.* (2014) have introduced a technique, known as filtered back projection (FBP), which can map a receptive field with similar accuracy to a 20 minute white noise STA in just 4 minutes. This technique can be modified to separate ON and OFF components in a receptive field, and can also map receptive fields of some direction selective retinal ganglion cells that are not well activated by white noise.

Changing to this method of receptive field measurement could enable finer sampling of the light level space in a shorter experimental time period, increasing the amount of useful data and also reducing the likelihood that recordings become unstable before the full experimental protocol is finished.

Behaviour

Finally, it would be very interesting to test whether the differences reported here are salient at the level of behaviour. The optomotor reflex can be used to assess spatial and temporal frequency tuning of a simple reflex (a mouse will track a moving grating with its head (Umino *et al.*, 2008)). In particular, performing this behavioural test at the same light levels used in this study could help to test the hypothesis that high temporal frequency tuning in cpfl1 retinal ganglion cells at low mesopic light levels may translate

into a behavioural shift in temporal frequency tuning.

7.2 Summary

The work I have undertaken in this thesis has revealed that loss of function in one photoreceptor cell class can indeed impact the visual processing of inputs from the remaining class. Particularly in the case of loss of cone function, these results suggest possible behavioural consequences that require follow-up experiments.

In addition, the changes in receptive field properties observed with light level in all animal models used here add to a developing understanding of RGC receptive fields as dynamic features which change as the visual environment does.

8 Bibliography

Allen, AE, & Lucas, RJ. 2016. Using silent substitution to track the mesopic transition from rod- to cone-based vision in mice. *Investigative Ophthalmology and Visual Science*, **57**(1), 276–287.

Allen, AE, Cameron, MA, Brown, TM, Vugler, AA, & Lucas, RJ. 2010. Visual responses in mice lacking critical components of all known retinal phototransduction cascades. *PloS ONE*, **5**(11), e15063.

Anderson, JR, Jones, BW, Watt, CB, Shaw, MV, Yang, JH, DeMill, D, Lauritzen, JS, Lin, Y, Rapp, KD, Mastronarde, D, Koshevoy, P, Grimm, B, Tasdizen, T, Whitaker, R, & Marc, RE. 2011. Exploring the retinal connectome. *Molecular Vision*, **17**, 355–379.

Ankerst, M, Breunig, MM, Kriegel, HP, & Sander, J. 1999. OPTICS : Ordering Points To Identify the Clustering Structure. *Pages 49–60 of: Proc. ACM SIGMOD Int. Conf. on Management of Data*.

Asteriti, S, Gargini, C, & Cangiano, L. 2014. Mouse rods signal through gap junctions with cones. *eLife*, **3**(1), e01386.

Ayoub, GS, & Copenhagen, DR. 1991. Application of a fluorometric method to measure glutamate release from single retinal photoreceptors. *Journal of neuroscience methods*, **37**(1), 7–14.

Basso, D, Pesarin, F, Salmaso, L, & Solari, A. 2009. *Permutation Tests for Stochastic Ordering and ANOVA: Theory and Applications with R.* New York: Springer Science & Business Media.

Baylor, DA. 1987. Photoreceptor signals and vision. Proctor lecture. *Investigative ophthalmology & visual science*, **28**(1), 34–49.

Baylor, DA, Fuortes, MGF, & O'Bryan, PM. 1971. Lateral interaction between vertebrate photoreceptors. *Vision research*, **45**(2), 305–314.

Baylor, DA, Lamb, TD, & Yau, KW. 1979. Responses of retinal rods to single photons. *J Physiol*, **288**(1), 613–634.

Baylor, DA, Nunn, BJ, & Schnapf, JL. 1984. The photocurrent, noise and spectral sensitivity of rods of the monkey Macaca fascicularis. *J Physiol*, **357**(1), 575–607.

Ben-Hur, A, & Guyon, I. 2003. Detecting stable clusters using principal component analysis. *Pages 159–182 of:* Brownstein, M.J., & Kohodursky, A. (eds), *Functional Genomics: Methods and Protocols.* Humana press.

Berson, DM, Dunn, FA, & Takao, M. 2002. Phototransduction by retinal ganglion cells that set the circadian clock. *Science*, **295**(1), 1070–3.

Bloomfield, SA, & Dacheux, RF. 2001. Rod vision: Pathways and processing in the mammalian retina. *Progress in retinal and eye research*, **20**(3), 351–84.

Bloomfield, SA, & Miller, RF. 1986. A functional organization of ON and OFF pathways in the rabbit retina. *The Journal of Neuroscience*, **6**(1), 1–13.

Buzsáki, G. 2004. Large-scale recording of neuronal ensembles. *Nature neuroscience*, **7**(5), 446–51.

Calvert, PD, Krasnoperova, NV, Lyubarsky, AL, Isayama, T, Nicoló, M, Kosaras, B,

Wong, G, Gannon, KS, Margolskee, RF, Sidman, RL, Pugh, EN, Makino, CL, & Lem, J. 2000. Phototransduction in transgenic mice after targeted deletion of the rod transducin alpha-subunit. *PNAS*, **97**(25), 13913–8.

Cameron, MA, & Lucas, RJ. 2009. Influence of the rod photoresponse on light adaptation and circadian rhythmicity in the cone ERG. *Molecular Vision*, **15**(1), 2209–16.

Cangiano, L, Asteriti, S, Cervetto, L, & Gargini, C. 2012. The photovoltage of rods and cones in the dark-adapted mouse retina. *The Journal of physiology*, **590**(16), 3841–55.

Carcieri, SM, Jacobs, AL, & Nirenberg, S. 2003. Classification of retinal ganglion cells: a statistical approach. *J Neurophysiol*, **90**(1), 1704–13.

Chang, B, Hawes, NL, Hurd, RE, Davisson, MT, Nusinowitz, S, & Heckenlively, JR. 2002. Retinal degeneration mutants in the mouse. *Vision Research*, **42**(1), 517–525.

Chang, B, Grau, T, Dangel, S, Hurd, R, Jurklies, B, Sener, EC, Andreasson, S, Dollfus, H, Baumann, B, Bolz, S, Artemyev, N, Kohl, S, Heckenlively, J, & Wissinger, B. 2009. A homologous genetic basis of the murine cpfl1 mutant and human achromatopsia linked to mutations in the PDE6C gene. *Proceedings of the National Academy of Sciences of the United States of America*, **106**(46), 19581–6.

Chen, S, & Li, W. 2012. A color-coding amacrine cell may provide a blue-Off signal in a mammalian retina. *Nature Neuroscience*, **15**(7), 954–956.

Cheong, SK, Tailby, C, Solomon, SG, & Martin, PR. 2013. Cortical-like receptive fields in the lateral geniculate nucleus of marmoset monkeys. *J Neurosci*, **33**(16), 6864–76.

Chichilnisky, EJ. 2001. A simple white noise analysis of neuronal light. *Network: Computation in Neural Systems*, **12**(1), 199–213.

Chichilnisky, EJ, & Kalmar, RS. 2002. Functional asymmetries in ON and OFF ganglion cells of primate retina. *The Journal of Neuroscience*, **22**(7), 2737–47.

Clark, DA, Benichou, R, Meister, M, & da Silveira, RA. 2013. Dynamical adaptation in photoreceptors. *PLoS Computational Biology*, **9**(11), e1003289.

Cliff, N. 1996. *Ordinal methods for behavioral data analysis.* Routledge.

Czeisler, CA, Shanahan, TL, Klerman, EB, Martens, H, Brotman, DJ, Emens, JS, Klein, T, & Rizzo, JF. 1995. Suppression of melatonin secretion in some blind patients by exposure to bright light. *The New England journal of medicine*, **332**(1), 6–11.

da Silveira, RA, & Roska, B. 2011. Cell types, circuits, computation. *Current opinion in neurobiology*, **21**(1), 664–71.

Dacey, DM, Liao, HW, Peterson, BB, Robinson, FR, Smith, VC, Pokorny, J, Yau, KW, & Gamlin, PD. 2005. Melanopsin-expressing ganglion cells in primate retina signal colour and irradiance and project to the LGN. *Nature*, **433**(1), 749–754.

Dacheux, RF, & Raviola, E. 1986. The rod pathway in the rabbit retina: a depolarizing bipolar and amacrine cell. *The Journal of Neuroscience*, **6**(2), 331–45.

Daszykowski, M, Walczak, B, & Massart, DL. 2001. Looking for natural patterns in data. Part 1. Density-based approach. *Chemometrics and Intelligent Laboratory Systems*, **56**(2), 83–92.

Daszykowski, M, Walczak, B, & Massart, DL. 2002. Looking for natural patterns in analytical data. 2. Tracing local density with OPTICS. *Journal of Chemical Information and Computer Sciences*, **42**(3), 500–507.

De Franceschi, G, Vivattanasarn, T, Saleem, AB, & Solomon, SG. 2016. Vision Guides Selection of Freeze or Flight Defense Strategies in Mice. *Current Biology*, **26**(1), 2150–2154.

Demb, JB. 2007. Cellular mechanisms for direction selectivity in the retina. *Neuron*, **55**(1), 179–86.

Demb, JB. 2008. Functional circuitry of visual adaptation in the retina. *The Journal of physiology*, **586**(18), 4377–4384.

Demb, JB, Haarsma, L, Freed, MA, & Sterling, P. 1999. Functional Circuitry of the Retinal Ganglion Cell's Nonlinear Receptive Field. *The Journal of Neuroscience*, **19**(22), 9756–9767.

DeVries, SH. 2000. Bipolar cells use kainate and AMPA receptors to filter visual information into separate channels. *Neuron*, **28**(1), 847–856.

DeVries, SH, & Baylor, DA. 1995. An alternative pathway for signal flow from rod photoreceptors to ganglion cells in mammalian retina. *Proceedings of the National Academy of Sciences of the United States of America*, **92**(23), 10658–62.

Dryja, TP, Hahn, LB, Reboul, T, & Arnaud, B. 1996. Missense mutation in the gene encoding the α subunit of rod transducin in the Nougaret form of congenital stationary night blindness. *Nature genetics*, **13**, 358–360.

Enroth-Cugell, C, & Freeman, AW. 1987. The receptive-field spatial structure of cat retinal Y cells. *J Phys*, **384**(1), 49–79.

Enroth-Cugell, C, & Robson, JG. 1966. The contrast sensitivity of retinal ganglion cells of the cat. *J Physiol*, **187**(1), 517–552.

Enroth-Cugell, C, & Robson, JG. 1984. Functional characteristics and diversity of cat retinal ganglion cells. Basic characteristics and quantitative description. *Investigative ophthalmology & visual science*, **25**(3), 250–67.

Eriksson, L, Johansson, E, Kettaneh-Wold, N, Trygg, C, Wikström, C, & Wold, S.

2006. PCA. *Pages 39–62 of: Multi- and Megavariate Data Analysis Part 1, Basic Principles and Applications*. Umetrics Academy.

Fadool, JM. 2003. Development of a rod photoreceptor mosaic revealed in transgenic zebrafish. *Developmental Biology*, **258**(2), 277–290.

Fairhall, Adrienne L, Burlingame, C Andrew, Narasimhan, Ramesh, Harris, Robert a, Puchalla, Jason L, & Berry, Michael J. 2006. Selectivity for multiple stimulus features in retinal ganglion cells. *Journal of neurophysiology*, **96**(1), 2724–38.

Farrow, K, & Masland, RH. 2011. Physiological clustering of visual channels in the mouse retina. *J Neurophysiol*, **105**(1), 1516–1530.

Farrow, K, Teixeira, M, Szikra, T, Viney, TJ, Balint, K, Yonehara, K, & Roska, B. 2013. Ambient illumination toggles a neuronal circuit switch in the retina and visual perception at cone threshold. *Neuron*, **78**(2), 325–338.

Field, GD, & Rieke, F. 2002. Nonlinear signal transfer from mouse rods to bipolar cells and implications for visual sensitivity. *Neuron*, **34**(5), 773–85.

Field, GD, Sher, A, Gauthier, JL, Greschner, M, Shlens, J, Litke, AM, & Chichilnisky, EJ. 2007. Spatial properties and functional organization of small bistratified ganglion cells in primate retina. *The Journal of Neuroscience*, **27**(48), 13261–13272.

Field, Greg D., Gauthier, Jeffrey L., Sher, Alexander, Greschner, Martin, Machado, Timothy a., Jepson, Lauren H., Shlens, Jonathon, Gunning, Deborah E., Mathieson, Keith, Dabrowski, Wladyslaw, Paninski, Liam, Litke, Alan M., & Chichilnisky, E. J. 2010. Functional connectivity in the retina at the resolution of photoreceptors. *Nature*, **467**(1), 673–677.

Frechette, ES, Sher, A, Grivich, MI, Petrusca, D, Litke, AM, & Chichilnisky, EJ.

2005. Fidelity of the ensemble code for visual motion in primate retina. *Journal of Neurophysiology*, **94**(1), 119–35.

Fu, Y, Kefalov, V, Luo, DG, Xue, T, & Yau, KW. 2008. Quantal noise from human red cone pigment. *Nature neuroscience*, **11**(5), 565–571.

Gao, F, Pang, JJ, & Wu, SM. 2013. Sign-preserving and sign-inverting synaptic interactions between rod and cone photoreceptors in the dark-adapted retina. *J Physiol*, **591**(22), 5711–5726.

Geffen, MN, de Vries, SEJ, & Meister, M. 2007. Retinal ganglion cells can rapidly change polarity from Off to On. *PLoS Biology*, **5**(3), e65.

Ghosh, KK, Bujan, S, Haverkamp, S, Feigenspan, A, & Wässle, H. 2004. Types of bipolar cells in the mouse retina. *The Journal of Comparative Neurology*, **469**(1), 70–82.

Gold, C, Henze, DA, Koch, C, & Buzsáki, G. 2006. On the origin of the extracellular action potential waveform: A modeling study. *Journal of Neurophysiology*, **95**(5), 3113–28.

Gollisch, T. 2013. Features and functions of nonlinear spatial integration by retinal ganglion cells. *Journal of physiology, Paris*, **107**(5), 338–48.

Gollisch, T, & Meister, M. 2008. Modeling convergent ON and OFF pathways in the early visual system. *Biological Cybernetics*, **99**(4), 263–78.

Gollisch, T, & Meister, M. 2010. Eye smarter than scientists believed: neural computations in circuits of the retina. *Neuron*, **65**(2), 150–64.

Grimes, WN, Schwartz, GW, & Rieke, F. 2014. The synaptic and circuit mechanisms underlying a change in spatial encoding in the retina. *Neuron*, **82**(2), 460–73.

Hack, I, Peichl, L, & Brandstätter, JH. 1999. An alternative pathway for rod signals in the rodent retina: rod photoreceptors, cone bipolar cells, and the localization of glutamate receptors. *PNAS*, **96**(24), 14130–5.

Hardie, RC. 2001. Phototransduction in Drosophila melanogaster. *Journal of Experimental Biology*, **204**(1), 3403–3409.

Hargrave, PA, & McDowell, JH. 1992. Rhodopsin and phototransduction: a model system for G protein-linked receptors. *The FASEB journal*, **6**(1), 2323–2331.

Hattar, S, Liao, HW, Takao, M, Berson, DM, & Yau, KW. 2002. Melanopsin-containing retinal ganglion cells: architecture, projections, and intrinsic photosensitivity. *Science*, **295**(5557), 1065–1070.

Hattar, S, Kumar, M, & Park, A. 2006. Central projections of melanopsinexpressing retinal ganglion cells in the mouse. *Journal of Comparative Neurology*, **497**(1), 326–349.

Haverkamp, S. 2006. Synaptic Plasticity in CNGA3-/- Mice: Cone Bipolar Cells React on the Missing Cone Input and Form Ectopic Synapses with Rods. *Journal of Neuroscience*, **26**(19), 5248–5255.

Haverkamp, S, Wässle, H, Duebel, J, Kuner, T, Augustine, GJ, Feng, G, & Euler, T. 2005. The primordial, blue-cone color system of the mouse retina. *The Journal of neuroscience*, **25**(22), 5438–45.

Hecht, BYS, Shlaer, S, & Pirenne, MH. 1942. Energy, quanta, and vision. *The Journal of General Physiology*, **25**(6), 819–840.

Hill, DN, Mehta, SB, & Kleinfeld, D. 2011. Quality metrics to accompany spike sorting of extracellular signals. *The Journal of Neuroscience*, **31**(24), 8699–705.

Hornstein, EP, Verweij, J, Li, PH, & Schnapf, JL. 2005. Gap-Junctional Coupling

and Absolute Sensitivity of Photoreceptors in Macaque Retina. *J Neurosci*, **25**(48), 11201–11209.

Huang, JY, & Protti, DA. 2016. The impact of inhibitory mechanisms in the inner retina on spatial tuning of RGCs. *Scientific Reports*, **6**(1), 21966.

Imai, H, Terakita, a, Tachibanaki, S, Imamoto, Y, Yoshizawa, T, & Shichida, Y. 1997. Photochemical and biochemical properties of chicken blue-sensitive cone visual pigment. *Biochemistry*, **36**(42), 12773–9.

Jarsky, T, Cembrowski, M, Logan, SM, Kath, WL, Riecke, H, Demb, JB, & Singer, JH. 2011. A synaptic mechanism for retinal adaptation to luminance and contrast. *The Journal of Neuroscience*, **31**(30), 11003–15.

Jeon, CJ, Strettoi, E, & Masland, RH. 1998. The major cell populations of the mouse retina. *The Journal of Neuroscience*, **18**(21), 8936–8946.

Johnston, J, Esposti, F, & Lagnado, L. 2012. Color Vision: Retinal Blues. *Current Biology*, **22**(16), 637–639.

Johnston, J, Ding, H, Seibel, SH, Esposti, F, & Lagnado, L. 2014. Rapid mapping of visual receptive fields by filtered back projection: application to multi-neuronal electrophysiology and imaging. *J Physiol*, **592**(22), 4839–54.

Jolliffe, IT. 2002. *Principal Component Analysis*. Second edn. New York: Springer.

Jones, JP, & Palmer, LA. 1987. An evaluation of the two-dimensional Gabor filter model of simple receptive fields in cat striate cortex. *Journal of Neurophysiology*, **58**(6), 1233–1258.

Kaardal, J, Fitzgerald, JD, Berry, MJ, & Sharpee, TO. 2013. Identifying Functional Bases for Multidimensional. *Neural Computation*, **25**(1), 1870–1890.

Kaplan, E, & Benardete, E. 2001. The dynamics of primate retinal ganglion cells. *Progress in brain research*.

Kay, K. 2013. *knkutils - https://github.com/kendrickkay/knkutils*.

Ke, JB, Wang, YV, Borghuis, BG, Cembrowski, MS, Riecke, H, Kath, WL, Demb, JB, & Singer, JH. 2014. Adaptation to background light enables contrast coding at rod bipolar cell synapses. *Neuron*, **81**(2), 388–401.

Keeler, CE, Sutcliffe, E, & Chaffee, EL. 1928. Normal and rodless retinae of the house mouse with respect to the electromotive force generated through stimulation by light. *PNAS*, **14**(1), 477–484.

Kefalov, V, Fu, Y, Marsh-Armstrong, N, & Yau, KW. 2003. Role of visual pigment properties in rod and cone phototransduction. *Nature*, **425**(6957), 526–531.

Kefalov, VJ. 2012. Rod and cone visual pigments and phototransduction through pharmacological, genetic, and physiological approaches. *The Journal of biological chemistry*, **287**(3), 1635–41.

Kim, IJ, Zhang, Y, Yamagata, M, Meister, M, & Sanes, JR. 2008. Molecular identification of a retinal cell type that responds to upward motion. *Nature*, **452**(1), 478–82.

Klerman, EB, Shanahan, TL, Brotman, DJ, Rimmer, DW, Emens, JS, Rizzo, JF, & Czeisler, CA. 2002. Photic Resetting of the Human Circadian Pacemaker in the Absence of Conscious Vision. *Journal of Biological Rhythms*, **17**(6), 548–555.

Kolb, H. 1995. Cone Pathways through the Retina. *In:* Kolb, H, Fernandez, E, & Nelson, R (eds), *Webvision: The Organization of the Retina and Visual System.* Salt Lake City (UT): University of Utah Health Sciences Center.

Kolb, H, & Famigilietti, EV. 1974. Rod and Cone Pathways in the Inner Plexiform Layer of Cat Retina. *Science*, **186**(4158), 47–49.

Kolesnikov, AV, Tang, PH, Parker, RO, Crouch, RK, & Kefalov, VJ. 2011. The mammalian cone visual cycle promotes rapid M/L-cone pigment regeneration independently of the interphotoreceptor retinoid-binding protein. *J Neurosci*, **31**(21), 7900–7909.

Kuffler, SW. 1952. Discharge patterns and functional organization of mammalian retina. *J Neurophysiol*, **16**(1), 37–68.

Lagnado, L. 2012. New light on photon detection. *J Physiol*, **590**(16), 3641–2.

Lamb, Trevor. 1995. Part XIV: Evolution of Phototransduction, Vertebrate Photoreceptors and Retina. *In:* Kolb, H, Fernandez, E, & Nelson, R (eds), *Webvision: The Organization of the Retina and Visual System.* Salt Lake City (UT): University of Utah Health Sciences Center.

Lebedev, DS, & Marshak, DW. 2007. Amacrine cell contributions to red-green color opponency in central primate retina: a model study. *Visual Neuroscience*, **24**(4), 535–47.

Lee, EJ, Han, JW, Kim, HJ, Kim, IB, Lee, MY, Oh, SJ, Chung, JW, & Chun, MH. 2003a. The immunocytochemical localization of connexin 36 at rod and cone gap junctions in the guinea pig retina. *European Journal of Neuroscience*, **18**(11), 2925–2934.

Lee, SC, Hayashida, Y, & Ishida, AT. 2003b. Availability of low-threshold Ca2+ current in retinal ganglion cells. *Journal of neurophysiology*, **90**(6), 3888–901.

Li, PH, & Verweij, J. 2012. Gap-junctional coupling of mammalian rod photoreceptors and its effect on visual detection. *J Neurosci*, **32**(10), 3552–3562.

Li, S, Huang, L, Xiao, X, Jia, X, Guo, X, & Zhang, Q. 2014. Identification of CNGA3 Mutations in 46 Families: Common Cause of Achromatopsia and Cone-Rod Dystrophies in Chinese Patients. *JAMA ophthalmology*, **132**(9), 1076–83.

Lidierth, M. 2009. sigTOOL: A MATLAB-based environment for sharing laboratory-developed software to analyze biological signals. *Journal of neuroscience methods*, **178**(1), 188–96.

Lyubarsky, AL, Falsini, B, Pennesi, ME, Valentini, P, & Pugh, EN. 1999. UV- and midwave-sensitive cone-driven retinal responses of the mouse: a possible phenotype for coexpression of cone photopigments. *The Journal of Neuroscience*, **19**(1), 442–455.

Ma, S, & Dai, Y. 2011. Principal component analysis based methods in bioinformatics studies. *Briefings in Bioinformatics*, **12**(6), 714–722.

Manly, BFJ. 2007. *Randomization, Bootstrap, and Monte Carlo Methods in Biology.* 3rd edn. London: Chapman & Hall.

Manookin, MB, Beaudoin, DL, Ernst, ZR, Flagel, LJ, & Demb, JB. 2008. Disinhibition combines with excitation to extend the operating range of the OFF visual pathway in daylight. *J Neurosci*, **28**(16), 4136–4150.

Marco, SD, Protti, DA, & Solomon, SG. 2013. Excitatory and inhibitory contributions to receptive fields of alpha-like retinal ganglion cells in mouse. *J Neurophysiol*, **110**(6), 1426–1440.

Markiewicz, T, & Osowski, S. 2006. Data Mining Techniques for Feature Selection in Blood Cell Recognition. *Pages 26–28 of: European Symposium on Artificial Neural Networks.*

Masland, RH. 2001a. Neuronal diversity in the retina. *Current opinion in neurobiology*, **11**(4), 431–6.

Masland, RH. 2001b. The fundamental plan of the retina. *Nature neuroscience*, **4**(9), 877–86.

Masland, RH, & Martin, PR. 2007. The unsolved mystery of vision. *Current biology*, **17**(15), 577–82.

Mattis, J, Tye, KM, Ferenczi, EA, Ramakrishnan, C, O'Shea, DJ, Prakash, R, Gunaydin, LA, Hyun, M, Fenno, LE, Gradinaru, V, Yizhar, O, & Deisseroth, K. 2012. Principles for applying optogenetic tools derived from direct comparative analysis of microbial opsins. *Nature Methods*, **9**(2), 159–172.

McFarland, JM, Cui, Y, & Butts, DA. 2013. Inferring nonlinear neuronal computation based on physiologically plausible inputs. *PLoS Computational Biology*, **9**(7), e1003143.

Miller, P. 2016. Dynamical systems, attractors, and neural circuits. *F1000Research*, **5**(992), 1–18.

Molnar, A, Hsueh, HA, Roska, B, & Werblin, FS. 2009. Crossover inhibition in the retina: Circuitry that compensates for nonlinear rectifying synaptic transmission. *Journal of Computational Neuroscience*, **27**(3), 569–590.

Münch, TA, & Tikidji-Hamburyan, A. 2014. The Output of the Retina Qualitatively Changes at Different Light Levels. *Page Abstract Number 5008 of: Invest Ophthalmol Vis Sci.*

Münch, TA, Azeredo, R, Siegert, S, Viney, TJ, Awatramani, GB, & Roska, B. 2009. Approach sensitivity in the retina processed by a multifunctional neural circuit. *Nature Neuroscience*, **12**(10), 1308–1316.

Naeem, MA, Chavali, VRM, Ali, S, Iqbal, M, Riazuddin, S, Khan, SN, Husnain, T, Sieving, PA, Ayyagari, R, Riazuddin, S, Hejtmancik, JF, & Riazuddin, SA. 2012. GNAT1 associated with autosomal recessive congenital stationary night blindness. *Investigative ophthalmology & visual science*, **53**(3), 1353–61.

Nelson, R, & Kolb, H. 1983. Synaptic patterns and response properties of bipolar and ganglion cells in the cat retina. *Vision research*, **23**(10), 1183–95.

Nickle, B, & Robinson, PR. 2007. The opsins of the vertebrate retina: insights from structural, biochemical, and evolutionary studies. *Cellular and molecular life sciences*, **64**(22), 2917–32.

Nikonov, SS, Kholodenko, R, Lem, J, & Pugh, EN. 2006. Physiological Features of the S- and M-cone Photoreceptors of Wild-type Mice from Single-cell Recordings. *Journal of General Physiology*, **127**(4), 359–374.

Nirenberg, S, Bomash, I, Pillow, JW, & Victor, JD. 2010. Heterogeneous Response Dynamics in Retinal Ganglion Cells: The Interplay of Predictive Coding and Adaptation. *J Neurophysiol*, **103**(1), 3184–3194.

Odermatt, B, Nikolaev, A, & Lagnado, L. 2012. Encoding of Luminance and Contrast by Linear and Nonlinear Synapses in the Retina. *Neuron*, **73**(4), 758–773.

Ortin-Martinez, A, Nadal-Nicola, FM, Jimenez-Lopez, M, Juan, ABJ, Nieto-Lopez, L, Garca-Ayuso, D, Villegas-Perez, MP, Vidal-Sanz, M, & Agudo-Barriuso, M. 2014. Number and Distribution of Mouse Retinal Cone Photoreceptors : Differences between an Albino (Swiss) and a Pigmented (C57/BL6) Strain. *PloS One*, **9**(7), e102392.

Osterberg, G. 1935. Topography of the layer of rods and cones in the human retina. *Acta Ophthalmol Suppl*, 1–103.

Pandarinath, C, Victor, JD, & Nirenberg, S. 2010. Symmetry breakdown in the ON and OFF pathways of the retina at night: functional implications. *The Journal of Neuroscience*, **30**(30), 10006–14.

Pang, JJ, Alexander, J, Lei, B, Deng, W, Zhang, K, Li, Q, Chang, B, & Hauswirth, WW. 2010. Achromatopsia as a Potential Candidate for Gene Therapy. *Adv Exp Med Biol*, **664**(1), 639–646.

Pang, JJ, Gao, F, & Wu, SM. 2012. Ionotropic glutamate receptors mediate OFF responses in light- adapted ON bipolar cells. *Vision Res*, **61**(1), 48–58.

Pearson, K. 1901. On lines and planes of closest fit to systems of points in space. *Philosophical Magazine*, **2**(1), 559–572.

Peng, YW, Hao, Y, Petters, RM, & Wong, F. 2000. Ectopic synaptogenesis in the mammalian retina caused by rod photoreceptor-specific mutations. *Nature neuroscience*, **3**(11), 1121–7.

Pillow, JW. 2005. *Neural coding and the statistical modeling of neuronal responses*. PhD, New York University.

Pillow, JW, & Simoncelli, EP. 2006. Dimensionality reduction in neural models : An information-theoretic generalization of spike-triggered average and covariance analysis. *Journal of Vision*, **6**(1), 414–428.

Piscopo, DM, El-danaf, RN, Huberman, AD, & Niell, CM. 2013. Diverse Visual Features Encoded in Mouse Lateral Geniculate Nucleus. *The Journal of Neuroscience*, **33**(11), 4642–4656.

Puchalla, JL, Schneidman, E, Harris, RA, & Berry, MJ. 2005. Redundancy in the population code of the retina. *Neuron*, **46**(3), 493–504.

Puller, C, & Haverkamp, S. 2011. Bipolar cell pathways for color vision in non-primate dichromats. *Visual neuroscience*, **28**(1), 51–60.

Quiroga, RQ, Nadasdy, Z, & Ben-Shaul, Y. 2004. Unsupervised spike detection and sorting with wavelets and superparamagnetic clustering. *Neural computation*, **16**(8), 1661–87.

Rattner, A, Sun, H, & Nathans, J. 1999. Molecular genetics of human retinal disease. *Annual review of genetics*, **33**(1), 89–131.

Raviola, Elio, & Gilula, NB. 1973. Gap junctions between photoreceptor cells in the vertebrate retina. *PNAS*, **70**(6), 1677–1681.

Redmond, TM, Yu, S, Lee, E, Bok, D, Hamasaki, D, Chen, N, Goletz, P, Ma, JX, Crouch, RK, & Pfeifer, K. 1998. Rpe65 is necessary for production of 11-cis-vitamin A in the retinal visual cycle. *Nature genetics*, **20**(4), 344–351.

Ribelayga, C, Cao, Y, & Mangel, SC. 2008. The circadian clock in the retina controls rod-cone coupling. *Neuron*, **59**(5), 790–801.

Rieke, F, & Baylor, D. 1998. Single-photon detection by rod cells of the retina. *Reviews of Modern Physics*, **70**(3), 1027–1036.

Ringnér, M. 2008. What is principal component analysis? *Nat Biotechnol*, **26**(3), 303–304.

Ronan, T, Qi, Z, & Naegle, KM. 2016. Avoiding common pitfalls when clustering biological data. *Science Signalling*, **432**(x), re6.

Rosa, JM, Ruehle, S, Ding, H, & Lagnado, L. 2016. Crossover Inhibition Generates Sustained Visual Responses in the Inner Retina. *Neuron*, **90**(2), 308–319.

Rust, NC, Schwartz, O, Movshon, J, & Simoncelli, EP. 2005. Spatiotemporal elements of macaque v1 receptive fields. *Neuron*, **46**(6), 945–56.

Saari, JC. 2000. Biochemistry of Visual Pigment Regeneration; The Friedenwald Lecture. *Investigative ophthalmology & visual science*, **41**(2), 337–348.

Sacks, O. 1997. *The island of the colorblind*. First amer edn. A.A. Knopf.

Sampath, AP, & Rieke, F. 2004. Selective transmission of single photon responses by saturation at the rod-to-rod bipolar synapse. *Neuron*, **41**(3), 431–43.

Schultze, M. 1866. *Zur Anatomie und Physiologie der Retina*. Bonn; Cohen.

Schwartz, G, & Rieke, F. 2011. Perspectives on: information and coding in mammalian sensory physiology: nonlinear spatial encoding by retinal ganglion cells: when 1 + 1 2. *The Journal of general physiology*, **138**(3), 283–90.

Schwartz, Gregory W, Okawa, Haruhisa, Dunn, Felice a, Morgan, Josh L, Kerschensteiner, Daniel, Wong, Rachel O, & Rieke, Fred. 2012. The spatial structure of a nonlinear receptive field. *Nature neuroscience*, **15**(11), 1572–80.

Schwartz, O, Pillow, JW, Rust, NC, & Simoncelli, EP. 2006. Spike-triggered neural characterization. *Journal of Vision*, **6**(1), 484–507.

Sekirnjak, C, Jepson, LH, Hottowy, P, Sher, A, Dabrowski, W, Litke, AM, & Chichilnisky, EJ. 2011. Changes in physiological properties of rat ganglion cells during retinal degeneration. *Journal of neurophysiology*, **105**(5), 2560–71.

Sheasby, BW, & Fohlmeister, JF. 1999. Impulse encoding across the dendritic morphologies of retinal ganglion cells. *Journal of neurophysiology*, **81**(1), 1685–1698.

Sher, A, & DeVries, SH. 2012. A non-canonical pathway for mammalian blue-green color vision. *Nature Neuroscience*, **15**(7), 952–953.

Söhl, G, Maxeiner, S, & Willecke, K. 2005. Expression and functions of neuronal gap junctions. *Nature reviews. Neuroscience*, **6**(3), 191–200.

Solomon, SG, & Tailby, C. 2010. Linear and nonlinear contributions to the visual sensitivity of neurons in primate lateral geniculate nucleus. *Journal of Neurophysiology*, **104**(1), 1884–1898.

Soucy, E, Wang, Y, Nirenberg, S, Nathans, J, & Meister, M. 1998. A novel signaling pathway from rod photoreceptors to ganglion cells in mammalian retina. *Neuron*, **21**(3), 481–93.

Stabell, B, & Stabell, U. 2013. *Duplicity Theory of Vision: From Newton to the Present*. Cambridge UK: Cambridge University Press.

Stephens, GJ, Johnson-Kerner, B, Bialek, W, & Ryu, WS. 2008. Dimensionality and dynamics in the behavior of C. elegans. *PLoS Computational Biology*, **4**(4), e1000028.

Strettoi, E, Dacheux, RF, & Raviola, E. 1990. Synaptic connections of rod bipolar cells in the inner plexiform layer of the rabbit retina. *J Comp Neurol*, **3**(295), 449–66.

Suh, B, & Baccus, SA. 2014. Building Blocks of Temporal Filters in Retinal Synapses. *PLoS Biology*, **12**(10), e1001973.

Sun, W, Deng, Q, Levick, WR, & He, S. 2006. ON direction-selective ganglion cells in the mouse retina. *The Journal of physiology*, **576**(1), 197–202.

Sundaram, V, Wilde, C, Aboshiha, J, Cowing, J, Han, C, Langlo, CS, Chana, R, Davidson, AE, Sergouniotis, PI, Bainbridge, JW, Ali, RR, Dubra, A, Rubin, G, Webster, AR, Moore, AT, Nardini, M, Carroll, J, & Michaelides, M. 2014. Retinal structure and function in achromatopsia: implications for gene therapy. *Ophthalmology*, **121**(1), 234–45.

Szikra, T, Trenholm, S, Drinnenberg, A, Jüttner, J, Raics, Z, Farrow, K, Biel, M,

Awatramani, G, Clark, DA, Sahel, JA, da Silveira, RA, & Roska, B. 2014. Rods in daylight act as relay cells for cone-driven horizontal cellmediated surround inhibition. *Nature Neuroscience*, **17**(12), 1728–1735.

Tian, L, & Kammermeier, PJ. 2006. G protein coupling profile of mGluR6 and expression of G alpha proteins in retinal ON bipolar cells. *Visual neuroscience*, **23**(6), 909–16.

Tikidji-Hamburyan, A, Reinhard, K, Seitter, H, Hovhannisyan, A, Procyk, CA, Allen, AE, Schenk, M, Lucas, RJ, & Munch, TA. 2015. Retinal output changes qualitatively with every change in ambient illuminance. *Nat Neurosci*, **18**(1), 66–74.

Tinsley, JN, Molodtsov, MI, Prevedel, R, Wartmann, D, Espigulé-Pons, J, Lauwers, M, & Vaziri, A. 2016. Direct detection of a single photon by humans. *Nature communications*, **7**(12172).

Tovee, MJ. 1994. The molecular genetics and evolution of primate colour vision. *Trends in neurosciences*, **17**(1), 30–7.

Troy, JB, Oh, JK, & Enroth-Cugell, C. 1993. Effect of ambient illumination on the spatial properties of the center and surround of Y-cell receptive fields. *Visual neuroscience*, **10**(4), 753–764.

Troy, JB, Bohnsack, DL, & Diller, LC. 1999. Spatial properties of the cat X-cell receptive field as a function of mean light level. *Visual neuroscience*, **16**(6), 1089–1104.

Tsukamoto, Y, & Omi, N. 2013. Functional allocation of synaptic contacts in microcircuits from rods via rod bipolar to AII amacrine cells in the mouse retina. *The Journal of comparative neurology*, **521**(15), 3541–55.

Tsukamoto, Y, Morigiwa, K, Ueda, M, & Sterling, P. 2001. Microcircuits for night vision in mouse retina. *The Journal of Neuroscience*, **21**(21), 8616–23.

Tsukamoto, Yoshihiko, & Omi, Naoko. 2014. Some OFF bipolar cell types make contact with both rods and cones in macaque and mouse retinas. *Frontiers in Neuroanatomy*, **8**(1), 105.

Umino, Y, Solessio, E, & Barlow, RB. 2008. Speed, spatial, and temporal tuning of rod and cone vision in mouse. *The Journal of Neuroscience*, **28**(1), 189–98.

Van Gelder, RN. 2008. Non-visual photoreception: sensing light without sight. *Current biology*, **18**(1), 38–9.

Venkataramani, S, & Taylor, WR. 2016. Synaptic Mechanisms Generating Orientation Selectivity in the ON Pathway of the Rabbit Retina. *J Neurosci*, **36**(11), 3336–3349.

Vlasits, AL, Bos, R, Morrie, RD, Fortuny, C, Flannery, JG, Feller, MB, & Rivlin-Etzion, M. 2014. Visual stimulation switches the polarity of excitatory input to starburst amacrine cells. *Neuron*, **83**(5), 1172–1184.

Völgyi, B, Chheda, S, & Bloomfield, SA. 2009. Tracer coupling patterns of the ganglion cell subtypes in the mouse retina. *Journal of Comparative Neurology*, **512**(5), 664–687.

Wall, ME, Rechtsteiner, A, & Rocha, LM. 2003. Singular value decomposition and principal component analysis. *Chap. 5, pages 91–109 of:* Berrar, D.P., Dubitzky, W., & Granzow, M. (eds), *A Practical Approach to Microarray Data Analysis*. Norwell, MA: Kluwer.

Wang, YV, Weick, M, & Demb, JB. 2011. Spectral and temporal sensitivity of cone-mediated responses in mouse retinal ganglion cells. *The Journal of Neuroscience*, **31**(21), 7670–81.

Wässle, H. 2004. Parallel processing in the mammalian retina. *Nature Reviews Neuroscience*, **5**(10), 747–57.

Weng, S, Sun, W, & He, S. 2005. Identification of ON-OFF direction-selective ganglion cells in the mouse retina. *The Journal of physiology*, **562**(3), 915–23.

Wolfe, J, & Palmer, LA. 1998. Temporal diversity in the lateral geniculate nucleus of cat. *Visual Neuroscience*, **15**(4), 653–75.

Wong, KY, Dunn, FA, Graham, DM, & Berson, DM. 2007. Synaptic influences on rat ganglion-cell photoreceptors. *The Journal of physiology*, **582**(1), 279–96.

Yang, CY, Zhang, J, & Yazulla, S. 2003. Differential synaptic organization of GABAergic bipolar cells and non-GABAergic (glutamatergic) bipolar cells in the tiger salamander retina. *The Journal of comparative neurology*, **455**(2), 187–97.

Yang, XL, & Wu, SM. 1991. Feedforward lateral inhibition in retinal bipolar cells: input-output relation of the horizontal cell-depolarizing bipolar cell synapse. *PNAS*, **88**(8), 3310–3.

Yau, KW. 1994. Phototransduction mechanism in retinal rods and cones; The Friedenwald Lecture. *Investigative ophthalmology & visual science*, **35**(1), 9–32.

Yilmaz, M, & Meister, M. 2013. Rapid innate defensive responses of mice to looming visual stimuli. *Current Biology*, **23**(20), 2011–2015.

Yonehara, K, Balint, K, Noda, M, Nagel, G, Bamberg, E, & Roska, B. 2011. Spatially asymmetric reorganization of inhibition establishes a motion-sensitive circuit. *Nature*, **469**(1), 407–10.

Zeitz, C. 2007. Molecular genetics and protein function involved in nocturnal vision. *Expert Review of Ophthalmology*, **2**(3), 467–485.

Zhang, Y, Kim, IJ, Sanes, JR, & Meister, M. 2012. The most numerous ganglion cell type of the mouse retina is a selective feature detector. *PNAS*, **109**(36), E2391–8.